

Multiscale Materials Design of Natural Exoskeletons:

Fish Armor

by

Juha Song

Submitted to the Department of Materials Science and Engineering
in partial fulfillment of the requirements for the degree of

Doctor of Philosophy in Materials Science and Engineering
at the
MASSACHUSETTS INSTITUTE OF TECHNOLOGY

September 2011

© Massachusetts Institute of Technology 2011. All rights reserved.

Author.....

Department of Materials Science and Engineering
July 6, 2011

Certified by.....

Mary C. Boyce
Gail E. Kendall Professor of Mechanical Engineering, Head of Department
Thesis Supervisor

Certified by.....

Christine Ortiz
Professor of Materials Science and Engineering
Thesis Supervisor

Accepted by.....

Christopher A. Schuh
Danae and Vasilios Salapatas Professor of Metallurgy
Chair, Departmental Committee on Graduate Students

Multiscale Materials Design of Natural Exoskeletons: Fish Armor

By
Juha Song

Submitted to the Department of Materials Science and Engineering
On July 6, 2011 in partial fulfillment of the
requirements for the degree of
Doctor of Philosophy in Materials Science and Engineering

Abstract

Biological materials have developed hierarchical and heterogeneous material nanostructures and microstructures to provide protection against various environmental threats that, in turn, provide bioinspired clues to man-made, protective material designs. In particular, designs of dermal fish armor are a tradeoff between protection and mobility. A comprehensive knowledge base of the materials and mechanical design principles of fish armor has broad applicability to the development of synthetic engineered protective/flexible materials. In this thesis, two fish armor model systems have been investigated by means of structure-property-function relationships, ultimately answering how the armor systems have been designed in response to their environmental threats.

The first model system, *Polypterus senegalus* are descendants of ancient fish and their body is covered by a natural armor consisting of small bony scales. The quad-layered armor scales are composed of ganoine, dentin, isopedine and bone, to protect against predatory biting attacks. First of all, multilayer design principles of *P. senegalus* scales were understood with respect to penetration resistance by the multiscale experimental and computational study. The quadlayered scales exhibit mechanical gradient within and between material layers and have geometrically corrugated junctions with an undetectable gradation; all of which lead to effective penetration resistance including load-dependent effective material properties, circumferential surface cracking, plastic dissipation in the underlying dentin layer, stress redistribution around the interfaces with suppression of interfacial failure. Secondly, since the outmost ganoine is structurally anisotropic, the roles of anisotropy of ganoine in the entire system have been investigated by combining orientation-dependant indentation and mechanical modeling. The elastic-plastic anisotropy of the ganoine layer enhances the load-dependent penetration resistance of the multilayered armor compared with the isotropic ganoine layer mainly by (i) enhancing the transmission of stress and dissipation to the underlying dentin layer, (ii) lowering the ganoine/dentin interfacial stresses and hence reducing any propensity toward delamination, and (iii) providing discrete structural pathways for cracks to propagate normal to the surface for easy arrest by the underlying dentin layer.

Inspired by *P. senegalus* scales, threat-protection interaction and structure-function relationships among various layered armor systems have been investigated using parametric studies with finite element (FE) models. Geometry, microstructure and mechanical properties of a threat system significantly influence its ability to effectively penetrate into the armor system or to be defeated by the armor. Simultaneously, three structure parameters of multilayered armor designs are mainly considered: (i) the thickness of the outmost layer; (ii) the quad-layered vs. bilayer structure; and (iii) the sequence of the outer two layers. The role of the armor microstructure in defeating threats as well as providing avenues of energy dissipation to withstand biting attacks is identified. Microstructural length scale and material property matching between the threat and armor is clearly observed. Bilayered and quadlayered models are mechanically comparable, but the quad-layer model achieves a weight reduction. Studies of predator-prey threat-protection interactions may lead to insights into tunability in mechanical functionality of each system in conjunction with adaptive phenotypic plasticity of the tooth and scale microstructure and geometry, “adaptive stalemates,” and the so-called evolutionary “arms race.”

The second model system, *Gasterosteus aculeatus*, is well-known for light-weight and morphologically varied armor structure among different *G. aculeatus* populations. Marine and freshwater *G. aculeatus* armor structures have been assessed quantitatively by micro-computed tomography (μ CT) technique. The convolution of plate geometry in conjunction with plate-to-plate overlap allows a relatively constant armor thickness to be maintained throughout the assembly, promoting spatially homogeneous protection and thereby avoiding weakness at the armor unit interconnections. Plate-to-plate junctures act to register and join the plates while permitting compliance in sliding and rotation in selected directions. SEM and μ CT revealed a porous, sandwich-like cross-section of lateral plates beneficial for bending stiffness and strength at minimum weight. Moreover, the structural parameters of the pelvic assemblies were also quantified via μ CT, which include the spatial dependence of the suture amplitude and frequency, the suture plate inclination angle, and the suture gap. Significant differences in these structural parameters were observed between the different *G. aculeatus* populations. Composite analytical and finite element computational models were developed and used in conjunction with the μ CT data to simulate the mechanical behavior of the pelvic assembly, to predict the effective suture stiffness and to understand the conformational change of the pelvic assembly from the “rest” to “offensive” states. This study elucidates the structural and functional differences between different divergent populations of *G. aculeatus* and serves as a model for other systems of interest in evolutionary biology.

Thesis Supervisor: Mary C. Boyce

Title: Gail E. Kendall Professor of Mechanical Engineering, Head of Department

Thesis Supervisor: Christine Ortiz

Title: Professor of Materials Science and Engineering

Acknowledgement

My five-year journey at MIT is ending. I dare say it was not easy at all, but it has been one of the most valuable experiences I have had. Back in 2006 when I came here with anxiety and ambition, I didn't think about this moment as it was too far for me to imagine. Now, I know how lucky I was to go through this period and get to this moment, and I realize how many great people have supported me and shared their time and experience with me. Here, I wish to express my heartfelt gratitude.

First of all, I owe my two advisors, Prof. Christine Ortiz and Prof. Mary C. Boyce, a great debt. Prof. Ortiz has encouraged me to think critically when setting up a new scientific problem and doing research. Prof. Boyce has taught me important principles of mechanics and provided thoughtful insights. Both professors have encouraged independent and creative research, training me to overcome the problems I faced. They allowed me to propose and try new ideas even though I couldn't be sure if they would work in practice. They also gave me unlimited opportunities to collaborate with other researchers from various backgrounds, which enriched my knowledge and experience and motivated me to explore a world to which I didn't yet belong. They have been intelligent, passionate, elegant, and patient as advisors and mentors. In fact, one of the best choices I made at MIT was to have both professors as my advisors. In the future, they will be my role models.

I would like to thank one of my committee members, Professor Edwin Thomas, who was the first professor I met at the department orientation. I cannot forget his opening remarks—how to survive at MIT. I am honored to share my last event with him as he also leaves MIT, where he has made enormous and unforgettable contributions. He has been working on various army projects; at every meeting he made invaluable comments on my natural armor systems in conjunction with human or vehicle armor systems.

I would also like to say that Professor Silvijka Gradečak's suggestions during our individual meetings improved this thesis, balancing specific research topics that have had a general impact on the whole engineering world.

All of my collaborators have long-lasting enthusiasm and thoughtful discussion for research. Prof. Matthew Wund, at the College of New Jersey, and Prof. Dan Gazit and his student Ilan, at Hebrew University, gladly shared their remarkable achievements with me, enabling me to explore new research areas with safe guidelines. Dr. Bruet, Dr. Wang, Dr. Yao, Dr. Li and Dr. Cebeci have been my great mentors and friends, and I benefited by working with these brilliant and outstanding researchers. I respect two architect friends, Steffen and Sergio, for their passion, talent, and creativity. I wish my only UROP, Johannes, good luck for his promising future. He always surprised me with his youth, fast learning, diligence, and passion for success.

I've taken advantage of belonging to two research groups. I would like to thank all of them for being great lab mates. Meredith is definitely more than a lab mate, and we've been together for five years. She listens to my worries, happiness, and hardships and cheers me up. Tim, Jeff, Carlos and Shawn helped me with their kind explanation about FEA simulations and analytical problems when I was confused. I thank Katia, now

a Harvard professor, for her great advice on my research and life. I miss the former group members, Damien, Kuangshin, Miao, Jae, Bobae, and Hsu-Yi, who provided much help to me. I was happy to have met Lin again because we didn't have much time to get to know each other when he was a student. I also thank Matt, Ashley, Ting Ting, Ling, Eric, Elaine, Chia-Ling, and Erica for making our group more pleasant and dynamic with their energy.

I would like to acknowledge Alan Schwartzman and the MIT Nanolab, Scott Speakman at the DMSE X-ray facility, Institute for Biotechnologies and its staff, and Ara Nazarian at the Center for Advanced Orthopaedic Studies, Beth Israel Deaconess Medical Center, for their endless efforts on maintenance, training, and technical support of equipment. Moreover, I would like to thank Jeremy, Tony, Una, Juliette and Angelita for their kind assistance whenever I needed them.

My personal life has also been enriched by many other friends in Korea, in the States and in many other countries. Their friendship encouraged me to keep going whenever I lost myself. Please understand my not acknowledging your names here. Like all warm birthday cards, new-year cards, postcards, or letters that you sent me, your names are always in my heart and in my storage boxes. Thank you for being my friends and supporting me no matter what I do.

Lastly, I would like to thank my family for their love and care. I couldn't be with them when they needed me, but they are always very patient and keep taking care of me in Korea. My father made me stronger, telling his life to me. He was one of the strongest persons I've ever known, and this five-year journey also awarded me the chance to understand his life—how he survived and how he kept his faith. Thanks to my mother for her immeasurable love and trust. My sister and brother are a part of me, and they fill my weaknesses with their capabilities.

"I do not know what I may appear to the world, but to myself I seem to have been only like a boy playing on the sea-shore, and diverting myself in now and then finding a smoother pebble or a prettier shell than ordinary, whilst the great ocean of truth lay all undiscovered before me."

— Isaac Newton (1643-1727)

“The scientist, by the very nature of his commitment, creates more and more questions, never fewer. Indeed the measure of our intellectual maturity, one philosopher suggests, is our capacity to feel less and less satisfied with our answers to better problems.”

— Gordon Allport (1897-1967)

Table of Contents

TABLE OF CONTENTS	9
LIST OF FIGURES	13
LIST OF TABLES.....	31
CHAPTER 1. INTRODUCTION.....	35
1.1. Opening Remarks	35
1.1.1. Learning from Nature: Bioinspiration.....	35
1.1.2. Structural Biological Materials	37
1.1.3. Fish Dermal Armor: Flexible and Protective Design.....	42
1.2. Thesis Outline.....	44
CHAPTER 2. BACKGROUND INFORMATION	49
2.1. Two Fish Armor Model Systems.....	49
2.2. <i>P. senegalus</i> Armor System.....	52
2.2.1. <i>P. senegalus</i> Scales	52
2.2.2. Potential Threats.....	54
2.2.3. Flexible Articulating Design of <i>P. senegalus</i> Armor	56
2.2.4. Bioinspired Flexible Articulating Armor Design.....	59
2.3. <i>G. aculeatus</i> Armor System.....	62
2.3.1. Morphological Variations of <i>G. aculeatus</i> Armor	62
2.3.2. Environmental Factors in Morphological Variations of Armor.....	66
CHAPTER 3. MULTILAYERED AND GRADED DESIGN	
OF <i>P. SENEGALUS</i> SCALES	69
3.1. Introduction	69
3.2. Methods	73
3.2.1. Microindentation	73
3.2.2. Finite Element Analysis (FEA) Modeling	73
3.3. Results	76
3.3.1. Plasticity of Individual Material Layers of <i>P. senegalus</i> Scales.....	76
3.3.2. Multilayering Effects of <i>P. senegalus</i> Scales.....	78

3.3.3. Penetration Resistance Mechanism of <i>P. senegalus</i> Scales	80
3.4. Discussion.....	83
3.5. Conclusion.....	85

**CHAPTER 4. ANISOTROPIC DESIGN
OF A MULTILAYERED *P. SENEGALUS* SCALE..... 87**

4.1. Introduction	87
4.2. Experimental Study	89
4.2.1. Methods.....	89
4.2.2. Results.....	91
4.3. Modeling Study	94
4.3.1. Methods.....	94
4.3.2. Results.....	100
4.4. Discussion.....	114
4.5. Conclusion.....	116

**CHAPTER 5. THREAT-PROTECTION MECHANISM
OF AN ARMORED FISH 119**

5.1. Introduction	119
5.2. Methods	123
5.2.1. Geometry of <i>P. senegalus</i> Teeth	123
5.2.1. Finite Element Analysis (FEA) Model.....	123
5.3. Results	127
5.3.1. The Effect of Tooth End-Radius	127
5.3.2. The Effect of the Mechanical Properties of the Tooth Enameloid.....	131
5.3.3. The Effect of the Tooth Enameloid Thickness.....	135
5.4. Discussion.....	138
5.5. Conclusion.....	142

**CHAPTER 6. THE ROLE OF MULTILAYERING
IN A NATURAL ARMOR 143**

6.1. Introduction	143
6.2. Methods	146
6.2.1. Threat Model.....	146
6.2.2. Scale Model.....	146
6.3. Results	150
6.3.1. Thickness Effect of the Outmost Ganoine Layer	150
6.3.2. Multilayered vs. Bilayered Structures.....	156
6.3.3. The Sequence of Layers in the Layered Structure	160

6.4.	Discussion.....	163
6.5.	Conclusion.....	170
CHAPTER 7. QUANTITATIVE MICROSTRUCTURAL STUDY		
OF MARINE THREESPINE STICKLEBACK ARMOR.....		171
7.1.	Introduction	171
7.2.	Methods	175
7.3.	Results	178
7.3.1.	Three-Dimensional Structure, Dimensions, and Geometry	178
7.3.2.	Three-Dimensional Structure, Dimensions, and Geometry	185
7.3.3.	Lateral Plate Articulation	188
7.3.4.	Porosity, Crystallography, and Composition	191
7.4.	Discussion.....	195
7.5.	Conclusions	198
CHAPTER 8. DESIGN AND BIOMECHANICAL FUNCTION		
OF THE PELVIC ASSEMBLY OF THREESPINE STICKLEBACK		199
8.1.	Introduction	199
8.2.	Methods	202
8.3.	Results	203
8.3.1.	Four Distinct Regions of Full-Morph Pelvic Assembly.....	203
8.3.2.	Two-Dimensional Morphological Features of Suture and their Mechanical Relevance	207
8.3.3.	Three-Dimensional Morphological Features of Suture and their Mechanical Relevance.....	208
8.3.4.	Potential Mechanical Roles of Pelvis in Conformational Transition from Rest to Offensive	209
8.4.	Discussion.....	216
8.5.	Conclusion	218
CHAPTER 9. CONCLUSION & FUTURE WORK		221
9.1.	Conclusion.....	221
9.2.	Future Work.....	226
9.2.1.	Failure Mechanisms of Biological Structural Materials	226
9.2.2.	Hybrid Material-Morphometric Exoskeletal Design.....	228
9.2.3.	Interdisciplinary Approach of <i>G. aculeatus</i> Armor	230
APPENDIX A. DETERMINATION		
OF BEST FIT TO INDENTATION CURVES.....		233

APPENDIX B. PREDICTION OF MULTILAYERED STRUCTURE BEHAVIOR DURING MICROINDENTATION	239
APPENDIX C. VALIDATION OF BOUNDARY CONDITIONS FOR MULTILAYER SIMULATIONS.....	245
APPENDIX D. MORPHOMETRIC PARAMETERS FROM MICROCT DATA ANALYSIS.....	255
APPENDIX E. MECHANICAL MODELING OF THE PELVIC ASSEMBLY OF THREESPINE STICKLEBACK	257
BIBLIOGRAPHY	261

List of Figures

- Figure 1-1. Bioinspiration and its related science and engineering disciplines; bioinspired structural materials, biomimetic materials for tissue engineering, bioinformatics and artificial intelligence, biomimetic synthesis, bioinspired sensors & actuators are active research fields in bioinspiration. 36
- Figure 1-2. A typical approach of bioinspired material systems in terms of a structure-property-function relationship for an understanding of design principles of natural model systems. 37
- Figure 1-3. Hierarchical structures of structural biological materials at multi-length scales; (a) nacre from red abalone *Haliotis rufescens* (from Barthelat's paper (Barthelat, 2010): p. 3, Fig. 2) and (b) human bone (from Rho's paper (Rho et al., 1998): p. 93, Fig. 1). 41
- Figure 1-4. Diagram of thesis organization. This thesis deals with two fish armor model systems, *Polypterus senegalus* and *Gasterosteus aculeatus* armor for an understanding of their design principles. 45
- Figure 2-1. Structure and development of *Polypterus senegalus* scales; (a) *P. senegalus* skeleton (Bruet et al., 2008), (b) scanning electron micrograph (SEM) of external and internal scale surfaces (Bruet et al., 2008), (c) schematic drawing of cross-section of a *P. senegalus* scale (Sire, 1990) and (d) the proposed main steps of scale formation in *P. senegalus* (Sire et al., 2009). G: ganoine, D: dentin, I: isopedine, OBP: osseous basal plate, SF: Sharpey's fibers. 53
- Figure 2-2. The morphology and fiber structure of flexible articulating *P. senegalus* armor; (a) anesthetized *P. senegalus* showing one extreme body curvature (photo taken by S. Reichert (Reichert, 2010)), (b) and (c) schematic drawings of (b) scale articulation in *P. senegalus* (*lateral view*) where dotted area indicate a row of scales that interlock via peg-and-socket articulation (*paraserial*) and overlapping scales in scale rows (*interserial*) (Gemballa and Bartsch, 2002), (c) details of scale articulation showing scale-to-scale interconnection in two directions with peg-and-socket joints and overlapping between scale rows (Gemballa and Bartsch, 2002), (d) oblique internal view of *P. senegalus* integument with four layers of the stratum compactum shown beneath the articulating scales (Gemballa and Bartsch, 2002) and (e)

	attachment lines of myosepta to <i>P. senegalus</i> skin (Gemballa and Roder, 2004).....	58
Figure 2-3.	Flexible articulating armor designs inspired by <i>P. senegalus</i> armor with the overall approach for the bioinspired design system (Ortiz et al., 2010; Reichert, 2010).	60
Figure 2-4.	The proof-of-concept prototype of flexible articulating armor designs inspired by <i>P. senegalus</i> armor: (a) 3D prototype that is made of two materials, fabricated by a multimaterial 3D printer (OBJET Connex500) (Reichert, 2010) and (b) anisotropic biomechanical behavior of the 3D prototype, exhibiting high bending resistance along with the peg-and-socket articulating direction (<i>top</i>) and high flexibility in the scale-to-scale overlapping direction (<i>bottom</i>).....	61
Figure 2-5.	Phenotypical variation (body form and external features) among <i>G. aculeatus</i> populations ; (a) a schematic drawing of various <i>G. aculeatus</i> populations and (b) the anterior region of <i>G. aculeatus</i> armor that displays three major armor components, dorsal spines with their basal plates, lateral plates and pelvic assembly. Fig. 2-4a was modified, based on Fig. 1.2 of ref (Bell and Foster, 1994).....	62
Figure 2-6.	Sequential reduction of <i>G. aculeatus</i> armor components: (a) lateral plates (Reimchen, 1983) and (b) pelvic assembly (Bell, 1987).	65
Figure 2-7.	Schematic diagram of energy allocation and its influence to a biological system (Wootton, 1994).....	67
Figure 3-1.	Structure and mechanical properties of <i>Polypterus senegalus</i> scale; (a) optical micrograph of the cross-section of an individual scale with an inlet showing four layers, and (b) average indentation modulus (E_{O-P}) and hardness (H_{O-P}), both reduced from Oliver-Pharr analysis (Oliver and Pharr, 1992) as a function of distance across the scale cross-section from ganoine to bone. The vertical error bars represent one standard deviation. ‘Epoxy’ is epoxy used for embedding. <i>Figure by B.J.F. Bruet</i>	71
Figure 3-2.	Structure and graded mechanical properties of the ganoine, dentin and their junction of a <i>P. senegalus</i> scale; (a) backscattered electron microscopy image of the cross-section of the ganoine-dentin junction (<i>image taken by B.J.F. Bruet</i>) and (b) average indentation modulus (E_{O-P}) and hardness (H_{O-P}), analyzed by Oliver-Pharr method (Oliver and Pharr, 1992) from ganoine to dentin. The vertical error bars represent one standard deviation and ‘epoxy’ is epoxy used for embedding (<i>experiment by B.J.F. Bruet</i>).	72
Figure 3-3.	Two-dimensional axisymmetric finite element analysis (FEA) models for predictions of mechanical properties of the <i>P. senegalus</i> scale; (a) schematic diagram of the nano- and micro-indentation FEA models, (b) three-	

dimensional geometry of a two-dimensional axisymmetric rigid conical indenter with a tip half angle of α and a tip end radius of R_{tip} , where $\alpha=70.3^\circ$ and $R_{tip} = 300$ nm for a Berkovich tip and $R_{tip} = 300$ nm for a Vickers tip and (c) multilayered structures of discrete (left) and gradient (right) models with their corresponding elastic modulus and yield strength distributions. 75

Figure 3-4. Mechanical properties derived from nanoindentation experiments across the cross-section of the ganoine-dentin-isopedine-bone material layers of an individual *P. senegalus* scale; (a) TMAFM amplitude image of the residual indents (500 μ N maximum load) on the cross-section of the dentin layer while other three material layers also exhibit the residual indents (data not shown, *images taken by B.J.F. Bruet*), and (b) average nanoindentation load-depth curves for all four material layers with horizontal error bars that represent one experiment standard deviation. FEA predicted curves were compared to the experimental curves, respectively. *Figure by B.J.F. Bruet.* 77

Figure 3-5. Predictions of effective microindentation mechanical properties of *P. senegalus* scale via multilayered FEA simulations; (a) simulated microindentation load-depth curves, (b) simulated effective indentation modulus, (c) simulated effective microhardness and experimentally measured values (OM, optical microscopy; AFM, atomic force microscopy), and (e) simulated effective energy dissipation..... 79

Figure 3-6. Simulated contours of stress, plastic strain and pressure fields of a *P. senegalus* scale via multilayered FEA simulations; (a) to (c) FEA predictions of von Mises stress field, S22, S11 and pressure at a maximum depth when fully loaded, and S23, S33 and plastic equivalent strain (PEEQ) after fully unloaded for three models— all ganoine (a), discrete (b) and gradient (c) models for microindentation at a maximum load of 1N..... 81

Figure 3-7. Topographic profiles, residual impressions of microindentation and fracture of an individual *P. senegalus* scale; (a) TMAFM amplitude image of a 1N-maximum-load microindentation *Image taken by B.J.F. Bruet*, (b) FEA prediction of the residual depth topography obtained from the gradient multilayer simulation and experimental height profiles that correspond to the red and blue lines as indicated in the TMAFM image (Fig. 3-7a), (c) optical micrograph of a 1N-maximum-load microindentation and (d) optical micrograph of a 2N-maximum-load microindentation showing circumferential cracks. 82

Figure 3-8. Microcracking in the material layers of an individual *P. senegalus* scale; (a) backscattering electron micrograph of cross-section of isopedine layers and (b) backscattering electron micrograph of cross-section of ganoine and dentin layers. Images were taken after 10s etching treatment using 35% H_3PO_4

	solution. White arrows of Figure 3-8(a) indicate microcracks of the individual isopedine sublayers. <i>Images taken by B.J.F. Bruet</i>	85
Figure 4-1.	The quad-layered structure of an individual <i>P. senegalus</i> scale where the anisotropy of the outmost individual layer (ganoine) is illustrated at the different levels of resolutions from the nano-sized building blocks to the hierarchical microstructure. <i>Figure by L. Wang</i>	88
Figure 4-2.	Individual <i>P. senegalus</i> scale cut in half and denoting two orthogonal orientation directions of nanoindentation experiments. “Surface orientation” represents loading parallel to the outer surface normal, denotes as the 3-axis, and “cross-section orientation” represents the loading perpendicular to the outer surface normal in the direction represented by the 1 in-plane axis.	90
Figure 4-3.	Nanostructure, microstructure, and fracture of the ganoine layer of a <i>P. senegalus</i> scale; (a) backscattered electron microscopy images of the cross section of ganoine and dentin layers of the polished <i>P. senegalus</i> scale (embedded in the epoxy resin) after etching with phosphoric acid for 20 s, and (b) - (d) SEM images of ganoine exposing the thin elongated HAP nanocrystals after the scale sample fractured and etched with (b) NaOCl for 5 min or (d) 0.5 M EDTA for 2 min, and (c, e) images modified by means of reversing contrast of (b) and (d), respectively, which show crack paths more clearly. (b) - (e) were not embedded in epoxy or polished. Arrows indicate the torturous crack paths crossing the neighboring rods.	92
Figure 4-4.	Averaged experimental curves on loading and unloading (number of experiments, n = 75) for both surface and cross-sectional directions. The horizontal bars indicate the maximum standard deviation of the curves for that particular dataset.	93
Figure 4-5.	RVE of ganoine nanostructure including HAP mineral crystals (dark gray) and organic matrix (light gray); (a) view of hexagonal arrangement of HAP crystals looking toward the top surface (down the 3-axis) and (b) 3D view of the RVE [square region in the center of (a)] consisting of transverse mineral elements. The 3-axis (normal to the surface direction) of the scale is also coincident with the crystallographic c-axis of the HAP crystals. <i>Figure by L. Wang</i>	95
Figure 4-6.	Two three-dimensional nanoindentation FEA models of; (a) continuum ganoine layer showing finer meshing in region directly below the indenter, and (b) discrete nanostructural ganoine layer consisting more than 100 nanocrystals surrounded by thin organic layers and being incorporated within the region directly below the indenter, where the HAP minerals are meshed with square cross sections.....	98

Figure 4-7. Predicted mechanical responses from RVE models subjected to various loading conditions; (a) microscopic stress-strain response of the RVE (A) for ganoine to uniaxial compression compared with a stress-strain curve (showing two yield points) for RVE (B) under off-axis compression where thin dashed lines are simulated curved from anisotropic material assumption, (b) microscopic stress-strain response of the RVE (A) for ganoine to simple shear deformation where thin dashed lines show the calculation of yield stress, (c) the Young's moduli and (d) yield stress determined from the stress-strain curves as a function of orientation, as represented by the angle, α , between the surface and cross-sectional orientations [Fig. 4-5b] (a second yield point is connected by dashed line). Values for off-axis axial modulus computed by transformation of the computed anisotropic stiffness tensor of each RVE case are given by the continuous curves. The directional dependence of the Young's modulus and yield stress is shown for three different RVEs: RVE (A) considers isotropic HAP crystals and transverse mineral elements, RVE (B) considers isotropic HAP crystals but lacks transverse mineral elements, and RVE (C) considers anisotropic HAP crystals and also includes transverse mineral elements. *Figure by L. Wang*..... 102

Figure 4-8. Simulation contours of equivalent stress (von Mises) for RVE (A) representing ganoine, Fig. 4-5(b), i.e., considering isotropic HAP and including transverse mineral elements, under a macroscopic strain of 10% for (a) $\alpha = 90^\circ$, (a) $\alpha = 45^\circ$, and (c) $\alpha = 0^\circ$, macroscopic shear strain of 10% in the plane with normal (d) $n = e_3$, (e) $n = 0.707e_1 + 0.707e_3$, and (f) $n = e_1$. (a) 1 – (f) 1 are corresponding plastic equivalent strain contours (PEEQ). *Figure by L. Wang*..... 103

Figure 4-9. Comparison of the average experimental curves to the FEA simulation curves obtained by virtual nanoindentation after fully anisotropic material set for ganoine was determined using the proper nanomechanical models; (i) isotropic properties with $E = 65$ GPa, $\nu = 0.3$, and $\sigma_Y = 1.53$ GPa (Table 4-2, row 1), (ii) anisotropic properties using data obtained from the nanomechanical modeling with isotropic HAP crystals (Table 4-3, row 1) and transverse mineral elements [RVE (A)], and (iii) discrete model assuming isotropic HAP rods. *Figure by L. Wang* 104

Figure 4-10. Simulation contours of stress distributions, plastic strain, and energy dissipation of the ganoine layer under nanoindentation with the loading parallel to the surface normal (3-axis). A comparison is shown between isotropic (Table 4-2, row 1), anisotropic (isotropic HAP crystals, Table 4-3, row 1), and transverse mineral elements [RVE (A), Fig. 4-5b], and discrete

models for 3D nanoindentation as indicated in Fig. 4-6b. *Figure by L. Wang*
 106

Figure 4-11. Simulation contours of stress distributions, plastic strain, and energy dissipation of the ganoine layer under nanoindentation with the loading perpendicular to the surface normal (along the 1-axis). A comparison is shown between isotropic (Table 4-2, row 1), anisotropic (isotropic HAP crystals, Table 4-3, row 1), and transverse mineral elements [RVE (A), Fig. 4-5b], and discrete models for 3D nanoindentation as indicated in Fig. 4-6b. *Figure by L. Wang* 107

Figure 4-12. Predictions of effective microindentation mechanical properties of the multilayered *P. senegalus* scale; notations include ‘monolithic isotropic ganoine’ or MIG, ‘isotropic ganoine multilayer’ or IGML, and ‘anisotropic ganoine multilayer’ or AGML, respectively; (a) simulated microindentation load-versus-depth curves, (b) simulated effective microhardness compared to experimentally measured values as a function of maximum indentation load (reported in Chapter 3, Fig. 3-5c) where OM and AFM indicate optical microscope and atomic force microscope, respectively, that were used to measure the residual area after unloading, (c) simulated effective energy dissipation as a function of maximum indentation load where dissipation energy was calculated as the area between the loading and unloading portion of the load-depth curves in microindentation after unloading and (d) simulated energy evolution (the work of indentation) of the whole multilayered structure [‘IGML’ (black lines) and ‘AGML’ (gray lines)], and the individual ganoine and dentin layers as a function of applied load up to a 1N maximum load, as well as on unloading. 110

Figure 4-13. Simulation contours of stress and plastic strain of *P. senegalus* scale under microindentation. FEA predictions of (a) S11, S22, S23, S33 and plastic stain, PE33 and PE23 at a maximum depth when fully loaded and (b) S23, S33 when fully unloaded for the two ‘isotropic ganoine multilayer’ or IGML, and ‘anisotropic ganoine multilayer’ or AGML, multilayered models. Arrows indicate the location of surface stresses on the stress contours, S11 and S22. 112

Figure 4-14. Simulation contours of plastic energy dissipation density and energy dissipation of *P. senegalus* scale under microindentation at 1N maximum load after fully unloaded. FEA predictions of (a) plastic energy dissipation density, (b) energy dissipation magnitude in separated ganoine and dentin layers with the proper scale bar for two ‘IGML’ and ‘AGML’ multilayered structures. The energy dissipation magnitude contour reflects the volumetric effect on energy dissipation density. The guidelines (white dashed lines on

- energy contours of dentin layers) show energy dissipation in dentin of the AGML model covers larger area (elongated shape) with relatively higher density or magnitude than in that of the IGML model. 113
- Figure 5-1. Territorial and predatory fighting between two comparable sized Polypterus or between species and its prey fish; (a) Ornate Polypterus Aggression Video, (b) Polypterus fights Video, (c) *olypterus endlicheri endlicheri* vs. *Polypterus ornatipinnis* Video, (d) Polypterus predation and (e) Miscellaneous Oddballs VII: Bichirs do eat fish. 122
- Figure 5-2. Morphology and geometric information of 25 *P. senegalus* teeth extracted from the premaxillary and maxillary regions; (a) optical microscope image of typical teeth of *P. senegalus* (b) scanning electron microscope (SEM) image of a typical individual *P. senegalus* tooth, showing an end radius of $\sim 14 \mu\text{m}$, (c) tooth end-radius distribution of *P. senegalus* measured using SEM images (n = number of teeth, m = mean, σ = standard deviation) and (d) a representative tooth of *P. senegalus* with definitions of relevant geometric parameters which include a half cone angle ($\theta/2$) of $\sim 22^\circ$, an end radius (R_{tooth}) of $\sim 12 \mu\text{m}$, enamel thickness, t_E , of $\sim 100 \mu\text{m}$ (Wacker et al., 2001) and a height, h , of $\sim 500 \mu\text{m}$ 124
- Figure 5-3. Two-dimensional axisymmetric finite element analysis (FEA) models of the *P. senegalus* scale and its corresponding hypothetical threat; (a) Schematic diagram of an individual tooth-armored scale system in *P. senegalus* during a hypothetical predatory attack illustrating the development of a multiaxial stress field in both the tooth and scale due to the localized penetration and (b) schematic of the corresponding finite element model approximating the hypothetical predatory attack shown in part (a). 125
- Figure 5-4. The effect of tooth end-radius (for a perfectly rigid tooth) on the predicted finite element simulations of the load-bearing capability and energy dissipation within an individual armored scale of *P. senegalus* during a virtual microindentation, simulating a hypothetical generic biting predatory attack; (a) Load-depth curves for three different tooth end-radii as a function of maximum load and (b) total energy dissipation and energy dissipation in the secondary underlying dentin layer as a function of maximum load for three different tooth end-radii. Tooth end-radii and penetration depths were normalized by the thickness of the outer ganoine layer. 129
- Figure 5-5. The effect of tooth end-radius (for a perfectly rigid tooth) on the predicted finite element simulations of the contours of stress and plastic strain within an individual armored scale of *P. senegalus* during a virtual microindentation, simulating a hypothetical generic predatory biting attack; Von Mises stress (S), S33, S23 (fully loaded to 0.75N) and fully unloaded

from 0.75N (PEEQ), for tooth end radii of 0.42, 1.25, and 2.5 normalized by the thickness of the outer ganoine layer. 130

Figure 5-6. The effect of tooth end-radius (for a perfectly rigid tooth) on the predicted finite element simulations of the contours of circumferential (S11) and radial stresses (S22) within an individual armored scale of *P. senegalus* during a virtual microindentation, simulating a hypothetical generic predatory biting attack; S11, S22 viewed along the indentation loading 3-axis for normalized tooth end radii of 0.42 (a), 1.25 (b) and 2.5 (c) at a maximum load of 0.75N.

..... 131

Figure 5-7. The effect of the mechanical properties (indentation stiffness and yield strength) of the tooth enamel relative to the scale ganoine, i.e., the mechanical ratio, $M_{E/G}$, on the normalized penetration depth and energy dissipation, predicted by finite element simulations during a virtual microindentation using a deformable tooth (three different tooth end-radii of 0.42, 1.25 and 2.5). that simulates a hypothetical generic predatory attack of *P. senegalus*; (a) load-depth curves of the whole tooth-scale system and scale system for $M_{E/G} = 0.5, 1$ and 2 at the normalized tooth end radius of 0.42, as compared to rigid tooth case, (b) normalized penetration depth for tooth end radii of 0.42, 1.25 and 2.5 as a function of $M_{E/G}$, and (c) energy dissipation in the tooth and the scale for normalized tooth end-radii of 0.42, 1.25 and 2.5 for $M_{E/G} = 0.5, 1.0, 2.0$. Penetration depths were normalized with the thickness of the ganoine layer and the energy dissipation of each component (tooth, scale) was normalized by the total energy dissipation (tooth + scale).

..... 133

Figure 5-8. The effect of the mechanical properties (indentation stiffness and yield strength) of the tooth enamel relative to the scale ganoine, i.e. the mechanical ratio, $M_{E/G}$, on the simulations of contours of stress and plastic equivalent strain, predicted by a virtual FEA microindentation using a deformable tooth which simulates a hypothetical generic predatory attack of *P. senegalus*: (a) Von Mises stress (S) at a maximum depth when fully loaded, and (b) equivalent plastic strain (PEEQ) when unloaded for three deformable tips with normalized tip end radii of 0.42, 1.25, and 2.5 with respect to the thickness of the ganoine layer at the mechanical ratios of enamel (tip) to ganoine (scale), 0.5, 1.0 and 2. 134

Figure 5-9. The effect of the tooth enamel thickness relative to the scale ganoine thickness ($t_{E/G}$) on the predicted load-depth behavior and normalized penetration depth (relative to ganoine thickness) for two different mechanical ratios of enamel to ganoine ($M_{E/G}$, indentation stiffness and yield strength) of 1 and 2, predicted by finite element analysis of a virtual microindentation

using a deformable tooth which simulates a hypothetical generic predatory attack of *P. senegalus*; (a) normalized load-depth curves of the whole tooth-scale system and scale system for $M_{E/G} = 1$ at the tooth end radius of 1.25 depending on the thickness of enamel, as compared to the monolithic enamel tooth case, and (b) normalized penetration depth for $M_{E/G} = 1$ and 2 as a function of $t_{E/G}$. A normalized tip end radius of 1.25 relative to the scale ganoine thickness was employed..... 136

Figure 5-10. The effect of the tooth enamel thickness relative to the scale ganoine thickness ($t_{E/G}$) on the simulations of contours of stress and plastic equivalent strain, predicted by finite element analysis of a virtual microindentation using a deformable tooth that simulates a hypothetical generic predatory attack of *P. senegalus*. FEA predictions of Von Mises stress (S), S22, S11 and S33 at a maximum depth when fully loaded, and S33, S23 and equivalent plastic strain (PEEQ) when fully unloaded for two thickness ratios of enamel to ganoine, 1 and 10, using a deformable tooth with a normalized tip end radius of 1.25 with respect to the thickness of the ganoine layer at the mechanical ratio of enamel to ganoine, $M_{E/G}=1$ 137

Figure 6-1. Design principles of multilayered natural exoskeletons; schematic diagram of an individual tooth-armored scale system in *P. senegalus* during a hypothetical attack. 144

Figure 6-2. Schematic drawing of threat and scale FEA models; (a) two indenter tips for virtual indentation models that are a rigid, Vickers tip with a half apex angle (α) of 70.3° and a tip end radius (R_{V-tip}) of $3.7 \mu\text{m}$; and a deformable, tooth-emulating tip with a half apex angle (α) of 22° , a tip end radius (R_{tooth}) of $14.7 \mu\text{m}$ and a total length (h) of $400 \mu\text{m}$, and (b) three multilayer FEA models that are (i) quad-layered models that mimicked the *P. senegalus* scale system with varying the outmost ganoine thickness, (ii) bi-layered models composed of two outer layers, ganoine and dentin with varying the ganoine thickness; and (iii) a ‘DGIB’ quad-layer model where the sequence of two outer layers, ganoine and dentin, were reversed, having the outmost dentin layer and underlying ganoine layer..... 148

Figure 6-3. The effect of layer thickness (for a perfectly rigid Vickers tip) on the predicted finite element simulations of the load-bearing capability and energy dissipation of the gan-dent bilayer FEA models during a virtual microindentation, simulating a Vickers indentation; (a) normalized load-depth curves for different ganoine thicknesses of bi-layered systems, (b) effective indentation modulus and weight per area as a function of ganoine thickness (t_g^n), and (c) effective microhardness and energy dissipation as a function of ganoine thickness (t_g^n). The ganoine thickness (t_g^n) varied from

0.75 % to 13.5 % of the total thickness (t_{total}^f) of the system. Penetration depths were also normalized the tip end radius of the Vickers tip (R_{V-tip}) and loads were normalized by the square of the tip end radius of the Vickers tip (R_{V-tip}^2). 151

Figure 6-4. The effect of layer thickness (for a perfectly rigid Vickers tip) on the predicted finite element simulations of the stress distribution on the surface of the bi-layered structure during a virtual microindentation; (a) radial stress field (S22) and (b) circumferential stress field (S11) on the surface of bi-layered structures with various ganoine thickness as a function of distance from the center of the indented site, and (c) the contours of circumferential (S11) and radial stresses (S22) viewed along the indentation loading 3-axis for normalized ganoine thicknesses ($t_{gan}^{n,V}$) of 0.8, 2.2, 3.2, 4.9 and 14.6. Distances from the center of the indented area on the ganoine surface were normalized with the tip end radius of the Vickers tip (R_{V-tip}). 152

Figure 6-5. The effect of layer thickness (for a deformable tooth indenter) on the predicted finite element simulations of the load-depth behavior and normalized penetration depths of the gan-dent bilayer FEA models during a virtual microindentation, simulating a hypothetical generic predatory attack of *P. senegalus*; (a) Normalized load-depth curves for different ganoine thicknesses of bi-layered systems; (b) normalized penetration depths with respect to the tip end radius of the tooth indenter (R_{tooth}) as a function of ganoine thickness for the gan-den bilayer models during the Vickers microindentation and hypothetical biting events. Penetration depths were normalized the tip end radius of the tooth indenter (R_{tooth}) and loads were normalized by the square of the tip end radius of the tooth tip (R_{tooth}^2). 154

Figure 6-6. The effect of layer thickness (t_g) on the simulations of contours of stress and plastic equivalent strain, predicted by finite element analysis of a virtual microindentation on the gan-dent bilayer models using a deformable tooth that simulates a hypothetical generic predatory attack of *P. senegalus*. FEA predictions of Von Mises stress (S), S22, S11 and S23 at a maximum depth when fully loaded, and equivalent plastic strain (PEEQ) and shear strain (PE23) when fully unloaded for three ganoine thicknesses, $t_g^{n,t} = 0.2, 0.8, 3.7$ 155

Figure 6-7. The effect of the number of layers (for a perfectly rigid Vickers tip) on the relative mechanical properties, energy dissipation, and density predicted with respect to those of ganoine by finite element simulations during a virtual Vickers microindentation; (a) relative stiffness, (b) relative hardness, (c) relative energy dissipation and (d) relative density as a function of ganoine thickness ($t_{gan}^{n,V}$) for the gan-den bilayer (black line with open circles), gan-

bone bilayer (blue line with open triangles) and quadlayer (red line with cross)..... 157

Figure 6-8. The effect of the number of layers (for a deformable tooth indenter) on the predicted finite element simulations of the load-depth behavior and normalized penetration depths of the gan-dent bilayer FEA models during a virtual microindentation, simulating a hypothetical generic predatory attack of *P. senegalus*; (a) Normalized load-depth curves for different ganoine thicknesses of gan-den bilayer and quadlayer systems, and (b) normalized penetration depths with respect to the total scale thickness (t_{total}^f) as a function of ganoine thickness for the gan-den/gan-bone bilayer and quadlayer models during hypothetical biting events. Penetration depths were normalized the tip end radius of the tooth indenter (R_{tooth}) or total scale thickness (t_{total}^f) and loads were normalized by the square of the tip end radius of the tooth tip (R_{tooth}^2): 158

Figure 6-9. The effect of the number of layers on the simulations of contours of stress and plastic equivalent strain, predicted by finite element analysis of a virtual microindentation on the gan-bone bilayer and quadlayer models using a deformable tooth that simulates a hypothetical generic predatory attack of *P. senegalus*. FEA predictions of S11 at a maximum depth when fully loaded, and shear strain (PE23) when fully unloaded for three ganoine thicknesses, (a) $t_g^{n,t} = 0.2$, (b) $t_g^{n,t} = 0.8$ and (c) $t_g^{n,t} = 1.2$ 159

Figure 6-10. The effect of layer sequence (for a perfectly rigid Vickers tip) on the predicted finite element simulations of the load-bearing capability and energy dissipation of the ‘GDIB’ (ganoine-dentin-isopedine-bone) and ‘DGIB’ (dentin-ganoine-isopedine-bone) quadlayer models during a virtual microindentation, simulating a Vickers indentation; (a) Load-depth curves for two different quadlayer systems, (b) effective indentation modulus, (c) effective microhardness, and (d) energy dissipation as a function of maximum indentation load. 161

Figure 6-11. The effect of sequence (for a perfectly rigid Vickers tip) on the simulations of contours of stress and plastic equivalent strain, predicted by finite element analysis of a virtual Vickers microindentation on the ‘GDIB’ and ‘DGIB’ quadlayer models. FEA predictions of Von Mises stress (S), S22, and S11 at a maximum depth when fully loaded, and S33, S23 and equivalent plastic strain (PEEQ) when fully unloaded at the maximum load of 0.5 N for (a) ‘GDIB’ quadlayer model and (b) ‘DGIB’ quadlayer model. 162

Figure 6-12. Proposed evolution process of the integumentary skeleton in non-tetrapods where two main streams of evolution from ancient fish appear depending on the way to reduce the weight of armor scales: (i) reduction of odontogenic

component among actinopterygians, and (ii) incorporated pore canal system among sarcopterygians (Sire et al., 2009). Images of fish scales were mainly from (Sire et al., 2009)..... 164

Figure 6-13. Material property charts (Wegst and Ashby, 2004) for natural materials, plotting (a) Young's modulus against density and (b) toughness against Young's modulus. Guidelines identify either structurally efficient materials which are light and stiff (a) or materials best able to resist fracture under various loading conditions (b). 167

Figure 7-1. Three-dimensional structure of armor plate assembly of marine *Gasterosteus aculeatus* (threespine stickleback); (a) photographs and schematic illustration and (b) μ CT images of disassembled armor components with dorsal spines (top), lateral plates (center), and pelvic girdle/spines (bottom) in rest position. "AB"= ascending branch of the pelvic girdle, "AP"= anterior process, "BP" = basal plate, "DS" = dorsal spines, "LL" = lateral line, "LP" = lateral plates, "PG" = pelvic girdle, "PS"= pelvic spines, and "TJ"= trochlear joint. 174

Figure 7-2. Quantitative measurement of the dimensions of a marine *Gasterosteus aculeatus* (threespine stickleback); (a) spatial distribution of thickness for an individual lateral plate (LP 10), *left*, and for the entire lateral plate assembly, *right*. (b) and (c) The schematic cross-section illustrations of entire plate assembly, as indicated in (a); (b) horizontal cross-section image of the assembly (S1) in the x - z plane and (c) vertical cross-section image of the assembly (S2) in the y - z plane), (d) The mean cross-sectional thickness (z -direction) as a function of lateral plate number, calculated from individual lateral plates (filled black square symbols), the non-overlapping regions of individual lateral plates (black triangle symbols), and the overlapping region between two lateral plates (red 'x' symbols) and (e) maximum lateral plate length (filled black circles), width (filled red circle symbols), and aspect ratio (black triangle symbols) as a function of their position in the armor assembly. 179

Figure 7-3. Lateral plate cross-section of a marine *Gasterosteus aculeatus* (threespine stickleback); (a) two- dimensional μ CT slices (*right*) corresponding to each section indicated in the three-dimensional structure (*left*) and (b) optical micrograph image of two interconnected lateral plates embedded in epoxy. The black arrow of (b) indicates the connective tissue between two lateral plates. 181

Figure 7-4. Microstructure of the pelvic girdle and spines of a marine *Gasterosteus aculeatus* (threespine stickleback); (a) to (d) three-dimensional μ CT images of pelvic spines with the pelvis and ventral plates when the spines are unlocked. (e) μ CT image of sectioned three-dimensional images of pelvic

girdle and spines corresponding to each section indicated in (d). Highlighted faces in red denote the cross-sectional surfaces. (f) An optical microscope image of a cross-section of a pelvic spine. The scale bar is represented for (a) to (e). “AB” = ascending branch, “AP” = anterior process, “PG” = pelvic girdle, “PP” = pelvic plate and “PS” = pelvic spines, “S” = median suture of pelvic girdle, “TJ” = trochlear joint, and “TP” = trochlear process. 183

Figure 7-5. Prototypes of 3D printing: (a) and (b) A pelvic girdle-spine assembly when the spines are unlocked; and (c) and (d) a porous internal structure of bilateral pelvic girdles..... 184

Figure 7-6. Surface morphology of lateral plate and pelvic spines of a marine *Gasterosteus aculeatus* (threespine stickleback); (a) μ CT image of lateral plate, exterior view (b-d) SEM images of lateral plate, exterior view, (e) μ CT image of lateral plate, interior view, (f-h) SEM images of lateral plate, interior view, (i) μ CT image of pelvic spine, exterior view, (j-l) SEM images of pelvic spine, exterior view. The black arrows of (h) indicate the connective tissue between two lateral plates..... 186

Figure 7-7. Surface topography of a lateral plate measured by surface profilometry; (a) three-dimensional topographical image for tubercles from the upper white square shown in μ CT image to the left, (b) three-dimensional topographical image for tubercles from the lower white square shown in μ CT image to the left. (c) Two-dimensional topographical image of a hexagonal tubercle array corresponding to (a), and (d) the height profile of tubercles as a function of distance across the surface from (c). (e) Two-dimensional topographical image of tubercles on the grooves corresponding to (b), and (f) the height profile of tubercles as a function of distance across the surface from (e). .. 187

Figure 7-8. Microstructure of the interconnecting joint in neighboring lateral plates; (a) SEM images of a socket (*left*) and a bony protrusion (*right*). (b) Three-dimensional μ CT image of a bony protrusion (LP 10), facing its mating socket of LP 9. (c) Three-dimensional μ CT images of neighboring lateral plates (LP 9 and 10) before and after interlocking. (d) Two-dimensional μ CT images of the interconnecting joint from posterior to ventral sides, as indicated in (c). LP 9 and LP 10 were represented in yellow and dark gray, respectively. 189

Figure 7-9. Prototypes of 3D printing: (a) and (b) two neighboring lateral plates (LP 9 and 10) before and after interlocking, exterior view; (c) and (d) two neighboring lateral plates (LP 9 and 10) before and after interlocking, interior view; (e) and (f) a sliding motion of the joint along the direction of the long axis of the ellipsoidal protrusion (the hinge sliding motion); and (g) and (h) a rotating motion of the joint about the major axis of the ellipse (the hinge

	rotation motion). A more limited rotation about the minor axis of the ellipse is also allowed by this joint (not shown).	190
Figure 7-10.	Pore size distribution of lateral plates (LP 9-12, N = 4) measured by a mercury porosimeter showing a bimodal distribution with two average pore sizes ($\mu_1 = 15 \mu\text{m}$, $\sigma_1 = 6 \mu\text{m}$, and $\mu_2 = 234 \mu\text{m}$, $\sigma_2 = 112 \mu\text{m}$).	192
Figure 7-11.	Chemical composition of the armor of the marine <i>Gasterosteus aculeatus</i> (threespine stickleback); (a) X-ray diffraction pattern of lateral plates and pelvic spines. Broad reflections corresponding to the characteristic peaks (●) of hydroxyapatite are compared. (b) Infrared spectrum of pelvic spine showing amide bands (●) and C-H bands (◆) from collagen fibers and absorbances for phosphate (▲) and carbonate ions (■) in the apatite phase (Doyle et al., 1975; Rehman and Bonfield, 1997; Chang and Tanaka, 2002).	193
Figure 7-12.	Quantitative analysis of mineral contents of the marine <i>Gasterosteus aculeatus</i> (threespine stickleback); (a) Mineral contents of three different cross-sections in a lateral plate (LP10), extracted from three fish samples measured by back-scattered electron microscopy (BSEM). (b) Mineral contents measured by energy dispersive X-ray (EDX) analysis combined with BE gray-level measurements of identical bone areas of (a).	194
Figure 8-1.	Two-dimensional morphology of the median suture of bilateral pelvic girdles from marine and freshwater <i>G. aculeatus</i> ; (a) Ventral view of three-dimensional μCT images of the pelvic girdles (rest position) from marine (left) and freshwater (right) <i>G. aculeatus</i> , (b) schematic diagram of a two-dimensional suture model, (c) to (e) the dorsal to ventral spatial distribution of: (c) relative amplitude (A/L), (d) spatial frequency (L/λ) and predicted suture stiffness of the median suture in both <i>G. aculeatus</i> populations, and (f) average stiffness and ID of four regions in marine and freshwater <i>G. aculeatus</i>	205
Figure 8-2.	Three-dimensional morphology of the median suture of the pelvic girdles from marine and freshwater <i>G. aculeatus</i> ; (a) lateral view of three-dimensional μCT images of the pelvic girdles (rest position) from marine (top) and freshwater (bottom) <i>G. aculeatus</i> with the schematic diagram of internal plates, (b) and (c) the dorsal to ventral spatial distribution of (b) z Height (H/L) and (c) inclination of the pelvic girdle in marine and freshwater <i>G. aculeatus</i> , (d) predicted bending stiffness in region II of the pelvic girdles for both <i>G. aculeatus</i> populations and (e) the coupling effect of inclined internal plates in bending stiffness.	206

- Figure 8-3. Conformational transition of pelvic spines (a) from rest to offensive and (b) offensive to rest. The images were taken from the animation movie created by S. Araya. 212
- Figure 8-4. Three-dimensional structures of pelvic assembly of a marine *G. aculeatus* in rest and offensive configurations; (a) Pelvic assembly, bottom view, (b) pelvic assembly, top view and (c) free body diagram of fully armored marine *G. aculeatus* armor when the two pelvic spines are fully extended during conformational transition from rest to offensive and three-dimensional structural comparison of pelvic girdle-spine assembly in two states (*rest vs. offensive*)..... 213
- Figure 8-5. Structural comparison of a full-morph pelvic assembly in conformational transition from rest to offensive; (a) three-dimensional structures of pelvic assembly in rest and offensive configurations, indicating the sectioned planes from the top to bottom ventral plates, (b) two dimensional y-z slices of four regions and (c) two dimensional x-y slices corresponding to each section (H1 to H4) indicated in the three-dimensional structure of (a)..... 214
- Figure 8-6. Stiffening mechanism of conformational transition of *G. aculeatus* pelvic assembly from the ‘rest’ to ‘offensive’ positions: (a) sketch of the top surfaces and internal layers and the whole structure with the applied moment (M), (b) and (c) max. in-plane principal stress distribution of (b) the whole pelvic girdle (top view, *top*; bottom view, *bottom*) and (c) the top surface (*top*) and internal plates (*bottom*) in the offensive position, (c) deformation of the outer top surface and the internal layers in two positions, (d) total contact area and moment of the whole structure as a function of the degree of rotation, and (e) the coupling effects of the rotation. Figure by Y.N. Li. 215
- Figure 8-7. Morphological variations of pelvic assembly; (a) full morph marine *G. aculeatus* from Rabbit Slough, (b) full morph freshwater *G. aculeatus* from Beverly Lake and (c) low morph freshwater *G. aculeatus* with loss of pelvic spines from Kalmbach Lake. 217
- Figure 9-1. Multiscale design principles used in the armor system of the fish *Polypterus senegalus*..... 224
- Figure 9-2. Multiscale design principles used in the armor system of the fish *Gasterosteus aculeatus* 225
- Figure 9-3. *In vitro/in vivo* microindentation by BioDentTM; (a) a schematic drawing of the BioDentTM instrument with the reference probe (left) and the test probe (right) (Randall et al., 2009), (b) a schematic drawing that shows how the reference probe/test probe assembly is working during *in vivo* indentation (Hansma et al., 2009) and (c) preliminary *in vitro* microindentation to the maximum load of ~ 3N on a *P. senegalus* scale in water with localized

circumferential cracks on the scale surface, demonstrating its multi-hit capability.....	227
Figure 9-4. Bioinspired hybrid exoskeletal designs in conjunction with material-based research; (a) variable property analysis (<i>left</i>) and fabrication (<i>right</i>) of a hybrid design, inspired by biological tissues, which was made of the aluminum and low carbon steel composite (N. Oxman) (Oxman, 2010) and (b) example of hybrid exoskeletal designs mimicking the spatial distribution of <i>P. senegalus</i> scales by combing two materials, hard (blue) and soft (yellow) materials through thickness.....	229
Figure 9-5. Natural selection mechanism by conventional approaches in evolutionary biology.....	230
Figure 9-6. Proposed natural selection mechanism in evolutionary biology by interdisciplinary approach (conventional evolutionary, genetic and engineering approaches).....	231
Figure A-1. Nanoindentation data of dentin compared to FEA elastic and elastic-perfectly plastic simulations plotted with error analysis. Averaged experimentally measured load vs. depth data for dentin (averaged over 20 experiments) and the FEA predictions assuming elastic behavior ($E=25$ GPa) and three cases of elastic-perfectly plastic behavior with (E, σ_y) pairs of (25 GPa, 530 MPa), (25 GPa, 600 MPa), and (25 GPa, 700 MPa). Also shown are the absolute value of the % error between each predicted curve and the experimental curve as a function of indentation load.....	234
Figure A-2. Generic representation of stress-strain curves including strain hardening behavior after yielding by means of two strain hardening models; (a) linear strain hardening model and (b) the Ramberg–Osgood strain hardening model (Ramberg and Osgood, 1943). In case of the Ramberg-Osgood model, strain corresponding to the yield point is the sum of the elastic and plastic components.....	235
Figure A-3. (a) Uniaxial elastic-plastic behavior of the elastic-plastic material (dentin) including the perfectly plastic case as well as linear hardening and Ramberg-Osgood hardening models and (b) indentation load vs. depth curves for dentin showing the averaged experimental curve (averaged over 20 experiments) and the FEA predictions using the indicated elastic-plastic material models which include post-yield strain hardening. Including strain hardening does not substantially improve the prediction when compared to use of an elastic-perfectly plastic model.....	236
Figure A-4. Residual surface topography as measured by AFM (measurements from five different experiments shown) and as predicted by the FEM simulations with the indicated elastic-plastic material models.....	238

Figure B-1. (a) Uniaxial elastic-plastic behavior of the four materials showing the elastic-perfectly plastic (EPP) case as well as Ramberg-Osgood (R-O) hardening model, and (b) simulated load versus depth curves for the microindentation of the multilayered finite element analysis (FEA) simulations showing loading and unloading to a maximum load of 1 N comparing the R-O strain hardening model to the EPP model.	240
Figure B-2. Simulation contours of stress components and plastic strain for the EPP case (top) and the R-O case (bottom). FEA prediction of von Mises field, S22, and S11 when fully loaded and S33, S23, plastic equivalent strain and pressure after fully unloaded for the two models for 1N maximum load indentation. The inclusion of strain hardening in the material behavior does not substantially change the overall stress fields or the local stress fields on the surface or at the junction, indicating both models provide the same conclusions regarding the load-resistance mechanisms of the multilayered scale.	241
Figure B-3. Uniaxial elastic-perfectly plastic behavior of the two outer layer materials (ganoine, dentin) in the multilayered models including those with rate dependent yield (σ_Y scaled according to $\dot{\epsilon}$, values provided to the right of each stress-strain curve).....	242
Figure B-4. Simulated microindentation load vs. depth curves comparing rate dependent models to rate independent models, Model 1: only ganoine is rate-dependent, Model 2: only dentin is rate-dependent, Model 3: ganoine and dentin are both rate-dependent, Model 4: ganoine and dentin are rate independent (i.e. the case reported in the manuscript). The effect of $\dot{\epsilon}$ was also investigated for Model 3.....	243
Figure C-1. Load-depth behavior of the ganoine-dentin-isopedine-bone quadlayer models that emulated <i>P. senegalus</i> scales subjected to hypothetical tooth biting at 0.75N of the initial load; (a) the case of the tooth biting with a tip end radius of $R_{tip}^n = 0.42$, (b) the case of the tooth biting with a tip end radius of $R_{tip}^n = 1.25$ and (c) the case of the tooth biting with a tip end radius of $R_{tip}^n = 2.5$. After the first biting occurred, four following biting were applied with the same work of indentation, resulting in the total biting cycles of five.....	247
Figure C-2. (a) Indentation loads and (b) tooth penetration depth into scale as a function of the number of cycles at different tip end radii of the threat models.....	248
Figure C-3. (a) Indentation loads and (b) tooth penetration depth into scale as a function of the number of cycles at different tip end radii of the threat models.....	249
Figure C-4. Rate-dependent mechanical behavior of soft tissue at the maximum indentation depth of 4 μm at three indentation rates of 4 $\mu\text{m/s}$, 0.13 $\mu\text{m/s}$, and 0.04 $\mu\text{m/s}$	250

Figure C-5. Load-depth curves of two ‘scale-only’ and ‘scale-tissue’ models at three indentation times of 1, 30 and 100s at the maximum load of 1 N.....	251
Figure C-6. Stress and strain contours of the ‘scale-only’ and ‘scale-tissue’ models when loading at the maximum load of 1 N and fully unloading.....	252
Figure C-7. (a) Energy dissipation of each material layers in the scale and tooth systems for the ‘scale-only’ and ‘scale-tissue’ model cases at three indentation times and (b) relative energy dissipation of dentin and ganoine of the scale system and enamel of the tooth system, indicating 99.9% of energy dissipation occurs in those three material layers.....	252
Figure E-1. The z-height profile and 1 st derivative of z-height of (a) marine <i>G. aculeatus</i> full-morph pelvic assembly and (b) freshwater <i>G. aculeatus</i> full morph pelvic assembly. Four regions are indicated based on the 1 st derivative of height.	257
Figure E-2. Sketch of the Representative Volume Elements (RVEs) of a pelvic median suture (left), and the free body diagram of a triangular tooth (right) under longitudinal loading (Li et al., <i>in review</i>).	258
Figure E-3. Schematic diagram of inclined plates between two ventral plates of a pelvic girdle; each cross-section of the plates has the inclination angle of φ , which is connected with top and bottom plates with the width of d. The skeleton of the structure has the thickness of t. The effective moment of inertia for the cross-section of each internal inclined plate is composed of three moments of inertia (I_0 , I_1 and I_2)......	259

List of Tables

Table 1-1. Structural biological materials found in nature (Wainwright et al., 1976).....	38
Table 1-2. Summary of the characteristics in the integumentary skeleton of jawed fish (Moss, 1963; Sire, 1990; Coburn and Gaglione, 1992; Raschi and Tabit, 1992; Sire et al., 2009). All fish scales are made of the same mineral component, calcium phosphate (mainly, hydroxyapatite) (Lowenstam and Weiner, 1989).	43
Table 2-1. Comparison of two fish armor model systems, <i>Polypterus senegalus</i> and <i>Gasterosteus aculeatus</i> (Hoogland et al., 1956; Meinke et al., 1979; Driessens and Verbeeck, 1990; Kodera, 1994; Reimchen, 1994; Long and Nipper, 1996; Daget et al., 2001; Bergstrom, 2002; Gemballa and Bartsch, 2002; Bell et al., 2004; Westneat, 2004; Marchinko and Schluter, 2007; Östlund-Nilsson et al., 2007; Bell et al., 2009).	51
Table 2-2. Three types of <i>P. senegalus</i> teeth (Clemen et al., 1998; Wacker et al., 2001). Images from ref. (Clemen et al., 1998) were modified in order to show the morphological features of each tooth clearly.....	55
Table 4-1. Mechanical properties of HAP crystals assumed in the nanomechanical model. The 3-axis was taken to be coincident with the crystallographic axis.....	96
Table 4-2. Isotropic material properties used in FEA model of microindentation into multilayered <i>P. senegalus</i> scale, obtained from isotropic elastic-plastic FEA fits to nanoindentation data for each layer as reported in Chapter 3.	99
Table 4-3. Predicted anisotropic material constants for ganoine layer from nanomechanical model of RVE with transverse mineral elements: (I) RVE consists of isotropic HAP mineral and (II) RVE consists of HAP mineral with elastic and plastic anisotropy (Lee et al., 2000; Viswanath et al., 2007).....	101
Table 4-4. O-P modulus and hardness obtained from experimental measurements and various simulation models: isotropic model, anisotropic model I where the HAP crystal is isotropic, anisotropic model II where the HAP crystal is anisotropic, and the discrete model.	108
Table 5-1. Mechanical properties and layer thickness values utilized in finite element simulations of predatory toothed biting attack on individual quad-layered ganoid scale of <i>P. senegalus</i> including the modulus (E), yield stress (σ_Y) and layer thickness values used for each of the four scale and two tooth material	

	layers. For the parametric studies, E, σ_Y , and the thickness of tooth enameloid was varied (Habelitz et al., 2001; Marshall et al., 2001; Lippert et al., 2004; Mahoney et al., 2004; Sasagawa et al., 2009; Sire et al., 2009).....	126
Table 5-2.	Comparison of <i>P. senegalus</i> tooth and scale systems in terms of shape, composite materials, multi-layered structure as well as the layer thickness.	140
Table 5-3.	Advantages and disadvantages of penetrating threat and corresponding protective natural armor systems	141
Table 6-1.	Summary of constitutive material layers, their typical mineral contents and sequence of three major fish scale types (ganoid, placoid and elasmoid) with example species (Sire, 1990; Raschi and Tabit, 1992; Sire et al., 2009).....	145
Table 6-2.	Mechanical properties and layer thickness values utilized in finite element (FE) simulations of Vickers microindentation and hypothetical biting attack on various layered structures. The modulus (E), yield stress (σ_Y) and layer thickness values used for each of the four scale and tooth material layers. For the parametric studies, ganoine thickness of three layered scale models was varied. The values in brackets in the first quadlayer model represent the used layer thicknesses of ganoine and dentin for the GDIB quadlayer model. ...	149
Table 6-3.	Tabulated advantages and disadvantages of multilayer designs depending on their structural parameters	169
Table 7-1.	The structural and material properties of the armor plate assembly of marine <i>Gasterosteus aculeatus</i> (threespine stickleback). Average thickness, bone volume and bone mineral density were determined by morphometric analysis of μ CT images. Mineral contents were measured by BSEM/EDX analysis. Volume porosity and density were obtained by mercury porosimetry. Areal porosity was measured using optical microscopy images. Tubercle dimensions, groove spacing and density of tubercles were calculated by using surface topography images taken by surface profilometry and SEM.....	196
Table A-1.	Assessment of the fit of elastic-perfectly plastic material models to the indentation load-depth data for dentin (where an average error during loading and unloading is obtained after constructing the error analysis curves illustrated in Fig. A-1 for each material)	234
Table A-2.	Assessment of the fit of various elastic-plastic material models to the indentation load-depth data for dentin (where an average error during loading and unloading is obtained after constructing the error analysis curves illustrated in Fig. A-3 for each material)	237
Table B-1.	Four types of rate-dependent FEA multilayered models.....	242

Table C-1. Biting force (from muscles of jaws) of several fish species. This is not the real actinf force for the biting event and mechanical advantage needs to be taken into account for the acting biting force at the tip end of teeth.	246
Table C-2. The type and frequency of the indentified food items found in the stomach of <i>Polypterus senegalus</i> (n = 80) from Lake Chad in Nigeria (Raji et al., 2003).	246
Table C-3. Material properties of individual scales and underlying organic tissues	250
Table D-1. Morphometric material parameters obtained from MicroCT data analysis by Scanco software (User's guide for microCT 40; Scanco Medical AG, Bassersdorf, Switzerland). Ratios (BV/TV, BS/TV, BS/BV) are the normalized indices. The model-independent indices are marked with an asterisk (*).	256

Chapter 1.

Introduction

1.1. Opening Remarks

1.1.1. Learning from Nature: Bioinspiration

Many biological materials often exhibit multifunctionality and superior capabilities with intricate and hierarchical structures as compared to man-made materials (Sanchez et al., 2005; Arciszewski and Cornell, 2006; Bar-Cohen, 2006; Ortiz and Boyce, 2008). As the current technology faces increased demands on multifunctional, biomedical, environment-friendly, and energy-efficient designs, scientists and engineers have sought for insights from the biological systems by identifying and understanding design principles that are emerging from nature. These efforts have opened the highly multidisciplinary research area, called ‘bioinspiration’ or ‘biomimetics’. The goal of bioinspiration is not just imitating a biological system as it is, but understanding, extracting and implementing its design principles on various aspects—materials, processes, mechanisms and methods—at different resolutions from small molecules to macroscopic structures with a wide range of material spectrum as opposed to the limited number of elements that organisms can utilize (Sanchez et al., 2005; Bar-Cohen, 2006; Ortiz and Boyce, 2008). According to designate applications, bioinspiration includes bioinspired structural materials, biomimetic materials for tissue engineering, bioinformatics and artificial intelligence, biomimetic synthesis, bioinspired sensors and actuators in conjunction with conventional science and engineering fields (Fig. 1-1). This thesis mainly focuses on bioinspired structural materials (highlighted in red in Fig. 1-1) for the development of protective and flexible material systems, e.g. human body armor, vehicle armor or industrial protective suits. This discipline is working with four major engineering fields, materials science & engineering, mechanical engineering, architecture and bioengineering, and I will present material and mechanical approaches in this thesis.

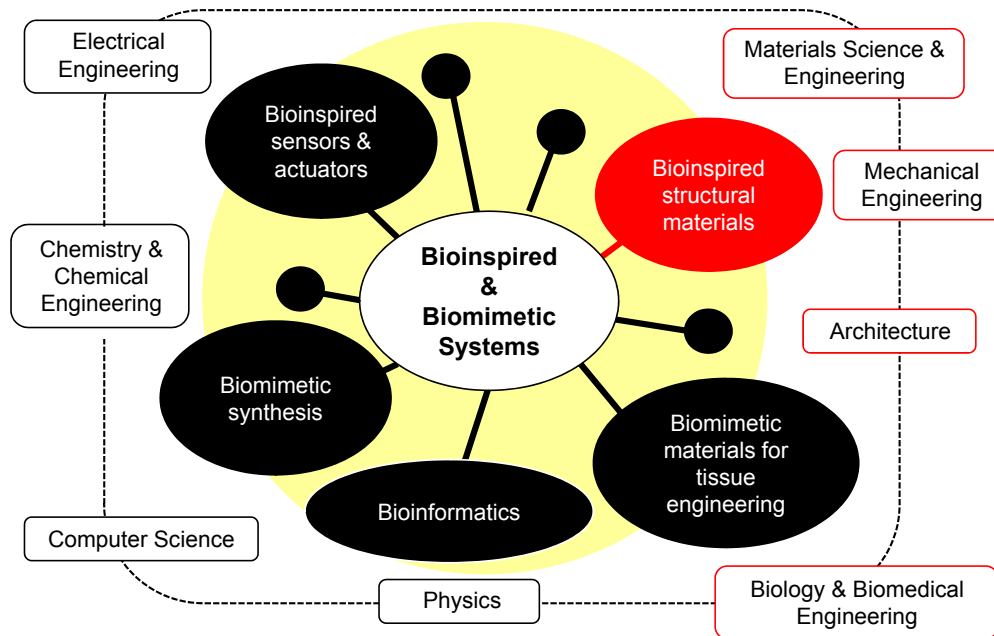


Figure 1-1. Bioinspiration and its related science and engineering disciplines; bioinspired structural materials, biomimetic materials for tissue engineering, bioinformatics and artificial intelligence, biomimetic synthesis, bioinspired sensors & actuators are active research fields in bioinspiration.

A general approach to a complex biological system has been proposed in terms of a structure-property-function relationship (Wainwright et al., 1976; Ortiz and Boyce, 2008; Dunlop et al., 2011). The biological structure of an organism has been created to be appropriate to some functions and has sometimes been reconstructed to acquire a certain function for better adaptation, resulting in divergent descendant species from their ancestors. Therefore, characterization and identification of a biological structure and following functional assessments based on the structural information are able to provide a fundamental understanding of the system, ultimately allowing universal and abstract design principles to be extracted for man-made designs (Arciszewski and Cornell, 2006). The diagram of figure 1-2 shows typical research processes appearing in various bioinspired systems (Wainwright et al., 1976; Weiner et al., 2000; Ortiz and Boyce, 2008; Dunlop et al., 2011). Foremost, the definitive objectives of a bioinspired research project should be proposed and then required functionality can be derived from the objectives. Among various biological systems, a proper model system can be selected based on its performance in response to the existing environmental conditions. Subsequently, the model system will be investigated in terms of structure-property-function relationships in order to obtain the design principles that will be implemented into man-made designs. In this thesis, this approach will be directly applied without or with modification for chosen model systems.

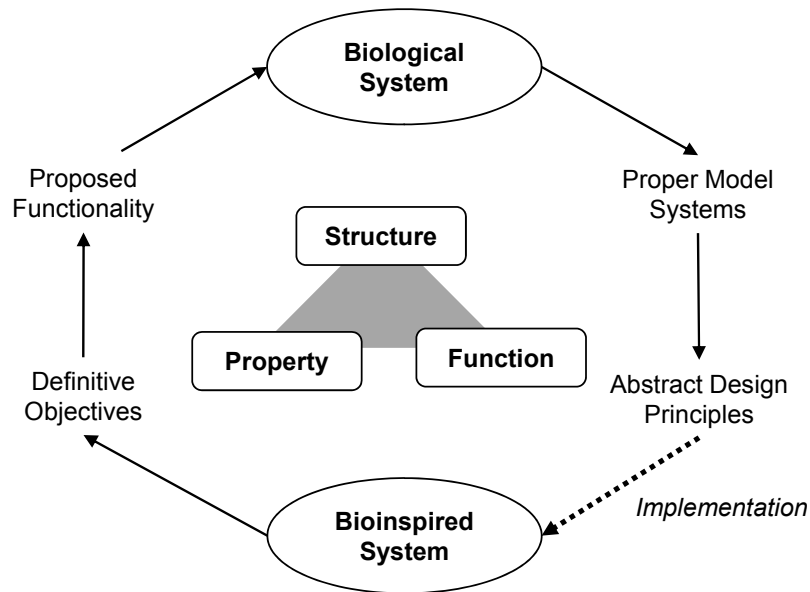


Figure 1-2. A typical approach of bioinspired material systems in terms of a structure-property-function relationship for an understanding of design principles of natural model systems

1.1.2. Structural Biological Materials

A class of natural materials, so-called ‘structural biological materials’, has varied complex, hierarchical and heterogeneous structures in order to support and resist loads in certain circumstances (Wainwright et al., 1976; Vincent, 1990; Elices, 2000). The examples and structural features of structural biological materials are shown in Table 1-1. In particular, many soft-bodied animals have developed natural body armor (e.g. mollusk (Li et al., 2004; Bruet et al., 2005) and turtle shells (Egginton et al., 1999; Wyneken et al., 2008), arthropod exoskeleton (Raabe et al., 2005), and bony fish scales (Bruet et al., 2008), etc.) over millions of years of evolution for protection and survivability against predatory and environmental threats (Arciszewski and Cornell, 2006). These armors possess intricate hierarchical microstructures which are composed of brittle inorganic bioceramics and compliant, extensible biopolymers and yet these composites exhibit a combination of excellent stiffness, strength, toughness and energy dissipation. These natural materials are a great untapped resource for providing new engineering designs for synthetic, biologically inspired protective material systems, e.g. human body armor or vehicle armor in the military or industry.

Nacreous layers of some mollusk shells and bone of vertebrates are the most famous and the most investigated among structural biological materials in terms of their featured hierarchical structures and mechanical design principles for increased strength,

Table 1-1. Structural biological materials found in nature (Wainwright et al., 1976)

Taxonomy structure	Example Species	Structural System	constitutive material	Featured Structure
Algae Diatoms (Hamm et al., 2003)	<ul style="list-style-type: none"> • Centrales : <i>Thalassiosira punctigera</i> <i>Coscinodiscus granii</i> • Pennales : <i>Fragilariopsis kerguelensis</i> 	frustule (shell)	silica organic components	<ul style="list-style-type: none"> • Silicified cell walls in the form of two shells • Manifold shape and intricate architecture
Plantae (Easterling et al., 1982)	Malvaceae : <i>Ochroma pyramidale</i>	wood	cellulose, lignin	Porous, layered fibrous structure
Animalia				
Porifera (Aizenberg et al., 2005; Woesz et al., 2006)	Euplectellidae : <i>Euplectella aspergillum</i> (sea sponge)	spicule	silica organic components	<ul style="list-style-type: none"> • Hexactinellid sponge-like spicules • Rigid basket and flexible spicules • Multilayered silica
Mollusca (Wainwright, 1969; Currey and Taylor, 1974; Chateigner et al., 2000; Li et al., 2004; Bruet et al., 2005; Lin et al., 2006)	Molluscs : <i>Halotis rufescens</i> <i>Crysmallon squamiferum</i> <i>Strombus gigas</i> <i>Tridacna gigas</i>	shell	calcium carbonate organic components	<p>often found as layered structures, where each layer is</p> <ul style="list-style-type: none"> • nacreous • prismatic • cross-lamellar • foliated • homogeneous
Arthropoda (Vincent and Wegst, 2004; Raabe et al., 2005; Cheng et al., 2008, 2009)	Crustacea : <i>Homarus americanus</i> Insecta : <i>Popillia japonica</i>	cuticle	chitin calcium carbonate chitin	Multilayered, plywood-like structure
Echinodermata (Wang et al., 1997; Chen, 2011)	Echinoida : <i>Colobocentrotus atratus</i>	spine test teeth	calcium carbonate organic components	Porous spines articulating with the test via ball-and-socket joints
Chordata -Vertebrata (Currey, 1999; Gupta et al., 2005; Imbeni et al., 2005; Tai et al., 2006; Buehler, 2007; Krauss et al., 2009; Sire et al., 2009)	Actinopterygii : <i>Polypterus senegalus</i> Reptilia : <i>Trachemys scripta elegans</i> Mammalia : <i>Homo sapiens</i>	bone tooth scale/scute bone tooth shell scale/scute bone tooth	hydroxyapatite protein (e.g. collagen, keratin) polysaccharide	Multilayered fish scales Porous, segmented turtle shell and suture Hierarchical, bone structure

and fracture toughness (Meyers et al., 2008; Barthelat, 2010; Dunlop and Fratzl, 2010; Launey et al., 2010; Lawn et al., 2010; Wang and Gupta, *In press*). Vertebrates have backbones and spinal columns to support their body and resist loads in various environments, as opposed to invertebrates that have hard external support structures, exoskeletons, instead of backbones (Wainwright et al., 1976). Vertebrate backbones are made of hydroxyapatite (HAP)-organic nanocomposites (bone) with a typical mineral content of up to 60 ~ 70 wt%, embedded in cellular matrices, while invertebrate exoskeletons have often highly mineralized calcium carbonate nanocomposite or densely-packed chitin-based polymeric multi-layered structures that experience direct contact with environmental stimuli. However, the design strategies of two different material systems show great similarities in deformation and toughening mechanisms for mechanical amplification, e.g. increasing inelastic behavior and resistance to crack propagation by utilizing a small amount of organic components (Wang and Gupta, *In press*).

Nacre (Barthelat and Espinosa, 2007; Ortiz and Boyce, 2008; Espinosa et al., 2009; Barthelat, 2010; Wang and Gupta, *In press*) is one of material layers found in mollusk exoskeletons, often located as an internal layer of multilayered structures, and a highly mineralized organic-inorganic nanocomposite with ~ 95 wt% calcium carbonate in the aragonite form. The building block of nacre is a polygonal mineral tablet with a diameter of 5 ~ 15 μm and a thickness of 0.5 ~ 1 μm . Individual tablets are spatially arranged in plane and stratified through thickness, similar to three-dimensional brick walls where the 5 % of organic components behave like adhesives, located at the interface between tablets. Other important structural features of nacre include nanoasperities on the surface of the tablets, mineral bridges between tablets, and a significant waviness of individual tablets. The hierarchical structures of nacre are shown at multi-length scales in Fig. 1-3a. Individual highly mineralized tablets of nacre have modulus of ~ 100 GPa (reaching the stiffness of aragonite). Tensile strength of nacre can reach ~ 120 MPa with observed straining hardening at ~ 1 % strain, as a result of collective tablet sliding that includes progressive tablet locking generated by the waviness of tablets and increased friction between tablets because of roughed surfaces and mineral bridges. The strain hardening mechanisms and enhanced inelastic behavior of nacre also contribute the amplified fracture toughness (~ 10 $\text{MPa}\cdot\text{m}^{1/2}$; ~ 3000 times tougher than aragonite) by increasing crack resistance, e.g. a large amount of energy dissipation, and the arrest of crack propagation. Attempts have been made to implement the material design principles of nacre into various man-made material systems, e.g. a multilayered alumina platelet-reinforced chitosan nanocomposite (Bonderer et al., 2008), a montmorillonite clay platelet-poly(vinyl alcohol) matrix nacre-mimetic artificial nanocomposite (Podsiadlo et al., 2007) and metallic-intermetallic laminate (MIL) composites (Vecchio, 2005), which showed improved mechanical performance (tensile

strength, fracture toughness) as compared to raw constitutive materials and even possessed multifunctionality by incorporated sensing capability.

Bone (Rho et al., 1998; Currey, 1999; Nalla et al., 2003; Tai et al., 2006; Tai et al., 2007; Espinosa et al., 2009; Launey et al., 2010; Wang and Gupta, *In press*) is typically found as a layered structure that consists of spongy-like trabecular bone capped with outer compact cortical bone. In particular, cortical bone mainly supports load by its intricate and hierarchical structure that provides important deformation and toughening mechanisms (Fig. 1-3b). Based on two basic building blocks (organic collagenous fibrils and hydroxyapatite minerals) at the nanoscale, micro-level building blocks of mineralized collagen fibrils are formed and arranged, resulting in a mineralized collagen fiber. Individual lamellae are again assembled by those mineralized collagen fibers, constructing an osteon that surrounds and protects blood vessels (a Haversian system). Haversian systems are connected with interstitial lamellar bone, occupying the volume of the outer bone layer. The size, density, and spatial distribution of the Haversian systems are inhomogeneous, which leads to the spatial variation of mechanical properties in bone with the increased capability of energy dissipation. Plastic deformation mechanisms of bone are facilitated by hydrogen-bond breakage in pure collagen molecules, fibrillar sliding of mineralized collagen fibrils or collagen fiber arrays and isolated microcracking at the nanoscale and the microscale. These plastic deformation mechanisms efficiently dissipate energy ahead of crack tips, forming a plastic zone. At the crack sites, the micro- and macro-level crack arrest mechanisms can be activated by sacrificial bond breakage, constrained microcracking around the crack, collagen-fibril and uncracked-ligament bridging and crack deflection and twist. These multidimensional toughening mechanisms vary with bone aging and disease. Therefore, a fundamental understanding on the origin of mechanical degradation in bone can provide insight into the development of diagnosis and therapeutic methods of bone aging and diseases in medical science.

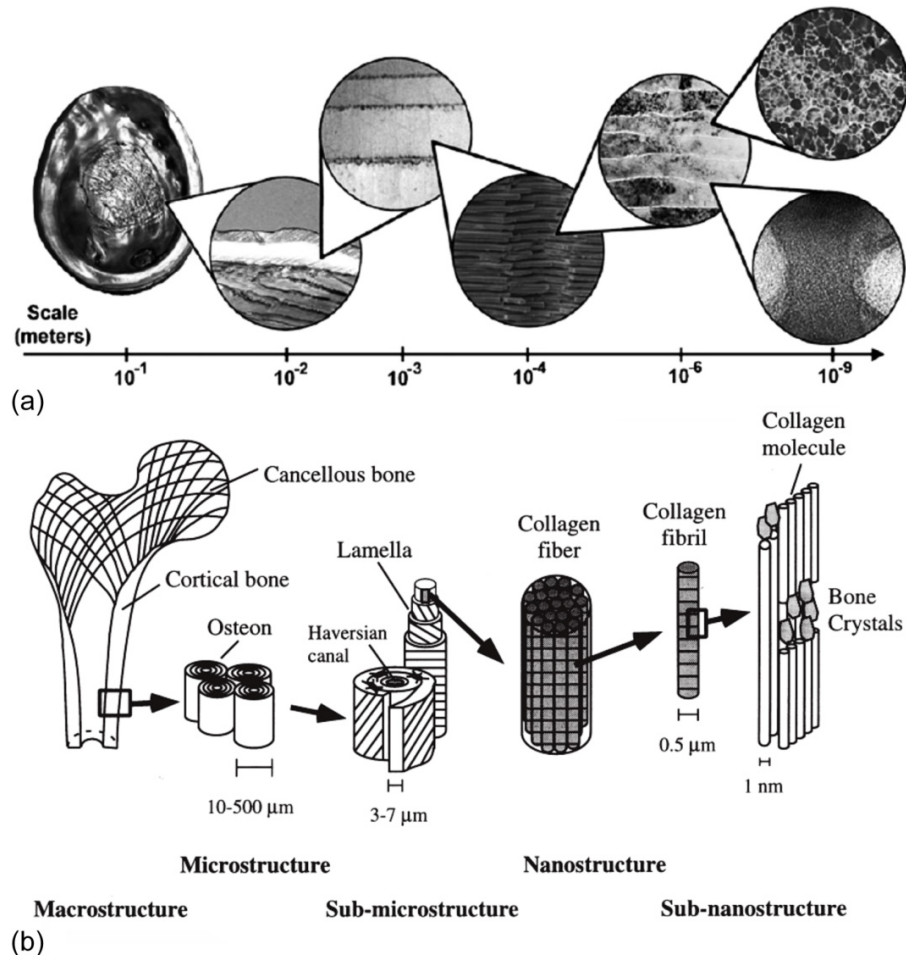


Figure 1-3. Hierarchical structures of structural biological materials at multi-length scales; (a) nacre from red abalone *Haliotis rufescens* (from Barthelat's paper (Barthelat, 2010): p. 3, Fig. 2) and (b) human bone (from Rho's paper (Rho et al., 1998): p. 93, Fig. 1).

1.1.3. Fish Dermal Armor: Flexible and Protective Design

This research focuses on "armored" fish which have highly mineralized articulating scales whereby the multilayered materials design of the individual scales works in conjunction with a host of larger length scale geometries and interlocking mechanisms to enable biomechanical flexibility and mobility. Armored fish, similar to early vertebrates, use calcium phosphate (primarily hydroxyapatite or HAP) as the mineral component because of the source of phosphate ions (Pautard, 1970; Halstead et al., 1974) (a key chemical agent for metabolism) as well as a greater chemical stability than calcium carbonate under physiological conditions associated with rapid pH change by production of lactic acid via glycolysis for ATP generation (Ruben and Bennett, 1987) (aerobic energy metabolism). This differs from other invertebrate exoskeletons such as those of mollusks and sea urchins which are generally composed of calcium carbonate.

Dermal armor of fish first appeared at the beginning of the Paleozoic period, approximately 500 million years ago (Hoedeman, 1975), with the rise of the Ostracoderms and became common among the earliest fish as protection in response to potential environmental threats, such as predators (Romer, 1933; Colbert, 1955). Scales of ancient fish typically possessed multilayered structures and varied geometries (Ørvig, 1968; Spearman, 1973). As fish became more predaceous through the Devonian period (Anderson and Westneat, 2007), the larger and heavier plates of dermal armor broke up into many smaller ones, the thickness of various material layers decreased (~1500 - 100 μm thick), and the number of material layers within the armor plates decreased (~4 to 1-3 layers) (Sire, 1990; Sire et al., 2009). These changes provided significant advantages including; decreased body weight, improved flexibility and maneuverability, and enhanced swimming speed (Romer, 1933). Habitats also expanded to include both fresh water and marine environments and correspondingly, extensive diversification took place due to abiotic factors such as salinity and temperature, and biotic factors such as competition and predation (Romer, 1933; Colbert, 1955; Hoedeman, 1975). Current living armored fish exhibit three major types of bony scales called ganoid, placoid and elasmoid which are categorized based on shape, layered microstructure as well as mineralization (Sire et al., 2009) as summarized in Table 1-2. The ganoid scales of the family Polypteridae retain a quad-layered scale structure, a characteristic of ancient palaeoniscoids (Meunier, 1980; Daget et al., 2001). The most wide-spread type of scale is the elasmoid, which are composed of thin, transparent, lamellar collagenous plates in which ganoine and osseous basal plate are reduced when compared to the ganoid or placoid (Sire, 1990; Sire et al., 2009). Elasmoid scales of some teleosts including *Gasterosteus aculeatus* exhibit a single layered structure where ganoine totally disappeared (Sire et al., 2009; Song et al., 2010). Current living species of armored fish retain a diversified set of dermal scales which efficiently protect underlying soft tissues by elegantly balancing protection, damage tolerance, weight, and mobility requirements

to maximize survivability (Ørvig, 1968; Sire, 1990; Reimchen, 1992; Cresko, 2008; Bell et al., 2009).

Table 1-2. Summary of the characteristics in the integumentary skeleton of jawed fish (Moss, 1963; Sire, 1990; Coburn and Gaglione, 1992; Raschi and Tabit, 1992; Sire et al., 2009). All fish scales are made of the same mineral component, calcium phosphate (mainly, hydroxyapatite) (Lowenstam and Weiner, 1989).

Taxon - Phylum: <i>Chordata</i>		Scale type	Number, type of layers	Mineral type	Mineral content (%)
Class	Order (representative species)				
Placodermi	<i>Extinct (fossils)</i>	Placoderm	3~4 Semidentin Spongiose Lamellar	HAP	NA
Chondrichthyes	Elasmobranchii - Batoidea (<i>rays, skates</i>)	Placoid	2 Enamel Dentine	HAP	< ~50 (dentin) > 90 (enamel)
	- Selachimorpha (<i>sharks</i>)				
	Holocephali - Chimaeriformes (<i>ratfish</i>)				
Actinopterygii (ray-finned fish)	Chondrostei - Polypteriformes (<i>bichirs, reedfish</i>)	Ganoid	2~4 Ganoine Dentin Isopedine Bone	HAP	20~98
	Chondrostei - Acipenseriformes (<i>sturgeons</i>)	Scutes	~2 Bone	HAP	NA
	Neopterygii - Holostei (<i>gars and bowfins</i>)	Ganoid	2~3 Ganoine Dentin Bone	HAP	20~98
	Neopterygii - Telostei Protacanthopterygii (<i>salmon, trout</i>)	Leptoid Elasmoid	2 Thin ganoine Isopedine (most)	HAP	16~59
	Acanthopterygii (<i>stickleback, bass, mackerel, tuna, flyingfish</i>)				

1.2. Thesis Outline

The ultimate goal of this thesis is to uncover/reveal/articulate materials and mechanical design principles of flexible fish armor, focusing on a few selected model species, and the relationship of their micro and macrostructures to their corresponding environments. An understanding of the structure-property-function relationships of fish scales has broad applicability to the development of synthetic engineered penetration-resistant/protective and flexible/light-weight materials. In this thesis, I will mainly focus on the protective design principles of fish armor systems, choosing two animal models: *Polypterus senegalus* (the bichir) and *Gasterosteus aculeatus* (the threespine stickleback). In particular, the multilayered design and three-dimensional complex geometry of those two fish armor systems will be intensively investigated in addition to material and mechanical characterization of individual constitutive layers. The mechanical interaction among constitutive layers of a multilayered structure and the articulation of structural elements via three-dimensional complex geometry also play key roles in mechanical functionality of a biological material system, which has not yet gained much attention. Therefore, this thesis can provide a comprehensive understanding of the entire biological material system. The outline of this thesis is shown in Fig. 1.4.

Chapter 2 provides background information of two model systems, *P. senegalus* and *G. aculeatus* armor. The first section of this chapter will focus on *P. senegalus* armor system, summarizing current knowledge of its mineralized scales, potential environmental threats, biomineralization mechanisms and scale-to-scale articulation. In particular, a recent collaboration work of this research project on articulation and flexibility of *P. senegalus* armor, forming the S.M. thesis of an architecture student, Mr. Steffen Reichert, will be introduced with proposed bioinspired flexible designs for man-made material systems. The second section will present *G. aculeatus* armor system that consists of two major armor components besides dorsal spines with their basal plates; (1) passive lateral plates covering its body from the anterior to the posterior in case of maximum protection, and (2) offensive pelvic assembly covering the ventral region of the anterior body. Morphological variation of *G. aculeatus* armor in response to various environmental constraints has been investigated by conventional and genetic approaches in the field of evolutionary biology. The current knowledge on biological, morphological and antipredatory features of *G. aculeatus* armor will be provided with introduction of research tools of evolutionary and comparative biology.

Chapters 3 to 6 of this thesis will explore the protective design of the individual *P. senegalus* armor units at nano and micro scales, providing a understanding of how various biological nano- and micro-structures of the individual armor units are designed for sustaining the particular loading situations (i.e. predatory attacks) experienced in their native environments. The other fish armor system, *G. aculeatus* armor will be presented

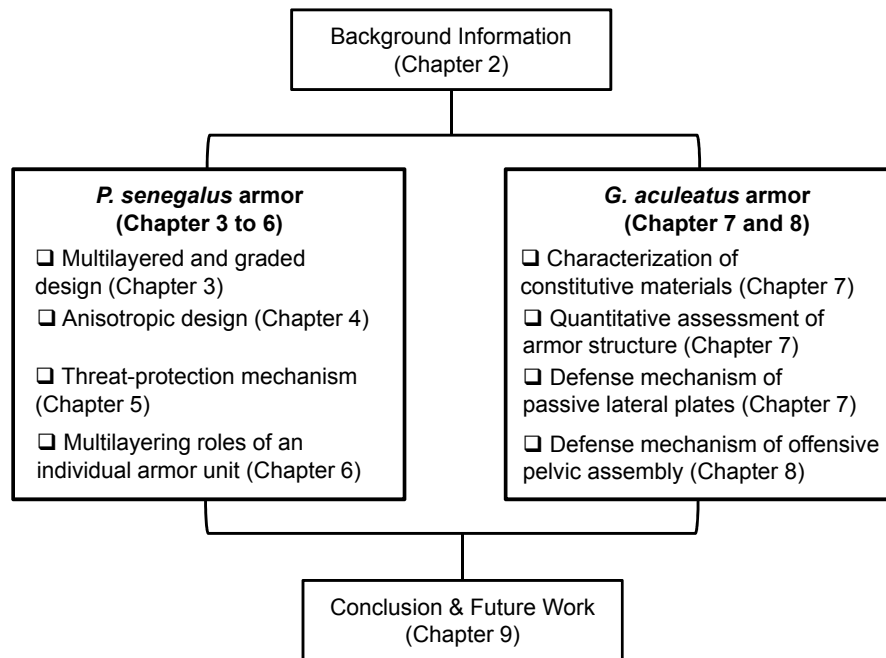


Figure 1-4. Diagram of thesis organization. This thesis deals with two fish armor model systems, *Polypterus senegalus* and *Gasterosteus aculeatus* armor for an understanding of their design principles.

in Chapter 7 and 8, focusing on two major armor components with their structural variation and defense mechanisms in response to coexisting environmental threats. The design principles of the armor system will be understood in the context of structure-property-function relationships.

In Chapter 3, a multiscale computation approach will be employed, using previous experimental results of microstructures and mechanical properties of *P. senegalus* scales in order to understand multilayering and grading design principles. First, nanoindentation computational models will be constructed to retrieve the elastic-plastic mechanical behavior of each material layer by fitting the predicted load-depth curves of nanoindentation simulation to the experimentally obtained nanoindentation curves. Then, measured and estimated material properties of individual constitutive layers in *P. senegalus* scales will be incorporated into the multilayered scale models that will be subject to various microindentation loads for predicting macroscopic mechanical behavior of the entire system to penetration events.

Chapter 4 focuses on the outmost ganoine layer of *P. senegalus* scales that serves as one of the first lines of defense against a penetrating attack. The individual layers of a multilayered system have their own unique nano/microstructures, constitutive law and mechanical behavior. In particular, hierarchical structural anisotropy is one of important and common features of many biological systems, which

originates from: (1) inherent anisotropy of the fundamental building blocks at the smallest scale, and (2) the controlled shape, orientation, and spatial placement of various structural elements in a composite system at a larger length scale. In this chapter, the mechanics of the ganoine anisotropy will be investigated via experiments and modeling. First, the mechanical anisotropy of ganoine will be experimentally assessed via instrumented nanoindentation in the surface and cross-sectional orientations. Then, anisotropic elastic-plastic nanomechanical models and nanoindentation models will be developed to obtain three-dimensional anisotropic elasticity and plasticity of the ganoine layer and also to reveal the role of the inherent anisotropy of the building blocks in the overall anisotropy of ganoine. Finally, the multilayered scale models with the anisotropic elastic-plastic ganoine will be constructed to reveal the role of the ganoine anisotropy in the entire multilayered structure, especially in terms of the penetration resistance and deformation of the scale.

In Chapter 5, the role of geometry, microstructure and deformability of the threat relative to that of the armor on threat-protection mechanical interactions will be investigated. Penetration resistance mechanisms of natural exoskeletons have three major mechanical strategies to minimize the back-displacements and stress levels transmitted to the underlying soft tissues and vital organs of the animal; (1) defeating the threat via deforming and/or fracturing the threat, (2) dissipating the energy of the threat via plastic deformation and/or a multitude of cracking events within the armor, and (3) combining both of these mechanisms. In Chapters 3 and 4, a predatory toothed bite on a *P. senegalus* ganoid scale has been idealized by an infinitely rigid indenter and penetrated into an individual quad-layered scale. In Chapter 5, the finite stiffness of the threat will be modeled as a deformable indenter, thereby more closely representing the true biological threat. The role of the threat (tooth) geometry (e.g. end-radius, cone angle), multi-layered structure, and deformability on penetration resistance, local stress and strain distributions, and energy dissipation of both the threat and armor during a virtual predatory biting attack will be parametrically studied. These results will lead to the formulation of a summary of advantageous and disadvantageous design strategies for the offensive threat and defensive protection.

In addition to threat-protection interaction in Chapter 5, Chapter 6 will expand the topic into design principles of the individual multilayered armor units in order to understand the optimized structure of the mineralized quad-layer scale design in *P. senegalus* by comparing various multilayered structures in terms of their predicted functionality, linking the scale design to its function with regards to the specific threat experienced in its environment while minimizing sacrifice of mobility. Three multilayered designs will be developed: (i) the thickness of the outer layer, ganoine; (ii) the quad-layered structure as compared to simpler bilayer structures; and (iii) the sequence of the outer two layers. The mechanical behavior of various multilayer designs

will be studied during penetration while weight will also be used as an additional comparative property. In order to understand the role of those three structural parameters, parametric studies via finite element analysis (FEA) simulations of virtual Vickers microindentation and hypothetical biting to various maximum loads will be carried out. Based on these results, variations in multilayered design of natural armor systems will be understood, in terms of a balance between protection and mobility in armor design.

The microstructure of field-caught marine *G. aculeatus* armor will be investigated by employing a quantitative, materials science-based approach in Chapter 7. Microcomputed tomography (μ CT) is a major tool of this study that can create full three-dimensional images of *G. aculeatus* armor (e.g. the dorsal spines and basal plate, lateral plates, pelvic girdle and spines) and assess structural and material properties (e.g. the spatial distribution of thickness, the cross-sectional geometry, plate-to-plate interconnections and overlap, bone mineral density, and bone volume). Three-dimensional printing will also be employed to fabricate scaled-up macroscopic prototypes using the μ CT data in order to visualize the detailed morphometry, as well as to better understand degrees of freedom and ranges of motion of the armor joints. Material characterizations of the lateral plates as well as pelvic assembly will be carried out, which will include (1) the analysis of porosity by mercury porosimetry, assessment of the mineral phase and content, (2) chemical composition of *G. aculeatus* armor by x-ray diffraction (XRD) technique, back-scattered electron microscopy (BSEM) and energy dispersive X-ray analysis (EDX) and (3) imaging of the interior and exterior surface topography of the lateral plates and pelvic spines by scanning electron microscopy (SEM) and surface profilometry. The design strategies of *G. aculeatus* armor will be proposed in terms of structure-function relationships based on their armor structures.

Chapter 8 will extensively focus on the design and function of the *G. aculeatus* pelvic assembly from a structural and biomechanical functional point of view, which is an excellent model system to investigate the genetic and ecological origins of adaptive phenotypic evolution. In particular, reduction of pelvic assembly in divergent *G. aculeatus* populations living in various freshwater environments is usually regarded as an indicator of phenotypic adaptation associated with a small number of genes. Pelvic reduction has been attributed to environmental constraints such as the increased difficulty of ion intake, a juvenile growth advantage of faster growth rates, enhanced mobility by reduced weight, and a decreased number of gape-limited piscivorous fish and birds. The quantitative μ CT imaging analysis and analytical/numerical mechanical models will be employed for the ancestral marine and descendent freshwater *G. aculeatus* pelvis that will be compared quantitatively in terms of structure-property-function relationships. Moreover, the offensive defense mechanism of fully-developed pelvic assembly will be proposed in conjunction with its conformational transition from rest to offensive.

Finally, Chapter 9 summarizes the key design principles of *P. senegalus* and *G. aculeatus* armor at multi-length scales, which include layered structures, a constitutive law of individual constitutive layers, compositional gradients, porosity, surface topology, geometry of armor geometry, scale-to-scale interlocking mechanisms and their relation to penetration resistance and biomechanical mobility. At the end, future work will be proposed: (1) fracture mechanisms of individual armor units under various loading/environmental conditions; (2) bioinspired protective/flexible armor designs combining multi-scale design principles of fish armor systems; and (3) comprehensive interdisciplinary approach of *G. aculeatus* study as a model system in the field of evolutionary biology.

Chapter 2.

Background Information

2.1. Two Fish Armor Model Systems

In this thesis, two fish armor model systems have been selected: *Polypterus senegalus* (bichir) and *Gasterosteus aculeatus* (threespine stickleback). Both *Polypterus senegalus* and *Gasterosteus aculeatus* belong to the phylum Chordata, the superclass Osteichthyes (bony fish), and the class Actinopterygii (ray-finned fish) (Sire, 1990; Östlund-Nilsson et al., 2007). The armored fish, *P. senegalus*, is predatory while the stickleback most often appears as prey with respect to other coexisting fish in their environment (Kodera, 1994; Reimchen, 1995). These two species of fish have very different armor design in terms of the multilayered structure of the armor unit, macroscopic geometry of the armor unit, interconnecting structures, and amount of body coverage (Barrett et al., 2008; Sire et al., 2009).

P. senegalus (the whole fish skeleton is shown in Fig. 2-1a) comes from an ancient fish family, which has existed since the Cretaceous period (> 96 million years ago (Daget et al., 2001)), and lives in freshwater swampy shallow floodplains and estuaries in Africa (Kodera, 1994). It has a rudimentary lung which allows it to leave the water for extended period (1~2 days) (Brainerd et al., 1989; Kodera, 1994). Moreover, as a hardy species, *P. senegalus* is reported to survive in some floodplains heated to the highest temperature during the dry season of Africa, where other fish can rarely inhabit (Kodera, 1994). The primary predators of *P. senegalus* are known to be its own species or its carnivorous vertebrate relatives (Hoedeman, 1975; Kodera, 1994). Biting takes place during territorial fighting (Kodera, 1994) and feeding (Markey et al., 2006) and, thus, the jaw structure and the skull of *P. senegalus* are capable of supporting powerful bites (Clemen et al., 1998; Wacker et al., 2001). This species of fish possesses tough, interlocking mineralized armored scales as protective body armor while still maintaining body flexibility and the ability to swim at high speed (Gemballa and Bartsch, 2002; Tytell and Lauder, 2002).

The second model system is also an armored fish species, the threespine stickleback, *Gasterosteus aculeatus*. *G. aculeatus* originated in marine environments (> 20 million years ago (Bell et al., 2009)) and has undergone dramatic diversification since the recent glacial period ~15,000 years ago, in particular populations that have migrated to and become isolated in freshwater environments (Bell and Foster, 1994; Hatfield, 1997; Östlund-Nilsson et al., 2007; Cresko, 2008). These different populations show pronounced alterations in body size, number of dorsal spines, pattern and number of lateral armor plates, and pelvic fin development, as well as differences in behavior (Reimchen, 1991; Bell and Foster, 1994; Reimchen, 1994; Reimchen, 1995; Cresko, 2008). Marine populations typically are fully armored and have a row of ~ 36 bony plates along both their sides while freshwater populations typically have only 6-9 armored plates. The loss of armor in freshwater populations is thought to be due to a variety of factors; low calcium levels making the production of armor more difficult thereby requiring more selective protection, abundant vegetation for hiding from predators, and a decreased number of predators (Reimchen, 1980; Giles, 1983; Reimchen, 1992; Kristjansson, 2005; Marchinko and Schluter, 2007; Östlund-Nilsson et al., 2007). *G. aculeatus* have evolved a more flexible, lightweight armor design presumably in order to provide rapid fast-start escape against encountered predators, as well as to prevent predators approaching to close proximity with their body by freezing and locking the spines in a defensive position in anticipation of an attack (Hoogland et al., 1956; Nelson, 1971; Reimchen, 1994; Bergstrom, 2002).

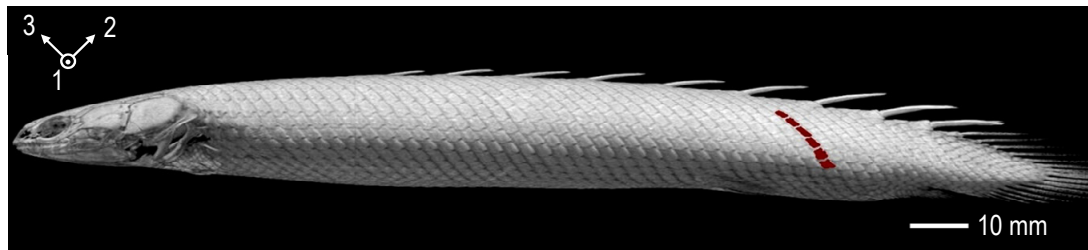
Table 2-1. Comparison of two fish armor model systems, *Polypterus senegalus* and *Gasterosteus aculeatus* (Hoogland et al., 1956; Meinke et al., 1979; Driessens and Verbeek, 1990; Kodera, 1994; Reimchen, 1994; Long and Nipper, 1996; Daget et al., 2001; Bergstrom, 2002; Gemballa and Bartsch, 2002; Bell et al., 2004; Westneat, 2004; Marchinko and Schluter, 2007; Östlund-Nilsson et al., 2007; Bell et al., 2009).

	<i>Polypterus senegalus</i>	<i>Gasterosteus aculeatus</i>
Scientific name	<i>Polypterus senegalus senegalus</i>	<i>Gasterosteus aculeatus aculeatus</i>
Common name	Senegal bichir, Cuvier's bichir, Dinosaur eel	Threespine stickleback, Three-spined stickleback
Taxonomy	Kingdom	Animalia
	Phylum	Chordata
	Class	Actinopterygii
	Order	Polypteriformes
	Family	Polypteridae
	Genus	Polypterus
	Species	<i>P. senegalus</i>
Origin	Geography	Africa: East, West and central
	Time	about 60 Myr ago
Environment	Freshwater	Anadromous, freshwater, brackish, marine
Temperature		25 ~ 27 °C
	Found to survive in hot floodplains	< 18 °C (prefer), Up to 28 °C (tolerate)
Salinity	< 0.5 ‰	Highly tolerant (0.5 ~ 50 ‰)
Size	up to ~ 40 cm	up to ~ 11 cm
Armor component	Rhomboid ganoid scales	Lateral plates (oval to rectangular) Pelvic assembly Dorsal spines
	Hydroxyapatite-organic composite (ganoine-dentin-isopedine-bone)	Hydroxyapatite-organic composite (lamellar bone)
	40 ~ 95 wt%	60 wt%
Armor Morphology	-Quad-layered microstructure - Interlocking via peg-and-socket articulation - No significant morphological variation	- Single layered, highly porous microstructure - Pelvic assembly (bilateral pelvic girdles with trochlear joints, ascending branches, anterior and posterior processes, articulating with pelvic spines) - Pronounced alterations of armor structures in response to various environment changes
Swimming maneuverability	-Slow swimmer, but swimming at high speeds if necessary -Body undulation/ body stiffness -Extreme body curvature	- fast start swimming when a predator is detected - reduction in lateral plates with increased swimming speed
Potential threat	Predator, territorial fighting; prone to in-fighting with its own species and conspecifics; jaw structure and skull are capable of supporting powerful bites	Prey, defense against predation; designed body armor components for rapid escape and prevention of predators approaching

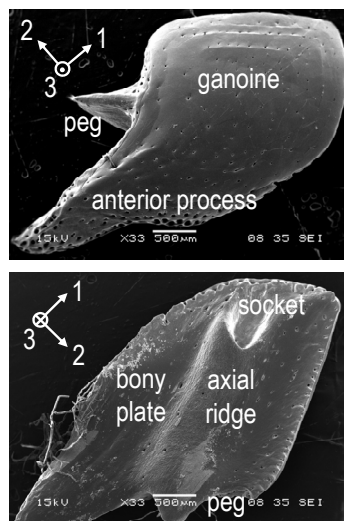
2.2. *P. senegalus* Armor System

2.2.1. *P. senegalus* Scales

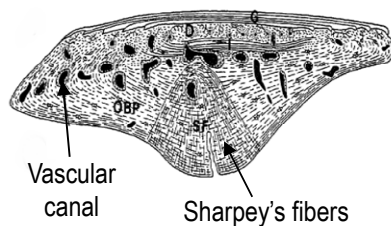
The scales of *P. senegalus* have conserved many characteristics of the ancestral type of dermal skeletal element, resembling that of ancient palaeoniscoids (Carroll, 1988; Sire et al., 2009), and are composed of four distinct inorganic-organic nanocomposite layers (Meinke et al., 1979; Meunier, 1987; Sire, 1994; Daget et al., 2001) as follows (from outer to inner surface): ganoine, dentin, isopedine, and the thickest osseous basal plate (Fig. 2-1c). The external and internal surface morphology of an individual diamond-shaped *P. senegalus* scale are shown in Fig. 2-1b, where a peg, a socket, anterior process, axial ridge appear. The juvenile *P. senegalus* scales are found to possess a thin isopedine layer (elasmodine) embedded in the dermis that exhibits a plywood-like structure, being gradually thickened and mineralized during growth (Sire, 1989). As compared to the adult *P. senegalus* scales, and mineralization processes of other fish scales, Sire et al. (Sire, 1990; Sire et al., 2009) have proposed the hypothesis of formation of *P. senegalus* scales with two type of cell condensations (Fig. 2-1d): (1) odontogenesis includes development of isopedine, dentin and hyper-mineralized ganoine layers; and (2) osteogenesis is the formation of the innermost thick, vascular osseous basal plate by osteoblasts from the dermis. In odontogenesis, vascular dentin is first formed by odontoblasts in the dermis using the preexisting elasmodine as a template, and subsequently ganoine begins to be deposited on the dentin layer by ameloblasts from the basal layer cells of epidermis (Sire, 1990). The latter osteogenic process allows collagenous connective fibers (e.g. Sharpey's fibers) to be incorporated into the osseous basal plate for the strong adhesion to the underlying organic fibers, stratum compactum, of the fish body (Sire, 1990; Gemballa and Bartsch, 2002; Sire et al., 2009). The different types of tissue development processes in *P. senegalus* scales result in the gradient of mineral contents that are correlated with material properties of each individual tissue layer as well as the interfaces between layers (Sire et al., 2009). The multilayered structure and mechanical properties of individual *P. senegalus* scales will be discussed in detail in Chapter 3 of this thesis.



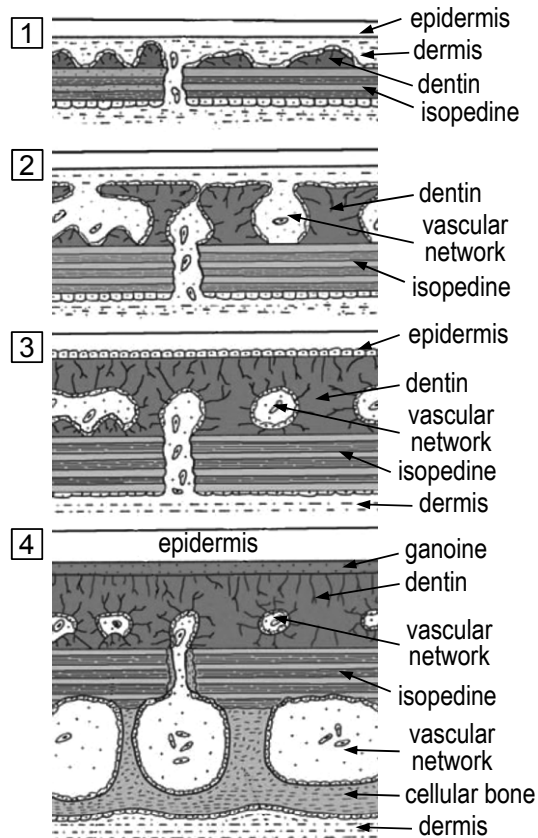
(a)



(b)



(c)



(d)

Figure 2-1. Structure and development of *Polypterus senegalus* scales; (a) *P. senegalus* skeleton¹ (Bruet et al., 2008), (b) scanning electron micrograph (SEM) of external and internal scale surfaces (Bruet et al., 2008), (c) schematic drawing of cross-section of a *P. senegalus* scale (Sire, 1990) and (d) the proposed main steps of scale formation in *P. senegalus* (Sire et al., 2009). G: ganoine, D: dentin, I: isopedine, OBP: osseous basal plate, SF: Sharpey's fibers.

¹ Original image from: Humphries, J. *Polypterus senegalus*, online digital morphology. Accessed May 2, 2011 at http://digimorph.Org/specimens/polypterus_senegalus/whole/ (Michigan Museum of Zoology) (ummz 195008), 2003

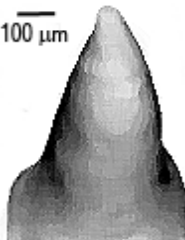
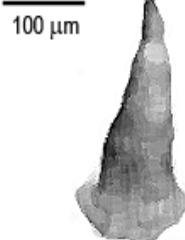
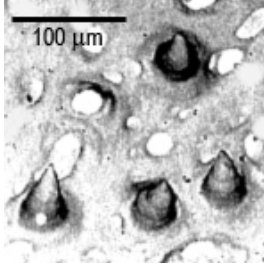
2.2.2. Potential Threats

P. senegalus is often ranked highest in the food chain of the ecosystem, thus the primary predators of *P. senegalus* are known to be its own species or its carnivorous vertebrate relatives (Hoedeman, 1975; Kodera, 1994). Territorial or predatory fighting among fish generally results in some degree of injury to the fish integument by tooth-biting. Severe injuries are local deformation of the individual plate armor units which extends downwards into the underlying soft tissues, and frequently lead to death due to infection (Reimchen, 1992). Some ganoid scales of *P. senegalus* were observed to be damaged after a territorial fighting took place with its relative (Kodera, 1994). Nevertheless, due to the confined damage within the scales, the underlying soft tissue remained intact and the scales were fully regenerated without further infection after a few weeks (Kodera, 1994). However, ironically the robust mineralized armor is vulnerable to parasite infection (Kodera, 1994).

As one of potential threats, *P. senegalus* teeth and jaw structures have evolved to support strong bites. The diet of *P. senegalus* is closely related to the development of its dentition and jaw structure and in the late aperiolarval phase of the development when almost all elements of dentition and jaw skeleton systems are established *P. senegalus* larvae become much more active to search for larger and live prey with the capability of hunting and biting (Clemen et al., 1998; Wacker et al., 2001). Adult *P. senegalus* have all monocuspid and conical teeth that are composed of cones of dentin capped with highly mineralized enameloid² (Wacker et al., 2001). The teeth are classified into three types in size and shape as indicated in Table 2-1. Type I tooth is a massive, broad-based tooth, an enameloid cap which occupies roughly a quarter of the tooth length from the tip. Type I teeth have various tip end radii and half tip angles, and are located on the premaxillary, maxillary, extopterygoid, dentary and prearticular of the skull. Type II teeth are slender and strongly curved, and the thickness of their sharp enameloid cap is about 35 % of the total tooth length. They are smaller than type I teeth, and are found on the dermopalatine, corenoids, and vomer and in some regions of the branchial apparatus. Type III teeth are the smallest among three type teeth and their acute enameloid cap fills up ~50% of the tooth length. A colony of type III teeth is found in the tooth fields of the entopterygoid, dermometapterygoid, parasphenoid, and on the tooth plates of the hypo- and basibranchials (Wacker et al., 2001). Adult *P. senegalus* are found to consume live fish (e.g. Tilapia) or invertebrates (e.g. dragonfly nymph, mayfly nymph) in their environments (Raji et al., 2003).

² Enameloid is topologically, functionally similar to enamel, but less ordered and non-prismatic crystalline arrangement due to the loose collagenous network makes it significantly different from enamel [sire, 2009].

Table 2-2. Three types of *P. senegalus* teeth (Clemen et al., 1998; Wacker et al., 2001). Images from ref. (Clemen et al., 1998) were modified in order to show the morphological features of each tooth clearly.

	Type I Tooth	Type II Tooth	Type III Tooth
Schematic drawing			
Shape	Cones with various tip end radii and half angles	Slender cone-shaped tooth with sharp tips	Sharp, slender cones
Size	the largest	moderate	the smallest, colonized
Location	premaxillary, maxillary, extopterygoid, dentary and prearticular	dermopalatine, corenoids, vomer, ceratobranchials, pharyngobranchials, and pharyngobranchial ligament	Entropterygoid, dermometapterygoid, parasphenoid, hypobranchials, basibranchials

When a biting event takes place, muscles bridging the segments of jaw skeleton are deformed along with jaw opening and closing and generated force from muscles are transmitted to the tips of jaw (Westneat, 2003, 2004). Mechanical advantage (MA) is associated with the efficiency of force transmission from muscles that is correlated with the velocity of jaw opening and closing, and biting force: low MA jaws emphasize velocity of jaw opening or closing; and high MA jaws transmit relatively more force in order to maximize biting force by sacrificing speed (Lauder, 1980; Westneat, 2004). In particular, *P. senegalus* transmits up to 42% of muscle force to the jaw tips for biting (Westneat, 2004). The pressurized jaw skeleton during biting events is supported by soft and compliant tissues such as Meckel's cartilage, sutures between hard elements of the skull or the spongy common pulpal regions that deform elastically, absorbing energy in order to minimize the failure of hard elements. Moreover, a replacement tooth coupled with each regular tooth exists, thus a fractured tooth can be substituted with its replacement for the fast recovery of biting capability (Clemen et al., 1998; Wacker et al., 2001; Sasagawa et al., 2009).

2.2.3. Flexible Articulating Design of *P. senegalus* Armor

During evolution, ancient armored fish were required to increase their swimming speed with enhanced body flexibility in order to adapt to their more predatory and dynamic environments. The larger and heavier plates of dermal armor broke up into many smaller ones with reduced weight. As a result, scale-to-scale articulation of fish integument became more elaborate to control the mechanical behavior of the entire armored assembly and consequently, body stiffness and maneuverability. In particular, ganoid fishes have been known to form extreme body curvatures (Fig. 2-2a) if necessary (e.g. C-start escape of *P. senegalus* (Tytell and Lauder, 2002)) even though their body is covered with tough mineralized scales for body protection from various environmental threats (Sire, 1990; Gemballa and Bartsch, 2002).

In *P. senegalus*, morphological features of individual scales play a key role in scale-to-scale articulations. A typical *P. senegalus* scale is rhomboid-shaped, having a peg in the dorsal margin and a socket in the ventral margin with a prominent protruding anterior process (Fig. 2-1b). The morphological variation of scales is closely related to body curvature, stiffness and undulatory wave motion during swimming (Long and Nipper, 1996; Gemballa and Bartsch, 2002; Tytell and Lauder, 2002). The squamation of *P. senegalus* scales (arrangement of scales) has been characterized in two anatomical body directions, paraserial and interserial directions as indicated in Fig. 2-2b and 2-2c. There are two distinguishable scale-to-scale interconnections in *P. senegalus* squamation: (i) peg-and-socket articulation where a peg of a scale inserts into a socket of the adjacent scale in the paraserial direction; and (ii) interserial overlapping of scales where the anterior margin of a paraserial scale row is overlapped by the posterior margin of the front scale row (Gemballa and Bartsch, 2002). A peg-and-socket articulation in the paraserial direction impedes the displacement of scales diagonally relative to each other, giving high bending stiffness to this local area, while laterally overlapping scales in the interserial direction allows neighboring scales to displace relative to each other, thereby providing body flexibility (Fig. 2-2b and 2-2c) (Gemballa and Bartsch, 2002).

The scale-to-scale articulations of *P. senegalus* armor include two important fiber systems to connect among scales as well as between scales and the soft body surface, and to regulate the spatial displacement of scales along with a body shape during swimming (Gemballa and Bartsch, 2002; Tytell and Lauder, 2002; Gemballa and Roder, 2004). One fiber system is Sharpey's fibers, a bundle of connective collagenous fibers, which firmly interconnect scales at the peg-and-socket joints, providing the reinforcement mechanism to the joints in addition to constraining degrees of freedom of the joints (Gemballa and Bartsch, 2002). The other fiber system is the few hundred micrometer-thick stratum compactum that is the layered, woven matrix with highly oriented collagenous fibers of each layer in paraserial or interserial directions, interconnecting the basal bones of *P. senegalus* scales and attaching discretized mineralized scales to the continuous body

surface (Gemballa and Bartsch, 2002; Gemballa and Roder, 2004). In addition, myosepta, the segment in between the myotome, intersects with the stratum compactum (Fig. 2-2d) and attaches to skin and vertebral column with three-dimensional morphology and architecture on the fish body (Fig. 2-2e). It is composed of stiff collagenous fibers that may provide important mechanical functions to the fish body during generation of bending, in body stiffness modulation or force transmission exerted by muscles (Azizi et al., 2002; Gemballa and Roder, 2004). Gembella and Röder have also proposed that myoseptal plays a key role in maintenance of body flexibility (Gemballa and Roder, 2004).

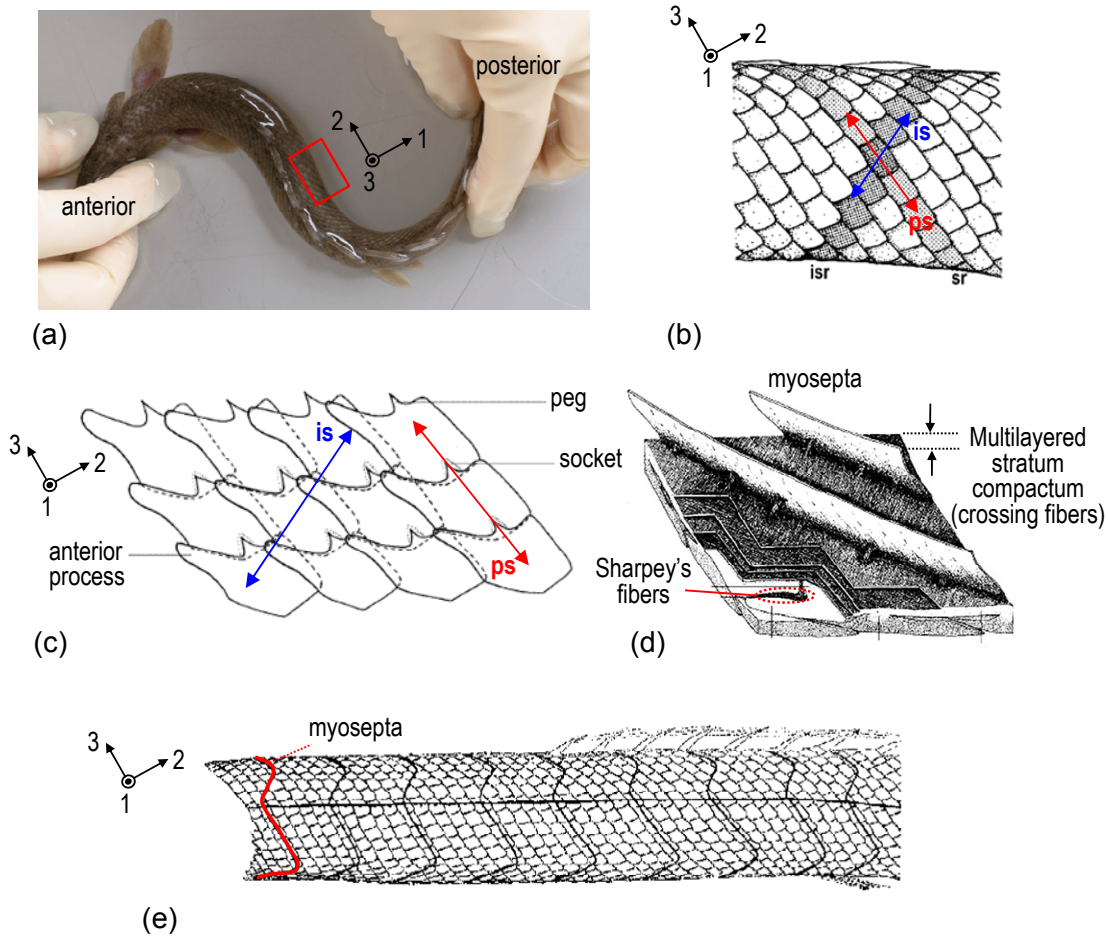


Figure 2-2. The morphology and fiber structure of flexible articulating *P. senegalus* armor; (a) anesthetized *P. senegalus* showing one extreme body curvature (photo taken by S. Reichert (Reichert, 2010)), (b) and (c) schematic drawings of (b) scale articulation in *P. senegalus* (*lateral view*) where dotted area indicate a row of scales that interlock via peg-and-socket articulation (*paraserial*) and overlapping scales in scale rows (*interserial*) (Gemballa and Bartsch, 2002), (c) details of scale articulation showing scale-to-scale interconnection in two directions with peg-and-socket joints and overlapping between scale rows (Gemballa and Bartsch, 2002), (d) oblique internal view of *P. senegalus* integument with four layers of the stratum compactum shown beneath the articulating scales (Gemballa and Bartsch, 2002) and (e) attachment lines of myosepta to *P. senegalus* skin (Gemballa and Roder, 2004).

2.2.4. Bioinspired Flexible Articulating Armor Design

The flexible armor design principles of *P. senegalus* have motivated bioinspired flexible armor designs that can achieve a balance between protection and flexibility/mobility for protective, synthetic man-made material systems. Remarkable progress has been made by my collaborator, S. Reichert in his master thesis (Reichert, 2010) who employed the overall approach to the bioinspired flexible armor designs as described in Fig. 2-3. There are two main processes to abstract and implement the design principles of *P. senegalus* armor: (i) constructing an individual unitized armor unit mimicking *P. senegalus* scales and (ii) incorporating two fiber systems (Sharpey's fibers and stratum compactum) into the peg-and-socket joints and the substrate of articulating scales as the interface between hard armor units and the soft matrix supporter (Reichert, 2010). This work has been submitted for the patent application (Ortiz et al., 2010).

Designs for individual armor units. Full three-dimensional geometric information of individual *P. senegalus* scales was obtained using microcomputed tomography (microCT) technique while complexity and details of the scale geometry were necessary to be reduced. Morphometric analysis and parametric modeling using landmark points placed on the contour of a three-dimensionally reconstructed scale enabled the extraction of important geometric features including peg and socket designs, and axial ridge. The simplified scale geometry was further smoothed and reconstructed about the center of mass, and was directly used for the design of an individual armor unit (Fig. 2-3).

Articulation of individual armor units. Two fiber systems of *P. senegalus* scales were also incorporated into the armor design in order to interconnect designed individual armor units and to attach them to a soft substrate support. Instead of highly aligned Sharpey's fibers at the peg-and-socket joints, the gap between a peg and its counterpart socket was filled with a softer and flexible material than the armor units. The axial ridge of armor units was directly attached to a stratum compactum-like thin substrate that was placed on a thick soft matrix supporter (Fig. 2-3).

3D prototype. A prototype of the established flexible armor design with five by five individual armor units was fabricated by multimaterial three-dimensional printing (multimaterial 3D printer, OBJET Connex500, Objet Geometries Inc., USA) as shown in Fig. 2-4a. Two commercially available materials were assigned to skeletal (white glassy polymer; Objet VeroWhite) and organic (yellow rubber; Objet TangoPlus DM9740) parts of the bioinspired design system, respectively. The preliminary mechanical tests with the prototype reveal the anisotropic biomechanical behavior (e.g. three-dimensional bending stiffness matrix) and the degrees of freedom (e.g. peg-and-socket joint that possesses a small level of scale rotations in x and y axes and a small level of extension in the paraserial direction) (Reichert, 2010) (Fig.2-4b).

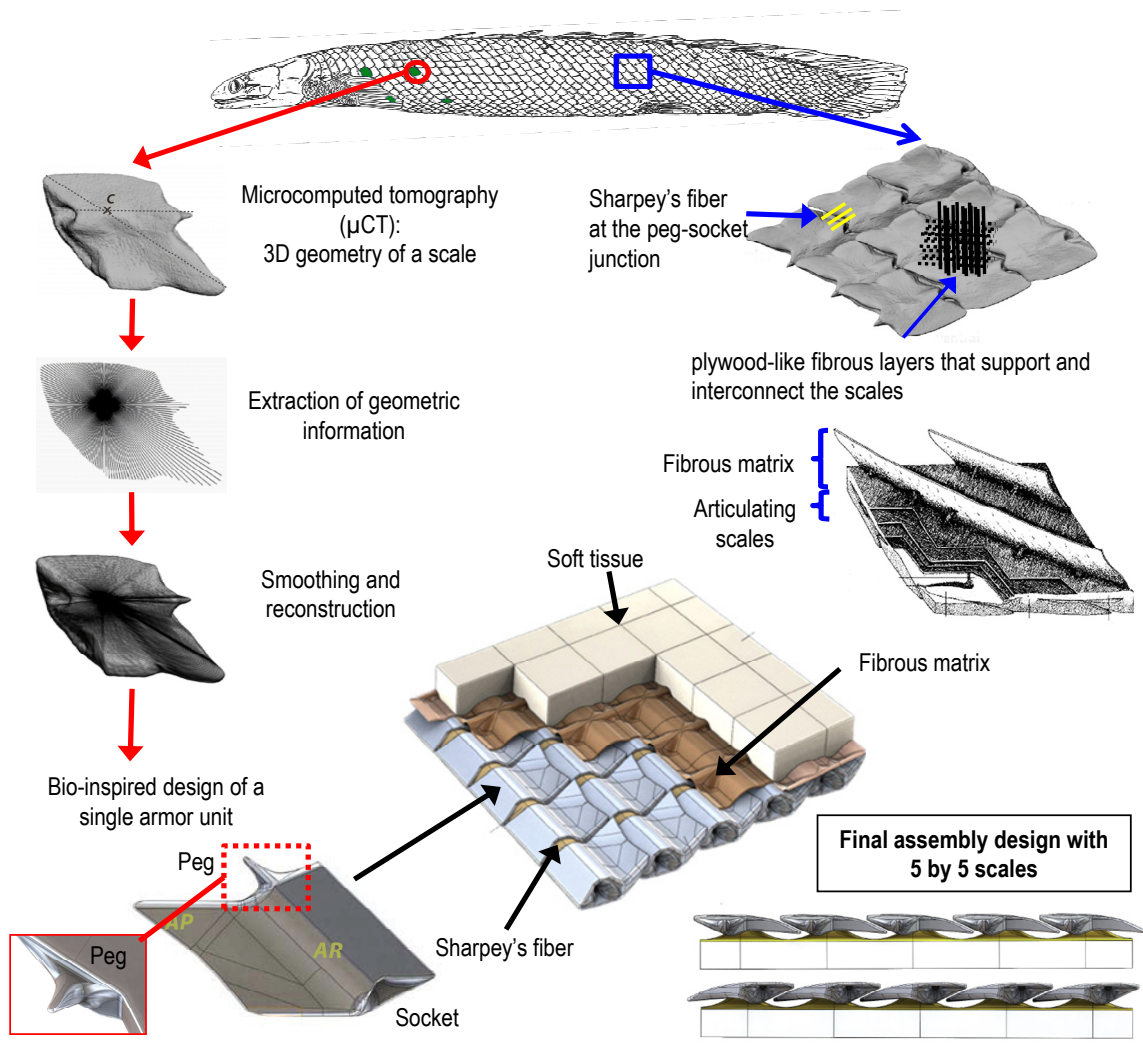


Figure 2-3. Flexible articulating armor designs inspired by *P. senegalus* armor with the overall approach for the bioinspired design system (Ortiz et al., 2010; Reichert, 2010).

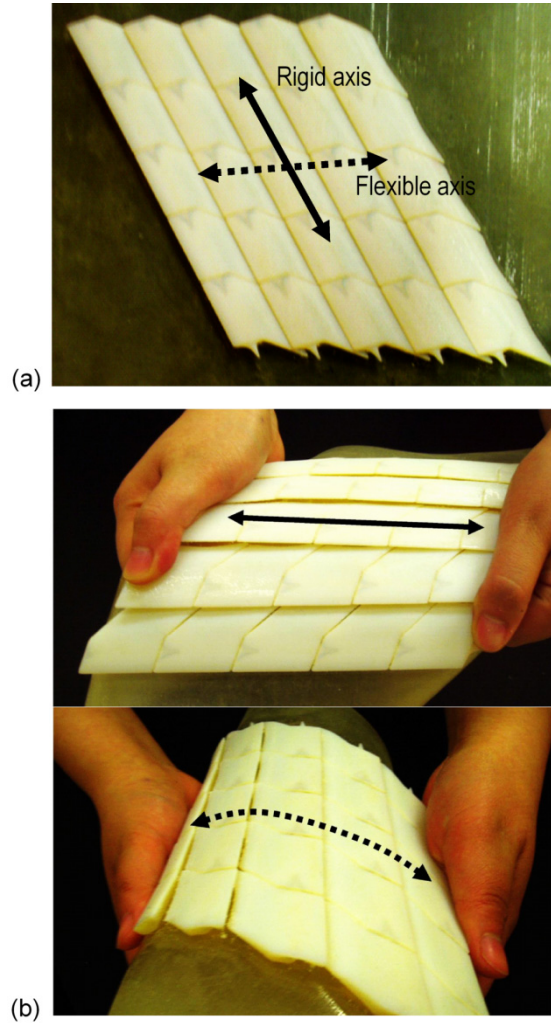


Figure 2-4. The proof-of-concept prototype of flexible articulating armor designs inspired by *P. senegalus* armor: (a) 3D prototype that is made of two materials, fabricated by a multimaterial 3D printer (OBJET Connex500) (Reichert, 2010) and (b) anisotropic biomechanical behavior of the 3D prototype, exhibiting high bending resistance along with the peg-and-socket articulating direction (*top*) and high flexibility in the scale-to-scale overlapping direction (*bottom*).

2.3. *G. aculeatus* Armor System

2.3.1. Morphological Variations of *G. aculeatus* Armor

One of the most popular and well-recognized organisms in the evolutionary biology world is *G. aculeatus*, threespine stickleback, because of their phenotypic diversity and relatively short evolutionary processes (Fig. 2-4) (Bell and Foster, 1994; Östlund-Nilsson et al., 2007). Among their morphological features, the armor structure is one of important evolutionary evidences, which is closely related to functionality and adaptation/fitness to the environments with significant predation by toothed predators or invertebrates (Bell and Foster, 1994; Reimchen, 1995; Huntingford and Coyle, 2007). Phenotypical stability among marine and anadromous *G. aculeatus* populations has been observed, exhibiting fully-developed armor structures, whereas freshwater populations possess phenotypical instability with various armor structures depending on their inhabitants (Bell and Foster, 1994). Generally speaking, *G. aculeatus* armor is composed of distinctive external bony armor components (a series of lateral plates, three dorsal spines, a pair of pelvic spines, and a complex pelvic girdle) (Nelson, 1971; Reimchen, 1983; Bell, 1987). The morphological variation of those armor components has been attributed to various freshwater environmental constraints as compared to marine environments (Bell and Foster, 1994).

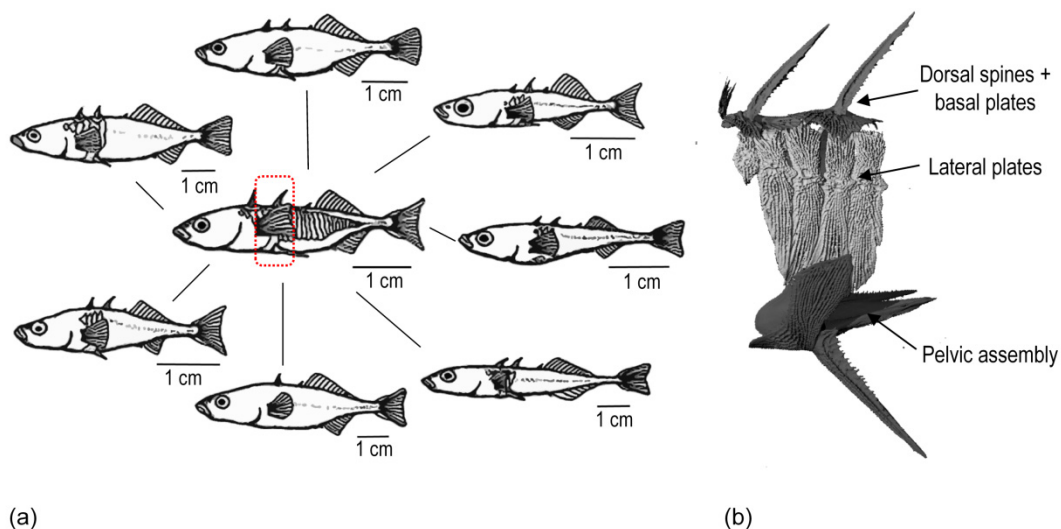


Figure 2-5. Phenotypical variation (body form and external features) among *G. aculeatus* populations ; (a) a schematic drawing of various *G. aculeatus* populations and (b) the anterior region of *G. aculeatus* armor that displays three major armor components, dorsal spines with their basal plates, lateral plates and pelvic assembly. Fig. 2-4a was modified, based on Fig. 1.2 of ref (Bell and Foster, 1994).

2.3.1.1 Morphological Variations of Lateral Plates

The *G. aculeatus* lateral plates are anisotropic in shape (oval to rectangular), conformal to the body of the fish, porous, and composed of acellular lamellar bone (Reimchen, 1983; Sire et al., 2009). The morphological variation observed in lateral plates is often recognized as three patterns: (1) full morph where ~ 36 lateral plates completely cover the flank of each body side, (2) partial morph where an unplated region appears, separating an abdominal plate row and plates on the caudal peduncle and (3) low morph where the small number of lateral plates (≤ 7) only occur in the anterior region of the body. Each plate morph exhibits the variation in the number of lateral plates, which may be influenced by the freshwater environments. The reduction pattern of abdominal lateral plates in the anterior region has been proposed by Reimchen (Reimchen, 1983). The position of individual plates related to the basal plates of dorsal spines and ascending branches of pelvic assembly was found to play a role in functionality of the *G. aculeatus* armor: the lateral plates bridging the basal plates and pelvic assembly would be the last in the reduction of lateral plates (Fig. 2-5a). The variation of lateral plates is classified with their reduction pattern and the total number of existing plates and has been used for quantitative analysis in evolutionary biology. The recent genetic studies have reported that the main genetic locus, *Eda*, controls plate reduction, which is also linked to loci involved in the regulation of salt secretion and parasite susceptibility (Colosimo et al., 2005; Marchinko and Schluter, 2007).

Predatory attack to *G. aculeatus* generally results in some degree of injury to the integument by tooth-biting (Reimchen, 1992). Severe injuries are local deformation of the individual plate armor units which extends downwards into the underlying soft tissues, and frequently lead to death due to infection. Lateral plates protect the body against a toothed predator effectively, indicating the exposed soft tissues where the coverage of lateral plates has limitation are easily punctured during attack with increased fatality (Reimchen, 1992, 1995). Evolutionary studies of *G. aculeatus* have reported that the number of lateral plates is positively correlated with the coexistence of a toothed predator (Reimchen, 2000).

2.3.1.2 Morphological Variations of Pelvic Assembly

The pelvic assembly is composed of two porous interdigitating ventral plates embedded in organic tissue which forms a suture (pelvic girdle), connected to two outer serrated, porous pelvic spines via the trochlear joints. The ventral plates have anterior and posterior processes from the anterior to the posterior and ascending branches in the dorsal direction that are attached to lateral plates (Nelson, 1971; Bell, 1987). Similar to lateral plates, the pelvic assembly among *G. aculeatus* populations also appears with three forms: a full morph that consists of bilateral pelvic girdles having posterior and anterior

processes, and ascending branches with or without pelvic spines; a partial morph where most of pelvic elements except for pelvic spines are preserved but size-reduced to different extents; and a low morph where the pelvic complex is completely lost or posterior and anterior processes and ascending branch are rudimentary with loss of spines (Nelson, 1971; Bell, 1987). Most *G. aculeatus* possess robust, full-morph pelvic assembly while some freshwater *G. aculeatus* have undergone significant pelvic reduction, in particular, in recently deglaciated lakes.

The patterns of pelvic reduction were observed to appear in two modes: paedomorphosis and gradual truncation of distal element (Fig. 2-5c) (Bell, 1987). Gradual truncation of distal element in pelvic assembly is dominant, with a typical sequential reduction: pelvic spine → posterior process → ascending branch → anterior process as shown in path 2 of Fig. 2-5b (Bell and Orti, 1994). Paedomorphosis mode of pelvic reduction resembles the reverse order of pelvic development: the last element of the pelvic development is the first to be lost (path 1 of Fig. 2-5b). Other modes of pelvic reduction have been observed including the abrupt pelvic reduction as described in path 3 of Fig. 2-5c (Bell, 1987; Bell and Orti, 1994). According to these patterns, structural elements of pelvic assembly can be scored from 4 (full morph) to 0 (complete loss) for each pelvic girdle, resulting in the total score of 8 to 0 depending on the degree of reduction (Bell, 1987). The scoring method has been widely used to define the morphological variation of pelvic assembly for quantitative comparison among *G. aculeatus* populations (Bell, 1987; Bell and Orti, 1994; Chan et al., 2010). Pelvic reduction is often regarded as an indicator of morphological adaptation largely dependent on a small number of genes (Shapiro et al., 2004; Chan et al., 2010). The reduction of pelvic assembly in the Paxton Lake benthic populations and in the Icelandic populations is mediated by *Pitx1* (Pituitary homeobox 1) that is involved in hind limb development (Shapiro et al., 2004). Instead of direct mutation in *Pitx1*, reversible regulatory changes are the key factor in the suppression of *Pitx1* expression (Shapiro et al., 2004; Kingsley and Peichel, 2007; Chan et al., 2010).

The pelvic spines can take on two main configurations; (1) in the absence of a predatory threat, a “rest” position whereby the long axis of the pelvic spines are adjacent and parallel to the long axis of ventral plates and (2) in the presence of a predatory threat, an “offensive” position whereby the spines rotate outward and take a position with their long axis perpendicular to the long axis of the ventral plates, thereby increasing the effective body size of the fish (Hoogland et al., 1956). During defense, the pelvic girdles have to support the pelvic spines against compression and bending and should minimize the back deflection of the soft tissues underneath the armor.

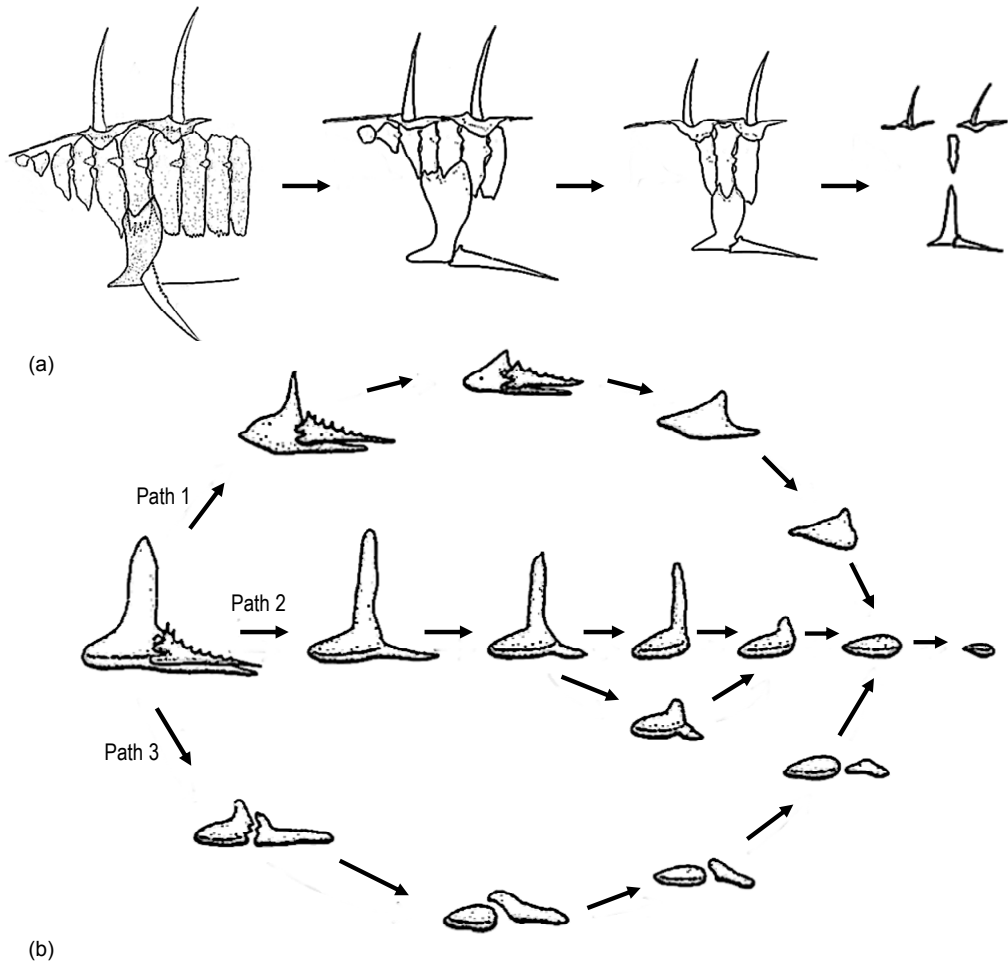


Figure 2-6. Sequential reduction of *G. aculeatus* armor components: (a) lateral plates (Reimchen, 1983) and (b) pelvic assembly (Bell, 1987).

2.3.2. Environmental Factors in Morphological Variations of Armor

Ancestral marine *G. aculeatus* are fully armored in their environments, whereas some of lacustrine and stream-dwelling *G. aculeatus* populations have reduced their armor structures in response to various freshwater environments (Bell and Foster, 1994). The driving force of this evolution may be the optimization of energetic cost. The total energy intake of an individual fish should be equivalent to the sum of the energy for maintenance and growth (Wootton, 1994). The energy intake depends on the amount of food consumption. The energy allocation can be constructed as a simple and conceptual optimization problem.

***min* total energy cost**

subject to:

total energy intake \geq **total energy cost**

total energy cost = metabolic energy (M) + activity energy (A)

+ digestion energy(D) + growth energy (G) + reproduction energy(R)

Constraint equation for M(i)

Constraint equation for A(ii)

Constraint equation for D(iii)

Constraint equation for G(iv)

Constraint equation for R(v)

The total energy cost is the sum of metabolic energy (the energy required for standard metabolism), activity energy (energy consumed by swimming), digestion energy (the energy cost for food processing), growth energy (storage energy for somatic growth) and reproduction energy (energy accumulated as reproductive products). The equations were modified based on the proposed equations of ref (Wootton, 1994). Individual constraint equations can be defined by the environmental factors with proper coefficients.

In the case that the environments have abundant food sources for *G. aculeatus*, constraints become less strict, compared to energetic cost, resulting in multiple optimal solutions. However, when the food becomes a limited source and total energy intake is smaller than the normal energy cost of the current fish status, the system will need to solve the new optimization problem in order to maximize survivability in a new set of constraints. The direction of optimization may reduce cost of individual energy costs. Figure 2-6 shows how a pattern of energy allocation influences a biological system for fitness to the environment (Wootton, 1994). In particular, mineralized armor components of *G. aculeatus* require biomineralization processes associated with Ca^{2+} intake from the environments, which belong to metabolism (Lowenstam and Weiner, 1989). Armor reduction occurring among freshwater *G. aculeatus* populations may decrease the amount of energy consumed for metabolic processes and may lower the required amount of Ca^{2+}

intake, giving more energy allocation to other energy components; for example, increased growth energy reduces time for growth that is beneficial for *G. aculeatus* that coexist with a size-selective predator in the environment (Reimchen, 1991). Moreover, decreased weight associated with reduced armor may decrease the amount of energy for activity (e.g. swimming), enhancing swimming speed and stamina (Bergstrom, 2002). Therefore, armor reduction can be induced by various environment factors, and, in turn, rearranges energy allocation to derive proper fitness components.

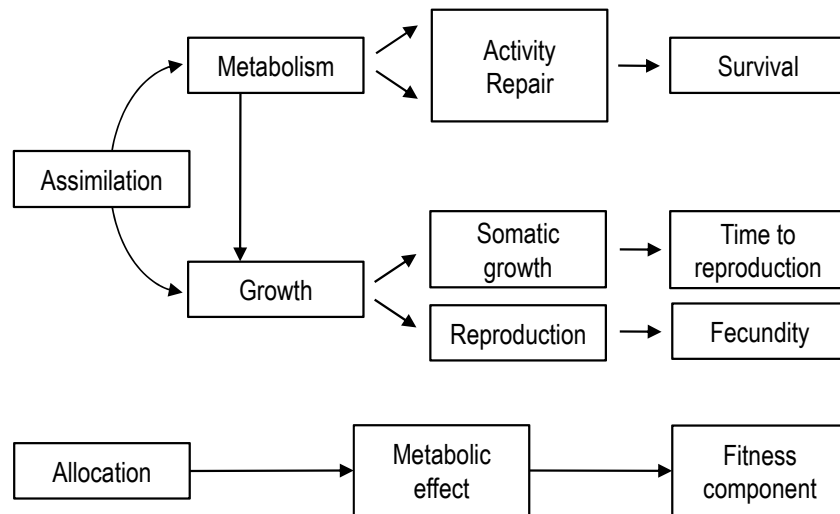


Figure 2-7. Schematic diagram of energy allocation and its influence to a biological system (Wootton, 1994)

Various environmental factors that may affect armor reduction in freshwater *G. aculeatus* populations have been proposed, investigated and related to behavior or genetic studies (Huntingford and Coyle, 2007). Here, three major environmental factors, predation, growth rate and calcium limitation, are briefly introduced, focusing on how they are correlated with armor structures. Even though those three factors are described individually in the following paragraphs, many evolutionary processes include multiple environmental factors, giving difficulty to determine which is the most dominant for variation of armor structures (Bell and Foster, 1994; Östlund-Nilsson et al., 2007).

Predation. Mechanical protection against tooth penetration is the major functionality of *G. aculeatus* armor. Significant correlation between the degree of armor and the type and number of predators has been proposed (Reimchen, 1995; Vamosi, 2003; Reimchen and Nosil, 2004). In the environments where gape-limited, toothed predators exist, *G. aculeatus* are mostly found to be heavily armored, whereas some freshwater populations exhibit armor reduction because of absence of the fish predators (Reimchen,

1994). As opposed to the vertebrate predators, invertebrate predators appear to be lethal to *G. aculeatus* populations that have full-morph pelvic assembly with longer pelvic spines because they can easily grab pelvic spines to catch the fish (Reimchen, 1980; Bell et al., 1993; Vamosi, 2002; Marchinko, 2009).

Growth rate. Growth rate is closely related to metabolism and saved energy from armor reduction can be used for growth energy. It has been reported that fewer lateral plates enhance the growth rate by comparing individuals with the different number of lateral plates (Marchinko and Schluter, 2007; Barrett et al., 2008). In particular, juvenile *G. aculeatus* are more vulnerable to size-dependant predation than adult *G. aculeatus*, thus faster growth become critical for survivability (Foster et al., 1988; Marchinko, 2009).

Calcium limitation. Calcium ions are the most important abiotic component in biomineralization (Lowenstam and Weiner, 1989), thus difficulty of calcium intake from environments can become a limiting factor for armor development (Giles, 1983). Even though various freshwater *G. aculeatus* populations have been observed with the concentration of calcium ions in their environments, it is hard to attribute only calcium limitation to armor reduction (Bell et al., 1985).

Chapter 3.

Multilayered and Graded Design of *P. senegalus*

Scales

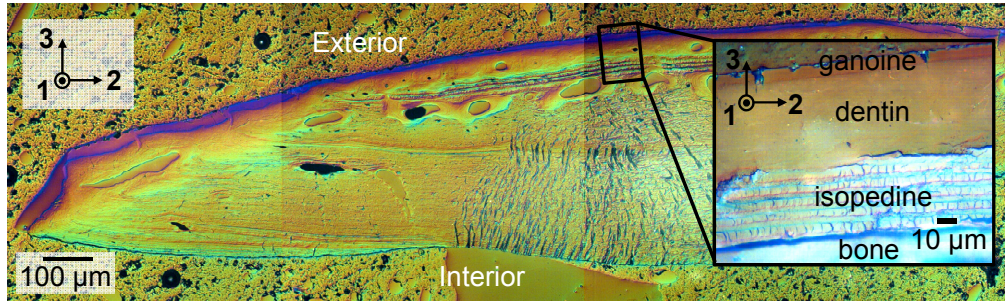
This chapter was published as a regular article: B.J.F. Bruet, J.H. Song, M.C. Boyce, and C. Ortiz, 'Materials design principles of ancient fish armour.' *Nature Materials*, 2008. 7(9): p. 748-756.

3.1. Introduction

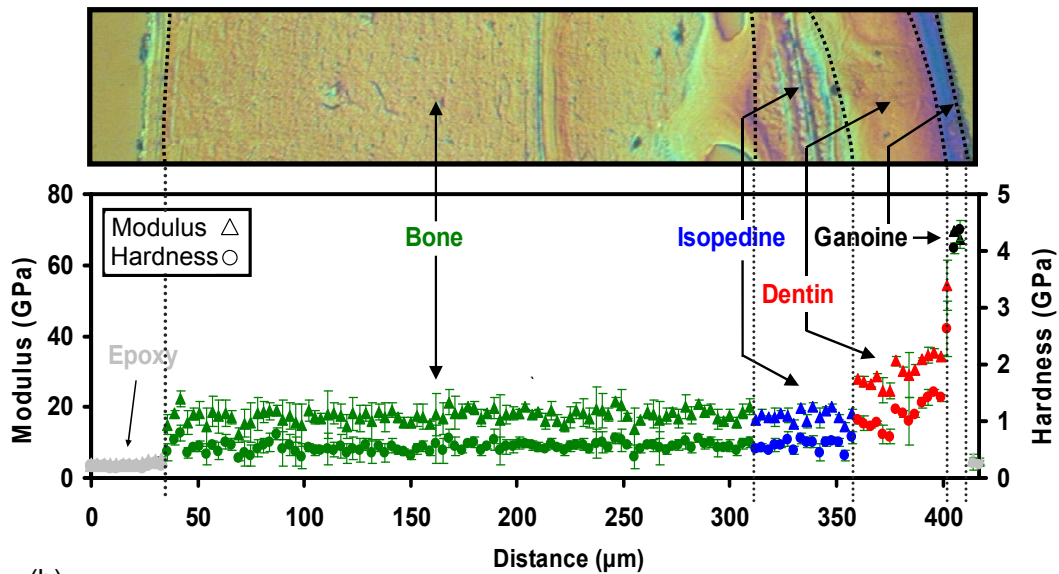
Dermal armor in fish first appeared during the beginning of the Paleozoic period during the Ordovician with the rise of the Ostracoderms ~500 million years ago (Hoedeman, 1975) and was common among these earliest fishes (Colbert, 1955). Romer in 1933 hypothesized that dermal armor served as a protection from predators (Romer, 1933) and subsequently a number of additional mechanical and non-mechanical functions have been proposed (Ørvig, 1968; Raschi and Tabit, 1992; Long and Nipper, 1996). As ancient fish became more predaceous (Anderson and Westneat, 2007), their armor evolved in terms of their multilayered material structures and overall geometries, e.g. larger plates broke up into many smaller ones, the thickness of various layers decreased, and the number of layers decreased; all of which would have decreased weight, improved flexibility and maneuverability, and increased speed (Colbert, 1955). Interestingly, many parallels can be found between the evolution of armor in the animal world and human-designed engineered body armor, both of which appear to be controlled by a balance between protection and mobility, in order to maximize survivability (Arciszewski and Cornell, 2006). The design strategies utilized by mineralized biological tissues, in general, is an area of great interest and much progress has been made in the understanding of concepts such as crystalline nucleation, growth, and morphology, biomacromolecular intercalation and reinforcement, modulation of crystal texture, stabilization of amorphous

phases, small length scale effects, heterogeneity and so on (Weiner and Addadi, 1997; Currey, 1999; Gao et al., 2003; Balooch et al., 2004; Fantner et al., 2005; Buehler, 2007; Tai et al., 2007). Little is known about the mechanical properties of individual dermal armor plates and scales. For example, the mechanical roles of the mathematical form of material property variations (e.g. gradients) both within and between various layers, the number of layers, the layer and junction thicknesses, structures, and geometries, the constitutive laws of each layer, etc. and more importantly, the relationship of these parameters to larger scale biomechanical performance and environmental stresses (e.g. predatory or territorial attacks).

In the first part of my thesis, *Polypterus senegalus* armor has been chosen as a fascinating model system. The body of *P. senegalus* is covered with the interlocking, quad-layered, mineralized scales that have conserved many characters of the ancestral type of dermal skeletal element resembling that of ancient palaeoniscoids (Carroll, 1988), possessing a multilayered structure of four different organic-inorganic nanocomposite material layers (from outer to inner surface); ganoine, dentin, isopedine and a bone basal plate (Fig. 3-1a) (Daget et al., 2001). The Oliver-Pharr (Oliver and Pharr, 1992) calculated indentation modulus, E_{O-P} , and hardness, H_{O-P} , of an individual scale from *P. senegalus*, obtained from instrumented nanoindentation, were found to decrease with distance from the outer to the inner surfaces of the scale (from ~62 to ~17 GPa and ~4.5 to ~0.54 GPa, respectively) as shown in Figure 3-1b. Each material layer has its own nanostructure and mechanical properties: 1) the outer ganoine layer possesses the highest average indentation modulus (~62 GPa) and hardness (~4.5 GPa) of the outer thinnest ganoine layer (thickness ~ 10 μm) that is consistent with its known highly mineralized (< 5% organic (Ørving, 1967)) non-collagenous structure consisting rod-like, pseudoprismatic crystallites of apatite (Meunier, 1980)) the second collagenous dentin layer (thickness ~ 50 μm) has a reduced mineral content compared to ganoine, but is still more mineralized than the osseous basal plate (Daget et al., 2001), displaying the mechanical properties of E_{O-P} and H_{O-P} , ~29 and 1.2 GPa, respectively; 3) the third layer, isopedine, consists of a uniform superimposition of orthogonal collagenous layers (thickness ~ 40 μm) that form a plywood-like structure and decrease in mineralization with distance towards the inner surface of the scale (Meunier, 1987), and is mechanically comparable to the underlying basal plates (E_{O-P} and H_{O-P} of ~17 and ~ 0.54 GPa); and 4) the innermost thickest basal osseous plate (thickness ~ 300 μm) is composed of a succession of vascularized bone lamellae, with the major axis of the collagen fibrils approximately parallel to the scale surface (Daget et al., 2001). Moreover, approximately negative linear gradations (from the outer to inner surface) in both E_{O-P} and H_{O-P} were mainly observed within the outer ganoine and underlying dentin layers as well as the ganoine-dentin junction (Fig. 3-2).



(a)



(b)

Figure 3-1. Structure and mechanical properties of *Polypterus senegalus* scale; (a) optical micrograph of the cross-section of an individual scale with an inset showing four layers, and (b) average indentation modulus (E_{O-P}) and hardness (H_{O-P}), both reduced from Oliver-Pharr analysis (Oliver and Pharr, 1992) as a function of distance across the scale cross-section from ganoine to bone. The vertical error bars represent one standard deviation. ‘Epoxy’ is epoxy used for embedding. *Figure by B.J.F. Bruet*

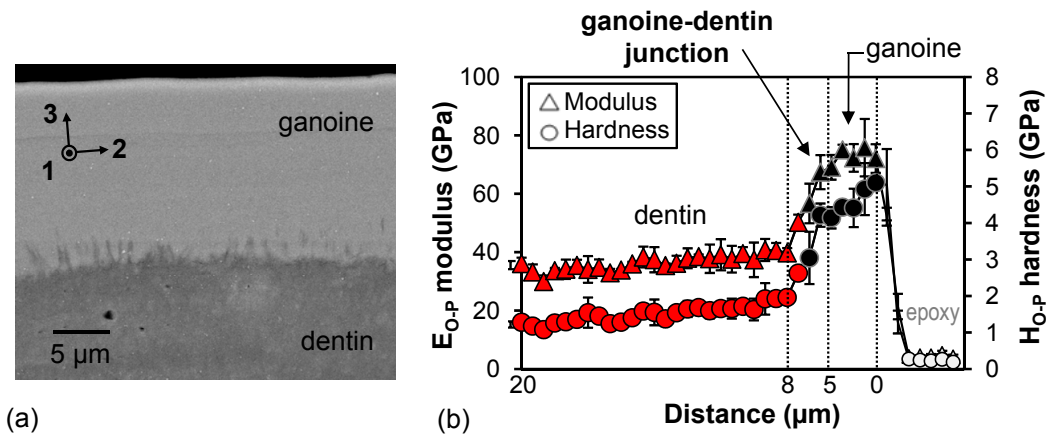


Figure 3-2. Structure and graded mechanical properties of the ganoine, dentin and their junction of a *P. senegalus* scale; (a) backscattered electron microscopy image of the cross-section of the ganoine-dentin junction (*image taken by B.J.F. Bruet*) and (b) average indentation modulus (E_{O-P}) and hardness (H_{O-P}), analyzed by Oliver-Pharr method (Oliver and Pharr, 1992) from ganoine to dentin. The vertical error bars represent one standard deviation and ‘epoxy’ is epoxy used for embedding (*experiment by B.J.F. Bruet*).

Here, I employ a multiscale computational approach, using previous experimental results of microstructures and mechanical properties of *P. senegalus* scales (Bruet, 2008) to elucidate such design principles, in particular with regards to multilayering and grading. Nanoindentation simulation results were fit to the experimentally obtained nanoindentation curves in order to retrieve plastic mechanical behavior of each material layer while virtual microindentation was carried out using the multilayered scale models at various loads for predicting microscopic mechanical behavior of the entire system. These general methodologies presented are applicable to a broad range of multilayered protective exoskeletal materials (e.g., crustacean (Raabe et al., 2005), insect (Barbakadze et al., 2006), gastropod mollusk (Weiner and Addadi, 1997), etc.) and able to yield a mechanistic understanding of how different organisms were designed, and possibly evolved, to sustain the loads they experience in their environment. Such fundamental knowledge, in particular threat-design relationships, holds great potential for the development of improved biologically-inspired structural materials (Ortiz and Boyce, 2008), for example soldier, first responder, and military vehicle armor applications.

3.2. Methods

3.2.1. Microindentation

The fresh and hydrated *P. senegalus* scales were stuck on a 12 mm steel disc by means of a cyanoacrylate glue (Loctite 495, Henkel KGaA, Düsseldorf, Germany). At least ten microindentation experiments were carried out in ambient conditions to each maximum load ranged from 0.25 to 2 N, assuring that the inter-indent spacing was always at least five times greater than the indent residual size in order to prevent any interaction between the indents. The probe tip end radius was indirectly measured using atomic force microscopy and found to be $\sim 3.7 \mu\text{m}$ (Bruet, 2008). The indented surface of the *P. senegalus* scales was observed using a Nikon Eclipse L150 (Tokyo, Japan) while the height profile of the residual impression was obtained using tapping mode atomic force microscope (TM-AFM) with Veeco Si cantilevers (V-shaped with approximately square pyramidal probe tip geometry, a tip half angle of $<17.5^\circ$; $l=125 \mu\text{m}$; $k < 40 \text{ N/m}$; and $R_{\text{tip}} < 10 \text{ nm}$).

3.2.2. Finite Element Analysis (FEA) Modeling

Nanoindentation model Nanoindentations were simulated using both two and three-dimensional nonlinear finite element analysis (FEA) models. Two-dimensional, axisymmetric FEA models were used with appropriate symmetry boundary conditions, assuming a material is isotropic. The three-dimensional geometry of a Berkovich indenter was approximated as a two-dimensional, conical-like axisymmetric indenter with the radius set to the tip radius of the Berkovich indenter; the tip cross-sectional area was the experimentally measured Berkovich tip area function (TAF). The FEA models were discretized four-node bilinear axisymmetric quadrilateral elements (CAX4R or CAX4H in ABQUS element library) and mesh convergence studies were assessed to determine the optimal mesh (1318 of elements) for accurate solutions. The two dimensional simulations were found to have more than 97 % accuracy as compared to fully three-dimensional simulations. The Berkovich indenter was modeled as a rigid conical-like indenter. Large deformation theory and frictionless contact between the indenter and material were assumed. The deformation mode was chosen as quasi-static. The constitutive behavior of each material layer of *P. senegalus* scales was modeled as isotropic elastic-perfectly plastic with two constant parameters, Young's modulus and Poisson's ratio ($E = 55 \text{ GPa}$ for ganoine, 25 GPa for dentin, $E = 16.5 \text{ GPa}$ for isopedine, $E = 15 \text{ GPa}$ for bone, and $\nu = 0.3$), and one free-standing parameter, yield stress, for the best fit to the experimental nanoindentation curves (Bruet, 2008). All of the nanoindentation simulations were conducted to a maximum load of $500 \mu\text{N}$ in accord

with the experiments. The schematic diagrams of the model and indenter tip information are shown in Figs. 3-3a and b.

Microindentation model The larger-length-scale biomechanical indentation of the entire *P. senegalus* scale was virtually performed using two axisymmetric, two-dimensional FEA models to/from various indentation loads ranged from 0.1 N to 1 N (Fig. 3-3c). The first, ‘discrete’, model was composed of the four material layers with thicknesses corresponding to their experimentally measured values, where each layer was assumed to possess isotropic, elastic-perfectly plastic constitutive behavior with Young’s modulus and yield stress taken as those reduced from FEA predictions of the averaged load-depth data by nanoindentation experiments (Bruet, 2008). The second, ‘gradient’, model was also composed of the four material layers with thicknesses corresponding to their experimentally measured values and assumed isotropic elastic-perfectly plastic material behavior, but incorporated linear gradients in Young’s modulus (E) that was scaled by the measured E_{O-P} gradient values and yield stress (σ_Y) that was scaled by the measured H_{O-P} gradient values within the ganoine and dentin layers, as well as the ganoine-dentin and dentin-isopedine junctions (Bruet, 2008). The predictions of these two multilayered models were compared with three simulations of a single homogeneous elastic-perfectly plastic layer of material with a thickness equivalent to that of the entire scale ($\sim 400 \mu\text{m}$): ganoine, dentin and bone. The two-dimensional axisymmetric indenters for the virtual microindentation had a conical tip geometry which emulates a Vickers microhardness tip (tip end radius $\sim 3.7 \mu\text{m}$, conical angle 70.3°) as indicated in Figure 3-3a and b. The effective microhardness was computed from the FEA simulations in a manner consistent with that used in the microhardness experiments, taking the indentation load and dividing by the residual contact area (i.e., the area corresponding to the radius of the residual indent impression after fully unloaded). Moreover, the effective stiffness was calculated via the O-P method using predicted virtual microindentation load-depth curves and energy dissipation was quantified by integrating the indentation loading-unloading cycle.

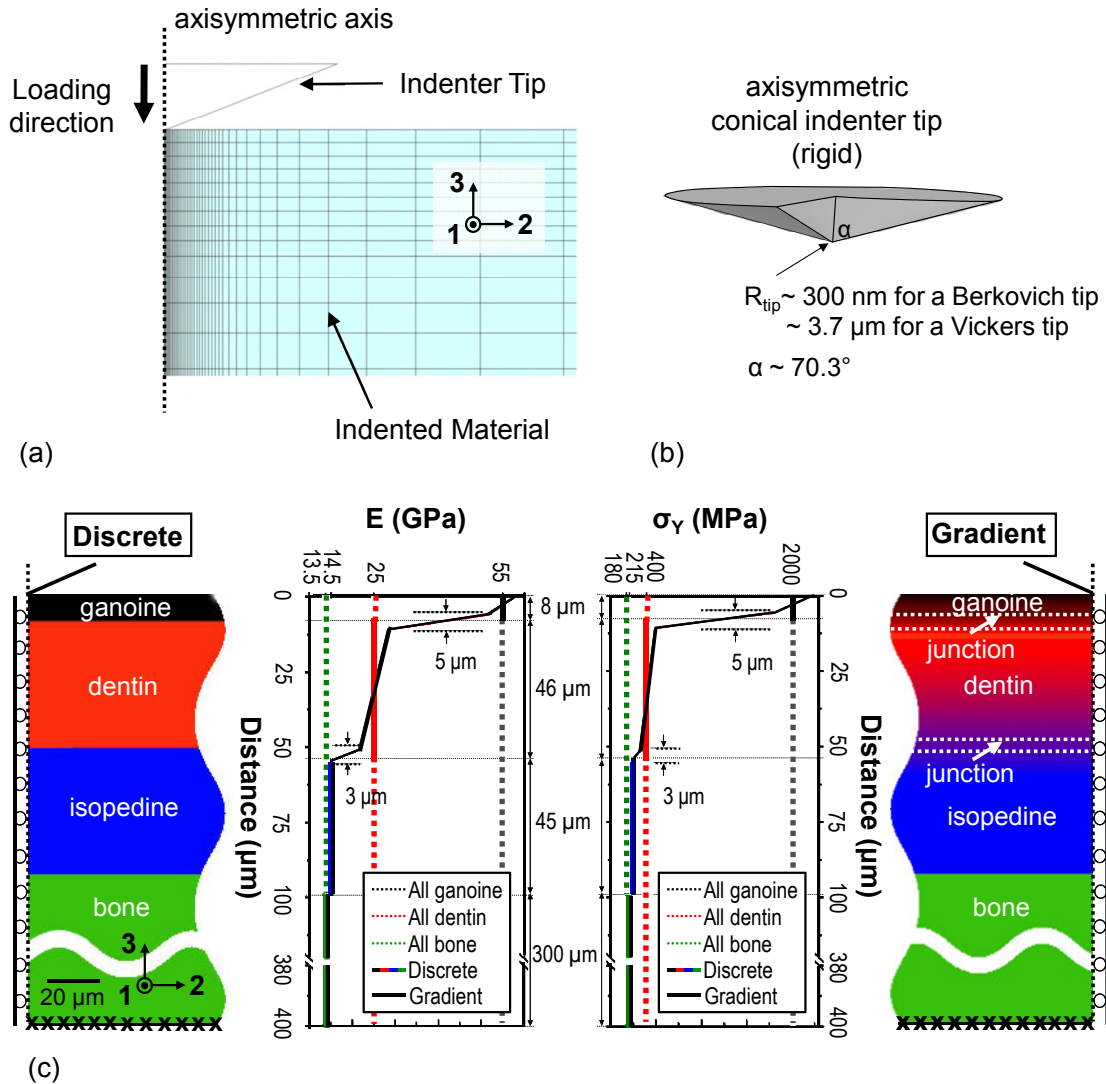
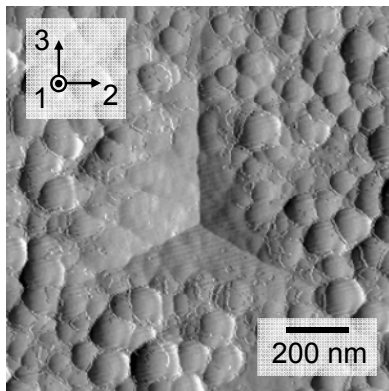


Figure 3-3. Two-dimensional axisymmetric finite element analysis (FEA) models for predictions of mechanical properties of the *P. senegalus* scale; (a) schematic diagram of the nano- and micro-indentation FEA models, (b) three-dimensional geometry of a two-dimensional axisymmetric rigid conical indenter with a tip half angle of α and a tip end radius of R_{tip} , where $\alpha=70.3^\circ$ and $R_{tip} = 300 \text{ nm}$ for a Berkovich tip and $R_{tip} = 300 \text{ nm}$ for a Vickers tip and (c) multilayered structures of discrete (left) and gradient (right) models with their corresponding elastic modulus and yield strength distributions.

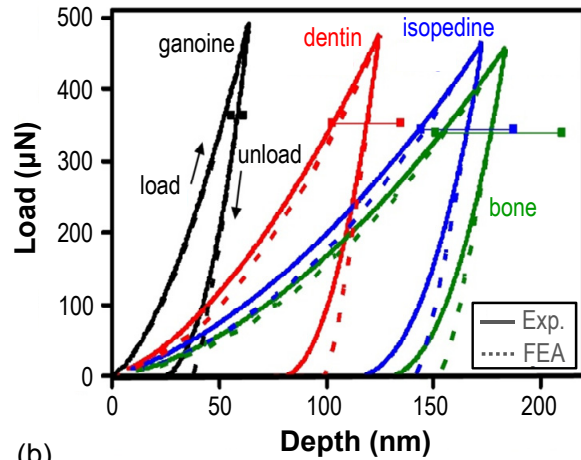
3.3. Results

3.3.1. Plasticity of Individual Material Layers of *P. senegalus* Scales

Organic-inorganic nanocomposites are able to deform plastically (Weiner and Addadi, 1997). The four material layers of *P. senegalus scales* exhibit significant plasticity during nanoindentation into each layer, confirmed by a finite residual depth of nanoindentation curves after unloading and residual impressions after nanoindentation tests that were directly imaged by TMAFM (Figs. 3-4a and b). Based on this observation, the averaged experimental load-depth data for each layer was fit to an isotropic, elastic-perfectly plastic FEA computational model, thereby the yield stress, σ_Y , was determined by a best fit to the averaged loading and unloading experimental data, with the indentation calculated from the FEA-predicted unloading slope (Pharr et al., 1992) matched to the experimentally calculated average E_{O-p} . Figure 3-4b shows good agreement between the FEA predictions and the experimental data, giving σ_Y values of 2000, 400, 215 and 180 MPa for the ganoine, dentin, isopedine and bone, respectively. Additionally, an extensive parametric study showed that the inclusion of post yield strain hardening (linear isotropic hardening, linear kinematics hardening and Ramberg-Osgood isotropic hardening) in the simulations had a minimal effect in providing an improved prediction of the nanoindentation load-depth data and the estimated yield stress (Appendix A). All materials were observed to undergo mechanical hysteresis, and energy dissipation (to the same maximum load of 500 μ N) increased with distance from the outer surface of the scale inward from ganoine ~ 5.98 pJ to bone ~ 23.79 pJ, implying increased plasticity towards the internal soft body.



(a)



(b)

Figure 3-4. Mechanical properties derived from nanoindentation experiments across the cross-section of the ganoine-dentin-isopedine-bone material layers of an individual *P. senegalus* scale; (a) TMAFM amplitude image of the residual indents (500 μN maximum load) on the cross-section of the dentin layer while other three material layers also exhibit the residual indents (data not shown, *images taken by B.J.F. Bruet*), and (b) average nanoindentation load-depth curves for all four material layers with horizontal error bars that represent one experiment standard deviation. FEA predicted curves were compared to the experimental curves, respectively. *Figure by B.J.F. Bruet*

3.3.2. Multilayering Effects of *P. senegalus* Scales

The role of the local multilayered and graded micromechanical properties in the larger-length-scale biomechanical microindentation of the entire *P. senegalus* scale was explored by constructing two multilayered ‘discrete’ and ‘gradient’ FEA models (Fig. 3-3c) that were compared with three single homogeneous ‘all ganoine’, ‘all dentin’, and ‘all bone’ FEA models. The two multilayered model predictions both tracked the ganoine load-depth curve up to ~ 0.01 N, and then at increasing penetrations fell in between the all ganoine and all dentin simulations (Fig. 3-5a). For the multilayered simulation, at a maximum load of 0.5 N, the indenter had penetrated $\sim 45\%$ of the way into the ganoine layer (Fig. 3-5a). There was minimal difference observed in the load-depth behavior for the discrete and gradient models, indicating that the overall microlayering (not the gradients) provides the effective ‘macroscopic’ mechanical load-depth resistance (which does not suggest that gradients do not play a role in penetration resistance, discussed further in the *section 3.3.3*).

The ‘effective’ behavior of the microlayered structures was further examined by reducing each load-depth behavior to an effective O-P modulus, effective microhardness and energy dissipation. Interestingly, a load-dependent effective modulus and microhardness are predicted for the multilayered models, which were not the case for the homogeneous systems (Figs. 3-5b and c). The effective modulus for these two models is seen to decrease nonlinearly from close to that of all ganoine at small maximum loads to values slightly below that of all dentine by a maximum load of 1 N which is corresponding to a penetration depth of $\sim 5.5 - 5.7 \mu\text{m}$, as shown in Fig. 3-5b. Hence, the underlying micromechanics of the multilayered structure directly govern the effective ‘macroscopic’ indentation modulus, where the indenter increasingly ‘senses’ the more compliant dentin layer as the indentation load is increased. For the multilayered simulations, the effective microhardness is also predicted to decrease sigmoidally between values corresponding to all ganoine (at small maximum loads < 0.1 N) and all dentin (1N maximum load, corresponding to a penetration depth of $\sim 5.5 - 5.7 \mu\text{m}$, Fig. 3-5c). The multilayered microhardness predictions were compared with experimentally measured Vickers hardness (measured using TMAFM and optical microscopy) on an individual *P. senegalus* scale, and the magnitude and load dependency was accurately captured. (Fig. 3-5c) The effective energy dissipation of the microlayered models were found to increase nonlinearly with maximum load and fell in between the all-ganoine and all-dentin curves, as shown in Fig. 3-5d.

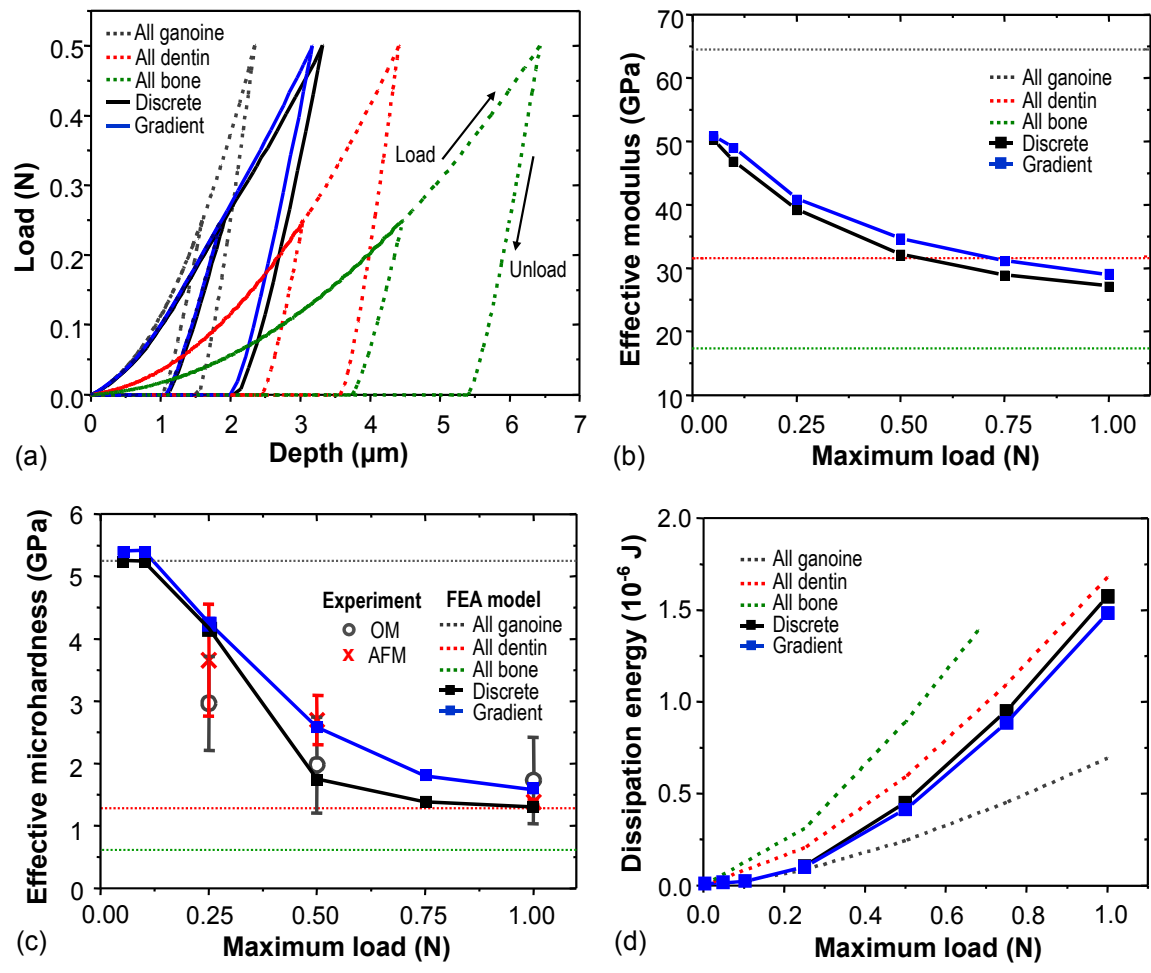


Figure 3-5. Predictions of effective microindentation mechanical properties of *P. senegalus* scale via multilayered FEA simulations; (a) simulated microindentation load-depth curves, (b) simulated effective indentation modulus, (c) simulated effective microhardness and experimentally measured values (OM, optical microscopy; AFM, atomic force microscopy), and (e) simulated effective energy dissipation.

3.3.3. Penetration Resistance Mechanism of *P. senegalus* Scales

The stress contours and plastic equivalent strain after unloading (maximum load of 1 N) for the simulated microindentation multilayer models are shown in Fig. 3-6, as compared with that of the all-ganoine materials. The gradient junction is observed to provide a transitional region for stress redistribution between layers of differing materials (Fig. 3-6c), as opposed to the abrupt changes observed in the discrete model (Fig. 3-6b). Such smoother stress gradients are expected to mitigate interface failure and increase interfacial toughness, thereby providing increased penetration resistance. Although the discrete and gradient multilayered systems achieve similar macroscopic effective indentation modulus and microhardness, the gradient case micromechanically achieves more gradual stress redistribution, providing robustness to interfacial failure. The plastic equivalent strain contours reveal the greater depths and greater area of plastic straining for the multilayer system compared with the all-ganoine model, due to the increased plastic strain of the underlying dentine, which possesses a lower σ_Y compared with ganoine; this correlates with the greater dissipation seen in the load-depth curves of Figure 3-4b. The simulations also show that the magnitude of the plastic strain in the ganoine layer of the multilayered system is lower than that experienced in the all ganoine system, even though the overall depth of penetration in the multilayer (5.46 – 5.72 μm) is more than twice that of the all-ganoine system (3.63 μm), a direct result of the dentine deformation accommodating the imposed penetration depth.

The 1 N maximum load is appropriate to estimate a brittle-failure condition for the ganoine because 1 N microhardness experiments were found to circumferentially crack in some cases and only plastically deform in other cases (Fig. 3-7)—indicating that the 1N case is at the border of meeting crack initiation conditions (Fig. 3-6). Contours of the radial stress, S22 (normal stress on the plane perpendicular to the 2 axis), reveal elevated tensile surface value (1.66 GPa) at the perimeter of the contact area (in the same region where the circumferential cracks are found), suggesting a maximum-normal-brittle-stress failure condition of 1.66 GPa.

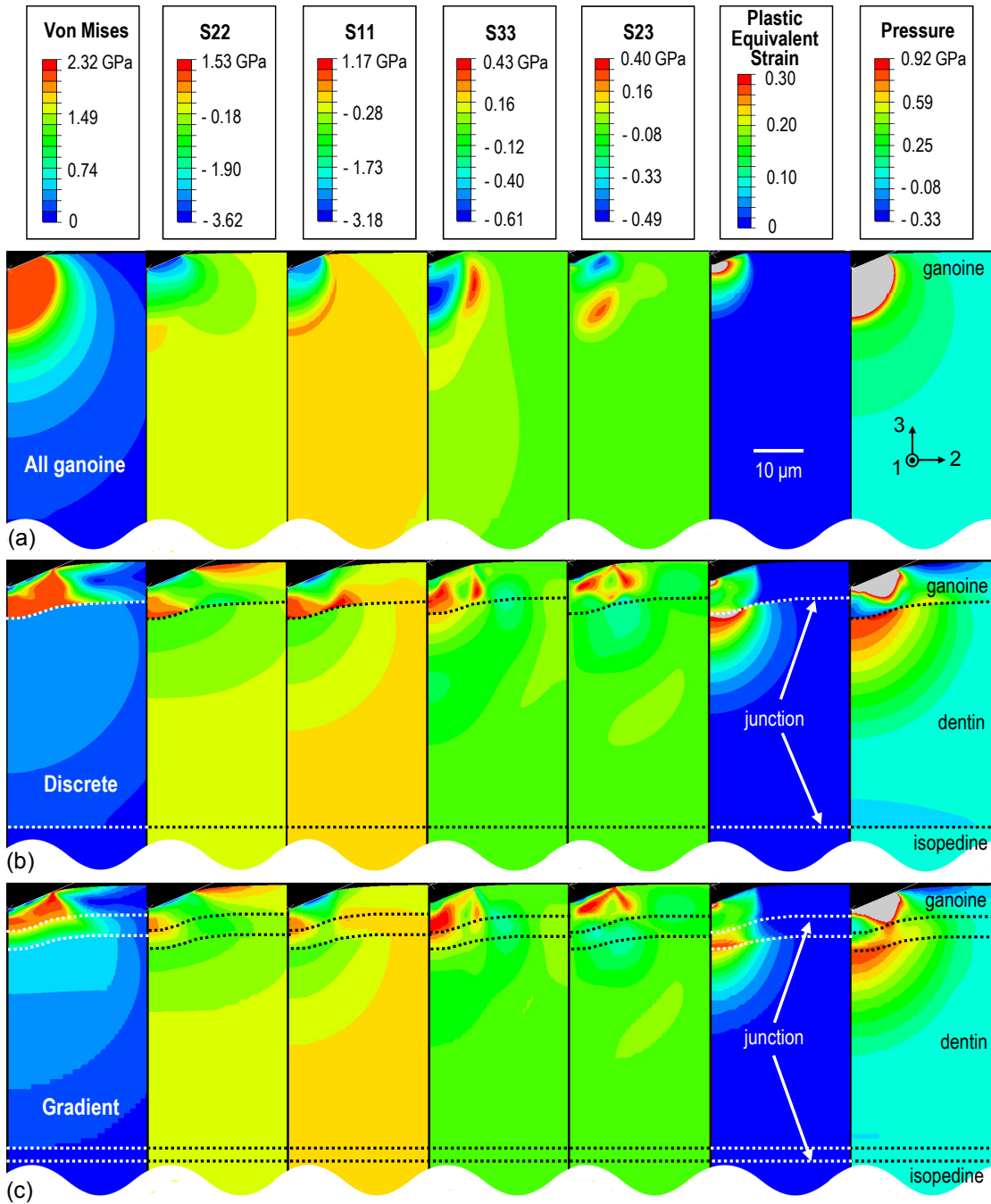


Figure 3-6. Simulated contours of stress, plastic strain and pressure fields of a *P. senegalus* scale via multilayered FEA simulations; (a) to (c) FEA predictions of von Mises stress field, S22, S11 and pressure at a maximum depth when fully loaded, and S23, S33 and plastic equivalent strain (PEEQ) after fully unloaded for three models— all ganoine (a), discrete (b) and gradient (c) models for microindentation at a maximum load of 1N.

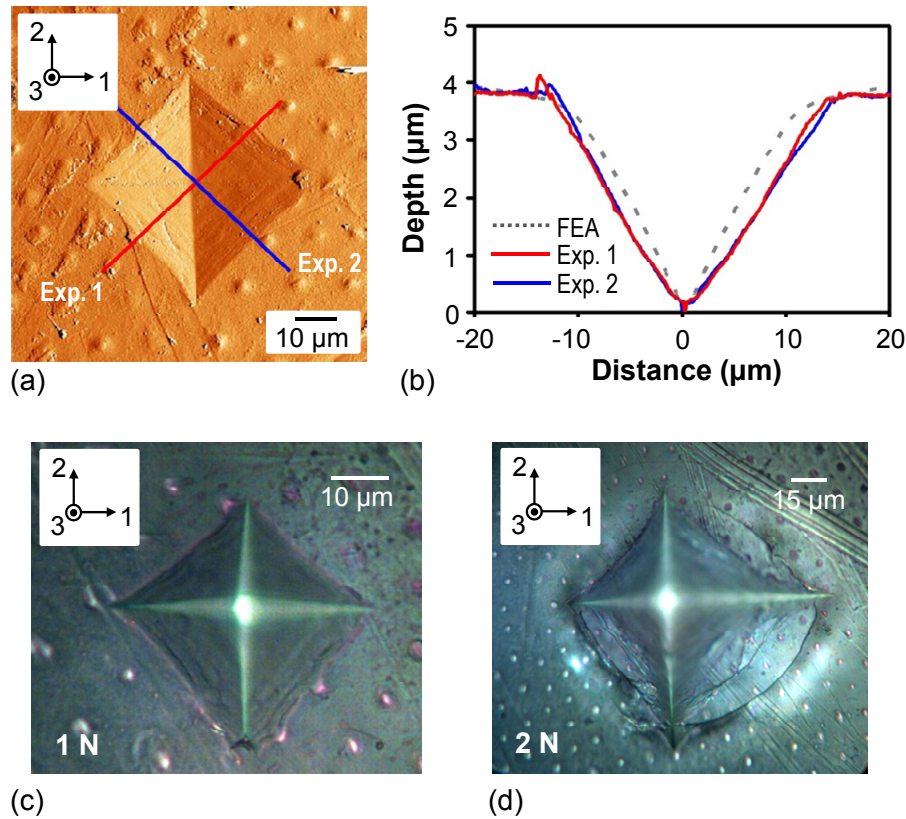


Figure 3-7. Topographic profiles, residual impressions of microindentation and fracture of an individual *P. senegalus* scale; (a) TMAFM amplitude image of a 1N-maximum-load microindentation *Image taken by B.J.F. Bruet*, (b) FEA prediction of the residual depth topography obtained from the gradient multilayer simulation and experimental height profiles that correspond to the red and blue lines as indicated in the TMAFM image (Fig. 3-7a), (c) optical micrograph of a 1N-maximum-load microindentation and (d) optical micrograph of a 2N-maximum-load microindentation showing circumferential cracks.

The values are lower and the regions of elevated stress are smaller in the gradient case than the discrete case, indicating an important smoothing role of the gradient in reducing the surface stresses. A second prominent surface failure condition is often radial cracks, which were not observed in these microhardness experiments; this is consistent with the simulation results, which show the surface circumferential stress values, S_{11} (normal stress on the plane perpendicular to the 1 axis), to be $< S_{22}$, initiating circumferential cracks would occur prior to any radial cracking. As seen in other multilayer systems (Jayachandran et al., 1995), the interfacial normal and shear stresses were found to be severe on unloading as shown in the S_{33} (normal stress on the plane perpendicular to the 3 axis) and S_{23} (shear stress on the plane perpendicular to the 3 axis acting in the 2 direction) contours of Figure 3-6. The stresses are found to be similar for the discrete and gradient systems with the expectation of a peak shear stress present on

the interface of the discrete system, which is absent from the gradient system. Excellent agreement between simulation and experiment was also demonstrated in comparison of the experimentally measured residual topography (Fig. 3-7). The 0.5 N cases deformed in an elastic-plastic manner with no cracks in most cases (~9 of 10 indents). For 1N, ~50% of the samples showed circumferential cracking. Circumferential cracks were observed in all of the 2.0 N cases (Fig. 3-7d).

3.4. Discussion

Although mineralized dermal fish scales serve many functional roles simultaneously (Ørvig, 1968; Raschi and Tabit, 1992; Long and Nipper, 1996), we limit our discussion here to protective biomechanical aspects. The primary predators of *P. senegalus* are known to be its own species or its carnivorous vertebrate relatives (Romer, 1933), and biting takes place during territorial fighting (Kodera, 1994) and feeding (Markey et al., 2006). In ancient times, many large invertebrates existed. For example, the carnivorous eurypterid was a giant arthropod that possessed biting mouth parts, grasping jaws, claws, spines and a spiked tail (Romer, 1933). Additionally, it has been suggested that the placoderm *Dukleosteus terelli* possessed a bite force large enough to puncture through the mineralized exoskeleton of its prey, to consume the flesh underneath (Anderson and Westneat, 2007). Mechanically, such predatory attacks would represent a dynamic (for *P. senegalus* (Lauder, 1980)) penetrating load (approximated by the multilayered indentation simulations), which involves a spatially localized, multiaxial and largely compressive stress field. *P. senegalus* shows a multilayered scale design over a micrometer-sized length scale, suggesting that the purpose of this design is for resistance to mechanical loads and deformations existing over these small length scales as well. For example, the teeth of a similar sized *P. senegalus* were measured to possess an end-radius of $14.7 \pm 8.8 \mu\text{m}$, ranging from ~ 3 to ~ 44 μm . A finite-element geometric representation of the teeth of *P. senegalus* was created and FEA indentation simulations carried out using these meshes (which are much larger than the standard Vickers microindenter, end radius ~ 3.7 μm) using the multilayered model. Moreover, Appendix B includes the discussion on the mechanical behavior of multilayer systems with more sophisticated elastic-plastic material models for the constituent layers during indentation. All of the trends and conclusions remained the same for multilayered FEA simulations with different types of indenter tips or more sophisticated constitutive laws of material layers. The detail simulation results will be presented and discussed in Chapter 5 and 6 of my thesis. Hence, the micrometer length scale and indentation mode of deformation within individual scales are physiologically important with regard to mitigating penetration and facilitating protection, working in conjunction with the larger, multiscale

structure of the armor, which enables a significant amount of biomechanical flexibility and maneuverability of the entire fish body (Gemballa and Bartsch, 2002).

This Chapter has focused on the fascinating, complex and multiscale materials design, in particular, multilayer and gradient material design principles of ancient fish armor in the context of its specific primary environmental threat (penetrating biting attacks) and mechanically protective function. One overarching mechanical design strategy is the juxtaposition of multiple distinct reinforcing layers, each of which has its own unique deformation and energy dissipation mechanisms. As the stiff ganoine transfers load through the ganoine-dentin junction, the underlying softer, more compliant dentin layer dissipates energy via plasticity at high enough loads. The ganoine thickness was selected (1) to simultaneously access the advantageous mechanical properties of the ganoine (hardness, stiffness) and underlying dentin (energy dissipation), (2) to reduce weight while maintaining the required mechanical properties and (3) to promote the advantageous circumferential cracking mechanisms ($S_{22} > S_{11}$), rather than disadvantageous radial cracking. The presence of the additional isopedine stratified layer with its plywood-like structure can serve as a second line of defense for deeper penetrations, preventing catastrophic crack propagation and increasing energy dissipation and fracture toughness. Microcracking was observed to be confined within the sublayers of the isopedine (Fig. 3-8a), where each individual layer has cracks running in approximately orthogonal directions but arrested at the edge of each sublayer. The underlying bone acts as the base skeletal physical support structure for normal physiological loading conditions, where plastic deformation takes place via mechanisms such as nanogranular friction (Tai et al., 2006), collagen fibril shear (Gupta et al., 2005) and denaturation (Tai et al., 2005), crack initiation-propagation (Nalla et al., 2003), intraorganic extensibility and sacrificial bone rupture (Fantner et al., 2005).

Additionally, we have observed that the ganoine-dentin junction in *P. senegalus* scales is able to arrest cracks (Fig. 3-8b), as in mammalian teeth (Imbeni et al., 2005). Localized internal fractures and detachment of pieces of the ganoine layer are seen, whereas the ganoine-dentin junction consistently remains intact (Fig. 3-8b), which may be a sacrificial mechanisms. The junctions between material layers are clearly ‘functionally graded’, that is, they possess a gradual spatial change in properties motivated by the performance requirements and are able to promote load transfer and stress redistribution, thereby suppressing plasticity, arresting cracks, improving adhesion and preventing delamination between dissimilar material layers (Suresh, 2001). Last, the corrugated junction between the layers is expected to lead to spatially heterogeneous stresses and a higher net interfacial compression, also resisting delamination (Shimizu and Macho, 2007). Such multiscale materials principles may be incorporated into the design of improved engineered biomimetic structural materials (Ortiz and Boyce, 2008).

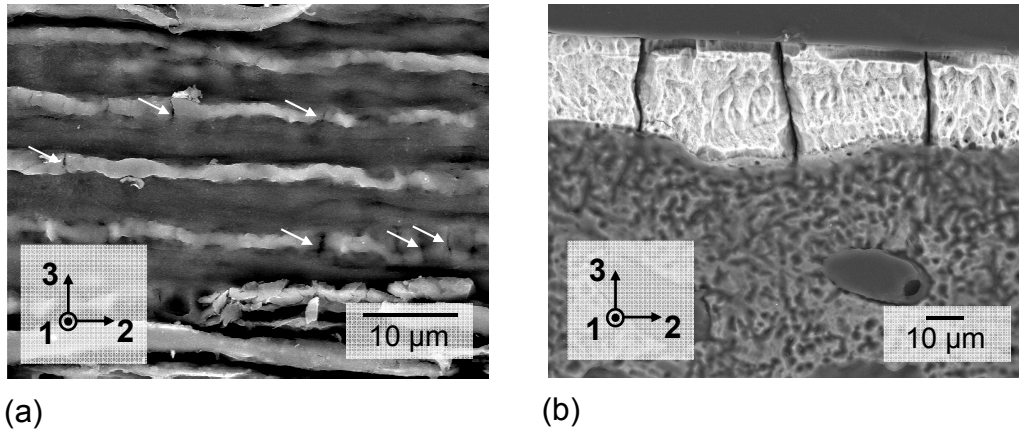


Figure 3-8. Microcracking in the material layers of an individual *P. senegalus* scale; (a) backscattering electron micrograph of cross-section of isopedine layers and (b) backscattering electron micrograph of cross-section of ganoine and dentin layers. Images were taken after 10s etching treatment using 35% H_3PO_4 solution. White arrows of Figure 3-8(a) indicate microcracks of the individual isopedine sublayers. *Images taken by B.J.F. Bruet*

3.5. Conclusion

The multiscale experimental and computational study revealed the materials design principles present within individual ganoid scales from a living *P. senegalus*, in particular with respect to penetration resistance (approximating a biting attack). These include the juxtaposition of multiple distinct reinforcing composite layers that individually undergo their own unique deformation mechanisms, a unique spatial functional form of mechanical properties with regions of differing levels of gradation within and between material layers, geometrically corrugated junctions between layers as well as layers with an undetectable gradation; all of which lead to microindentation responses that exhibit load-dependent effective material properties, circumferential surface cracking, plastic dissipation in the underlying dentin layer, and orthogonal microcracking in laminated sublayers. The knowledge of the structure-property-function relationships of dermal scales of armored *P. senegalus* fish could enable pathways to improved bioinspired human body armor and vehicle armor.

Chapter 4.

Anisotropic Design of a Multilayered *P. senegalus*

Scale

This chapter was published as a regular article: L.F. Wang, J.H. Song, C. Ortiz, and M.C. Boyce, 'Anisotropic design of a multilayered biological exoskeleton.' *Journal of Materials Research*, 2009. 24(12): p. 3477-3494.

4.1. Introduction

Hierarchical structural anisotropy is a salient feature of many biological materials, for example, bone (Fritsch and Hellmich, 2007), nacre (Barthelat et al., 2006), wood (Bucur and Declercq, 2006), tendon (Nicholls et al., 1983), skin (Vogel, 2003), cartilage (Woo et al., 1976), tooth (White et al., 2001), etc. In such materials, two types of anisotropy may exist. Firstly, at the smallest length scale, "inherent" anisotropy of the fundamental building blocks, e.g. mineral crystallinity (Katz and Ukrainci.K, 1971) and for organic constituents, anisotropic molecular structures (Dill, 1990; Ng et al., 2003; Bozec et al., 2007). Secondly, at a larger length scale, the controlled shape, orientation, and spatial placement of various structural elements in a composite or hybrid material (Tirrel, 1994), e.g. as dictated by biomineralization processes (Lowenstam and Weiner, 1989), may also induce a "geometric" anisotropy. Specifics of those combined anisotropic contributions or the composite structural arrangement can result in macroscopic direction-dependent elastic and plastic mechanical properties (e.g. nacreous mollusk shell layers, mineralized tendon, etc.), while other biological materials are known to possess direction-independent mechanical properties (e.g. echinoderm calcite, crossed-lamellar mollusk shell layers, lamellar bone, etc.) as needed for their particular biomechanical functions (Wainwright, 1969; Weiner et al., 2000). Even in the systems that exhibit direction-independent material properties, underlying inherent/geometric

anisotropies exist that affect local stress and strain distributions, the corresponding energy dissipation contributions, and the ultimate fracture mechanisms. Lastly, many physiological loading cases are multiaxial and may produce properties that appear to be direction-independent, but are in fact anisotropic in uniaxial situations.

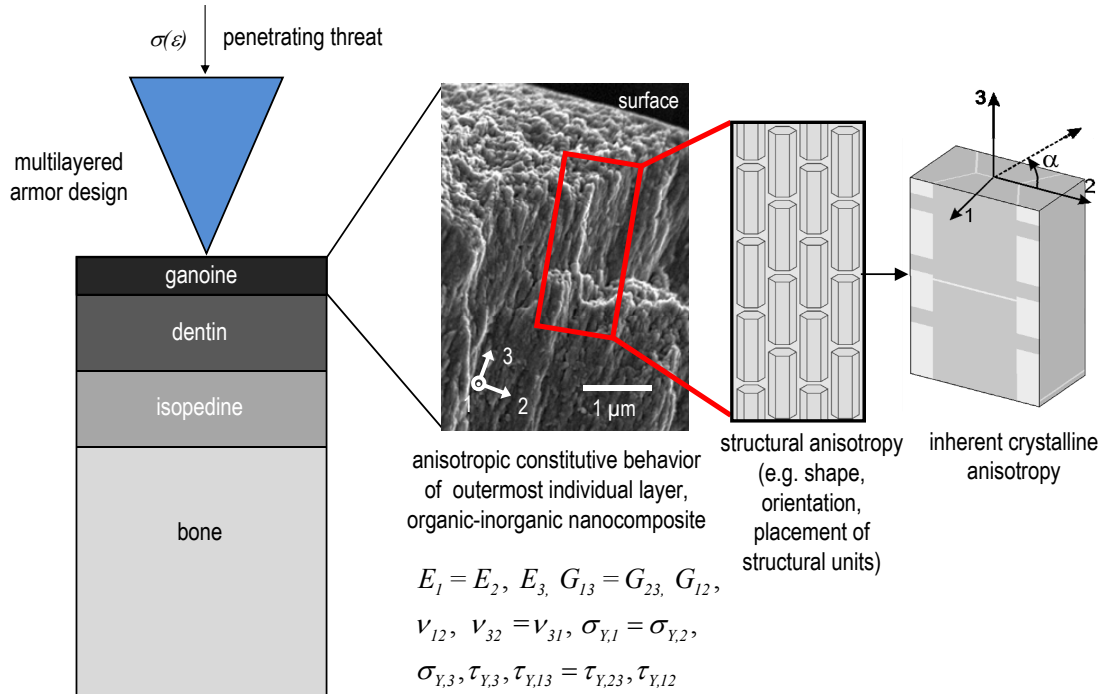


Figure 4-1. The quad-layered structure of an individual *P. senegalus* scale where the anisotropy of the outmost individual layer (ganoine) is illustrated at the different levels of resolutions from the nano-sized building blocks to the hierarchical microstructure. *Figure by L. Wang*

In most biological exoskeletons, or "natural armor," a multilayered structure exists where each layer is composed of a different nanocomposite material with varying types and degrees of structural and mechanical anisotropy. Among juxtaposed layers of many exoskeletal structures, the outermost layers are frequently known to exhibit controlled orientation of anisotropically shaped mineral crystals of specific crystallographic orientations. For example, in the outer layers/shells of American lobster (Al-Sawalmih et al., 2008), mollusk shells (Chateigner et al., 2000), chicken eggshell (Parsons, 1982) and giant barnacles (Rodriguez-Navarro et al., 2006), the crystallographic *c*-axis is found to be oriented approximately perpendicular to the surface and parallel to the long axis of the rod-like crystals. Similarly, in the outer enamel layers of teeth, the crystallographic *c*-axis of hydroxyapatite (HAP) is also parallel to the long axis of the crystals and approximately perpendicular to the surface (Driessens and Verbeeck, 1990). Here, we examine the effect of this anisotropy by focusing on ganoine, the outermost, ganoine, of the mineralized scales of the ancient fish *Polypterus senegalus* (Fig. 4-1). The scales of *P. senegalus*

possess four distinct inorganic-organic nanocomposite layers as follows (from outer to inner surface): ganoine (~ 10 μm in thickness), dentin (~ 50 μm in thickness), isopedine (~ 40 μm in thickness), and bone (~300 μm in thickness), as indicated in Chapter 3. Ganoine is known to be enamel-like (Daget et al., 2001) and possesses an anisotropic nanostructure composed of rod-like HAP nanocrystals (Meunier, 1980) with their long axis aligned approximately perpendicular to the scale surface (Fig. 4-1) along with organic matrix (Ørvig, 1967). As with the other natural armor systems described previously, this anisotropic ganoine layer serves as one of the first lines of defense against penetrating attacks. In this study, we investigate the mechanics of the ganoine anisotropy through experiments and modeling; in particular the role of structural anisotropy of the ganoine layer in the penetration/indentation resistance of the entire multilayered scale. First, the mechanical anisotropy of ganoine was experimentally assessed via instrumented nanoindentation in the surface and cross-sectional orientations (i.e., indentation modulus, hardness). An anisotropic elastic-plastic nanomechanical model, capturing a representative volume element (RVE) that idealizes the random heterogeneous structure as a periodic arrangement of hexagonally packed HAP rods surrounded by an organic matrix, was constructed through finite element analysis (FEA) and subjected to multiple loading conditions; these nanomechanical models were then used to obtain the anisotropic elasticity and plasticity of the ganoine layer and also to reveal the contribution of the crystalline anisotropy of the HAP crystal (as opposed to geometric anisotropy) to the overall anisotropy of the ganoine. The anisotropic nanomechanical modeling results were used in simulation of the nanoindentation of ganoine in orthogonal directions and then compared with experimental nanoindentation data. Furthermore, the anisotropic elastic-plastic behavior was captured in a continuum-level constitutive model to reveal the role of the ganoine anisotropy in the entire multilayered ganoine-dentine-isopedine-bone multilayered exoskeletal structure, especially in terms of the penetration resistance and deformation of the scale.

4.2. Experimental Study

4.2.1. Methods

Scale removal A living *Polypterus senegalus* (length ~ 20 cm) was anesthetized and a row of four scales surgically dissected off from the 49th row on the left flank (posterior region). Tricaine methanesulfonate (MS-222, Sigma-Aldrich, St. Louis, MO) was used for general anesthesia, prepared at the concentration of 1.6 g/500 mL H₂O with 3 pellets of KOH for neutralization. The fish was subsequently removed and immersed in a mixture of 50 /50 MS-222 and water from the tank to maintain anesthetization.

Afterward, the fish was treated with tetracycline (250 mg, Thomas Laboratories, Tolleson, AZ).

Sample preparation Individual scales were initially cut in half with a razor blade. One half of each scale was designated for testing parallel to the surface normal (surface orientation) and the other half of the scale was designated for testing perpendicular to the surface normal (cross-sectional orientation), as shown in Fig. 4-2. Samples were sectioned using a diamond impregnated annular wafering saw (Isomet 5000, Buehler, Lake Bluff, IL) at 800–900 rpm and then polished stepwise with 6 and 1 μm silica nanoparticles on a soft pad (Buehler), followed by 500 nm silica nanoparticles on microcloth (Buehler). The root mean square (RMS) surface roughness of all polished samples was measured using tapping mode atomic force microscopy (TM-AFM; Digital Instruments Multimode SPM IV, Veeco, Santa Barbara, CA) and found to be less than ~ 2 nm. After polishing, it was determined by scanning electron microscopy (SEM) of the cross sections that ~ 5 μm of material was removed, leaving a ~ 10 μm thick ganoine layer.

Scanning Electron Microscopy Fractured scales were etched briefly either with 5.25% NaOCl (Sigma-Aldrich), pH balanced to 7 with HCl (slight deorganification), with ethylenediaminetetraacetic acid (EDTA, 0.5 M, Sigma-Aldrich) for 2 min (slight demineralization) or with phosphoric acid for 20 s (slight demineralization) to more clearly reveal their microstructure and nanostructure. Samples were fixed on a steel support using conductive tape and then sputter-coated with 5 nm of gold in a Denton Vacuum Desk II (Moorestown, NJ). SEM samples were imaged in a JEOL JSM 6060 (Peabody, MA) scanning electron microscope at 10 kV acceleration voltage. Backscattered electron microscope (BSEM) images were taken with the JEOL JSM-6700F.

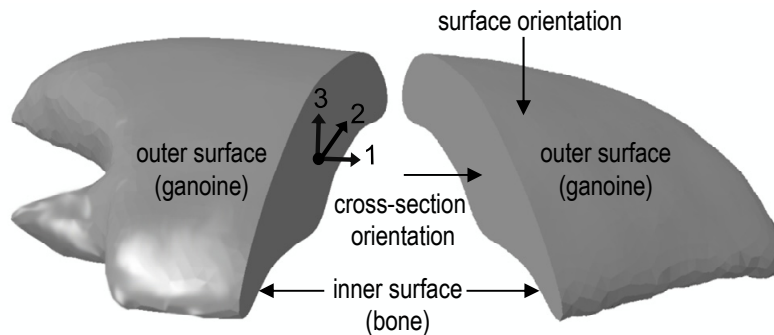


Figure 4-2. Individual *P. senegalus* scale cut in half and denoting two orthogonal orientation directions of nanoindentation experiments. “Surface orientation” represents loading parallel to the outer surface normal, denotes as the 3-axis, and “cross-section orientation” represents the loading perpendicular to the outer surface normal in the direction represented by the 1 in-plane axis.

Nanoindentation Samples were attached to a steel puck using a cyanoacrylate glue (Loctite 495, Hankel KGaA, Düsseldorf, Germany) and then tested in both the surface (load parallel to surface normal) and cross-sectional (load perpendicular to surface normal) directions. Both sets of nanomechanical experiments were carried out at a depth (parallel to the surface normal) of 5 μm , which is prior to the depth where a decreasing gradient in mechanical properties is known to begin as shown in Fig. 3-2b. Nanoindentation experiments were performed on loading and unloading in ambient conditions using a Triboindenter (Hysitron, Inc., Minneapolis, MN) with a Berkovich diamond probe tip (end radius ~ 300 nm). Multiple indents were performed to provide statistically meaningful data sets. The applied load function was divided into five segments: (1) the first segment that consists of a 3 second hold at zero force allowing tip-sample equilibrium; (2) the second segment that is a loading regime with a constant loading rate of 50 $\mu\text{N/s}$; (3) the third segment with a hold period at the maximum load of 500 μN for 5s; (4) the fourth segment that decreases the load until reaching zero force with an unloading rate equivalent to that of the second segment; and (5) the last fifth segment with a 3 second hold at zero force for a purpose of calculating the final drift rate of the piezo. A constant loading/unloading rate of 100 $\mu\text{N/s}$, a maximum load of 500 μN and a lateral interindent spacing of 3 μm were used. Approximately 100 indents per sample were performed in each of the two orthogonal directions. The probe tip area function $[A(h_c)]$, which is the projected area of the Berkovich probe tip as a function of the contact depth h_c , and frame compliance were calibrated prior to each set of experiments using a fused quartz sample. The load-depth curves from multiple experiments to the maximum indentation load of 500 μN and from different sample locations were averaged with calculated standard deviation. The Oliver-Pharr analysis (Pharr et al., 1992) was used to reduce effective material properties from the nanoindentation force-depth data into indentation stiffness and hardness.

4.2.2. Results

4.2.2.1 Ultrastructure of ganoine

As I have described in Chapter 3, upon dehydration of the scales of *P. senegalus* microcracks are observed to occur perpendicular to the scale surface within the ganoine layer which are arrested by the underlying dentin, suggesting that the structural anisotropy of the ganoine plays a role in the mechanical functionality of the scale (Figs. 3-8b and 4-3a). Figures 4-3b to 4-3e elucidate the fine nanostructural anisotropy of the ganoine layer at higher resolutions. Elongated rod-like and well-packed HAP crystals are clearly visualized with an average diameter of ~ 50 nm and an average length of a few hundred nm, which exhibit a discontinuous and tortuous crack propagation path through

the thickness of the ganoine layer as indicated with black arrows in Figs. 4-3(c) and 4-3(e). The long axis of the crystals is aligned approximately perpendicular to the scale surface. The ganoine nanostructure does exhibit some heterogeneity in size distribution, as well as axial orientation angle, and the surfaces of the nanocrystals do not appear smooth but corrugated.

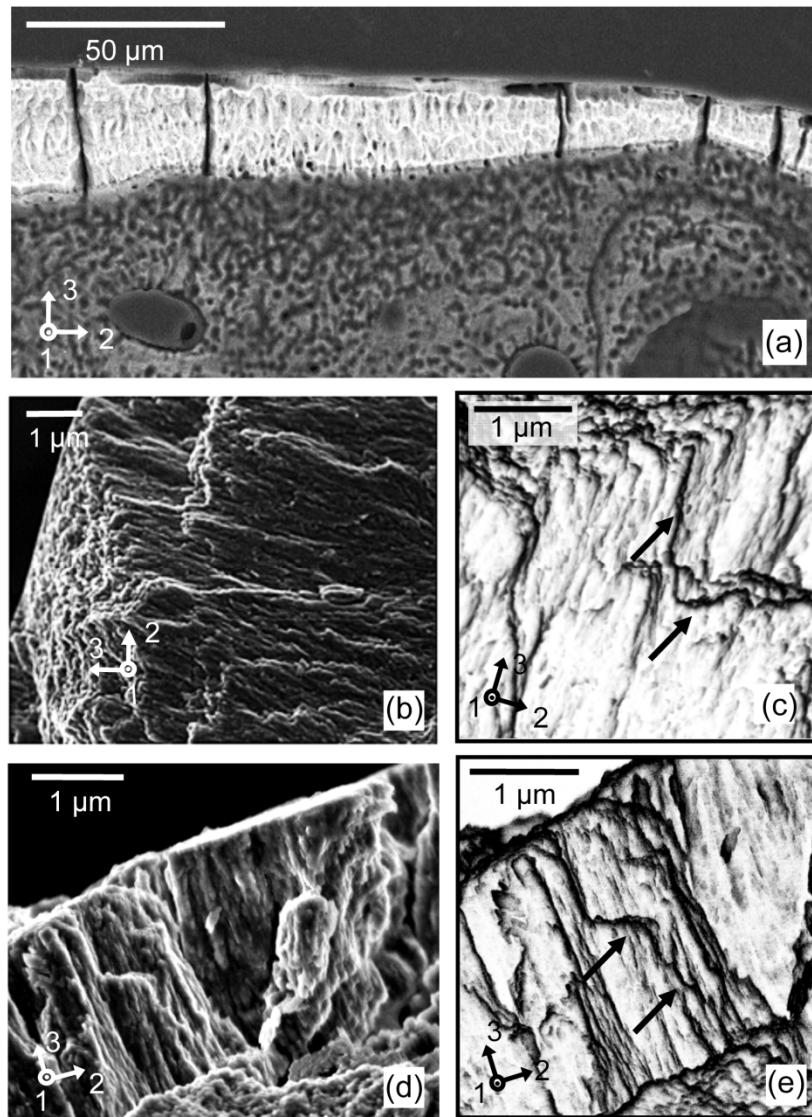


Figure 4-3. Nanostructure, microstructure, and fracture of the ganoine layer of a *P. senegalus* scale; (a) backscattered electron microscopy images of the cross section of ganoine and dentin layers of the polished *P. senegalus* scale (embedded in the epoxy resin) after etching with phosphoric acid for 20 s, and (b) - (d) SEM images of ganoine exposing the thin elongated HAP nanocrystals after the scale sample fractured and etched with (b) NaOCl for 5 min or (d) 0.5 M EDTA for 2 min, and (c, e) images modified by means of reversing contrast of (b) and (d), respectively, which show crack paths more clearly. (b) - (e) were not embedded in epoxy or polished. Arrows indicate the torturous crack paths crossing the neighboring rods.

4.2.2.2 Nanoindentation

The averaged nanoindentation data (load versus depth) for the surface and cross-sectional directions (Fig. 4-4) display an indistinguishable mechanical response. The average indentation stiffness was determined by means of the O-P method (Pharr et al., 1992) via the experimentally measured slope of the unloading load-depth curve, S , and the maximum projected contact area, $A(h_c)$, where h_c is the contact depth. S was evaluated at 95% - 20% of the maximum load, P_{\max} . $A(h_c)$ was estimated from a sixth-order polynomial fit accounting for nonideal tip geometry on a standard fused quartz sample. Hardness values were calculated as $P_{\max}/A(h_c)$. Using this method, indentation moduli and hardness values were calculated to be 74.8 ± 5.0 GPa, 3.98 ± 0.27 GPa (surface orientation) and 75.1 ± 8.0 GPa, 3.92 ± 0.34 GPa (cross-section orientation), respectively, consistent with Figure 3-1b and 3-2b of Chapter 3. Note that the O-P method assumes isotropy and is herein used only as a means for reducing effective indentation modulus and hardness for comparison purposes. Unpaired student t-tests confirmed that both the average indentation stiffness and hardness were not statistically different for the two orientations tested ($p > 0.05$).

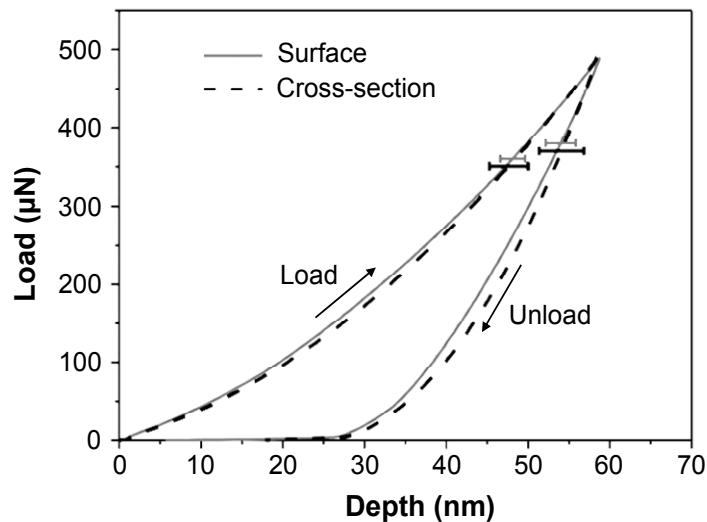


Figure 4-4. Averaged experimental curves on loading and unloading (number of experiments, $n = 75$) for both surface and cross-sectional directions. The horizontal bars indicate the maximum standard deviation of the curves for that particular dataset.

4.3. Modeling Study

The mechanical behaviour of ganoine was further studied using three levels of modelling. First, at the smallest length scale nanomechanical modelling of an RVE of the ganoine organic-inorganic composite nanostructure was carried out to compute the anisotropic elastic-plastic constitutive behaviour and mechanical properties. Second, these latter data were used to simulate the surface and cross-section nanoindentation of ganoine for comparison with experiments and to provide insight into the deformation and dissipation mechanisms beneath the indenter. Thirdly, larger-length scale simulations of microindentation of the ganoine/dentin/isopedine/bone multilayered structure were conducted to explore the role of ganoine anisotropy in the penetration resistance of the scales.

4.3.1. Methods

4.3.1.1 Nanomechanical modeling

Nanomechanical modelling was used to determine the overall anisotropic mechanical behaviour of the biological composite material (ganoine) based on the constituent material mechanical properties (hydroxyapatite and organic) in conjunction with an RVE of the nanostructure. The nanomechanical RVE model construction consists of: (i) a description of the geometry of the nanostructure; (ii) a description of the mechanical behavior of the constituent materials; and (iii) a description of the periodic boundary conditions, the loading conditions, and the determination of the composite response (here, the stress-strain response) of the RVE during the different loading scenarios.

RVE geometry description Based on the SEM images (Fig. 4-3), the ganoine nanostructure can be described as composed of well-packed HAP crystals discontinuous through the ganoine layer, interacting through their rough surfaces, and separated by thin adhesive layers of organic. This structure is here idealized as a composite of a staggered and hexagonally-packed distribution of HAP crystals (cross-sectional length of ~40 nm and axial length of ~220 nm) in an organic matrix (thickness assumed to be 2 nm, based on known mineral volume fraction of ~95% (Ørvig, 1967)), as shown in Fig. 4-5. The periodically repeating nature of the RVE is captured by general periodic boundary conditions on the displacements (Danielsson et al., 2002, 2007). In the real structure, the distributed and irregular alignment of the crystallites together with the prism-to-prism interlocking surface roughness (Figs. 4-3b to 3e) interrupts the continuity of the organic matrix and, hence, is expected to provide additional resistance to shear deformation between neighboring crystallites. To capture this effect in our idealized RVE in a simplified manner, transverse mineral elements were introduced to emulate the

mechanical effect of the alignment and surface roughness (Fig. 4-5b). Simulations were conducted with and without transverse mineral elements to understand its role on effective anisotropic properties.

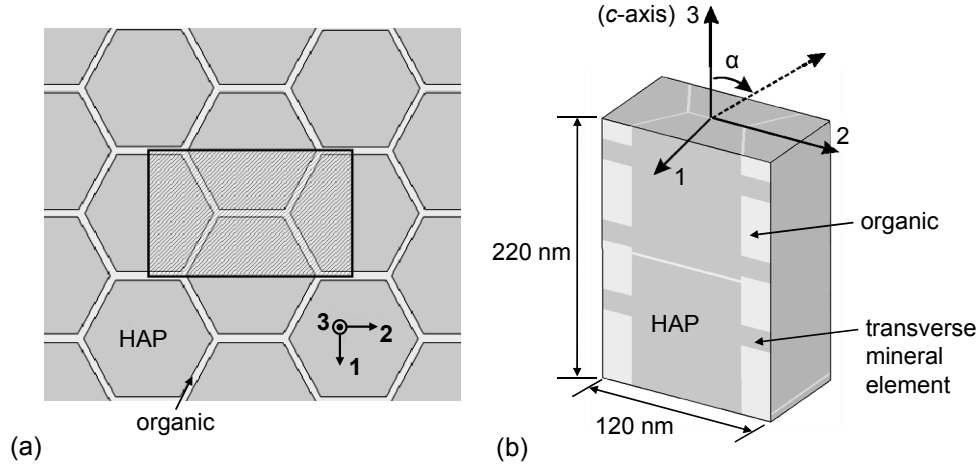


Figure 4-5. RVE of ganoine nanostructure including HAP mineral crystals (dark gray) and organic matrix (light gray); (a) view of hexagonal arrangement of HAP crystals looking toward the top surface (down the 3-axis) and (b) 3D view of the RVE [square region in the center of (a)] consisting of transverse mineral elements. The 3-axis (normal to the surface direction) of the scale is also coincident with the crystallographic c -axis of the HAP crystals. *Figure by L. Wang*

Description of the mechanical behavior of the constituent materials The mechanical behavior of the constituent HAP crystals and the organic matrix must be specified in the model. The anisotropic elasticity of HAP single crystals (which possess a transversely isotropic hexagonal lattice) has been obtained by using empirical potentials (Lee et al., 2000). For biological composites, it is expected that the modulus values do not reach these ideal values as a result of differences in density, purity (including intercalated organic), chemical composition and porosity of the HAP phase (Posner and Betts, 1981; Driessens and Verbeeck, 1990; Leventouri, 2006; Weiner, 2006; Rey et al., 2007). Hence, we take the anisotropic base properties of the pure crystal (Lee et al., 2000) and scale these down, keeping the same anisotropy ratios to account for this biological reality (Table 4-1). The anisotropic yield behavior of single crystals of HAP has been explored in hardness tests (Viswanath et al., 2007) that find hardness values parallel and transverse to the c -axis to be 9.7 GPa and 8.8 GPa, respectively. Hence, the HAP elastic properties were downscaled by a factor of 1.36 and the yield stress downscaled by 1.18 (corresponding a hardness/yield stress ratio of 3), keeping the correct anisotropy ratios (Table 4-1). These scaling factors used to obtain the anisotropic moduli and yield stress values were determined by iteratively fitting to experimental nanoindentation data (Fig. 4-4). With this said, other sources of increased compliance, such as a more compliant or thicker organic matrix, reduced degree of crystal alignment, or reduced density of

transverse mineral elements, cannot be conclusively excluded. The details of such microstructural features were incorporated to the best of our knowledge into the simulations based on current experimental data. For comparison, simulations were also carried out assuming the HAP to be isotropic where best fits to nanoindentation data yielded elastic properties of $E = 80$ GPa, $\nu = 0.3$ and an isotropic yield stress of 2.6 GPa for the HAP (Table 4-1). The organic matrix has mechanical properties much lower in magnitude compared to the mineral HAP crystals; a value of 4.3 GPa for the elastic modulus and a yield stress of 400 MPa of the organic were assumed, consistent with values used in other studies (Spears, 1997; Katti et al., 2001).

Table 4-1. Mechanical properties of HAP crystals assumed in the nanomechanical model. The 3-axis was taken to be coincident with the crystallographic axis

	$E_1 = E_2$ (GPa)	E_3 (GPa)	G_{12} (GPa)	ν_{12}	ν_{13}	$\sigma_{Y,1} = \sigma_{Y,2}$ (GPa)	$\sigma_{Y,3}$ (GPa)	$\tau_{Y,13} = \tau_{Y,23}$ (GPa)	$\tau_{Y,12}$ (GPa)
Isotropic	80	80	30.8	0.30	0.30	2.60	2.60	1.50	1.50
Anisotropic	86.4	73.6	24.5	0.23	0.29	2.47	2.73	1.50	1.43

Description of the periodic boundary conditions and calculation of the effective behavior of the RVE Periodic boundary conditions were applied to ensure the compatibility of neighboring RVEs during deformation. The RVE was subjected to various deformation histories in the FEA-based simulations (ABAQUS/standard) as described below. The averaged anisotropic elastic-plastic mechanical response of the RVE for each case was calculated through virtual work considerations using the method detailed in Refs. (Danielsson et al., 2002, 2007). The highly packed arrangement of HAP in the ganoine (Fig. 4-5a) together with the symmetry of the HAP crystal structure suggests transversely isotropic elastic properties for the ganoine with the isotropy plane being orthogonal to the 3-axis, as shown in Fig. 4-5b. The crystallographic c -axis was taken to be coincident with the long axis of the HAP rods, similar to that known for tooth enamel (Driessens and Verbeeck, 1990). There are five independent properties characterizing the elastic response of a transversely isotropic material ($E_1 = E_2$, E_3 ; $G_{13} = G_{23}$, ν_{12} , ν_{13}). Two uniaxial stress loadings and two shear loadings in different directions were applied to the RVE to determine the effective composite anisotropic elastic constants and yield stresses. To investigate the elastic-plastic response of the structure in different orientations, the RVE was also subjected to off-axis loadings. As shown in Fig. 4-5b, uniaxial compression was applied to the RVE in directions $\alpha = 0^\circ$, 15° , 30° , 45° , 60° , 75° , and 90° away from the rod axis.

4.3.1.2 Nanoindentation model

Nanoindentations into the surface and cross section of ganoine were simulated using three-dimensional nonlinear finite element analysis. The full nanoindentation process was modeled using one-quarter of the geometry of the system together with appropriate symmetry boundary conditions. The ganoine was discretized with eight-node linear hybrid brick elements (C3D8H in ABAQUS/standard element library, Providence, RI). Mesh convergence was assessed and a mesh of 16,704 elements was found to provide an accurate solution (Fig. 4-6a). The Berkovich indenter was modeled as a rigid conical-like indenter; the tip cross-sectional area was the experimentally measured Berkovich tip area function (TAF). The surface-to-surface contact between the indenter surface and the ganoine surface was specified to be frictionless with no overclosure. The constitutive behavior of the ganoine was modeled in three ways: (i) isotropic elastic-perfectly plastic with Young's modulus $E = 65$ GPa, Poisson's ratio $\nu = 0.3$, yield stress $\sigma_Y = 1.53$ GPa (data obtained from fitting results to averaged nanoindentation data, Fig. 4-4) as I did in Chapter 3; (ii) anisotropic elastic-anisotropic plastic with the properties obtained from the nanomechanical modeling (values to be reported in Table 4-3) and the anisotropic yield modeled using the Hill anisotropic yield condition; (iii) discrete modeling of the HAP rods and organic matrix layers in the indentation region including transverse mineral elements (Fig. 4-6b), to scale with the indenter geometry, and outer surrounding ganoine regions following the corresponding continuum level anisotropic-elastic/anisotropic plastic constitutive representation. In the FEA models, all of the nanoindentation simulations were conducted to a maximum load of 500 μN in accord with the experiments; surface and cross-sectional indents were simulated for all three cases of material description described previously.

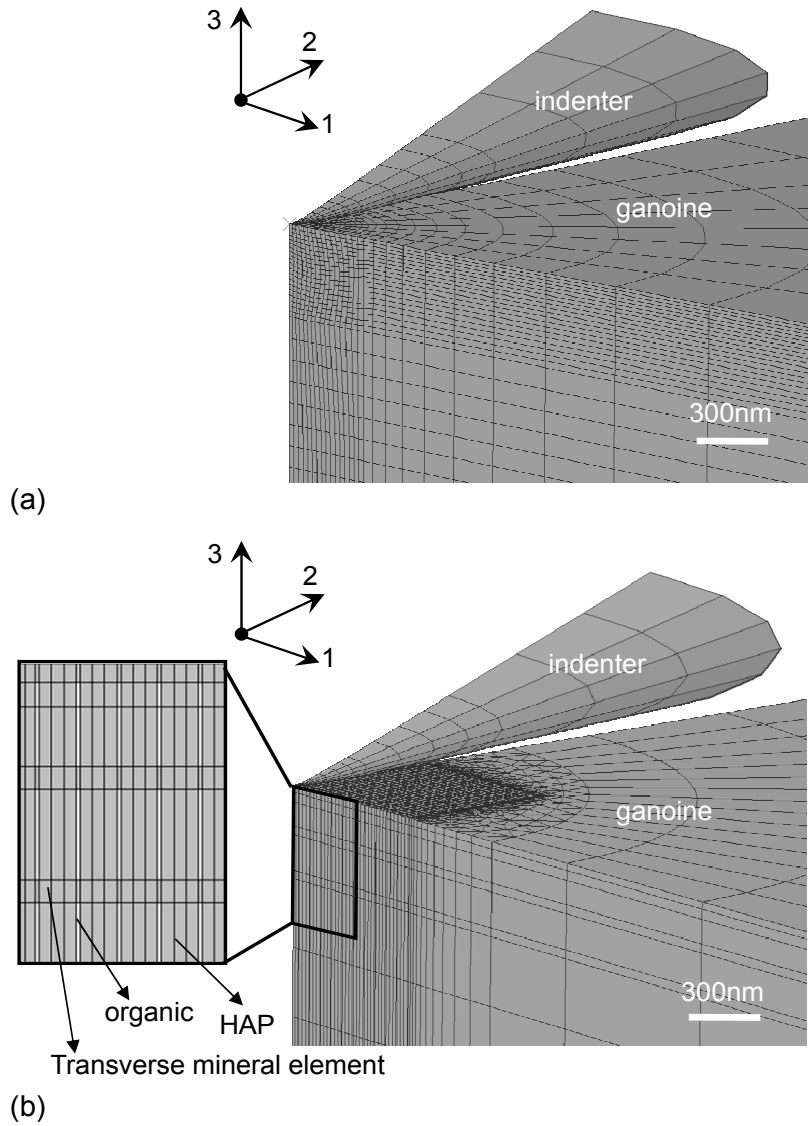


Figure 4-6. Two three-dimensional nanoindentation FEA models of; (a) continuum ganoine layer showing finer meshing in region directly below the indenter, and (b) discrete nanostructural ganoine layer consisting more than 100 nanocrystals surrounded by thin organic layers and being incorporated within the region directly below the indenter, where the HAP minerals are meshed with square cross sections.

4.3.1.3 Microindentation model

Microindentation into the multilayered ganoine/dentin/isopedine/bone scale was simulated using nonlinear FEA to/from indentation loads of 0.25 N, 0.50 N, 0.75 N, and 1.0 N. Simulation details follow those described in Chapter 3 with the exception of the constitutive modeling of the ganoine layer. The indenter for the microindentation has a conical tip geometry that emulates a Vickers microhardness tip with a radius of 3.7 μm in accord with the microhardness experiments of Chapter 3. The effective microhardness was computed from the FEA simulations in a manner consistent with that used in the microhardness experiments, taking the indentation load and divided by the residual contact area (i.e., the area corresponding to the radius of the residual indent impression after unloading is complete). The role of ganoine anisotropy on the micro-level penetration resistance of the multilayered scale was explored by comparatively varying the ganoine constitutive behavior in the FEA models. In the first model, presented as “discrete” model in Chapter 3, the four material layers with thicknesses corresponding to their experimentally measured values (8, 46, 45, and 300 μm from outer to inner) were each taken to possess isotropic, elastic-perfectly plastic constitutive behavior; this multilayer model is referred to as the isotropic ganoine multilayer (IGML). The material constants have been reduced from nanoindentation data on the individual layers and are provided in Table 4-2. For the second model, the dentin, isopedine, and bone layer were taken to be isotropic, and the ganoine is taken to be anisotropic; this model is referred to as the anisotropic ganoine multilayer (AGML). In this model, the ganoine layer was represented by a continuum level constitutive model of the anisotropic elastic/anisotropic plastic behavior used also in the nanoindentation simulations describe previously with the properties reduced from the nanomechanical modeling simulations (values to be reported in Table 4-3); the anisotropic plasticity was captured using the Hill anisotropic yield condition. In order to compare both multilayer models, simulations of indentation into a monolithic isotropic ganoine (to be referred to as MIG) material were conducted.

Table 4-2. Isotropic material properties used in FEA model of microindentation into multilayered *P. senegalus* scale, obtained from isotropic elastic-plastic FEA fits to nanoindentation data for each layer as reported in Chapter 3.

	Thickness (μm)	Modulus (GPa)	Yield strength (GPa)
Ganoine	3	65	1.53
Dentin	46	25	0.40
Isopedine	45	14.5	0.215
Bone	300	13.5	0.18

4.3.2. Results

4.3.2.1 Nanomechanical modeling

Figures 4-7a and 4-7b depict the ganoine stress-strain responses computed from the ganoine nanomechanical model simulations for the RVE which considers the HAP rods to be inherently isotropic and the matrix continuity to be interrupted by transverse mineral elements (henceforth referred to as RVE (A)). Results considering uniaxial compressions in directions aligned with, 45° off-axis from, and transverse to the long axis of the HAP rods as well as shear in the planes with normals defined by $\mathbf{n} = \mathbf{e}_3$, $\mathbf{n} = 0.707 \mathbf{e}_1 + 0.707 \mathbf{e}_3$, and $\mathbf{n} = \mathbf{e}_1$. The axial modulus and yield strength in the direction aligned with the prism axis are 15% and 26% larger than the transverse values. The off-axis axial response has the lowest modulus and strength since it samples the shearing of the matrix. The shear modulus and yield strength in the transverse plane are 13% and 100% larger than the out-of-plane values, respectively; the off-axis shear has the greatest shear modulus and shear strength as a result of the unfavorable orientation of the organic layers during this shear loading. Table 4-3 provides the full set of anisotropic material constants for the ganoine layer determined from the complete simulated response (including lateral contractions during uniaxial stress conditions) of the simulation. A second set of material properties was also deduced for the case where the HAP crystal response was taken to be anisotropic with the crystal properties previously listed in Table 4-1.

The directional dependence of the Young's modulus and axial yield stress were computed from simulations of uniaxial loading in different directions and are shown in Fig. 4-7c and 4-7d, respectively. Results for RVE (A) are compared to two other RVEs: RVE (B), which considers isotropic HAP crystals but lacks transverse mineral elements; and RVE (C), which considers anisotropic HAP crystals and includes transverse mineral elements. Values for off-axis axial modulus were also computed by transformation of the computed anisotropic stiffness tensor of each RVE case, giving the continuous curves of Fig. 4-7c, which are fully consistent with the values, computed via off-axis simulations. Examining the results of RVE (A), the transverse modulus and yield stress ($\sim 90^\circ$) are observed to be lower than the axial axis values ($\sim 0^\circ$, by 13 and 21%, respectively); the lowest values occur off-axis ($\sim 45^\circ$) because of the extensive shearing of the matrix. Comparing RVE (A) to RVE (B), we find the presence of transverse mineral elements to provide a modest increase in the modulus (Fig. 4-7c) in all directions as expected; the transverse mineral elements have a dramatic effect on off-axis yield (up to four times smaller) since the absence of transverse minerals enables easy shear yielding of the matrix when loading off-axis (Fig. 4-7d). Interestingly, a "double yield" is observed for RVE (B) when loading at $\alpha = 75^\circ$ (Fig. 4-7d) where the first yield occurs at a low stress because of matrix shear. However, as deformation progresses, the HAP rods rotate (unhindered by the lack of transverse mineral elements) and the axial stress needed to

provide a resolved shear stress that would yield the matrix layer monotonically increases until reaching a point where yielding of the HAP is reached. This can be interpreted as a geometrically induced self-hardening mechanism. Comparing results of RVE (A) to RVE (C) reveals the influence of the HAP crystal anisotropy on the anisotropic response of the ganoine. The modest inherent elastic anisotropy of the HAP crystal offsets some aspects of the geometric anisotropy, giving a transverse modulus slightly higher than the axial modulus (Table 4-3, Fig. 4-7c). The yield stress is slightly increased in an approximately proportional manner because of the anisotropic yielding of the HAP crystal. Although these results are based on RVEs of an idealized microstructure of ganoine, they do reveal that the anisotropic mechanical feature of primary importance is the reduced shear stiffness and yield stress relative to the axial and transverse properties.

Figure 4-8 depicts contours of scalar equivalent stress (von Mises) and equivalent plastic strain for RVE (A) under the macroscopic compression strain of 10% and macroscopic shear strain of 10%. These contours demonstrate the deformation mechanisms of the direction-dependent yield behavior of Fig. 4-7d described previously. Compression along the long axis requires direct axial loading of the HAP rods as best seen in the stress contours where, as expected, off-axis loading gives extensive shearing of the matrix (as best seen in the plastic strain contours) at relatively low stress (as seen by comparing the stress contours of the different directions). Similar comparisons of contours for the simple shear loading conditions reveal how different regions and volumes of matrix govern yielding in the different loading directions.

Table 4-3. Predicted anisotropic material constants for ganoine layer from nanomechanical model of RVE with transverse mineral elements: (I) RVE consists of isotropic HAP mineral and (II) RVE consists of HAP mineral with elastic and plastic anisotropy (Lee et al., 2000; Viswanath et al., 2007).

	$E_1 = E_2$ (GPa)	E_3 (GPa)	$G_{13} = G_{23}$ (GPa)	G_{12} (GPa)	ν_{12}	$\nu_{32} = \nu_{31}$	$\sigma_{Y,1} = \sigma_{Y,2}$ (GPa)	$\sigma_{Y,3}$ (GPa)	$\tau_{Y,13} = \tau_{Y,23}$ (GPa)	$\tau_{Y,12}$ (GPa)
I (isotropic HAP crystal)	63.5	73.1	23.0	25.0	0.29	0.25	2.05	2.60	0.57	1.16
II (anisotropic HAP crystal)	69.7	64.0	20.7	28.4	0.36	0.18	2.13	2.70	0.54	1.07

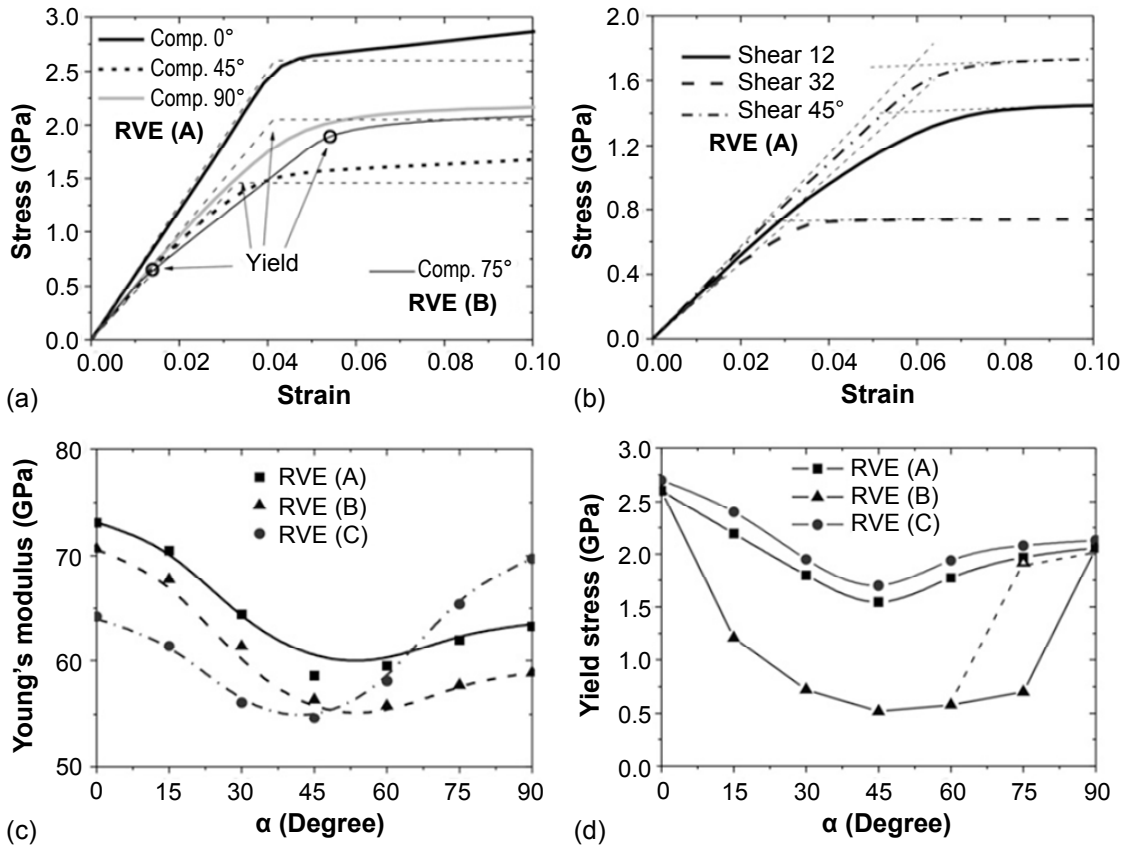


Figure 4-7. Predicted mechanical responses from RVE models subjected to various loading conditions; (a) microscopic stress-strain response of the *RVE (A)* for ganoine to uniaxial compression compared with a stress-strain curve (showing two yield points) for *RVE (B)* under off-axis compression where thin dashed lines are simulated curved from anisotropic material assumption, (b) microscopic stress-strain response of the *RVE (A)* for ganoine to simple shear deformation where thin dashed lines show the calculation of yield stress, (c) the Young's moduli and (d) yield stress determined from the stress-strain curves as a function of orientation, as represented by the angle, α , between the surface and cross-sectional orientations [Fig. 4-5b] (a second yield point is connected by dashed line). Values for off-axis axial modulus computed by transformation of the computed anisotropic stiffness tensor of each RVE case are given by the continuous curves. The directional dependence of the Young's modulus and yield stress is shown for three different RVEs: *RVE (A)* considers isotropic HAP crystals and transverse mineral elements, *RVE (B)* considers isotropic HAP crystals but lacks transverse mineral elements, and *RVE (C)* considers anisotropic HAP crystals and also includes transverse mineral elements. *Figure by L. Wang*

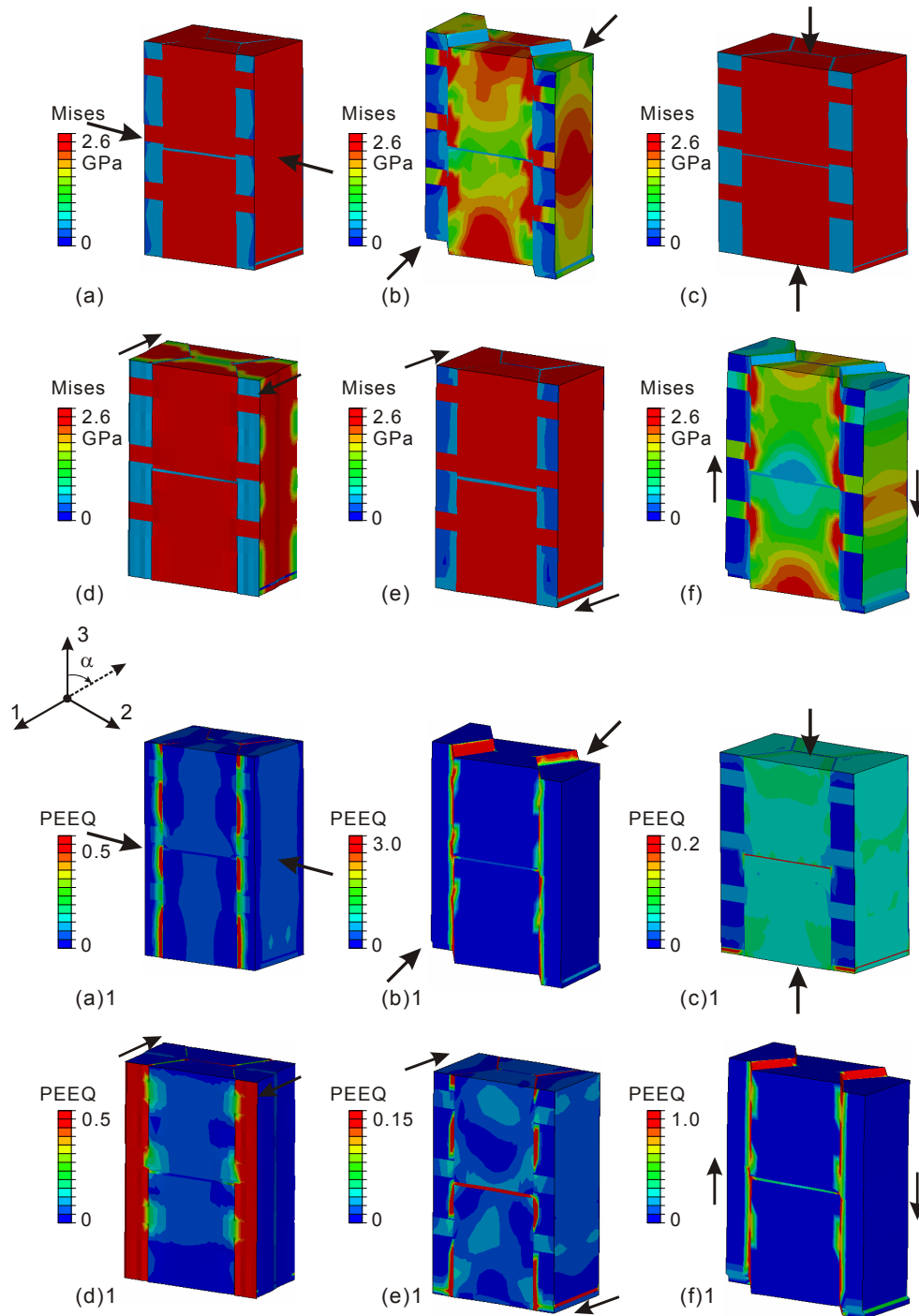


Figure 4-8. Simulation contours of equivalent stress (von Mises) for RVE (A) representing ganoine, Fig. 4-5(b), i.e., considering isotropic HAP and including transverse mineral elements, under a macroscopic strain of 10% for (a) $\alpha = 90^\circ$, (a) $\alpha = 45^\circ$, and (c) $\alpha = 0^\circ$, macroscopic shear strain of 10% in the plane with normal (d) $n = e_3$, (e) $n = 0.707e_1 + 0.707e_3$, and (f) $n = e_1$. (a) 1 – (f) 1 are corresponding plastic equivalent strain contours (PEEQ). *Figure by L. Wang*

4.3.2.2 Nanoindentation model

Figure 4-9 plots experiment and simulation results for load versus depth response of nanoindentation into the surface and the cross section of ganoine, where simulation results consider the three representations of the ganoine constitutive behavior described in the methods section 4.3.1.2: isotropic ($E = 65$ GPa, $\nu = 0.3$, $\sigma_Y = 1.53$ GPa), anisotropic (with material property I in Table 4-3, isotropic HAP with transverse mineral elements), and discrete model (with isotropic HAP and transverse mineral elements). Consistent with the experimental data, the predicted load-depth curves for all material constitutive behaviors also indicate no directional dependence which implies apparent isotropy of the indentation modulus and hardness, despite the anisotropic microstructure of the ganoine. However, interestingly, the local stress and strain distributions and underlying deformation mechanisms are found to depend on the material behavior (discussed next).

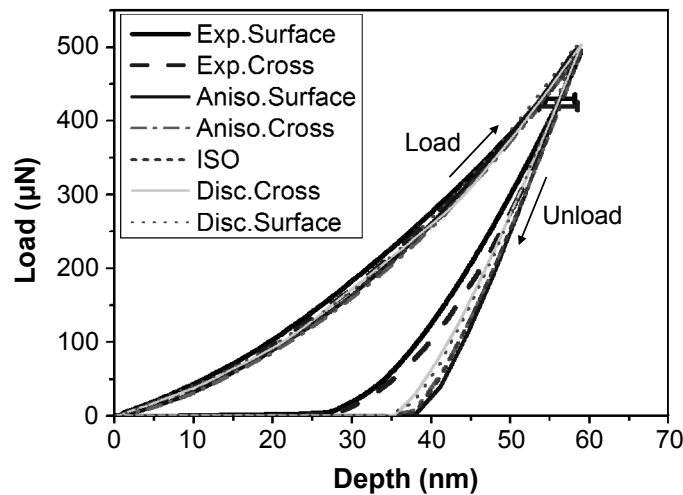


Figure 4-9. Comparison of the average experimental curves to the FEA simulation curves obtained by virtual nanoindentation after fully anisotropic material set for ganoine was determined using the proper nanomechanical models; (i) isotropic properties with $E = 65$ GPa, $\nu = 0.3$, and $\sigma_Y = 1.53$ GPa (Table 4-2, row 1), (ii) anisotropic properties using data obtained from the nanomechanical modeling with isotropic HAP crystals (Table 4-3, row 1) and transverse mineral elements [RVE (A)], and (iii) discrete model assuming isotropic HAP rods. *Figure by L. Wang*

During indentation, the indenter induces inhomogeneous multiaxial stress and strain fields in the ganoine. The stress and strain fields are governed by the constitutive response of the ganoine and the geometry of the indenter. Figures 4-10 and 4-11 show the stress and plastic strain contours for the simulated nanoindentations into the top surface and the cross section of the ganoine, respectively. The simulation results are compared

for three representations of the constitutive behavior of the ganoine: isotropic ($E = 65$ GPa, $\nu = 0.3$, $\sigma_Y = 1.53$ GPa, Table 4-2), anisotropic (with isotropic HAP, material property I in Table 4-3), and discrete model (with isotropic HAP). Indentation is, in general, accommodated by compressing material beneath the indenter and shearing material away from under the indenter. Comparing the anisotropic ganoine case to the isotropic case, the compressive normal stress (S33) is seen to occur in a narrower band and to extend to deeper depths for the anisotropic cases (Fig. 4-10) as a consequence of the more diffuse plastic shear straining (PE13) that occurs at lower shear stress (S13) for the anisotropic case (a direct consequence of the reduced shear yield stress). This has consequences in how load and deformation are transmitted to the underlying dentin layer during microindentation of the multilayered scale (discussed in section 4.3.2.3). Comparison of the continuum constitutive behavior of ganoine to the discrete structural representation of ganoine reveals the role of the rod-like nanostructure during nanoindentation. Large bands of intense plastic deformation are observed in the organic matrix layers and yielding of the HAP rods and transverse mineral elements also takes place and contributes to the total energy dissipation density (see the shear contours of Figs. 4-10 and 4-11). While the discrete model captures the separate contributions of the HAP prisms and the organic layers, comparison of the discrete model results to the continuum anisotropic model results shows very similar overall contours even for this nanoindentation where the length scale of the rod width is of order the depth of the indentation; hence, these results also show that use of the continuum level anisotropic model will be sufficient to capture the anisotropic behavior of the ganoine during the larger length scale microindentation simulations. It should be noted that anisotropy of HAP doesn't affect the stress/strain distributions in these nanoindentation models because the geometric anisotropy of the ganoine structure and constitutive HAP and organic behaviors dominate the stress and strain fields. Table 4-4 compares O-P modulus and O-P hardness values obtained from experimental measurements and from the simulations assuming the different material models including isotropic model, anisotropic model (with material properties I or HAP isotropic and II or HAP anisotropic, Table 4-3), and discrete model. The effective indentation modulus and hardness were reduced from the load-depth curves using the Oliver-Pharr method (which assumes the material to be homogeneous and isotropic).

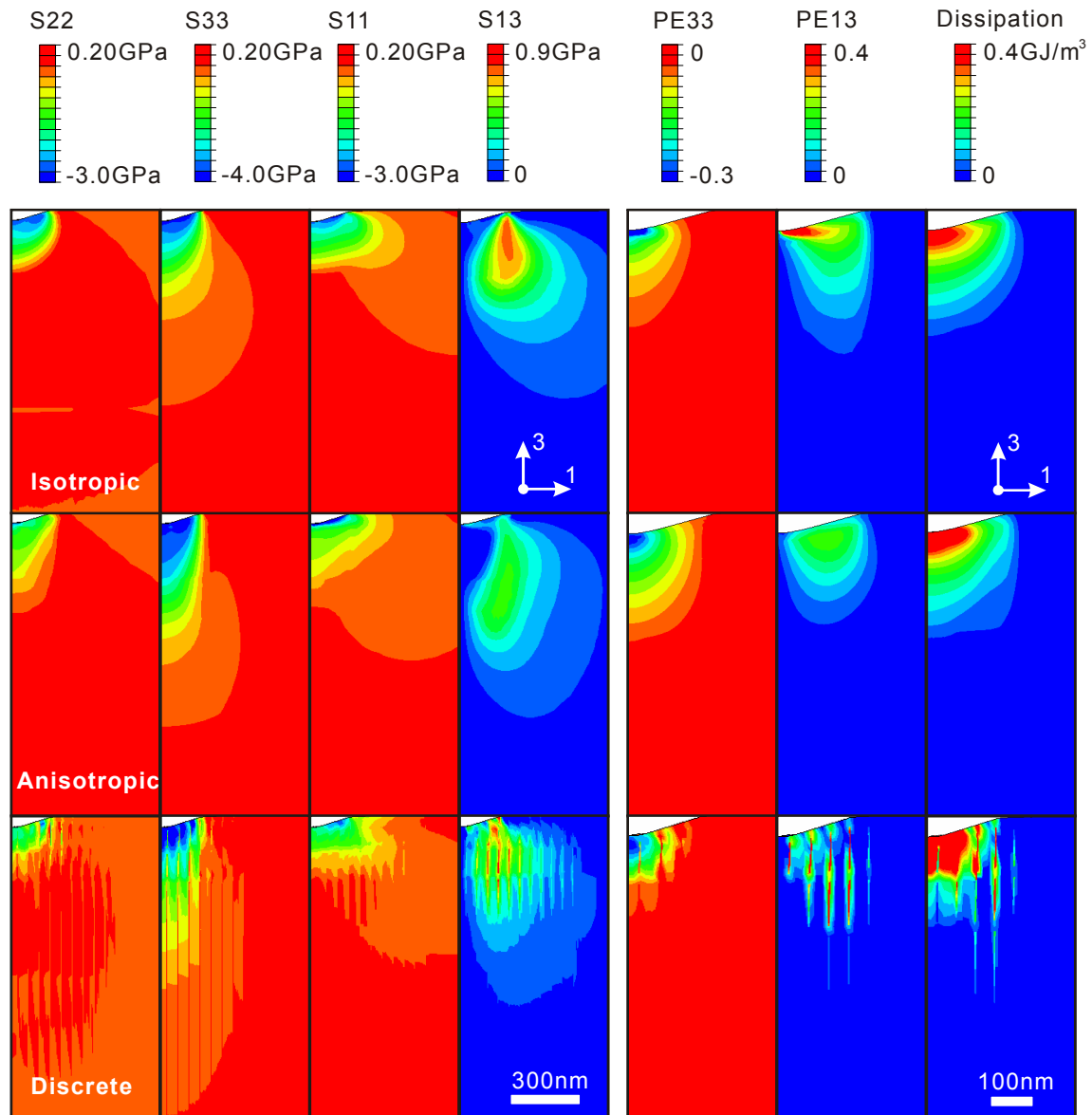


Figure 4-10. Simulation contours of stress distributions, plastic strain, and energy dissipation of the goiaine layer under nanoindentation with the loading parallel to the surface normal (3-axis). A comparison is shown between isotropic (Table 4-2, row 1), anisotropic (isotropic HAP crystals, Table 4-3, row 1), and transverse mineral elements [RVE (A), Fig. 4-5b], and discrete models for 3D nanoindentation as indicated in Fig. 4-6b. *Figure by L. Wang*

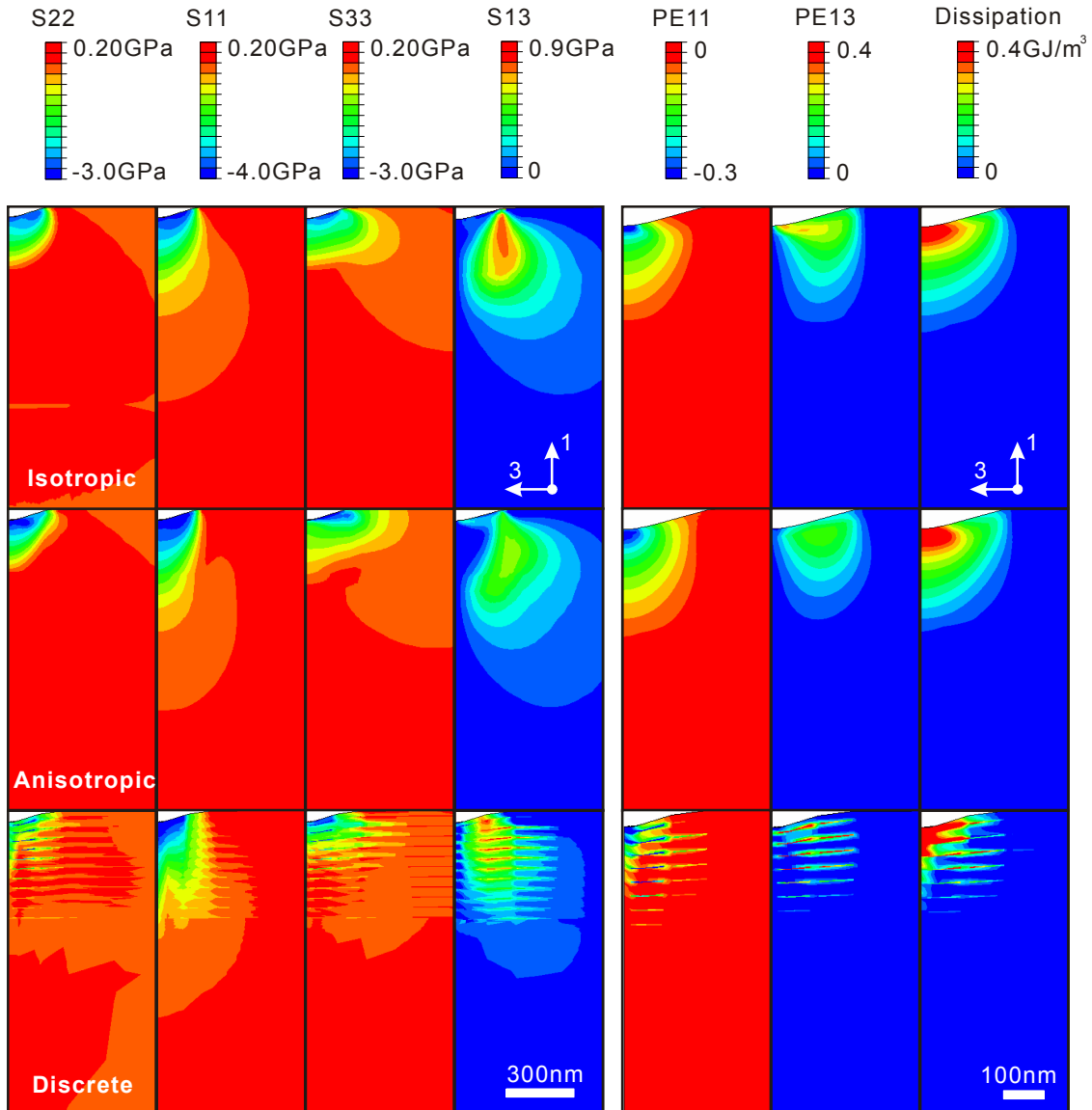


Figure 4-11. Simulation contours of stress distributions, plastic strain, and energy dissipation of the ganoine layer under nanoindentation with the loading perpendicular to the surface normal (along the 1-axis). A comparison is shown between isotropic (Table 4-2, row 1), anisotropic (isotropic HAP crystals, Table 4-3, row 1), and transverse mineral elements [RVE (A), Fig. 4-5b], and discrete models for 3D nanoindentation as indicated in Fig. 4-6b. *Figure by L. Wang*

Table 4-4. O-P modulus and hardness obtained from experimental measurements and various simulation models: isotropic model, anisotropic model I where the HAP crystal is isotropic, anisotropic model II where the HAP crystal is anisotropic, and the discrete model.

	O-P Modulus (GPa)		O-P Hardness (GPa)	
	Surface	Cross-section	Surface	Cross-section
Experiments	74.8 ± 5.0	75.1 ± 8.2	3.98 ± 0.27	3.92 ± 0.34
Isotropic model	75.6	75.6	3.70	3.70
Anisotropic model I (HAP isotropic)	77.2	70.8	3.86	3.86
Anisotropic model II (HAP anisotropic)	67.7	74.2	3.82	3.92
Discrete model	74.2	70.9	4.12	4.04

4.3.2.3 Microindentation model

The role of ganoine anisotropy in the larger length-scale biomechanical microindentation of the multilayered *P. senegalus* scale was explored by constructing two FEA models, the ‘isotropic ganoine multilayer (IGML)’ (described and reported in Chapter 3) and the ‘anisotropic ganoine multilayer (AGML)’ as described in the methods section. We recall that, despite the clearly anisotropic microstructure of the ganoine layer, the experimental and predicted load-depth behavior and effective indentation modulus and indentation hardness were found to be independent of direction and to also be independent of constitutive representation (i.e., whether ganoine was modeled as isotropic, anisotropic or discrete). However, the underlying deformation mechanisms, revealed in the simulations, had subtle dependencies on anisotropy. Here, the effect of ganoine anisotropy on the effective microindentation behavior of the multilayered structure is explored—examining the effect of both the effective force-depth behavior and the underlying deformation and dissipation mechanisms.

Figure 4-12a depicts the load-depth curves of the IGML and AGML multilayered structures to/from maximum loads of 0.5 and 1N, compared with a simulation of monolithic isotropic ganoine (MIG). As also previously found in the ganoine nanoindentation cases, the IGML and AGML load-depth behaviors and corresponding reduced material properties were found to be nearly identical, giving effective modulus (~30 GPa), effective microhardness (~1.7 to 1.8 GPa), and energy dissipation (1.6 to ~1.65 μJ). Indentation to/from different maximum load levels reveals the effective microhardness for both models to decrease nonlinearly with increasing indentation load

(Fig. 4-12b). The predicted microhardness values show good agreement with the experimentally measured Vicker's microhardness (Fig. 4-12b). In the 0.25 and 0.5 N microindentation experiments, most samples (~9 of 10 indents) were observed to deform in an elastic-plastic manner with no surface cracks observed (Chapter 3). In the 1N cases, ~50% of the samples (~ 5 of 10 indents) showed circumferential surface cracking (Chapter 3). Circumferential cracks were observed in all of the 2N cases (10 of 10 indents, Chapter 3).

The predicted effective total energy dissipation (area between the loading and unloading force-depth curves, e.g. Fig. 4-12a) as a function of maximum indentation load for the IGML and AGML microlayered models were found to be indistinguishable, increasing nonlinearly from close to that of the MIG model at small maximum loads to values nearly double the dissipation energy of the MIG at a maximum load of 1N (Fig. 4-12c). The evolution of the work of indentation during loading and unloading of the entire multilayered structure, as well as the individual contributions of the ganoine and the dentin layers is provided in Fig. 4-12d. For both the IGML and AGML systems, a nonlinear increase in the work of indentation is observed during loading followed by the elastic recovery during unloading. Although both the IGML and AGML microlayered models exhibit a similar total energy evolution during loading and unloading, locally the ganoine and dentin layers in the IGML and the AGML structures contribute differently to the total energy evolution. During the early loading stage ($< 0.25\text{N}$), the ganoine and dentin layers of AGML case partition energy in a manner similar to that found in the IGML case. However, as the load is further increased, the energy dissipation contribution of the dentin in the AGML case begins to increase more significantly than in the IGML case (because of dentin yielding earlier and, hence, greater plastic dissipation in dentin in the AGML case). At a maximum load of 1N, the contributions to the work of indentation from ganoine and from dentin differ for the IGML and AGML models; with dentin in the AGML case contributing 60% of the dissipation compared to 50% for the IGML case.

Contour plots of stress and plastic strain are shown in Fig. 4-13 when fully loaded to 1N and after fully unloaded from 1N. The normal stress fields, S22 and S33, of the anisotropic ganoine layer are observed to be higher in magnitude than those of the isotropic ganoine layer, whereas the shear stress (S23) magnitudes (~540MPa) in the AGML are significantly lower than that of ganoine in the "IGML" model (~ 900 MPa); these contrasts are a direct consequence of the anisotropic ganoine possessing enhanced axial moduli, enhanced axial yield stresses, reduced shear moduli and reduced shear yield stresses compared with the isotropic ganoine. Therefore, although the stress contours of the two multilayered systems show different stress fields and magnitudes in stress component levels, the two multilayered systems in the end achieve similar effective load-depth behaviors, microhardness values, and energy dissipation.

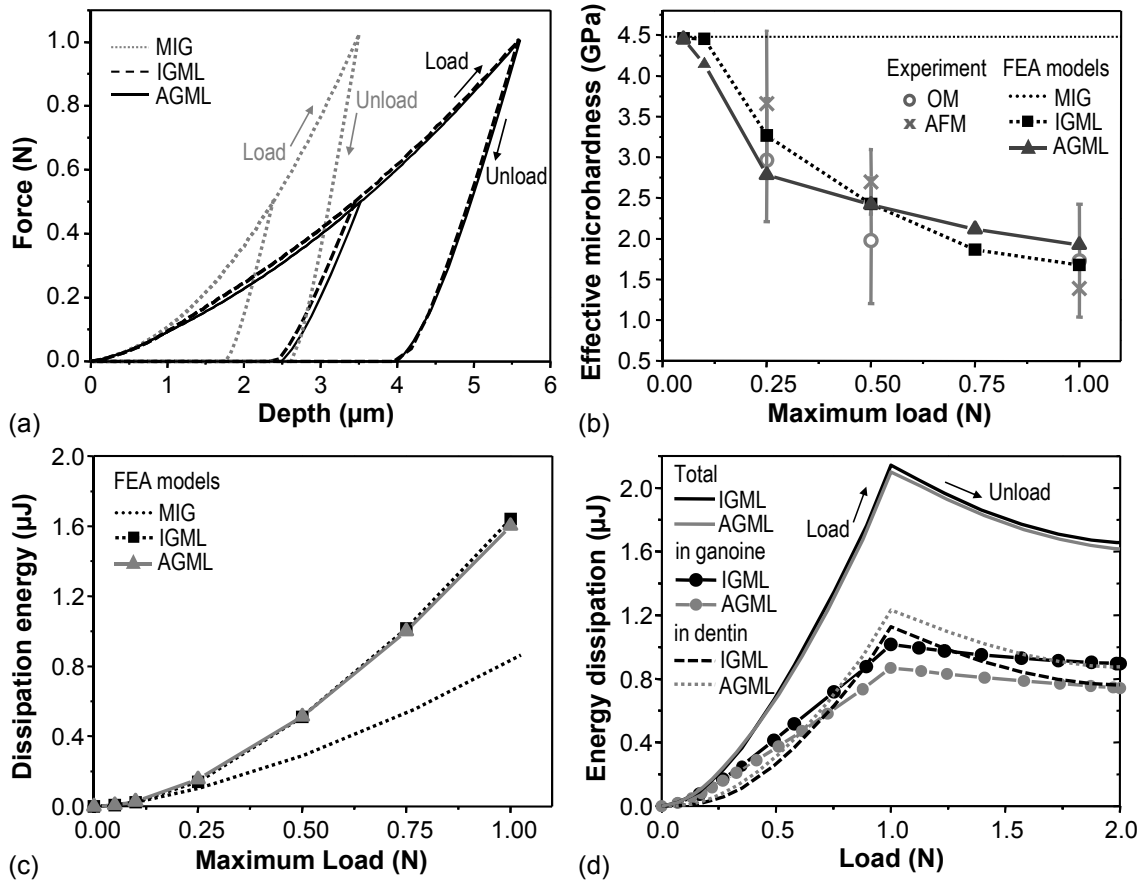


Figure 4-12. Predictions of effective microindentation mechanical properties of the multilayered *P. senegalus* scale; notations include ‘monolithic isotropic ganoine’ or MIG, ‘isotropic ganoine multilayer’ or IGML, and ‘anisotropic ganoine multilayer’ or AGML, respectively; (a) simulated microindentation load-versus-depth curves, (b) simulated effective microhardness compared to experimentally measured values as a function of maximum indentation load (reported in Chapter 3, Fig. 3-5c) where OM and AFM indicate optical microscope and atomic force microscope, respectively, that were used to measure the residual area after unloading, (c) simulated effective energy dissipation as a function of maximum indentation load where dissipation energy was calculated as the area between the loading and unloading portion of the load-depth curves in microindentation after unloading and (d) simulated energy evolution (the work of indentation) of the whole multilayered structure [‘IGML’ (black lines) and ‘AGML’ (gray lines)], and the individual ganoine and dentin layers as a function of applied load up to a 1N maximum load, as well as on unloading.

In Chapter 3, the 1N maximum load experiments and simulations were used to estimate a maximum normal stress brittle-failure condition for the ganoine: experimentally, circumferential cracks were observed on the surface during microhardness experiments at 1N maximum load. Using contours of the radial stress, S22, at this maximum load level gave a critical normal stress of ~ 1.1 GPa from results of our “IGML” model. Here, contours of S22 from both the “IGML” and the “AGML” multilayer models compute similar magnitudes in tensile S22 surface values whereas their circumferential stress fields (S33) exhibit compressive values at the surface, again suggesting that circumferential cracking on the surface is the preferred failure mode in these multilayered systems. These results also indicate that the anisotropy is not the primary structural property governing this aspect of the surface stress distribution, but instead it is the contrast in the ganoine and dentin behavior that gives this mechanical behavior. However, after circumferential cracking is initiated, the anisotropic rod-like structure will facilitate the propagation vertically which is more advantageous since it can be arrested by the energy dissipating dentin layer, rather than propagating in other directions (e.g. radially), which could lead to catastrophic structural failure in other multilayer systems. Additionally, the interfacial normal and shear stresses in the AGML case are known to be important factors in the interfacial failure in other multilayer systems, e.g. ref. (Jayachandran et al., 1995). The interfacial (and close to interface) shear stresses in the AGML case (S23) are found to be significantly lower during loading than those in the IGML case, a consequence of the lower shear yield stress (τ_{y23}). Upon unloading, a peak shear stress is present on the interface of both cases but is lower in the AGML case. The lower shear yield stress (τ_{y23}) of the anisotropic ganoine is seen to favor plastic deformation via plastic shear straining (comparing PE23 contours) and thus to also promote a radial spreading of plastic deformation in the ganoine layer (PE23 contours) compared with more direct compression straining (comparing PE33 contours). The different plastic straining of the ganoine layer in the two cases is observed to result in different curvatures of the ganoine/dentin interface. The plasticity in the underlying dentin layer is spatially more elongated in depth for the anisotropic ganoine compared to the isotropic case (PE23, PE33).

Contours of plastic energy dissipation density (energy dissipation per unit volume) and energy dissipation magnitude (dissipation energy accounting for the volume over which the dissipation occurs—although this is mesh dependent quantity, it provides a useful comparison between cases when the same mesh is used) for each layer when fully unloaded are depicted in Fig. 4-14. The contours of each layer are scaled differently in order to better reveal the contributions of each layer. Plastic energy dissipation density contours in Fig. 4-14a show the overall plastic deformation reveals less plasticity in the ganoine layer accompanied by greater dissipation in the dentin layer for the AGML case. In the energy dissipation magnitude contours (Fig. 4-14b), taking into account the volume

over which the energy dissipation occurs enables assessment of where energy dissipation is dominant within a layer as well as comparison between cases. In particular, the dissipation magnitude contours capture the increased volume of points as one moves radially outward away from the axis of indentation, revealing the dominant dissipation role around the perimeter of indentation; these contours also reveal the more prevalent dissipation role of dentin in the AGML and of ganoine in the IGML. Both forms of energy contours reflect greater energy dissipation in dentin in the AGML (Fig. 4-12).

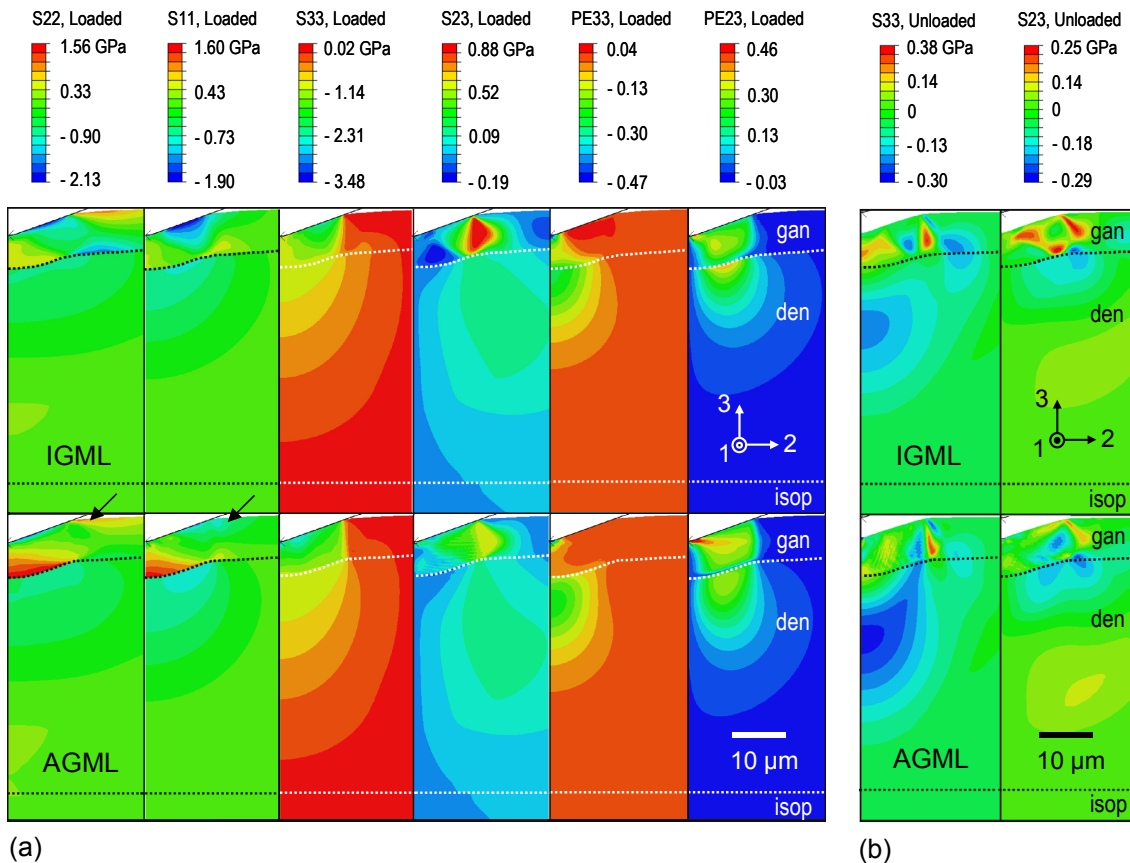


Figure 4-13. Simulation contours of stress and plastic strain of *P. senegalus* scale under microindentation. FEA predictions of (a) S11, S22, S23, S33 and plastic stain, PE33 and PE23 at a maximum depth when fully loaded and (b) S23, S33 when fully unloaded for the two ‘isotropic ganoine multilayer’ or IGML, and ‘anisotropic ganoine multilayer’ or AGML, multilayered models. Arrows indicate the location of surface stresses on the stress contours, S11 and S22.

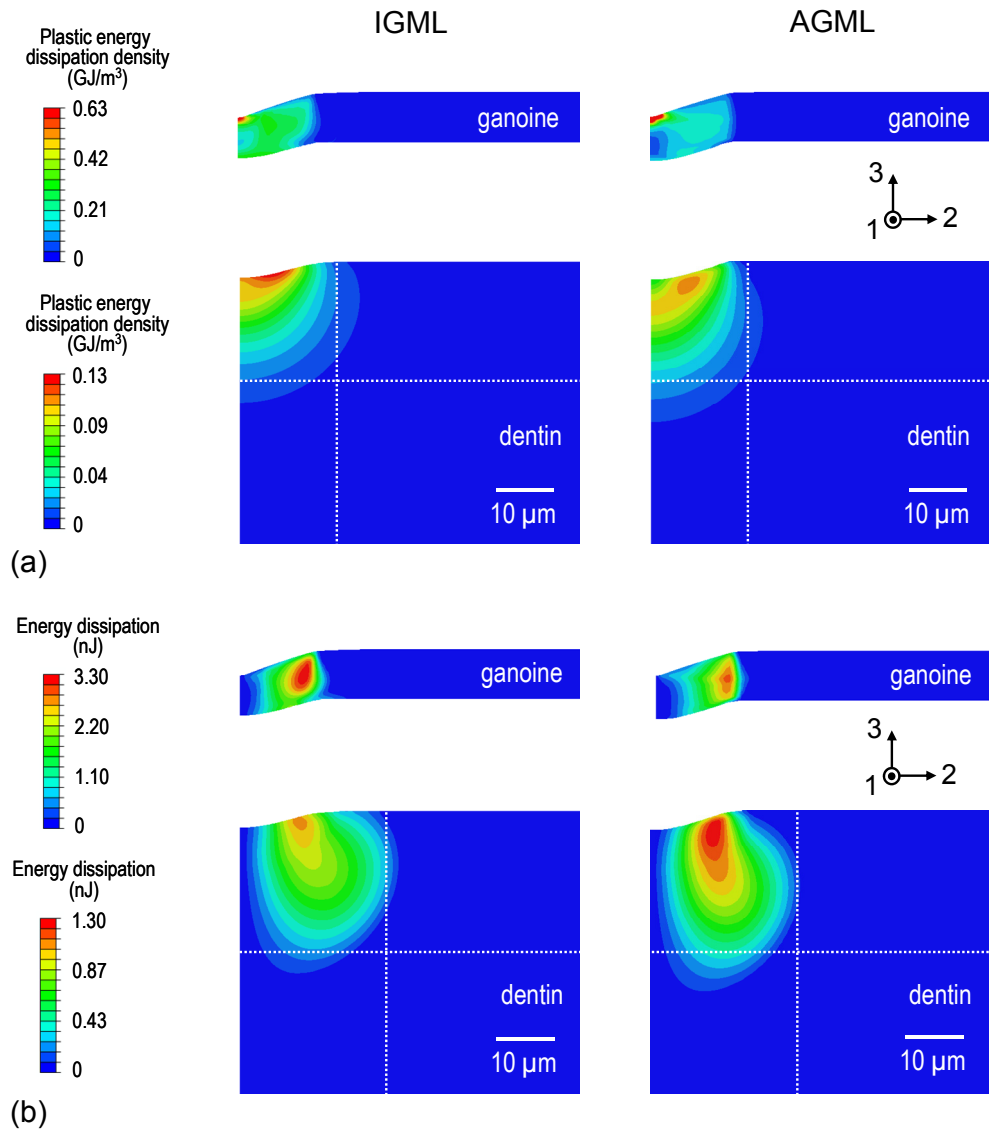


Figure 4-14. Simulation contours of plastic energy dissipation density and energy dissipation of *P. senegalus* scale under microindentation at 1N maximum load after fully unloaded. FEA predictions of (a) plastic energy dissipation density, (b) energy dissipation magnitude in separated ganoine and dentin layers with the proper scale bar for two ‘IGML’ and ‘AGML’ multilayered structures. The energy dissipation magnitude contour reflects the volumetric effect on energy dissipation density. The guidelines (white dashed lines on energy contours of dentin layers) show energy dissipation in dentin of the AGML model covers larger area (elongated shape) with relatively higher density or magnitude than in that of the IGML model.

4.4. Discussion

A major threat to *P. senegalus* is biting from its own species, which takes place during territorial fighting and feeding (Markey et al., 2006). The tooth geometry and size makes these penetration biting events approximately analogous to microindentation. In Chapter 3, I demonstrated that the micron-scale multilayered structure acts to provide an initially stiff and hard line of defense against low load events, governed by the behavior of the outer ganoine layer. This behavior transitions to an increasingly dissipative response with increasing penetration load where the underlying softer dentin provides the dissipation. The goal of this study was to investigate the role of the anisotropy of the prismatic-like ganoine structure in this load-dependent penetration resistance of the entire multilayered armor. The design principles identified are expected to be relevant to a broad array of biological exoskeletons, since many different species exhibit similar nanostructures in their outermost layers (Parsons, 1982; Chateigner et al., 2000; Rodriguez-Navarro et al., 2006; Al-Sawalmih et al., 2008), and to the development of improved biologically-inspired structural materials.

Nanomechanical modeling results revealed that the unique structure of ganoine does indeed result in elastic-plastic mechanical anisotropy (transverse isotropy) of the composite material. The balance between smaller length scale "inherent" anisotropy of the crystalline HAP and larger length scale "geometric" anisotropy of the HAP-organic composite nanostructure was explored, a topic relevant for most biological composites. Since the HAP crystal is modestly anisotropic, it has a minimal effect on the anisotropic elastic-plastic response of the ganoine composite, which is rather dominated by geometric anisotropy of the composite nanostructure. This minimal effect of HAP anisotropy has also been reported on other composite systems (e.g. bone (Fritsch and Hellmich, 2007)). Enhanced axial and transverse moduli (and yield stresses) and significantly reduced shear moduli (and yield stresses) were predicted. The shear moduli also correlate with reduced off-axis axial moduli and yield stresses, which result from shear deformation of the organic interlayers. Transverse mineral elements, representing mineral prism-to-prism surface roughness and adjacent rod interlocking, provided significant resistance to shear.

Even though ganoine was determined to be mechanically anisotropic, surprisingly this constitutive behavior does not result in a direction-dependent indentation modulus or hardness. However, comparison of simulations assuming an isotropic ganoine stress-strain behavior with those assuming anisotropic stress-strain behavior did result in different local stress and strain fields accommodating the imposed indentation; in particular, greater shearing at lower shear stresses are found to accommodate indentation in the anisotropic material, and the compressive stress and strain fields directly beneath the indenter are found to extend to deeper depths. These observations suggest that the

anisotropic ganoine behavior may influence the behavior of the multilayered scale during microindentation.

To understand the role of ganoine anisotropy in resisting penetrating bite attacks, the behavior of the multilayered structure during microindentation assuming an isotropic ganoine layer was compared with that obtained assuming the ganoine layer to be anisotropic. At low indentation loads ($< 0.15\text{N}$), the indentation modulus and hardness for the multilayered structure are close to that of monolithic ganoine in both experiments and modeling (this is the case whether ganoine is modeled as isotropic or anisotropic). The indentation modulus and hardness are found to decrease with an increase in indentation load – this is found in both experiments and in simulations; the simulation results for these properties being independent of the anisotropic vs. isotropic representation of the ganoine. However, as with the nanoindentation simulations, the spatial distributions of local stress and strain differed between the anisotropic and isotropic cases. With increasing indentation load, the anisotropic stiffness and yield strength of the ganoine were found to promote a greater level of plastic deformation in the dentin in radial and depth directions. This increasing volume of plastic deformation in the underlying dentin layer promotes the use of the dentin layer as the major dissipation element in the multilayered structure, in essence "protecting" the outer ganoine layer by limiting the strain and stress that the ganoine will experience. The anisotropic constitutive behavior of the ganoine also spreads the plastic deformation and energy dissipation to a greater volume of material overall.

Both the isotropic and anisotropic treatments of the ganoine stress-strain behavior are found to result in tensile radial stress field (S22) and compressive circumferential stress field (S11) on the surface around the indentation perimeter; the tensile radial stress promotes circumferential cracking whereas the compressive circumferential stress suppresses radial cracking. Circumferential cracking would be a favored failure event since it would be localized to the indentation region and would not be a propagating failure across the scale. Moreover, the discrete prism structure does provide the fracture pathway (normal to the scale surface between HAP rods) after initiation of circumferential cracks. Such failure pathways lead to the localized damage in the ganoine and then are easily arrested by the ductile dentin layer. These different findings of the underlying deformation, stress and dissipation behavior when the outer layer is slightly anisotropic rather than isotropic motivates a more thorough parametric investigation into the potential of using and designing anisotropic outer (and inner) layers to promote dissipation during penetration events.

The results in this Chapter on ganoine are expected to be relevant as well for human teeth. Human teeth are composed of an outer enamel layer that has a composite HAP-organic structure of similar composition to ganoine also followed by an underlying dentin layer. However, there are a number of notable differences between these two

systems; (1) the ganoine thickness is $\sim 10 \mu\text{m}$ in contrast to tooth enamel which has thickness $> \text{mm}$ presumably due to the larger length scale of the mastication process and (2) tooth enamel has an additional higher order level of anisotropic structural geometric hierarchy whereby the HAP nanocrystals self-assemble into micrometer-scale "rods" with their long axes perpendicular to the tooth surface (absent in ganoine). The anisotropic elastic and plastic properties reported in this Chapter for ganoine are consistent with those previously reported for intra-rod tooth enamel (Habelitz et al., 2001). Larger length scale mechanical experiments involving multiple rods revealed amplified mechanical anisotropy compared to the constituent enamel composite, elucidating the effect of the second level of structural hierarchy (Spears, 1997; Habelitz et al., 2001). An FEA study considered different anisotropy ratios for enamel and demonstrated that an increasing anisotropic nature would more directly transfer stresses to underlying compliant dentine and thus to reduce the potential for tooth fracture (Spears et al., 1993), a result consistent with those obtained for ganoine here. Lastly, similar to ganoine, this anisotropic structure is assumed to be beneficial in directing crack propagation vertically down into the dentin to be arrested by the dentin layer (Hassan et al., 1981).

This study emphasizes the critical importance of the anisotropy of structural biological material at the nanoscale and the microscale in achieving macroscale mechanical properties to optimize penetration resistance and protection. The fundamental understanding of this optimization in a multilayered natural armor structure suggests an anisotropic design to improve biomimetic systems.

4.5. Conclusion

Biological materials have developed hierarchical and heterogeneous material nanostructures and microstructures to provide protection against various environmental threats that, in turn, provide bioinspired clues to improve human body armor. In this study, a multiscale experimental and computational approach has been presented to investigate the anisotropic design principles of a ganoid scale of an ancient fish, *Polypterus senegalus*, which possesses unique quad-layered structure at the micron scale with nanostructural material constituting each layer. The elastic-plastic anisotropy of the outmost ganoine layer enhances the load-dependent penetration resistance of the multilayered armor compared with the isotropic ganoine layer by (i) retaining the effective indentation modulus and hardness properties, (ii) enhancing the transmission of stress and dissipation to the underlying dentin layer, (iii) lowering the ganoine/dentin interfacial stresses and hence reducing any propensity toward delamination, (iv) retaining the suppression of catastrophic radial surface cracking, and favoring localized circumferential cracking, and (v) providing discrete structural pathways (interprism) for circumferential cracks to propagate normal to the surface for easy arrest by the

underlying dentin layer and hence containing damage locally. These results indicate the potential to use anisotropy of the individual layers as a means for design optimization of hierarchically structured material systems for dissipative armor.

Chapter 5.

Threat-Protection Mechanism of an Armored Fish

This chapter was published as a regular article: J.H. Song, C. Ortiz, and M.C. Boyce, 'Threat-protection mechanics of an armored fish.' *Journal of the Mechanical Behavior of Biomedical Materials*, 2011. 4: p. 699-712.

5.1. Introduction

It has been hypothesized that environmental and predatory threats are critical factors in the protective functional design of biological exoskeletons or “natural armor,” which arise through processes such as co-evolution and escalation between predators and prey (Vermeij, 1987; Dietl and Kelley, 2002). Evidence for predator-related exoskeletal damage and repair has been reported extensively in the literature (Reimchen, 1988; Mapes et al., 1989; Mcclanahan and Muthiga, 1989; Kodera, 1994; Zuschin et al., 2003). One common mode of predator attack is a localized penetration or indentation into an exoskeleton with a relatively sharper object (e.g., tooth, claw, beak, shell protrusions, etc.) (Vermeij, 1987; Zuschin et al., 2003) that induces complex local multiaxial stress and strain concentrations, which dissipate the energy of the attack and can potentially lead to failure or fracture of the armor and/or threat as shown in Chapter 3 and 4 of this thesis. Biological armor systems utilize many protective structural design principles to resist penetrating attacks (Ortiz and Boyce, 2008) including, for example, local energy-dissipating inorganic-organic composite nano- and microstructures (Currey and Taylor, 1974; Wang et al., 2001), multilayering and grading in Chapter 3 of this thesis, crystallographic and shape-based anisotropy in Chapter 4 of this thesis, fibrous reinforcement at joints (Gemballa and Bartsch, 2002), and active offensive components (Hoogland et al., 1956; Reimchen, 1988). Mechanical strategies for resisting penetration include: (1) armor which defeats the threat via deforming and/or fracturing the threat, (2) armor which dissipates the energy of the threat via plastic deformation and/or a multitude of cracking events within the armor, and (3) a combination of both of these mechanisms.

In all cases, the armor design also needs to minimize the back-displacements and stress levels transmitted to the underlying soft tissues and vital organs of the animal. In this study, the role of geometry, microstructure and deformability of the threat relative to that of the armor on threat-protection mechanical interactions (e.g. penetration resistance, energy dissipation, local stress/strain distributions, etc.) are investigated. Such a mechanistic approach to predator-prey offensive and defensive interactions is relevant to elucidating universal principles that direct ecological interactions and resulting evolutionary outcomes (Herre, 1999; Dietl and Kelley, 2002) and also can provide insights in the design of synthetic protective systems.

The model system chosen is the “living fossil” fish *Polypterus senegalus*, which possesses a particularly robust and efficient ganoid armor (Sire, 1990) and belongs to the ancient family *Polypteridae*, which appeared 96 Myr ago in the Cretaceous period (Daget et al., 2001) and still lives today at the bottom of freshwater, muddy shallows and estuaries in Africa (Kodera, 1994). A “living fossil” generally refers to a living species that is anatomically similar to fossil species which first appeared early in the history of the lineage (when the ancestral form first appeared before evolutionary processes), thereby having experienced a long period of evolutionary stasis (Eldredge and Stanley, 1984). The existence of living fossils has been attributed to stabilizing selection caused by particular ecological circumstances, e.g. reduced competition, isolated habitats, etc. (Darwin, 1859). The scales of *P. senegalus* retain many characteristics of the dermal armor of ancient palaeoniscoids and possess four mineralized layers (from outer to inner); ganoine, dentin, isopedine, and bone (Sire, 1994; Sire et al., 2009). The ganoid armor of ancient palaeoniscoids would have been exposed to the many large extinct invertebrate predators that existed at that time (Romer, 1933; Ørving, 1968; Brett and Walker, 2002). Today, the primary predators of *P. senegalus* are known to be members of its own species and its carnivorous vertebrate relatives (Romer, 1933). Powerful bites occur during territorial fighting and feeding, posing significant risk of injury (Kodera, 1994) (Fig. 5-1a and 5-1b). *P. senegalus* feeds opportunistically, and easily preys on many animals it can fit in its mouth via biting, including fishes (including its own species), frogs, insects, and crustaceans (Kodera, 1994; Raji et al., 2003) (Fig. 5-1c to 5-1e).

Here, the interaction between the ganoid armor of *P. senegalus* and one of its current most aggressive threats, a biting attack by its own species, was simulated and studied. The teeth of *P. senegalus* are monocuspid and conical, and consist of two layers—a cone of dentin capped by an outer layer of enameloid (Fig. 5-2a and 5-2b) (Clemen et al., 1998; Wacker et al., 2001), both of which are comparable in material properties and length scale to the dentin and ganoine layers of the armor. In Chapter 3 and 4 of this thesis, a predatory toothed bite on a *P. senegalus* ganoid scale was approximated computationally using finite element analysis (FEA) where the tooth was idealized by an infinitely rigid indenter and penetrated into an individual quad-layered

scale. In this Chapter, the indenter is modeled as deformable, thereby more closely representing the true biological threat, i.e. the tooth. The geometry of the indenter was approximated from optical and scanning electron microscopy images of typical *P. senegalus* teeth. The role of the threat (tooth) geometry (e.g. end-radius, cone angle), multi-layered structure, and deformability on penetration resistance, local stress and strain distributions, and energy dissipation of both the threat and armor during a virtual predatory biting attack was parametrically studied. Based on these results, a summary of advantageous and disadvantageous design strategies for the offensive threat and defensive protection was formulated. Studies of such a system where the offensive threat and defensive protection are comparable may lead to insights into adaptive phenotypic plasticity of tooth and scale microstructure, predator-prey “adaptive stalemates” and the so-called evolutionary “arms race” (Agrawal, 2001; Dietl and Kelley, 2002).

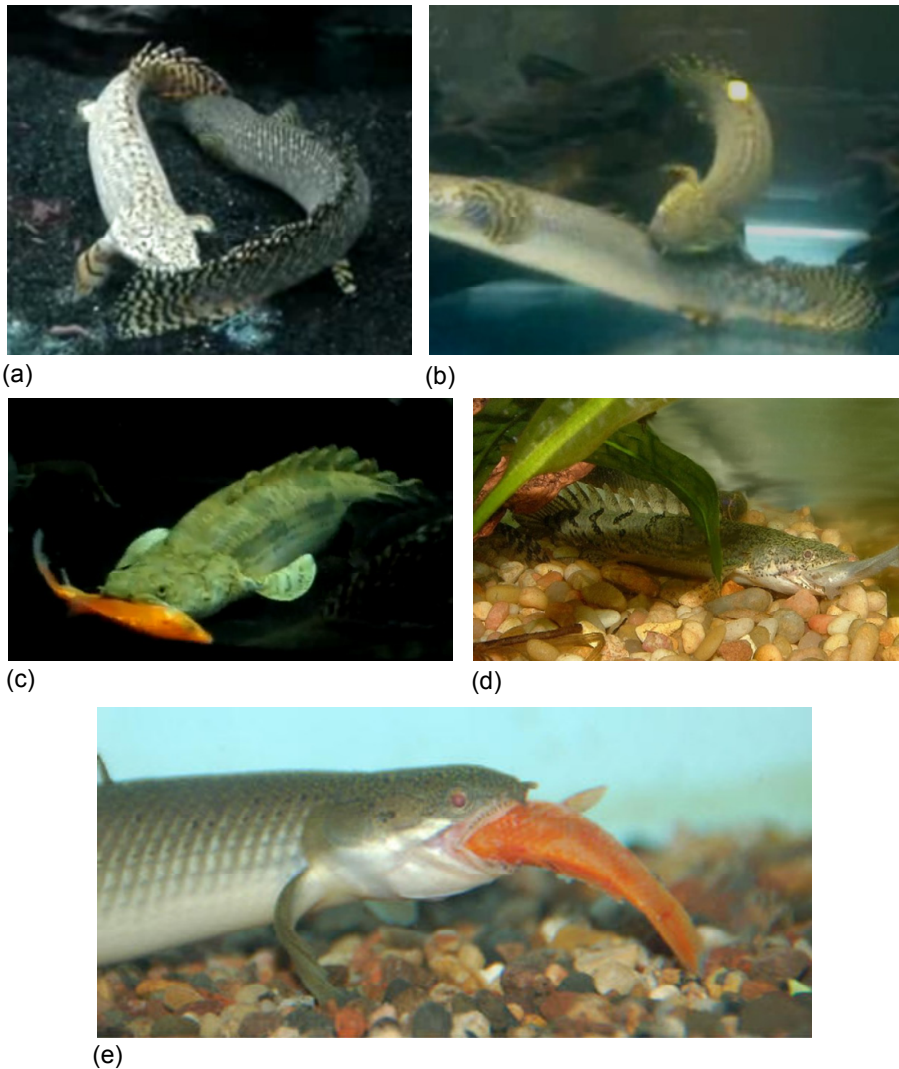


Figure 5-1. Territorial and predatory fighting between two comparable sized *Polypterus* or between species and its prey fish; (a) Ornate Polypterus Aggression Video³, (b) Polypterus fights Video⁴, (c) *olypterus endlicheri endlicheri* vs. *Polypterus ornatipinnis* Video⁵, (d) Polypterus predation⁶ and (e) Miscellaneous Oddballs VII: Bichirs do eat fish⁷.

³ YouTube, Web, created on Sept. 20, 2007, Last accessed on April 18, 2011, <http://www.youtube.com/watch?v=51oLrMBqN3s&feature=related>

⁴ YouTube, Web, created on July 17, 2007, Last accessed on April 18, 2011, <http://www.youtube.com/watch?v=q1Xc2WP7KQk&feature=related>

⁵ YouTube, Web, created on Jan. 14, 2007, Last accessed on April 18, 2011, <http://www.youtube.com/watch?v=um3P1-GUYy0&NR=1>

⁶ 55 for senegal bichir and others, African theme, Aquatic Predators: Primitive Fishes Forum - Bichirs and Rope Fish, Web, created on Nov. 18, 2005, Last accessed on April 18, 2011, <http://www.freewebs.com/fruitbat/Pdelhezi22b.jpg>,

⁷ Aqualand, Last accessed on April 18, 2011, <http://aqualandpetsplus.com/Oddbal1410.jpg>

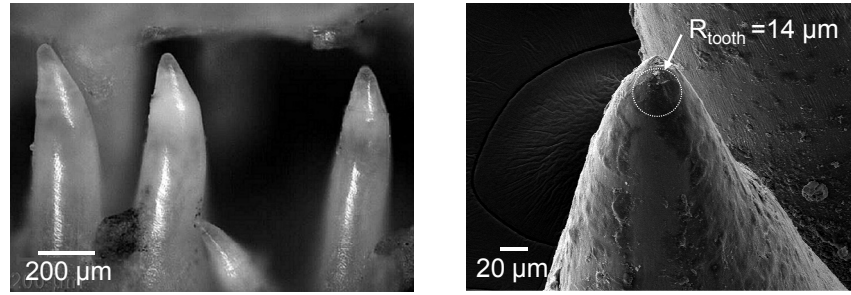
5.2. Methods

5.2.1. Geometry of *P. senegalus* Teeth

The skull of a *P. senegalus* specimen was extracted from its dead body (total length: ~ 15 cm). Teeth from the upper jaw were imaged using an optical microscope (Eclipse L150, Nikon, Japan) and scanning electron microscope (SEM, JEOL JSM 6060, Peabody, MA). SEM samples were imaged at a 10 kV acceleration voltage after fixation on a steel support using conductive tape and sputter-coating with ~ 5 nm of gold-palladium in a Denton Vacuum Desk II (Moorestown, NJ). The geometry of 25 of teeth from the premaxillary and maxillary regions was quantified using optical and SEM images including; half cone angles, height, end radii, and shape. The teeth were found to be monocuspid and conical (Fig. 5-2a and 5-2b). The tooth-end radii (measured by SEM) varied between 5 and 30 μm (mean \pm standard deviation = $11.7 \pm 5.6 \mu\text{m}$ (Fig. 5-2c), a half cone angle ($\theta/2$) of $\sim 22^\circ$, and a total height of $\sim 500 \mu\text{m}$ (Fig. 5-2d). *P. senegalus* teeth consist of two material layers—a cone of dentin capped by an outer layer of enameloid, equal to approximately a quarter of the total tooth height, thickness $\sim 100 \mu\text{m}$ (Clemen et al., 1998; Wacker et al., 2001). Enameloid is a hypermineralized tissue containing non-prismatic, apatite crystals and a collagenous organic matrix (Sasagawa et al., 2009). Ganoine is also hypermineralized (<5 wt.% organic) and enamel-like, but in contrast to enameloid, is non-collagenous and composed of rod-like and pseudoprismatic apatite crystallites aligning perpendicular to the surface (Ørvig, 1967; Meunier, 1987; Sasagawa et al., 2009; Sire et al., 2009). Dentin consists of collagen and apatite with a reduced mineral content ($\sim 70\text{-}80 \text{ wt}\%$) relative to enamel and ganoine (Driessens and Verbeeck, 1990; Daget et al., 2001; Sire et al., 2009).

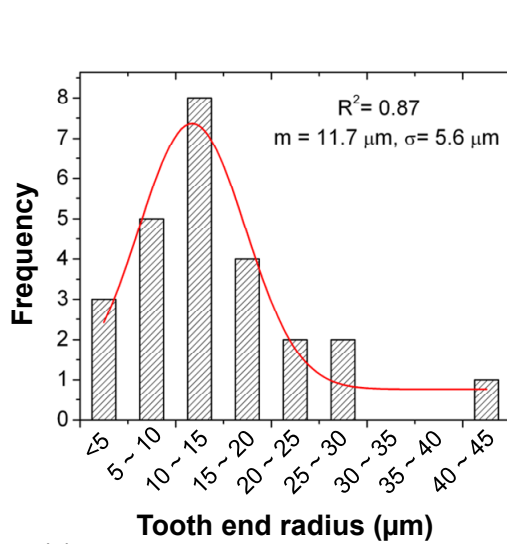
5.2.1. Finite Element Analysis (FEA) Model

A hypothetical predatory biting attack of an individual *P. senegalus* tooth penetrating into an individual *P. senegalus* ganoid scale was simulated using nonlinear finite element analysis (FEA) (ABAQUS/standard). Biting events were modeled as a penetration of an indenter into an individual quad-layered scale; the symmetry of the geometry and materials allowed for axisymmetric simulations (Fig. 5-3). Indentations were carried out for loading and unloading up to maximum loads of 0.25, 0.50, and 0.75 N. This virtual microindentation induces complex local multiaxial stress and strain concentrations in both armor and threat systems as shown in Fig. 5-3a. I note that microcracking was not a dominant mechanism of plasticity in the ganoine and dentin for maximum loads below 1 N and cracking is observed to initiate above $\sim 1 \text{ N}$ in Vickers

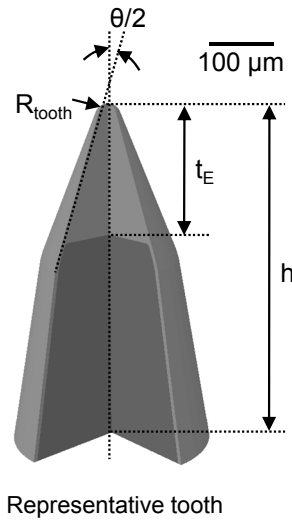


(a)

(b)



(c)



(d)

Figure 5-2. Morphology and geometric information of 25 *P. senegalus* teeth extracted from the premaxillary and maxillary regions; (a) optical microscope image of typical teeth of *P. senegalus* (b) scanning electron microscope (SEM) image of a typical individual *P. senegalus* tooth, showing an end radius of $\sim 14 \mu\text{m}$, (c) tooth end-radius distribution of *P. senegalus* measured using SEM images (n = number of teeth, m = mean, σ = standard deviation) and (d) a representative tooth of *P. senegalus* with definitions of relevant geometric parameters which include a half cone angle ($\theta/2$) of $\sim 22^\circ$, an end radius (R_{tooth}) of $\sim 12 \mu\text{m}$, enamel thickness, t_E , of $\sim 100 \mu\text{m}$ (Wacker et al., 2001) and a height, h , of $\sim 500 \mu\text{m}$.

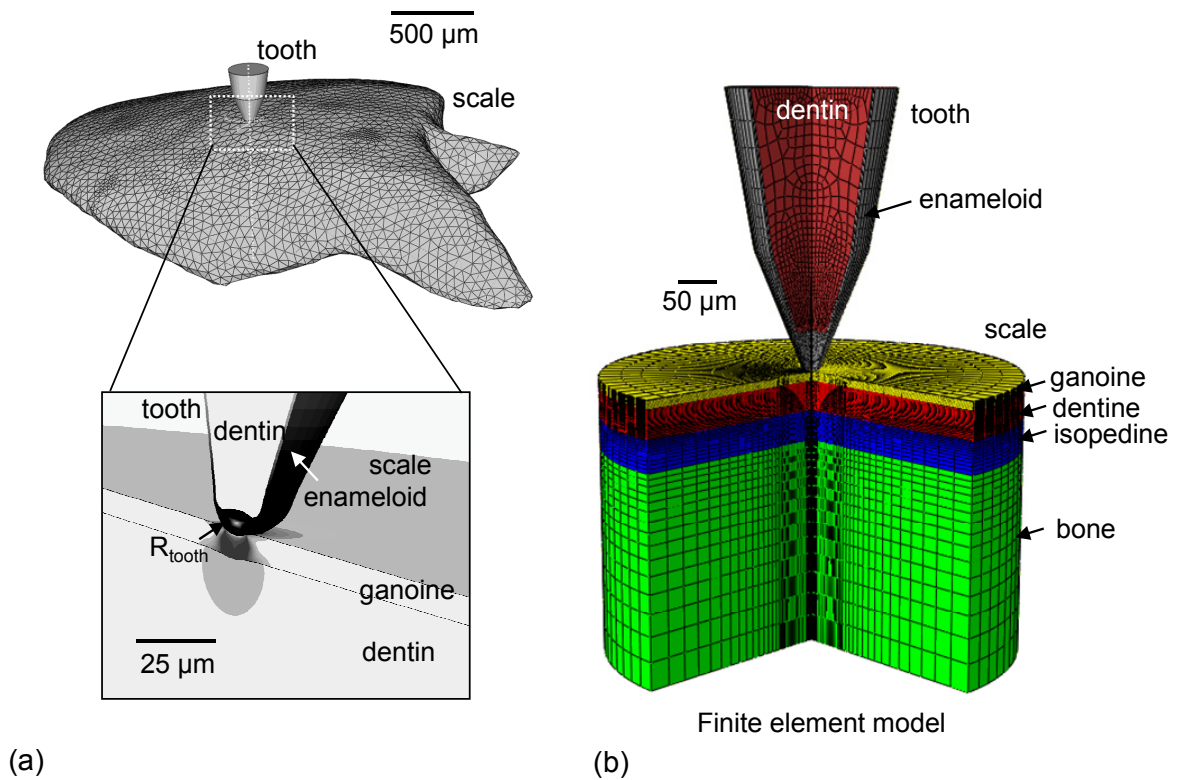


Figure 5-3. Two-dimensional axisymmetric finite element analysis (FEA) models of the *P. senegalus* scale and its corresponding hypothetical threat; (a) Schematic diagram of an individual tooth-armored scale system in *P. senegalus* during a hypothetical predatory attack illustrating the development of a multiaxial stress field in both the tooth and scale due to the localized penetration and (b) schematic of the corresponding finite element model approximating the hypothetical predatory attack shown in part (a).

microindentation as indicated in Chapter 3 of this thesis. Hence, these loads were chosen for comparison of the effect of a deformable tooth compared to a rigid indenter. Theoretical *P. senegalus* biting force was predicted and proposed in Appendix C.

Scale model. The quad-layered ganoine / dentin / isopedine / bone scale was constructed as described in methods section of Chapter 3 and 4 (Fig. 5-3b). The bottom surface of the scale model was fixed with no movement allowed and the individual scale was assumed to be large enough as compared to local penetration events (Fig. 5-3a and 5-3b). The interfaces between material layers were assumed to be perfectly bonded with a discrete change in mechanical properties from one layer to another (Appendix C). The modulus (E) and yield stress (σ_Y) values used for each of the four scale material layers were quantified via nanoindentation and FEA methods (Table 5-1). In this Chapter, I focused on penetrations which were localized to the top two layers of the armor for the load levels examined here and do not extended deeply into the third or fourth layers (isopedine and bone) of the armor.

Table 5-1. Mechanical properties and layer thickness values utilized in finite element simulations of predatory toothed biting attack on individual quad-layered ganoid scale of *P. senegalus* including the modulus (E), yield stress (σ_Y) and layer thickness values used for each of the four scale and two tooth material layers. For the parametric studies, E, σ_Y , and the thickness of tooth enameloid was varied (Habelitz et al., 2001; Marshall et al., 2001; Lippert et al., 2004; Mahoney et al., 2004; Sasagawa et al., 2009; Sire et al., 2009).

Material Layers of FEA models		Modulus, E (GPa)	Yield stress, σ_Y (GPa)	Layer thickness (μm)
Scale	Ganoine (outer)	55	2	12
	Dentin	25	0.4	45
	Isopedine	14.5	0.22	43
	Bone (inner)	13.5	0.18	300
Monolithic rigid tooth	Enameloid	Rigid	Rigid	400
Monolithic deformable tooth	Enameloid	25 - 165	0.4 - 6	400
Bi-layered, deformable tooth	Enameloid	55, 110	2, 4	0 - 400
	Dentin	25	0.4	0 - 400

Tooth model. A representative model tooth was constructed (Fig. 5-2d and 5-3b) based on the geometric information provided by optical microscopy and SEM (i.e. half cone angle of 22° and a height of $500 \mu\text{m}$). Indentation was applied by displacing the distal end of the tooth (distal to the contact with the scale) towards the scale whereupon the proximal tip of the tooth penetrated into the scale and, depending on the tooth structure and properties, also began to deform. Parametric studies were carried out on the role of the tooth deformability, multi-layered structure, size scale and geometry on penetration resistance, local stress and strain distributions, and energy dissipation of both the tooth and armor during indentation (Table 5-1).

First, virtual indentations were performed by a perfectly rigid tooth for three different tooth end-radii ($R_{\text{tooth}} = 5, 15$ and $30 \mu\text{m}$), chosen based on the experimentally measured distribution (Fig. 5-1c). The tooth end radii were normalized by the ganoine thickness ($t_G = 12 \mu\text{m}$) utilized in the scale model ($R_{\text{tooth}}^n = R_{\text{tooth}}/t_G$). Axisymmetric rigid elements (RAX2 in ABAQUS element library) were used for the perfectly rigid tooth model.

The second set of simulations were carried out using a deformable monolithic enameloid tooth that were entirely composed of enamel and the mechanical properties of the tooth enameloid (subscript “E”) were varied while the ganoine (subscript “G”) mechanical properties were kept constant. The ratio of the mechanical properties of the tooth enameloid relative to the ganoine layer of the scale model is henceforth defined as the mechanical ratio, $M_{E/G}$, and is applied to both the modulus and the yield stress (i.e.,

$M_{E/G}$ = modulus ratio = E_E/E_G = yield stress ratio = $\sigma_{Y,E}/\sigma_{Y,G}$). $M_{E/G}$ was varied between 0.5 and 3, where the ratio of modulus to yield strength for the enameloid was maintained at a constant of $E/\sigma_Y = 22.5$ which was assumed to be equivalent to the experimentally determined E/σ_Y of ganoine in Chapter 3. Three different tooth end radii ($R_{\text{tooth}} = 5, 15$ and $30 \mu\text{m}$) were employed for these simulations as well.

The third set of simulations involved a bi-layered tooth model composed of an outer enameloid layer and inner dentin layer. The mechanical properties of the enameloid were, firstly, assumed to be the same as the scale ganoine ($E = 55 \text{ GPa}$, $\sigma_Y = 2 \text{ GPa}$) and, secondly, $2\times$ stiffer and harder than the scale ganoine. The tooth dentin was assumed to have the same mechanical properties as the scale dentin ($E = 25 \text{ GPa}$, $\sigma_Y = 400 \text{ MPa}$). The thickness of the enameloid layer was varied from 3 to $200 \mu\text{m}$ and was normalized by the ganoine thickness ($t_G = 12 \mu\text{m}$), $t_{E/G}$. For the deformable tooth models, four-node bilinear axisymmetric quadrilateral elements (CAX4R or CAX4H in ABAQUS element library) were used with optimized meshes for convergence.

Simulated indentation curves were reported as load versus normalized penetration depth where the penetration depth was normalized by the ganoine thickness (h/t_G). Total energy dissipation by all layers (for the loads and depths used in these simulations, only ganoine and dentin contribute) was calculated, which corresponds to the area between the loading and unloading curves. Energy dissipation contributed by each layer was also calculated. Local stress and strain contours in the vicinity of the contact point were reported as Von Mises stress (S), circumferential stress (S11), radial stress (S22), interfacial normal stress (S33), shear stress (S23) (GPa), as well as the equivalent plastic strain (PEEQ).

5.3. Results

5.3.1. The Effect of Tooth End-Radius

The sharpness of the tooth relative to the ganoine layer was found to have a large effect on penetration resistance into the quad-layered scale as evidenced by the force versus depth curves (Fig. 5-4a), the corresponding energy dissipation (Fig. 5-4b), and the details of the stress and strain distributions (Figs. 5-5 and 5-6). As the tooth becomes sharper for the given half cone angle of 22 degrees, in particular as the tooth end-radius is reduced below the thickness of ganoine layer ($R_{\text{tooth}} = 5 \mu\text{m}$, $R_{\text{tooth}}^n = 0.42$), the penetration depth increases dramatically allowing the tooth penetration to essentially reach the underlying dentin layer as the load approaches 1N (Fig. 5-4a). At the loads and depths utilized in these simulations, only the two outer layers of the scale (ganoine and dentin) contribute to the deformation (as will be shown later in the contours of Fig. 5-5). The total energy dissipation (Fig. 5-4b, symbols) increases with maximum load with the

rate of increase (nonlinearity of Fig. 5-4b, symbols) enhanced by tooth sharpness. The contributions of the energy dissipation for the ganoine and dentin layers depend on the tooth end-radius (Fig. 5-4b, bar graphs), with the dentin contributing relatively more for blunter teeth. The deformation by the blunt indenter results in a more pressure-dominated uniaxial strain-like condition beneath the indenter as compared to the condition of ganoine shearing away and up along the side of the cone angle for the case of the sharp indenter. This difference leads to greater plastic deformation of the ganoine with the sharp indenter which in turn leads to greater energy dissipation needed to accommodate a sharp indentation at any given load compared to the blunt indenters (where the same load by a blunt indenter is accommodated more by a nearly uniaxial strain-like compression condition beneath the indenter which is a pressure dominated condition with less dissipation). The relative contribution of dentin to the energy dissipation increases with increasing indenter radius – again, due to a more dominant pressure as opposed to shear condition in the ganoine when the indenter radius is blunt, e.g. for the blunt tooth ($R_{\text{tooth}}^n = 2.5$) at a 0.75 N maximum load, the dentin dissipates approximately 30% of the total energy as compared to 8% for the sharper tooth ($R_{\text{tooth}}^n = 0.42$). However, in all cases the ganoine dissipates more energy via plastic deformation than the dentin.

The calculated contours for stress and plastic equivalent strain are shown in Fig. 5-5 when fully loaded to 0.75 N (S, S33, S23) and after fully unloaded from 0.75 N (PEEQ). The sharpest tooth ($R_{\text{tooth}} = 5 \mu\text{m}$, $R_{\text{tooth}}^n = 0.42$) induces larger areas and greater magnitudes of stress and plastic deformation in both the ganoine and dentin layers compared to the blunter teeth (Fig. 5-5), clearly showing the shearing up the side of the cone angle leading to a pileup on the surface (S23 contours). The blunt indenters instead give a more compression (S33 contours) and pressure focused deformation beneath the indenter with a single vertical shear band emanating into the ganoine from the edge of the contact. The unloaded plastic strain contours reveal the extensive permanent impression from the sharp indenter (again indicative of the plasticity-dominated nature of this indentation), as compared to the near full recovery from the blunt indentation (where the stress field was more pressure dominated and elastic as compared to one of extensive plastic shear). The plastic strain contours also reveal the plasticity in both the ganoine and the dentin, again showing the dentin to contribute to the dissipation and its relative contribution to be greater during the blunt indentation. Lastly, for the sharpest tooth, the surface tensile circumferential stress (S11) and compressive radial stress (S22) are conducive to initiating disadvantageous radial cracking around the pile-up of the surface (Fig. 6). In contrast, the blunter teeth ($R_{\text{tooth}} = 15 \mu\text{m}$, $R_{\text{tooth}}^n = 1.25$ and $R_{\text{tooth}} = 30 \mu\text{m}$, $R_{\text{tooth}}^n = 2.5$) exhibit a sign inversion with compressive circumferential (S11) and tensile radial (S22) stress fields on the ganoine surface, promoting more advantageous circumferential cracking (Fig. 5-6).

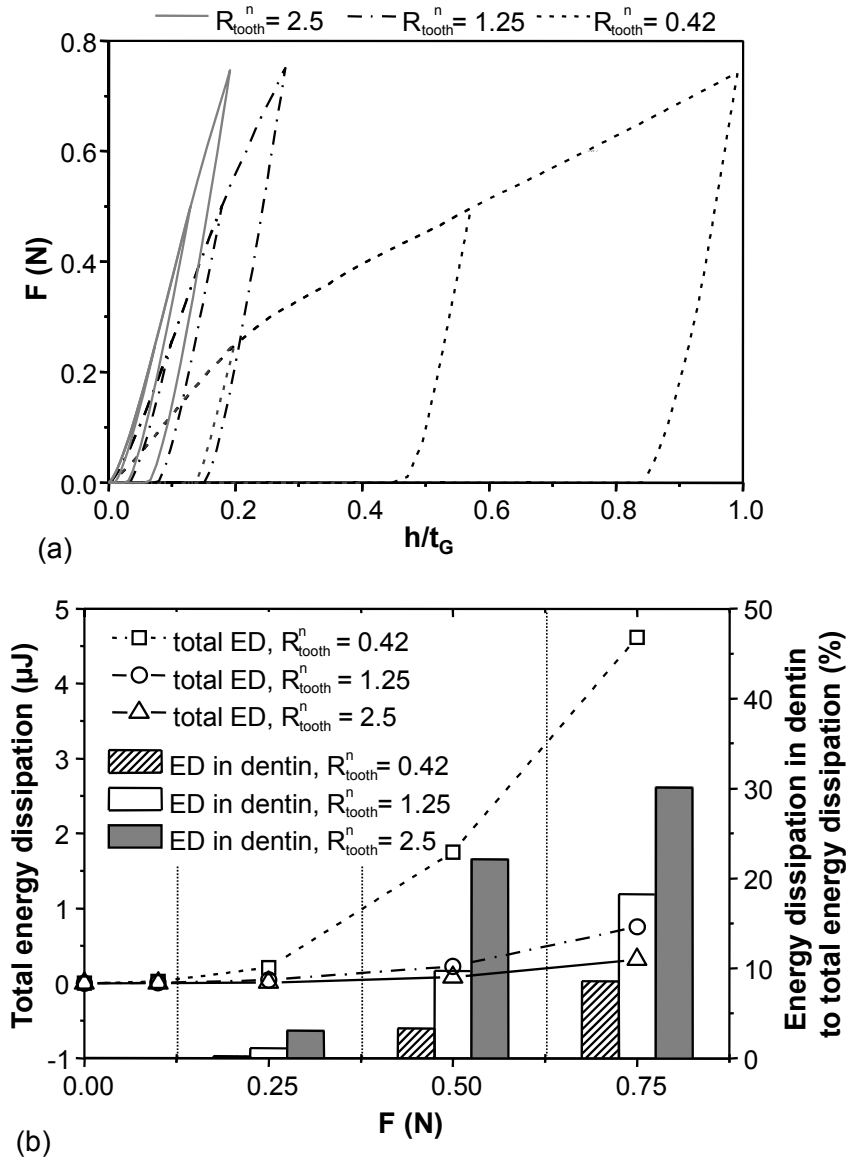


Figure 5-4. The effect of tooth end-radius (for a perfectly rigid tooth) on the predicted finite element simulations of the load-bearing capability and energy dissipation within an individual armored scale of *P. senegalus* during a virtual microindentation, simulating a hypothetical generic biting predatory attack; (a) Load-depth curves for three different tooth end-radii as a function of maximum load and (b) total energy dissipation and energy dissipation in the secondary underlying dentin layer as a function of maximum load for three different tooth end-radii. Tooth end-radii and penetration depths were normalized by the thickness of the outer ganoine layer.

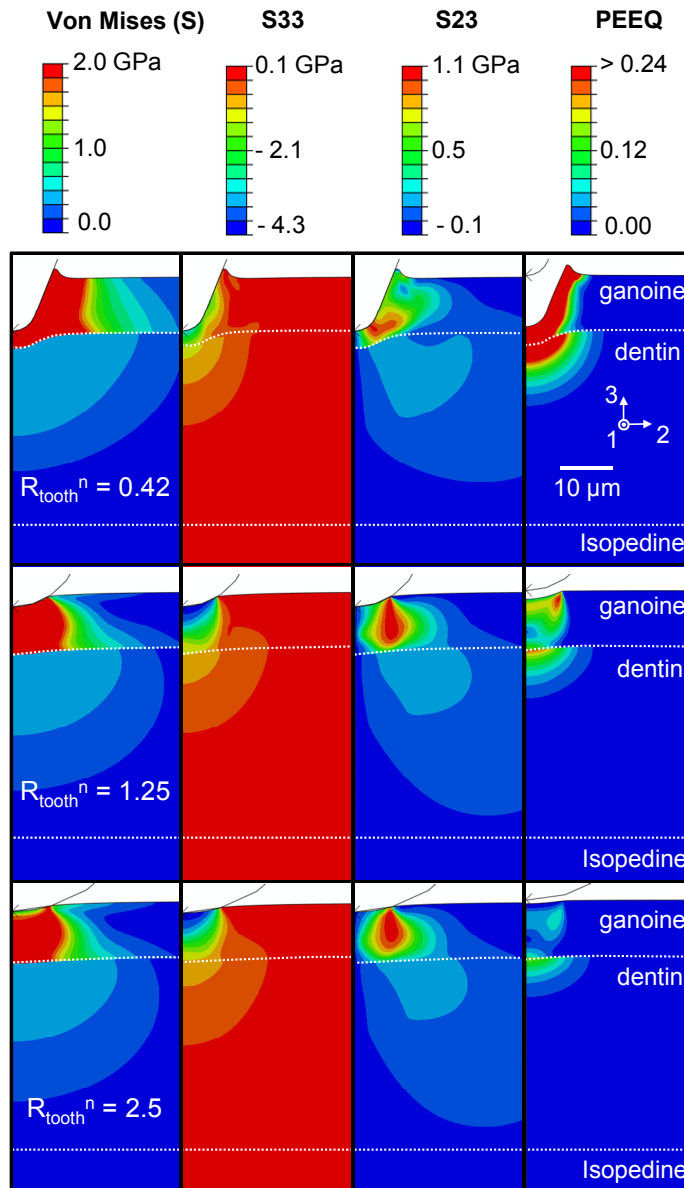


Figure 5-5. The effect of tooth end-radius (for a perfectly rigid tooth) on the predicted finite element simulations of the contours of stress and plastic strain within an individual armored scale of *P. senegalus* during a virtual microindentation, simulating a hypothetical generic predatory biting attack; Von Mises stress (S), S33, S23 (fully loaded to 0.75N) and fully unloaded from 0.75N (PEEQ), for tooth end radii of 0.42, 1.25, and 2.5 normalized by the thickness of the outer ganoine layer.

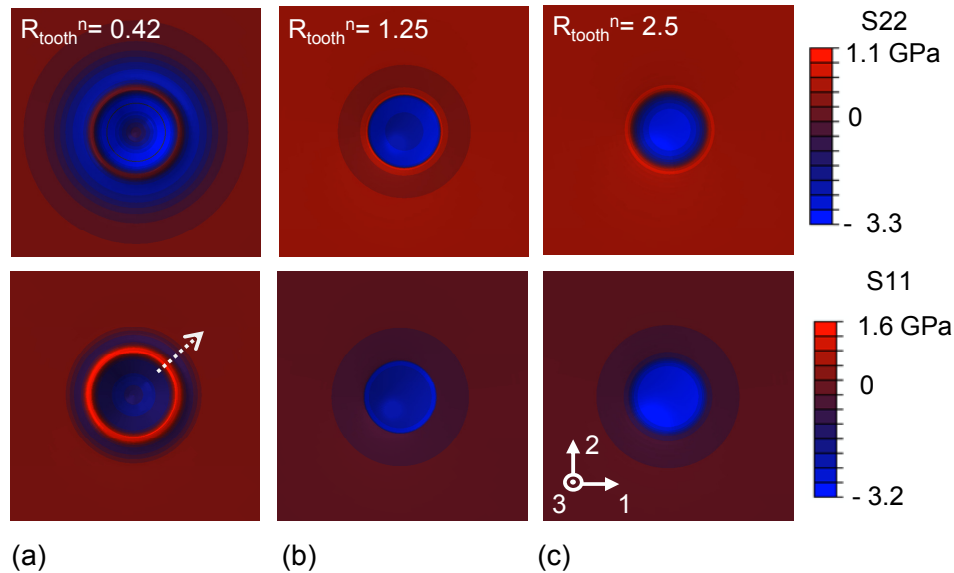


Figure 5-6. The effect of tooth end-radius (for a perfectly rigid tooth) on the predicted finite element simulations of the contours of circumferential (S11) and radial stresses (S22) within an individual armored scale of *P. senegalus* during a virtual microindentation, simulating a hypothetical generic predatory biting attack; S11, S22 viewed along the indentation loading 3-axis for normalized tooth end radii of 0.42 (a), 1.25 (b) and 2.5 (c) at a maximum load of 0.75N.

5.3.2. The Effect of the Mechanical Properties of the Tooth Enameloid

The microstructure and mechanical properties of the teeth are in reality comparable to those of the scale and are, thus, expected to have an important role on the mechanics of penetration events. The effect of allowing the tooth to be deformable has significant consequences on the force vs. indentation “depth” results (Fig. 5-7a), the depth of the tooth penetration into the scale (Fig 5-7b), the energy dissipation (Fig. 5-7c) and the nature of the stress and strain distributions (Fig 5-8). Fig. 5-7a shows that an increase in deformability of the tooth (i.e., as the mechanical ratio $M_{E/G}$ decreases) results in a marked shift of force vs. depth (i.e. penetration into the scale) curves to the left along the depth axis relative to the perfectly rigid tooth (Fig. 5-7a, black solid line) where, for any given indentation load, there is a dramatic reduction in penetration of the tooth into the scale as $M_{E/G}$ is reduced. However, this decrease is accompanied by an increase in the total deformation (displacement of the top surface of the tooth which includes the effects of penetration into the scale as well as tooth deformation) where Fig. 5-7a, solid lines, show a shift of force vs. depth curves to the right along the depth-axis, relative to the perfectly rigid tooth (Fig. 5-7a, black solid line). This trend holds for the sharp as well as the blunt indenters. The penetration into the scale under an indentation load of 0.75N is

shown as a function of $M_{E/G}$ in Fig. 5-7b, revealing that once $M_{E/G}$ is greater than 1.5, the tooth is essentially rigid compared to the scale.

When the tooth enameloid is taken to be more compliant and softer than the ganoine ($M_{E/G} = 0.5$), the tooth exhibits the greatest deformation and exhibits the lowest penetration efficiency into the scale (Fig. 5-7a and 5-8). The scale in turn responds in an elastic manner since the stress levels needed to plastically deform the tooth are never at a high enough a level to yield the ganoine (Fig. 5-8). Therefore, this is a situation where the armor “defeats” the threat and the energy of the biting attack is dissipated by the deformation of the tooth as opposed to the deformation of the armor. When the material properties of the tooth enameloid are comparable to the scale ganoine ($M_{E/G}=1$), the indentation is accommodated by deformation of both the tooth and the scale (Fig. 5-7 and 5-8). In this case, the shape of the tooth leads to a stress field that first yields the tooth (particularly the sharp tooth) whereby, once the tooth has yielded it essentially becomes more compliant than the still elastic ganoine and deformation and dissipation primarily occurs in the tooth. For these reasons, a stronger dependence of the dissipation (Fig. 5-7c) and deformation (Fig. 5-8) are observed on indenter radius for the case of the mechanically matching threat and armor than for the other cases. When $M_{E/G}$ is increased beyond 1.5, the tooth essentially behaves as a rigid entity (Fig. 5-7a to 5-7c; 5-8). Examining the case of $M_{E/G} = 2$, the depth is nearly completely attributable to penetration of the tooth into the scale. Dissipation is all seen to be attributed to plasticity within the scale (with contribution from both the ganoine and the dentin of the scale) and the stress and strain contours are nearly identical to those when the indenter is rigid (this observation holds for the sharp as well as the blunt indenters).

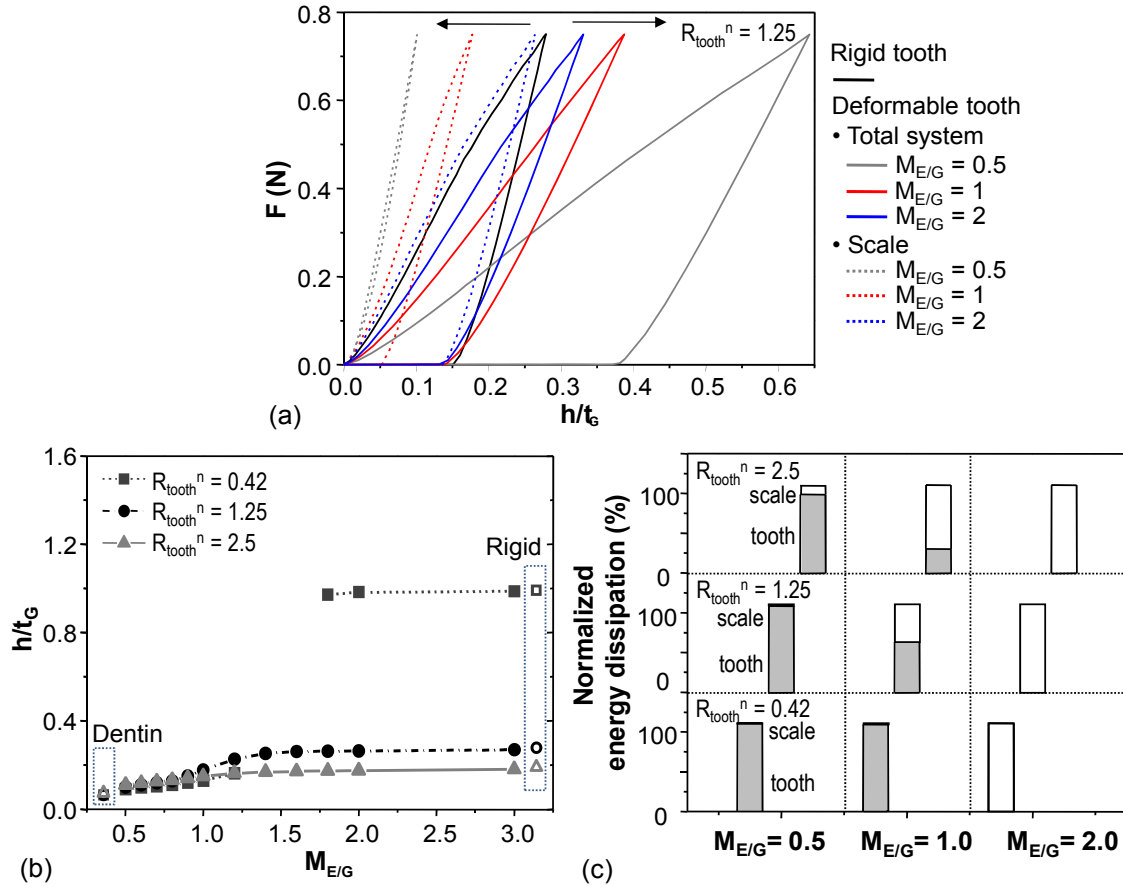


Figure 5-7. The effect of the mechanical properties (indentation stiffness and yield strength) of the tooth enamel relative to the scale ganoine, i.e., the mechanical ratio, $M_{E/G}$, on the normalized penetration depth and energy dissipation, predicted by finite element simulations during a virtual microindentation using a deformable tooth (three different tooth end-radii of 0.42, 1.25 and 2.5), that simulates a hypothetical generic predatory attack of *P. senegalus*; (a) load-depth curves of the whole tooth-scale system and scale system for $M_{E/G} = 0.5, 1$ and 2 at the normalized tooth end radius of 0.42, as compared to rigid tooth case, (b) normalized penetration depth for tooth end radii of 0.42, 1.25 and 2.5 as a function of $M_{E/G}$, and (c) energy dissipation in the tooth and the scale for normalized tooth end-radii of 0.42, 1.25 and 2.5 for $M_{E/G} = 0.5, 1.0, 2.0$. Penetration depths were normalized with the thickness of the ganoine layer and the energy dissipation of each component (tooth, scale) was normalized by the total energy dissipation (tooth + scale).

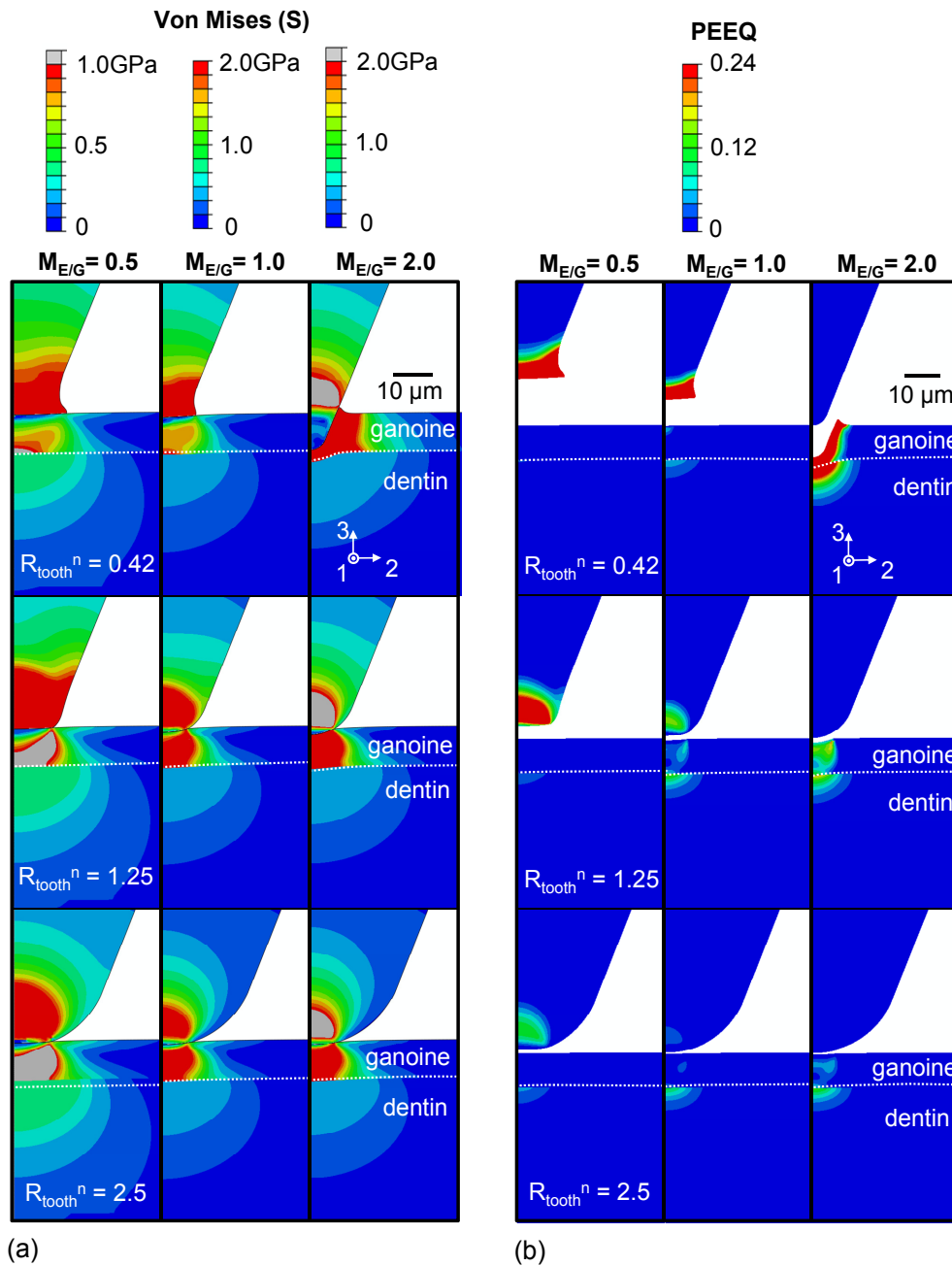


Figure 5-8. The effect of the mechanical properties (indentation stiffness and yield strength) of the tooth enamel relative to the scale ganoine, i.e. the mechanical ratio, $M_{E/G}$, on the simulations of contours of stress and plastic equivalent strain, predicted by a virtual FEA microindentation using a deformable tooth which simulates a hypothetical generic predatory attack of *P. senegalus*: (a) Von Mises stress (S) at a maximum depth when fully loaded, and (b) equivalent plastic strain (PEEQ) when unloaded for three deformable tips with normalized tip end radii of 0.42, 1.25, and 2.5 with respect to the thickness of the ganoine layer at the mechanical ratios of enamel (tip) to ganoine (scale), 0.5, 1.0 and 2.

5.3.3. The Effect of the Tooth Enameloid Thickness

Here, the role of the underlying dentin layer is explored by varying the thickness of the enameloid cap while fixing the external geometry of the tooth. The load-depth indentation behavior for the bi-layered tooth model was observed to depend on the tooth enameloid thickness ($R_{\text{tooth}}^n = 1.25$, $M_{E/G} = 1$ and 2 ; Fig. 5-9a). As the tooth enameloid thickness relative to the ganoine layer is increased ($t_{E/G} = 0.5 \rightarrow 10$), penetration into the scale increases (Fig. 5-9a, dashed lines, shift of force vs. depth curves to the right of the depth-axis) and total deformation (scale penetration plus tooth apex displacement) is reduced (Fig. 5-9a, solid lines, shift of force vs. depth curves to the left of the x-axis) relative to and approaching the all enameloid tooth (Fig. 5-9a, black solid line). Above $t_{E/G} \sim 2$, the tooth penetration into the scale exhibits identical behavior ($R_{\text{tooth}}^n = 1.25$, $M_{E/G} = 1$ and 2 ; Fig. 5-9a) equivalent to that of a monolithic all-enameloid tooth. A quantitative assessment of penetration into the scale (h/t_G) as a function of enameloid thickness ($t_{E/G}$) is provided in Fig. 5-9b. and shows that for $t_{E/G} \leq 2$, the scale penetration depths decrease as the enameloid becomes thinner and for $t_{E/G} > 2$, the penetration events are independent of enameloid thickness and the tooth behaves as a monolithic enameloid tip. This overall trend for scale penetration as a function of enameloid thickness was similar for both $M_{E/G} = 1$ and 2 .

Stress and strain contours of the tooth-scale system were found to depend on the tooth enameloid thickness relative to the scale ganoine ($t_{E/G} = 1$ and 10 , $M_{E/G} = 1$, Fig. 5-10). The thinner the enameloid layer, the more compliant the system and the more stress and strain incurred by the dentin layer. Highly localized normal and shear stress fields around the junction between the enameloid and dentin layers in the tooth model are observed. The thick enameloid layer ($t_{E/G} = 10$) does not transfer the load into the dentin layer and concentrated stress fields were observed near the apex of the tooth, indicating the increased probability of the fracture at this location. This suggests that any cracks that may initiate in sharp and thick enamel caps might be arrested by or near the dentin junction. While the enamel thickness (for the cases of $t_{E/G} = 1$ and 10) show an influence of the bilayer on the stress and strain fields within the tooth, the stress and strain fields in the scale for these two cases are nearly identical. This is expected for this case where $M_{E/G} = 1$ and would also be anticipated for cases where $M_{E/G} > 1$. For cases where $M_{E/G} < 1$, the deformation of the enameloid cap would be more severe and, therefore, a greater interaction with deformation of the tooth dentin would be expected which, in turn, would influence the extent of penetration into the scale.

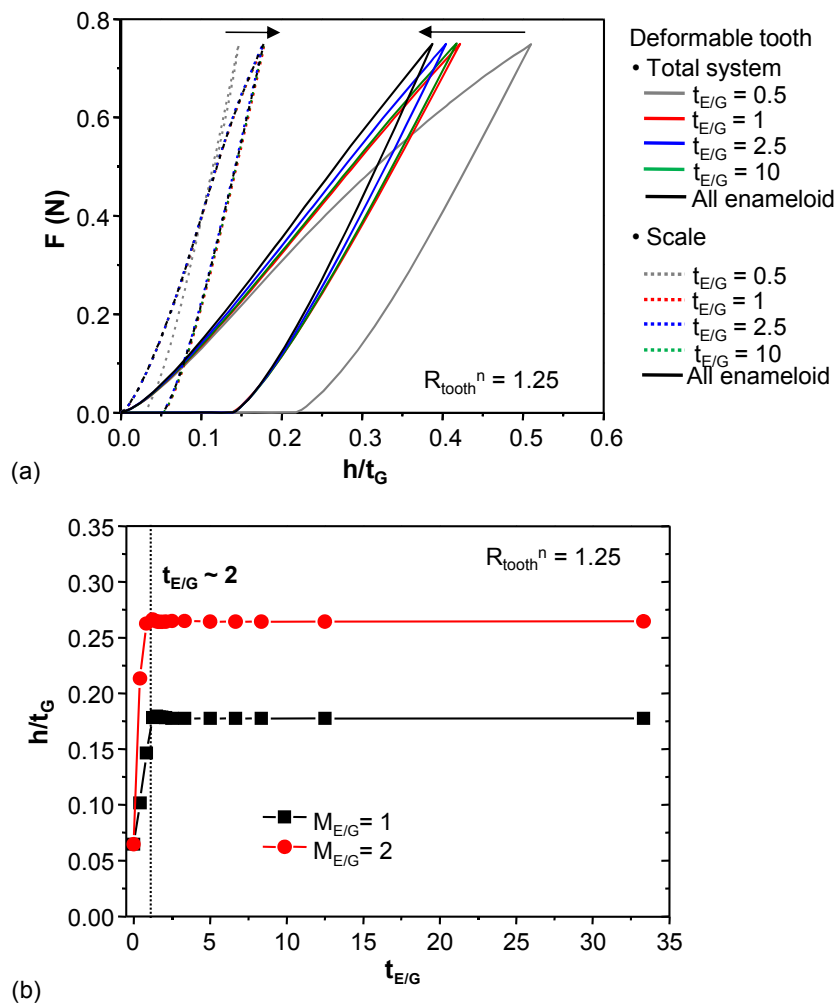


Figure 5-9. The effect of the tooth enamel thickness relative to the scale ganoine thickness ($t_{E/G}$) on the predicted load-depth behavior and normalized penetration depth (relative to ganoine thickness) for two different mechanical ratios of enamel to ganoine ($M_{E/G}$, indentation stiffness and yield strength) of 1 and 2, predicted by finite element analysis of a virtual microindentation using a deformable tooth which simulates a hypothetical generic predatory attack of *P. senegalus*; (a) normalized load-depth curves of the whole tooth-scale system and scale system for $M_{E/G} = 1$ at the tooth end radius of 1.25 depending on the thickness of enamel, as compared to the monolithic enamel tooth case, and (b) normalized penetration depth for $M_{E/G} = 1$ and 2 as a function of $t_{E/G}$. A normalized tip end radius of 1.25 relative to the scale ganoine thickness was employed.

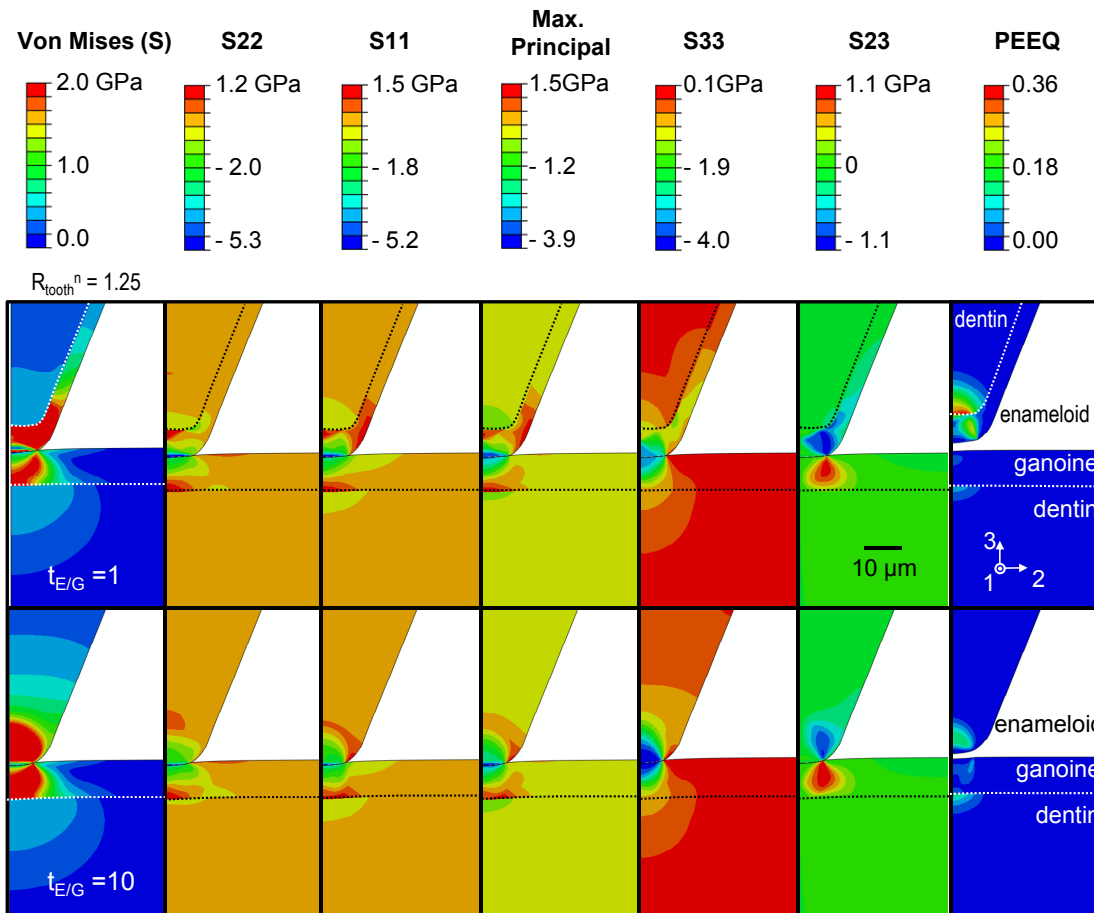


Figure 5-10. The effect of the tooth enamel thickness relative to the scale ganoine thickness ($t_{E/G}$) on the simulations of contours of stress and plastic equivalent strain, predicted by finite element analysis of a virtual microindentation using a deformable tooth that simulates a hypothetical generic predatory attack of *P. senegalus*. FEA predictions of Von Mises stress (S), S22, S11 and S33 at a maximum depth when fully loaded, and S33, S23 and equivalent plastic strain (PEEQ) when fully unloaded for two thickness ratios of enamel to ganoine, 1 and 10, using a deformable tooth with a normalized tip end radius of 1.25 with respect to the thickness of the ganoine layer at the mechanical ratio of enamel to ganoine, $M_{E/G}=1$.

5.4. Discussion

Predator-prey interactions are widely thought to lead to so-called “evolutionary arms races” in which predators evolve enhanced weapons and prey improved defensive capabilities (Vermeij, 1987; Agrawal, 2001; Dietl and Kelley, 2002). The process leads to progressive elaboration of weapons and defenses, and in some may result in “adaptive stalemates” due to costs, tradeoffs, and constraints (Vermeij, 1987; Agrawal, 2001; Dietl and Kelley, 2002). For example, interactions between snails (gastropod mollusks) and crabs that prey upon them, can lead to the evolution of thicker, larger shells, external shell ornamentation, and variable macroscopic shell geometries in prey and strong, geometrically-specialized claws of the crab (Vermeij, 1987; Hughes, 1989; Dietl and Kelley, 2002). Prey handling by crabs has been observed (Elner, 1978; Williams, 1978; Hughes, 1989; Seed and Hughes, 1995), shell failure modes documented (Zuschin et al., 2003), shell failure loads measured (Elner, 1978; Hughes, 1989), crab claw forces analyzed (Taylor, 2000), and the effectiveness of crab claw morphologies considered (Seed and Hughes, 1995). In another case, the magnitude and contribution of the impact and cavitation forces generated by the thoracic raptorial appendage hammer of the mantis shrimp (stomatopods) was experimentally quantified using high speed imaging, force measurements and acoustic analysis (Patek and Caldwell, 2005). These raptorial appendages are known to be able to fracture the shells of snails, crabs, and clams, and the number of strikes needed to catastrophically break shells of various sizes has been recorded, as well as differences in attacking methods to improve efficiency (e.g. impact of shell apex, lip, shearing of side whorls, use of diactyl tip for more compliant tissues) (Caldwell and Dingle, 1975). For predatory fish, the biomechanics of biting and the generation of bite forces has been considered (Westneat, 2004), for example for the placoderm *Dunkleosteus terrelli* by analyzing the anatomical configurations of the skull, thoracic shield, mandible and jaw depressor muscle (Anderson and Westneat, 2007). Evidence for predation-related exoskeletal penetration and repair in armored fish has been reported in the literature (Reimchen, 1988; Mapes et al., 1989; Mcclanahan and Muthiga, 1989; Kodera, 1994). A substantial literature also exists on the origins of natural armor strength and toughness (Currey and Taylor, 1974; Bruet et al., 2005; Barthelat and Espinosa, 2007).

It is instructive to consider the specialized case of fighting between the same species where the threat and protection are comparable, such as the case of *P. senegalus* studied here. Stomatopods, for example, fight territorially amongst each other, resulting in threat damage in the form of missing raptorial appendages or a diactyl with a broken heel (Caldwell and Dingle, 1975). However, they are known to use less lethal modified strikes with a closed diactyl against competitors of the same species which are directed at the heavily armored ridged telson or tail shell, which is conversely used as a protective

shield during fighting and as an enclosure to seal and block off the entrance to their dwellings (Caldwell and Dingle, 1975). Telson armoring among various species of stomatopods has been observed to correlate with strike crushing power (Caldwell and Dingle, 1975). Only where there is intense competition for dwelling space do a few species of stomatopods use lethal strikes at the head and thorax of its opponent (Caldwell and Dingle, 1975).

While there is much interest in this area, the detailed mechanical mechanisms of the interaction between the protective structures of prey and the offensive structures of predators, and the roles of material, microstructure, and geometric design on these interactions has yet to be explored rigorously. Here, we have focused on a single common type of threat, in particular for armored fish, a localized penetration approximating a toothed biting attack. We present a general methodology that can be expanded to other types of predatory attacks which exhibit different types of mechanical loading situations, such as peeling, drilling, hammering, and fatigue loading (Vermeij, 1987), as well as threats and natural armor systems with varied geometric characteristics (internal porosity, corrugations, buttresses (Vermeij, 1987); tooth and claw morphologies (Seed and Hughes, 1995)) and active offensive components (Hoogland et al., 1956; Reimchen, 1983). While the predator and prey under investigation in this study (both *P. senegalus*) are comparable, parametric simulations enabled assessment of asymmetric situations (inequality, where the armor or threat are significantly weaker or stronger relative to each other) and specifically, the determination of under what conditions and how the offensive threat or defensive protection would dominate in the interaction. Failure of the armor could result in internal soft tissue and organ damage leading to death, infection, as well as subsequent predatory and territorial fighting vulnerability (Reimchen, 1988; Mapes et al., 1989; Mcclanahan and Muthiga, 1989; Kodera, 1994; Zuschin et al., 2003). Failure of a tooth can lead to reduced feeding rates and territorial fighting vulnerability (Magalhaes, 1948; Kent, 1983; Geller, 1990). A fundamental understanding of threat-protection design principles and mechanisms underlying predator-prey interactions has great potential to yield insights into evolutionary pathways (Vermeij, 1987; Dietl and Kelley, 2002).

The relevant geometric and material features of the offensive threat (tooth) and defensive protection (armored scale) for *P. senegalus* are summarized in Table 5-2. Here, we see that a length-scale matching takes place between the threat (represented by the tooth end-radius) and the protective outer layer of the armor (ganoine thickness), in order that the underlying energy dissipating layers of the scale (dentin) may be accessed and more efficiently contribute to protection and penetration resistance during an interaction. There is also a matching between constituent materials and the outer bi-layered microstructural arrangement employed in the threat and protective structures (enameloid-dentin for the tooth vs. ganoine-dentin for the scale). For the case of extremely aggressive

threats and higher loading situations, the scale armor maintains additional safety mechanisms via its additional two innermost underlying layers (isopedine, bone) that are absent in the tooth microstructure. The thickness of the outermost layer is an order of magnitude larger for the tooth enameloid compared to the scale ganoine, likely in order to compensate for increased stress/strain concentrations due to the reduced radius of curvature of the tooth compared to the scale (discussed further below). Phenotypic plasticity resulting in changes in structure, length scale, and geometry, of both the scales and teeth can result in changes of their function and effectiveness. Even though I focus on the tooth in this Chapter, it should be noted that phenotypic plasticity can be beneficial for the scale as well (for example, variable number, thickness, and porosity of material layers).

Table 5-2. Comparison of *P. senegalus* tooth and scale systems in terms of shape, composite materials, multi-layered structure as well as the layer thickness.

	Tooth	Armored Scale
Geometry	relatively sharp (~ 15 μm end-radius)	relatively flat
Materials	apatite + organic	
Layer sequence	enameloid (stiff, hard) dentin (more compliant, ductile)	ganoine (stiffes, hardest) dentin isopedine bone (most compliant, ductile) ↓
Thickness of the outmost layer	~ 100 μm (enameloid)	~ 15 μm of (ganoine)

The design advantages and disadvantages for a localized penetrating threat and its corresponding protective natural armor are shown in Table 5-3. For the threat, sharpening, increasing mechanical properties (e.g. stiffness, hardness, strength), and increasing the thickness of the outer hypermineralized capping layer, will enable increased efficiency of penetration and wear resistance, e.g. chiton or sea urchin teeth that are sharpened and strengthened by incorporating iron or magnesium ions in them (Wang et al., 1997; van der Wal et al., 2000). Sharper threats also maintain the advantage of inducing local stress distributions in the armor that promote radial cracking, as opposed to blunter tips which are expected to induce circumferential cracking modes. Conversely, sharper teeth will result in large disadvantageous stress concentrations in the threat making it vulnerable to crack initiation, propagation, and ultimately failure. Catastrophic fracture of the entire tooth is mitigated by the bi-layered structure composed of a thick, stiff, hard enameloid outer layer encapsulating a more compliant, soft and ductile dentin

inner core which provides toughness, energy dissipation, and can arrest cracks emanating from the enameloid (Wang et al., 1997; Imbeni et al., 2005). However, for sharper teeth the high stress concentrations resulting in plasticity and potentially fracture of the enameloid layer are expected to result in disadvantageous blunting during subsequent attacks, thereby reducing penetration effectiveness (Appendix C). Lastly, energetic costs associated with biomineralization, in particular of the hypermineralized tooth enameloid layer exist.

Table 5-3. Advantages and disadvantages of penetrating threat and corresponding protective natural armor systems

System	Advantages	Disadvantages
Predatory Threat	<ol style="list-style-type: none"> 1. Increased sharpness (penetration, permanent damage to armor, advantages radial cracking promoted) 2. Increased mechanical properties (stiffness, hardness, strength) 3. Thick capping layer (penetration, permanent damage to armor) 4. Bi-layered structure (toughness, crack arrest) 	<ol style="list-style-type: none"> 1. Sharper, thicker capping layers leads to intense and larger stress/strain fields in threat, reduction in use of more efficient underlying layers for energy dissipation 2. Thicker hypermineralized capping layers; energetic cost biomineralization, weight 3. Blunter tips promote disadvantageous circumferential cracking
Prey Armor	<ol style="list-style-type: none"> 1. Increased flatness (reduce stress/strain concentrations) 2. Comparable or greater mechanical properties to threat 3. Optimal thickness of the hardest and stiffest outmost layer, resulting in the minimizing energy cost and armor weight / maximizing penetration resistance, sacrificial fracture 4. Multi-layered structure to provide effective penetration resistance, toughness, and non-catastrophic pathways for energy dissipation 	<ol style="list-style-type: none"> 1. Larger volume compared to threat that leads to higher energetic cost for biomineralization, weight 2. Thicker hypermineralized capping layers; energetic cost biomineralization, weight

There are two main strategies for effective defense mechanisms of armor systems: defeating threats by means of deforming or fracturing the threat and, hence, eliminating its ability to penetrate, or, alternatively, providing non-catastrophic, sacrificial avenues for deformation and fracture events within the armor microstructure to dissipate the energy of the attack without allowing full penetration. The multilayered microstructural design of the armored scale provides for both of these strategies. Defeating the threat system requires the relatively large radius of curvature as compared to the threat

geometry, as well as mechanical matching where ideally the armor should have comparable or higher mechanical properties than the threat. The first line of defense is the outer ganoine layer which has high stiffness and strength which can act to defeat nominal threats. Energy dissipation mechanisms of armor systems are also then controlled by their microstructures and composites structures and composition. Indeed, the organic matrix of mineralized tissues plays a key role in energy dissipation (Wang et al., 2001). Graded mechanical properties in connection with mineral contents such as the *P. senegalus* scale system provide multilayering effects that alter the surface failure modes, redistribute stress and strain distributions and effective energy dissipation by utilizing the underlying compliant layers. Often the two strategies of defeating the threat and dissipating the threat attack are combined in one armor system to maximize penetration resistance, as I have found in the *P. senegalus* system. However, the highly mineralized layer of the armor system also requires larger energy and related mineral sources from the environment during biomineralization. Therefore, reduction of the total mineralization processes may be advantageous by optimizing the thickness of each layer in the system.

5.5. Conclusion

It has been hypothesized that predatory threats are a critical factor in the protective functional design of biological exoskeletons or “natural armor,” having arisen through evolutionary processes. Parametric studies on *P. senegalus* armor and its hypothetical threat reveal the effects of tooth geometry, microstructure and mechanical properties on its ability to effectively penetrate into the scale or to be defeated by the scale, in particular the deformation of the tooth versus that of the scale during a biting attack. Simultaneously, the role of the scale microstructure in defeating threats as well as providing avenues of energy dissipation to withstand biting attacks is identified. Microstructural length scale and material property length scale matching between the threat and armor is observed. Based on these results, formulated advantageous and disadvantageous design strategies for the offensive threat and defensive protection may lead to insights into adaptive phenotypic plasticity of the tooth and scale microstructure and geometry, “adaptive stalemates” and the so-called evolutionary “arms race.”

Chapter 6.

The Role of Multilayering in a Natural Armor

6.1. Introduction

Many natural armor systems (e.g. mollusk and turtle shells, brachiopod and, arthropod exoskeleton, mineralized fish scales, etc.) are composed of a relatively small number (typically one to four) of juxtaposed material layers which provide protection against predatory and environmental attacks (Fig. 6-1) (Uozumi and Suzuki, 1981; Vermeij, 1982; Parker et al., 1998; Cheng et al., 2008; Schmahl et al., 2008; Wyneken et al., 2008; Cheng et al., 2009; Sire et al., 2009). In particular, the armored fish is an excellent model system to study the effect of multilayering because of the diversity of microstructures and direct relation to evolutionary states. Multilayered dermal armor of fish, for example, first appeared at the beginning of the Paleozoic period, approximately 500 million years ago, with the rise of the Ostracoderms and became common among the earliest fish. As fish became more predaceous through the Devonian period, the larger and heavier plates of dermal armor plates broke up into many smaller ones, the thickness of various material layers decreased (~1500 - 100 μm), and the number of material layers within the armor plates decreased (~4 to 1-3 layers). Hence, physical protection was reduced while simultaneously body weight was decreased, flexibility and maneuverability improved, and swimming speed enhanced. Current living armored fish exhibit three major types of bony scales: ganoid (quad-layered; ganoine, dentin, isopedine, bone), placoid (bi-layered; ganoine, bonedentin) and elasmoid (outer hypermineralized layer and mono-layered bone) (Table 6-1) (Colbert, 1955; Ørvig, 1968; Hoedeman, 1975; Sire, 1990; Coburn and Gaglione, 1992; Daget et al., 2001; Anderson and Westneat, 2007; Sire et al., 2009).

In previous Chapters of this thesis, mechanical properties (e.g. stiffness and hardness) of the individual *P. senegalus* scales were found to be decreased gradually

from the hardest and stiffest outmost ganoine layer to the softest and most compliant inner bone as well as around the junctions between ganoine and dentin or dentin and isopedine. The functionally graded mechanical design of the scales provides penetration resistance against the potential threats by means of advantageous circumferential cracking, effective energy dissipation and suppressed interfacial failure with minimal back deflection of the underlying soft tissues. Moreover, armor systems take advantages of interaction with potential threats, optimizing energetic costs by length scale matching (e.g. layer thickness, curvature) and defeating threats by mechanical matching (e.g. enamel of threat/enamel-like ganoine of armor). Multilayer design strategies associated with the spatial distribution of mechanical properties play a key role in defense mechanisms of armor systems, in particular, fish armor that has been evolved, achieving a balance between mobility (e.g. reducing armor weight) and protection (e.g. increasing effective stiffness and hardness) as indicated in Fig. 6-1 (Sire et al., 2009).

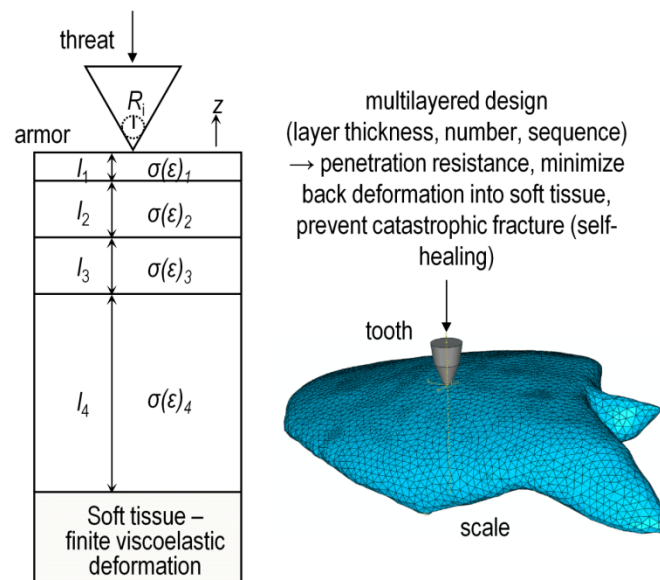


Figure 6-1. Design principles of multilayered natural exoskeletons; schematic diagram of an individual tooth-armored scale system in *P. senegalus* during a hypothetical attack.

In order to understand the optimized structure of the mineralized quad-layered scale design, here I compare various multilayered structures in terms of their predicted functionality, linking the scale design to its function with regards to the specific threat experienced in its environment while minimizing sacrifice of mobility. In particular, three multilayered designs were taken into consideration: (i) the thickness of the outer layer, ganoine; (ii) the quad-layered structure as compared to simpler bilayer structures; and (iii) the sequence of the outer two layers. The mechanical behavior of various multilayer designs was studied during penetration, and weight was also used as an additional

comparative property. In order to understand the role of those three structural parameters, parametric studies via finite element analysis (FEA) simulations of virtual Vickers microindentation and hypothetical biting to various maximum loads were conducted. The scaling effect of the system was also examined by using dimensionless parameters after normalization. Based on these results, variations in multilayered design of natural armor systems were understood, in terms of a balance between protection and mobility in armor design.

Table 6-1. Summary of constitutive material layers, their typical mineral contents and sequence of three major fish scale types (ganoid, placoid and elasmoid) with example species (Sire, 1990; Raschi and Tabit, 1992; Sire et al., 2009)

Scale type	Constitute material layer	Mineral Content	Layer Sequence		Example species
Ganoid	ganoine	~ 95 wt% (Ørvig, 1967)	ganoine (dentin) (isopedine) bone	<i>outer</i> ↓ <i>inner</i>	<ul style="list-style-type: none"> ● Chondrostei/Polypteriformes : <i>bichirs, reedfish</i> ● Neopterygii/Holostei : <i>gars and bowfins</i>
	dentin	~ 60 wt% (Driessens and Verbeeck, 1990)			
	isopedine	10 ~ 60 wt% (Moss, 1963; Driessens and Verbeeck, 1990)			
	bone				
Placoid	enamel	~ 98 % (Driessens and Verbeeck, 1990)	enamel	<i>outer</i>	<ul style="list-style-type: none"> ● Elasmobranchii/Batoidea : rays, skates ● Elasmobranchii/Selachimorpha : sharks ● Holocephali/Chimaeriformes : ratfish
	dentin	~ 60 % (Driessens and Verbeeck, 1990)	dentin	<i>inner</i>	
Elasmoid	limiting layer	~ 98 % (Driessens and Verbeeck, 1990)	limiting layer elasmodine	<i>outer</i> <i>inner</i>	Most current living fish species <ul style="list-style-type: none"> ● Neopterygii/Telostei -Protacanthopterygii : <i>salmon, trout</i> -Acanthopterygii : <i>stickleback, bass, mackerel, tuna, flyingfish</i>
	elasmodine	10 ~ 50 % (Moss, 1963; Driessens and Verbeeck, 1990; Ikoma et al., 2003)			

6.2. Methods

Penetration of a threat into individual *P. senegalus* ganoid scales was simulated using nonlinear finite element analysis (FEA) (ABAQUS/standard). Penetration events including Vickers microindentation and hypothetical biting events were modeled as a penetration of a rigid Vickers indenter or tooth-emulating indenter (an enamel tooth) into an individual scale. The symmetry of the geometry and materials allowed for axisymmetric simulations and virtual indentations were carried out for loading and unloading up to maximum loads of 0.25, 0.50, 0.75, and 1 N. These penetration events induce complex local multiaxial stress and strain concentrations in both the armor and threat systems. In Chapter 3, microcracking has been observed in Vickers microindentation experiments for maximum loads above 1N. Herein, these loads were chosen for comparison of the effect of a multilayered structure in *P. senegalus* scales to alternative layered structures by varying the thickness or sequence of the four constitutive layers, ganoine, dentin, isopedine and bone of *P. senegalus* scales.

6.2.1. Threat Model

Two types of indenters were used for threat model systems: (1) the Vickers indenter was taken to be perfectly rigid, with conical tip geometry, emulating a Vickers microhardness tip with a radius (R_{V-tip}) of 3.7 μm and a half tip angle (α) of 70.3° (Fig. 6-2a, *top*); and (2) the tooth-emulating indenter was constructed based on geometric information provided in Chapter 5, e.g. a half cone angle (α) of 22°, a height (h) of 400 μm , and a tip end radius (R_{tooth}) of 15 μm (Fig. 6-2a, *bottom*) and was assumed to be as deformable as the ganoine layer of the scale armor system. Axisymmetric rigid elements (RAX2 in ABAQUS element library) were used for the perfectly rigid Vickers tip while four-node bilinear axisymmetric quadrilateral elements (CAX4R in ABAQUS element library) were used with optimized meshes for convergence for the deformable tooth-emulating indenter.

6.2.2. Scale Model

The multilayered scale models were constructed via established protocols and boundary conditions in Chapter 3 (Fig. 6-2b) using four-node bilinear axisymmetric quadrilateral elements (CAX4R in ABAQUS element library) with optimized meshes for convergence. The bottom surface of the scale model was fixed with no movement allowed and the individual scale was assumed to be large enough as compared to local penetration events. The interfaces between material layers were assumed to be perfectly bonded with a discrete change in mechanical properties from one layer to another. The

modulus (E) and yield stress (σ_Y) values used for each of the four scale material layers were quantified via nanoindentation and FEA methods as described in detail in Chapter 3 (Table 6-2). Parametric studies were carried out on the role of layer thickness, number and sequence of multilayer design on penetration resistance, local stress and strain distributions, and energy dissipation of the armor system during indentation.

To address the thickness effect of ganoine layer, ganoine-dentin and ganoine-bone bilayered discrete FEA models for the simulation were constructed. In addition, the weight issue was also considered because too thick ganoine layer will make the armor heavier and affect the mobility of fish. The density of the ganoine, ρ_{ganoine} , was taken to be equivalent to that of enamel $\approx 2.8 \text{ g/cm}^3$, ρ_{dentin} was taken to be equivalent to that of human dentin $\approx 2.12 \text{ g/cm}^3$, and ρ_{bone} was assume to be equivalent to that of human bone $\approx 1.60 \text{ g/cm}^3$ based on the mineral content (30~40 wt%) of both layers (Table 6-2) (Driessens and Verbeeck, 1990). The total thickness of all ganoine-dentin bilayer structures (t_{total}^f) was fixed as $400 \text{ }\mu\text{m}$ with thickness of ganoine layer (t_{gan}) varying from 3 to $54 \text{ }\mu\text{m}$ (Fig. 6-2b). The virtual microindentation was done at the maximum load of 1 N. In Chapter 5, the thickness of the outmost layer in multilayered armor systems was found to be closely related to the tip end radius of threats. Therefore, the varied ganoine thickness (t_{gan}) was normalized by the tip end radius of either the Vicker's top or tooth-emulating tip ($R_{V\text{-tip}}$ or R_{tooth}), denoted as $t_{\text{gan}}^{n,V} (= t_{\text{gan}}/R_{V\text{-tip}})$ or $t_{\text{gan}}^{n,t} (= t_{\text{gan}}/R_{\text{tooth}})$.

The second set of simulations was carried out with the number of layers varied in the scale system. In addition to the aforementioned bi-layered models, ganoine-dentin-isopedine-bone quadlayer discrete FEA models which emulate the quadlayer structure of *P. senegalus* scales were constructed. The total thickness of both bilayer and quadlayer structures (t_{total}^f) was fixed as $400 \text{ }\mu\text{m}$ with varied thicknesses of ganoine (t_{gan}) from 3 to $54 \text{ }\mu\text{m}$. Moreover, the thicknesses (t_{iso}^f and t_{bone}^f) of isopedine and bone layers in quadlayer structures were fixed as $40 \text{ }\mu\text{m}$ and $300 \text{ }\mu\text{m}$, respectively (Fig. 6-2b) and their density was also taken to be equivalent to that of human bone $\approx 1.60 \text{ g/cm}^3$ based on the mineral content (30~40 wt%) of both layers. The ganoine thickness was also normalized by the tip end radius of either the Vicker's tip or tooth-emulating tip ($R_{V\text{-tip}}$ or R_{tooth}), represented as $t_{\text{gan}}^{n,V} (= t_{\text{gan}}/R_{V\text{-tip}})$ or $t_{\text{gan}}^{n,t} (= t_{\text{gan}}/R_{\text{tooth}})$.

In order to explore the sequence effect to the load-resistance mechanism, I developed a discrete "reverse" quadlayer model which consists of four material layers (ganoine, dentin, isopedine and bone), but where the order of two outer layers (ganoine and dentin) were reversed so the more compliant and softer dentin layer was located at the surface followed by the harder and stiffer ganoine layer.

Simulated indentation curves were reported as force versus normalized penetration depth where the penetration depth was normalized by the tip end radius of an indenter ($h/R_{V\text{-tip}}$ or h/R_{tooth}) and force by the square of the tip end radius of an indenter ($F/R_{V\text{-tip}}^2$ or F/R_{tooth}^2). The Effective indentation modulus and microhardness were

reduced from the simulated indentation curves using the Oliver-Pharr method (Oliver and Pharr, 1992) and were plotted as a function of the ganoine thickness or maximum indentation loads. Total energy dissipation by all layers was calculated, which corresponds to the area between the loading and unloading curves. Local stress and strain contours in the vicinity of the contact point were reported as Von Mises stress (S), circumferential stress (S11), radial stress (S22), interfacial normal stress (S33), shear stress (S23), as well as the plastic equivalent strain (PEEQ).

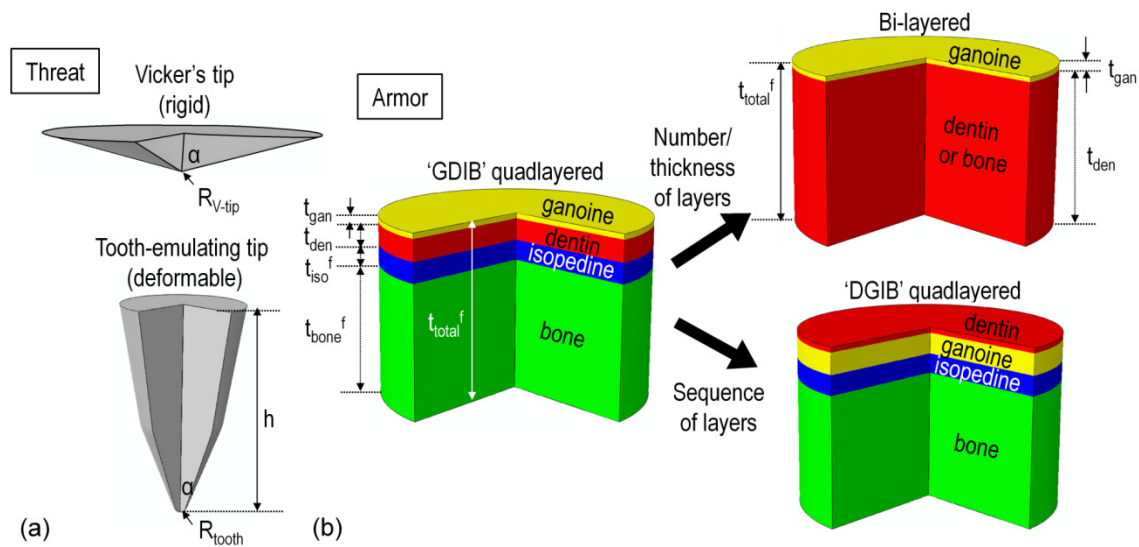


Figure 6-2. Schematic drawing of threat and scale FEA models; (a) two indenter tips for virtual indentation models that are a rigid, Vickers tip with a half apex angle (α) of 70.3° and a tip end radius ($R_{V\text{-tip}}$) of $3.7\ \mu\text{m}$; and a deformable, tooth-emulating tip with a half apex angle (α) of 22° , a tip end radius (R_{tooth}) of $14.7\ \mu\text{m}$ and a total length (h) of $400\ \mu\text{m}$, and (b) three multilayer FEA models that are (i) quad-layered models that mimicked the *P. senegalus* scale system with varying the outmost ganoine thickness, (ii) bi-layered models composed of two outer layers, ganoine and dentin with varying the ganoine thickness; and (iii) a 'DGIB' quad-layer model where the sequence of two outer layers, ganoine and dentin, were reversed, having the outmost dentin layer and underlying ganoine layer.

Table 6-2. Mechanical properties and layer thickness values utilized in finite element (FE) simulations of Vickers microindentation and hypothetical biting attack on various layered structures. The modulus (E), yield stress (σ_Y) and layer thickness values used for each of the four scale and tooth material layers. For the parametric studies, ganoine thickness of three layered scale models was varied. The values in brackets in the first quadlayer model represent the used layer thicknesses of ganoine and dentin for the GDIB quadlayer model.

Material Layers of FEA models		Modulus, E (GPa)	Yield stress, σ_Y (GPa)	Layer thickness (μm)
Quadlayer model (GDIB quadlayer model)	ganoine (outer)	55	2	3 ~ 54 (12)
	dentin	25	0.4	6 ~ 57 (48)
	isopedine	14.5	0.22	40
	bone (inner)	13.5	0.18	300
	Total thickness			400
DGIB quadlayer model	dentin (outer)	25	0.4	12
	ganoine	55	2	48
	isopedine	14.5	0.22	40
	bone (inner)	13.5	0.18	300
	Total thickness			400
gan-dent bilayer model	ganoine (outer)	55	2	3 ~ 54
	dentin	25	0.4	346 ~ 397
	Total thickness			400
gan-bone bilayer model	Ganoine (outer)	55	2	3 ~ 54
	bone	13.5	0.18	346 ~ 397
	Total thickness			400
Vickers indenter	-	Rigid	Rigid	infinite
Monolithic deformable tooth	Enameloid	55	2	400

6.3. Results

6.3.1. Thickness Effect of the Outmost Ganoine Layer

Virtual microindentation using a rigid Vickers indenter predicted the load-depth behavior and effective material properties (e.g. indentation modulus, microhardness, dissipation energy, and areal density) of ganoine-dentin bilayered structures. In Figure 6-3, the mechanical behavior of bilayered structures with thick ganoine layers ($t_{\text{gan}}^{\text{n,V}} \geq 6.5$) become very close to that of the single ganoine while the bilayered structure with ganoine thickness less than $t_{\text{gan}}^{\text{n,V}} = 2.2$ behaves like dentin. The ganoine thickness within a range of $2.2 \leq t_{\text{gan}}^{\text{n,V}} \leq 6.5$ was found to leverage conflicting mechanical properties (e.g. hardness/stiffness vs. energy dissipation) of the layered system, providing the bilayering effects. In addition, these bilayered structures are also beneficial in terms of mobility, which can reduce their weight up to $\sim 75\%$ of the single ganoine layered model, having comparable material properties to ganoine (Fig. 6-3b). Moreover, the ganoine thickness influences the surface stress fields of bi-layer systems as shown in Fig. 6-4a and b. The bilayered structure with too thin ($t_{\text{gan}}^{\text{n,V}} = 0.8$) or too thick ($t_{\text{gan}}^{\text{n,V}} \geq 6.5$) ganoine layer shows tensile circumferential stress field (S11), implying both too thin and too thick ganoine layers may initiate the radial crack on the surface against the rigid indenter. In contrast, the ganoine layer with the thickness of $2.2 \leq t_{\text{gan}}^{\text{n}} < 6.5$ suppresses the tensile circumferential stress field (S11) effectively, and instead promotes the tensile radial stress field to localize the circumferential crack on the surface. This observation is clearly coincident with stress contours of figure 6-4c. At $t_{\text{gan}}^{\text{n,V}} = 0.8$, the tensile circumferential stress (S11) and tensile radial stress (S22) are conducive to initiating both radial and circumferential cracking around the pile-up of the surface. On the other hand, the ganoine thicknesses of $t_{\text{gan}}^{\text{n}} = 2.2$ and 3.2 exhibit compressive circumferential (S11) and tensile radial (S22) stress fields on the ganoine surface, promoting more advantageous circumferential cracking. In the case of $t_{\text{gan}}^{\text{n}} = 4.9$ and 14.6 a sign inversion with tensile circumferential (S11) and compressive radial (S22) stress fields (Fig. 6-4c) is observed, indicating radial cracking is more dominant.

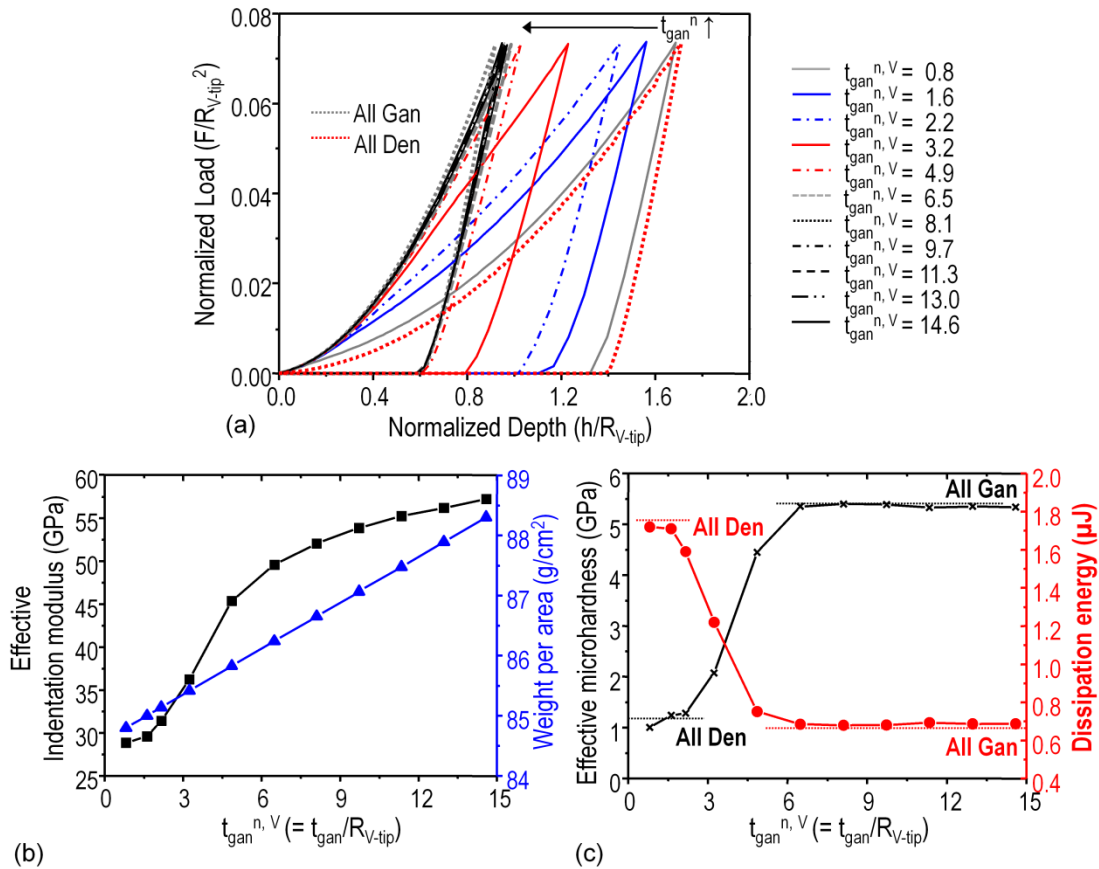


Figure 6-3. The effect of layer thickness (for a perfectly rigid Vickers tip) on the predicted finite element simulations of the load-bearing capability and energy dissipation of the gan-dent bilayer FEA models during a virtual microindentation, simulating a Vickers indentation; (a) normalized load-depth curves for different ganoine thicknesses of bi-layered systems, (b) effective indentation modulus and weight per area as a function of ganoine thickness (t_g^n), and (c) effective microhardness and energy dissipation as a function of ganoine thickness (t_g^n). The ganoine thickness (t_g^n) varied from 0.75 % to 13.5 % of the total thickness (t_{total}^1) of the system. Penetration depths were also normalized the tip end radius of the Vickers tip (R_{V-tip}) and loads were normalized by the square of the tip end radius of the Vickers tip (R_{V-tip}^2).

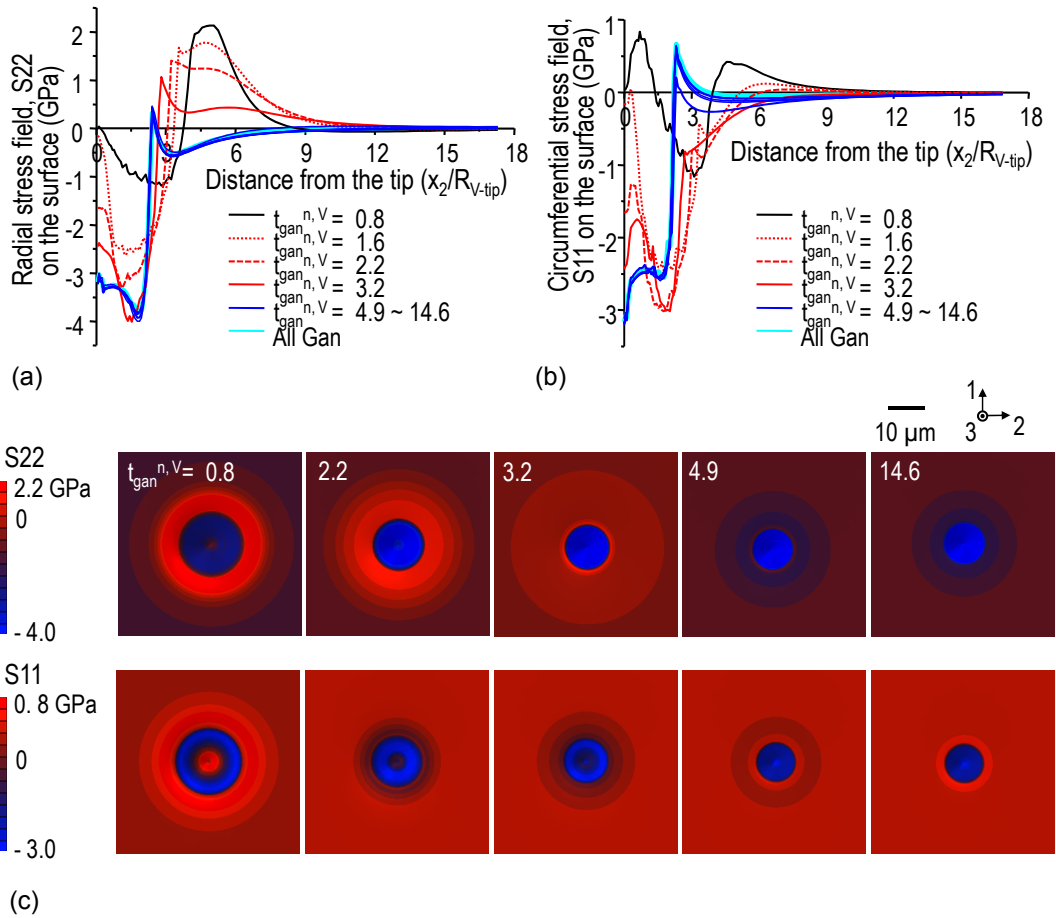
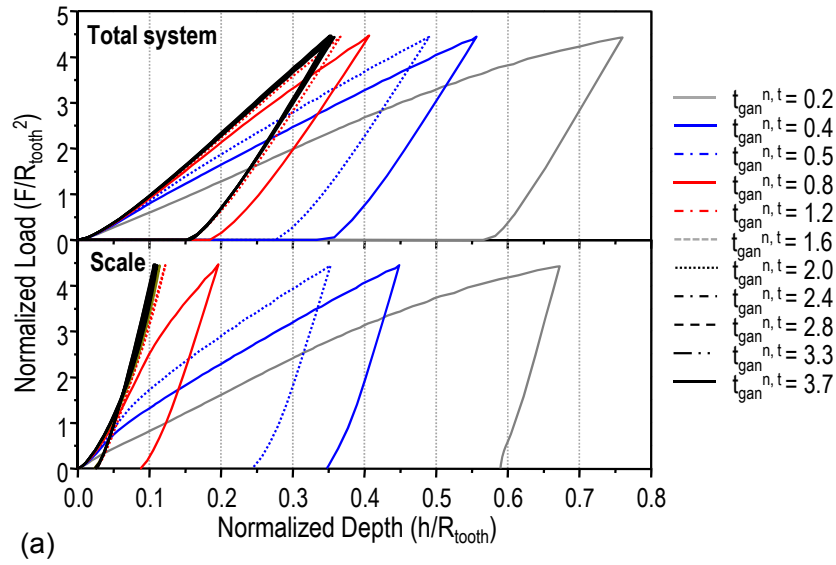


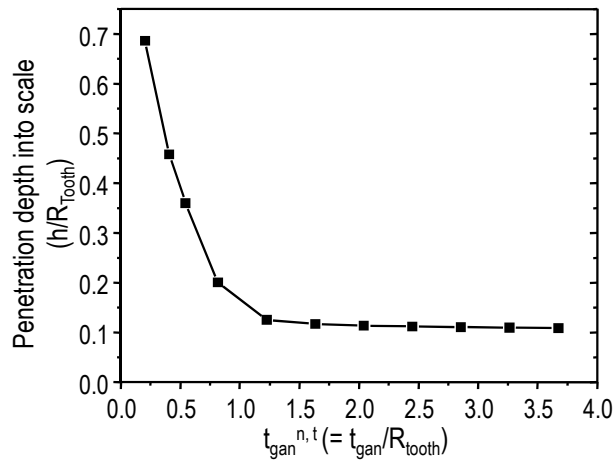
Figure 6-4. The effect of layer thickness (for a perfectly rigid Vickers tip) on the predicted finite element simulations of the stress distribution on the surface of the bi-layered structure during a virtual microindentation; (a) radial stress field (S22) and (b) circumferential stress field (S11) on the surface of bi-layered structures with various ganoine thickness as a function of distance from the center of the indented site, and (c) the contours of circumferential (S11) and radial stresses (S22) viewed along the indentation loading 3-axis for normalized ganoine thicknesses ($t_{\text{gan}}^{n,V}$) of 0.8, 2.2, 3.2, 4.9 and 14.6. Distances from the center of the indented area on the ganoine surface were normalized with the tip end radius of the Vickers tip ($R_{V\text{-tip}}$).

The results of hypothetical attacks using the deformable tooth-emulating indenter are shown in Fig. 6-5 and 6-6. The effect of allowing the indenter to be deformable has significant consequences on the force vs. indentation “depth” results (Fig. 6-5a), the depth of the tooth penetration into the scale (Fig. 6-5b), and the nature of the stress and strain distributions (Fig 6-6). Figure 6-5a shows that an increase of the ganoine thickness (i.e., as $t_{\text{gan}}^{n,t}$ increases) results in a marked shift of force vs. depth (i.e. penetration into the scale) curves to the left along the depth axis relative to the case of $t_{\text{gan}}^{n,t} = 3.7$ (Fig. 6-5a, black lines). There is a dramatic reduction in penetration of the tooth into the scale as the ganoine thickness increases up to $t_{\text{gan}}^{n,t} = 1.2$ when the ganoine thickness becomes similar to the tip end radius of the tooth indenter. The penetration into the scale under an indentation load of 1 N is shown as a function of $t_{\text{gan}}^{n,t}$ in Fig. 6-5b, revealing that once $t_{\text{gan}}^{n,t}$ is greater than 0.8, the bilayered structure behaves like a monolithic ganoine structure.

The calculated contours for stress and plastic equivalent strain are shown in Fig. 6-6 when fully loaded to 1 N (S, S11, S22, S23) and after fully unloaded from 1 N (PEEQ, PE23). A thin ganoine layer ($t_{\text{gan}}^{n,t} = 0.2$) induces larger areas and greater magnitudes of stress and plastic deformation in both the ganoine and dentin layers compared to the tooth indenter (Fig. 6-6), and shearing along with the interface between ganoine and dentin (S23 contours) is clearly observed. Moreover, the effective material properties of this bilayered structure with too thin ganoine ($t_{\text{gan}}^{n,t} = 0.2$) are close to dentin (Fig. 6-3b and c), allowing the tooth indenter to become essentially rigid because of the mechanical ratio of two systems. As the ganoine thickness increases, the effective mechanical properties of the bilayered structure become close to those of ganoine as well as the tooth system: the magnitudes of stress fields on the ganoine surface is greatly reduced with smaller areas of plastic deformation. No significant shearing is also observed around the ganoine-dentin interface. At $t_{\text{gan}}^{n,t} = 3.7$, the ganoine layer of the scale is elastically deformed with perfect recovery and tensile stress fields do not appear on the surface of the layer.



(a)



(b)

Figure 6-5. The effect of layer thickness (for a deformable tooth indenter) on the predicted finite element simulations of the load-depth behavior and normalized penetration depths of the gan-dent bilayer FEA models during a virtual microindentation, simulating a hypothetical generic predatory attack of *P. senegalus*; (a) Normalized load-depth curves for different ganoine thicknesses of bi-layered systems; (b) normalized penetration depths with respect to the tip end radius of the tooth indenter (R_{tooth}) as a function of ganoine thickness for the gan-den bilayer models during the Vickers microindentation and hypothetical biting events. Penetration depths were normalized the tip end radius of the tooth indenter (R_{tooth}) and loads were normalized by the square of the tip end radius of the tooth tip (R_{tooth}^2).

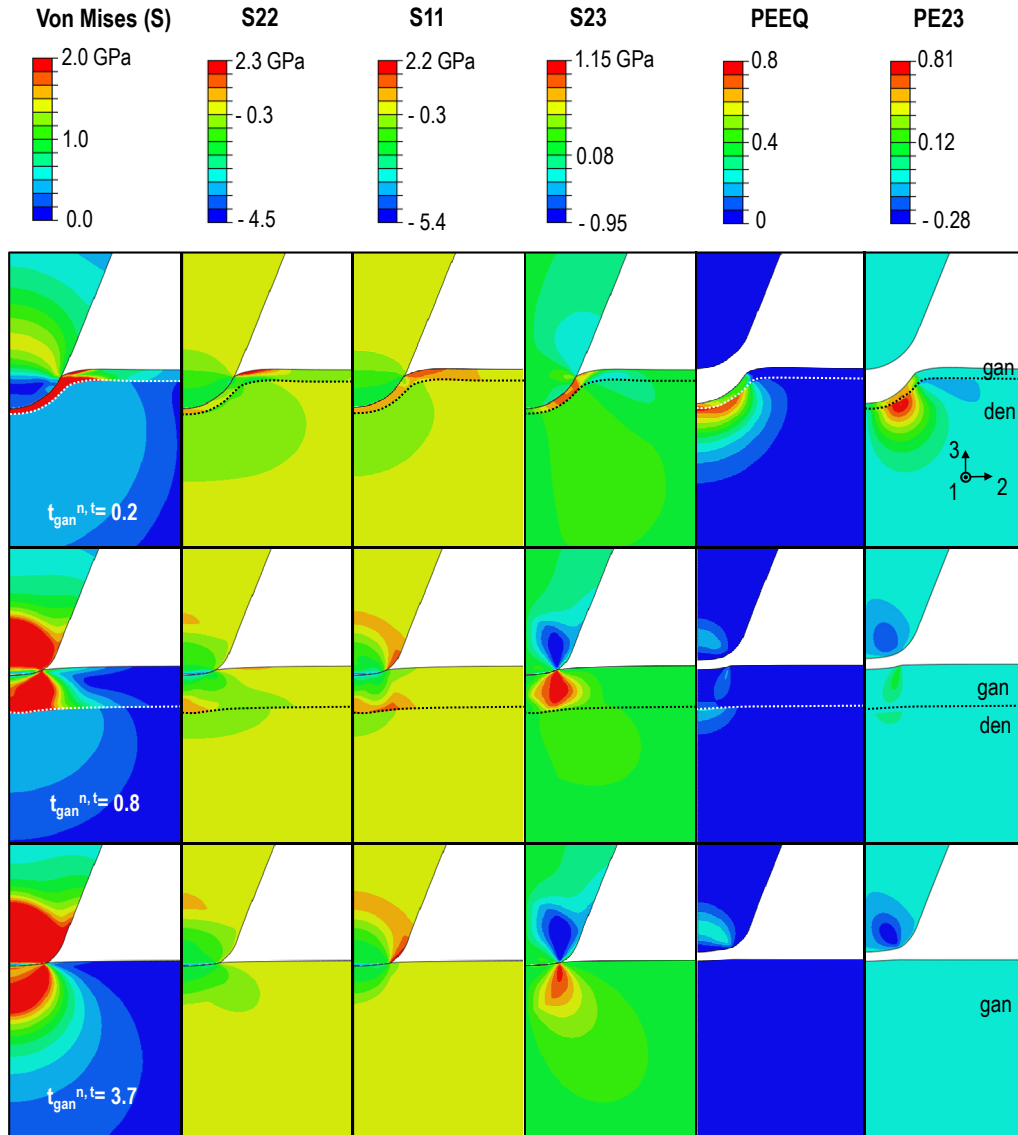


Figure 6-6. The effect of layer thickness (t_g) on the simulations of contours of stress and plastic equivalent strain, predicted by finite element analysis of a virtual microindentation on the gan-dent bilayer models using a deformable tooth that simulates a hypothetical generic predatory attack of *P. senegalus*. FEA predictions of Von Mises stress (S), S22, S11 and S23 at a maximum depth when fully loaded, and equivalent plastic strain (PEEQ) and shear strain (PE23) when fully unloaded for three ganoine thicknesses, $t_g^{n,t} = 0.2, 0.8, 3.7$.

6.3.2. Multilayered vs. Bilayered Structures

The fish armor design ultimately aims for a balance between protection and weight/mobility. To achieve this balance, the weight reduction of the armor should be attempted without any sacrifice of protection by substituting the dentin layer of the bilayered structure with the lighter and less mineralized layers such as isopedine and bone that have relatively low density ($\rho_{\text{bone}} \approx 1.6 \text{ g/cm}^3$) comparing to dentin ($\rho_{\text{dentin}} \approx 2.12 \text{ g/cm}^3$) because of less mineral contents. The bilayered model consisting of ganoine and dentin (gan-den bilayer) was compared to two multilayered models, (i) the alternative bilayered model (gan-bone bilayer) that has bone instead of dentin, and (ii) the ganoine-dentin-isopedine-bone quadlayer model in terms of material properties (e.g. stiffness, hardness, dissipation energy and density) which were predicted by virtual Vickers microindentation and then normalized by those of ganoine, as shown in Fig. 6-7. Stiffness, hardness, and energy dissipation for gan-den bilayered and quadlayered models become almost identical when $t_{\text{gan}}^{n, V}$ is larger than 8.1. Nevertheless, the quad-layer model can achieve a significant weight reduction up to $\sim 80 \text{ wt}\%$ of the gan-den bilayered model. In case of the gan-bone bilayered structure, stiffness and hardness are consistently lower than those of other two multilayered systems (Fig. 6-7a and b). However, at $t_{\text{gan}}^{n, V} = 14.6$, all mechanical properties become almost identical to those of the quadlayered model. In particular, even though at the same ganoine thickness the gan-bone bilayered is lighter than the quadlayered model, the slope of its weight increment along with the addition of ganoine is stiffer than one of the quadlayered model, thereby the density of those two layered systems becomes eventually identical at $t_{\text{gan}}^{n, V} = 16.2$ (Fig. 6-7d).

The mechanical behavior of the three layered systems was also observed using the deformable tooth-emulating indenter. Figure 6-8a shows that the load-depth behavior of the gan-den bilayered and quadlayered models is almost identical. As the ganoine layer is thin ($t_{\text{gan}}^{n, t} < 3.7$), the quadlayered structure is more compliant and softer than the gan-den bilayered one and this trend was also found in the case of the gan-bone bilayered model (data not shown). The normalized penetration depth at the hypothetical biting force of 1 N was plotted as a function of $t_{\text{gan}}^{n, t}$ (Fig. 6-8b). The deformable tooth indenter experienced almost same penetration resistance by both the gan-den bilayered and quadlayered systems. Interestingly, the tooth can penetrate deeper into the gan-bone bilayered structure up to $t_{\text{gan}}^{n, t} = 1.6$ when the penetration resistance of the gan-bone bilayered structure becomes close to that of the quadlayered system.

The calculated contours for stress and plastic strain are shown in Fig. 6-9 when fully loaded to 1 N (S11) and after fully unloaded from 1 N (PE23) with three ganoine thicknesses, $t_{\text{gan}}^{n, t} = 0.2, 0.8$ and 3.7 . The quadlayered system was compared with gan-bone bilayered system in order to explore the essential differences between two ganoid structures found in nature. These two multilayered systems were found to possess almost identical mechanical properties and relative density at the same ganoine thickness in Fig.

6-8. However, the predicted stress and strain contours indicate the gan-bone bilayer model is more susceptible to surface and interfacial failure than the quadlayer model in the case of $t_{\text{gan}}^{n,t} = 0.2$ because of the elevated tensile radial stress field (S11) on the surface and larger shear strain mismatch around the ganoine-bone interface. As the ganoine thickness increases, the radial stress field (S11) of the gan-bone bilayer model is altered from tension to compression and the magnitude of its interfacial shear strain field (PE23) is also reduced, suppressing interfacial failure. The ganoine-dentin interface appears to be more tolerant to the ganoine thickness than the ganoine-bone interface because of the smaller difference in mechanical properties.

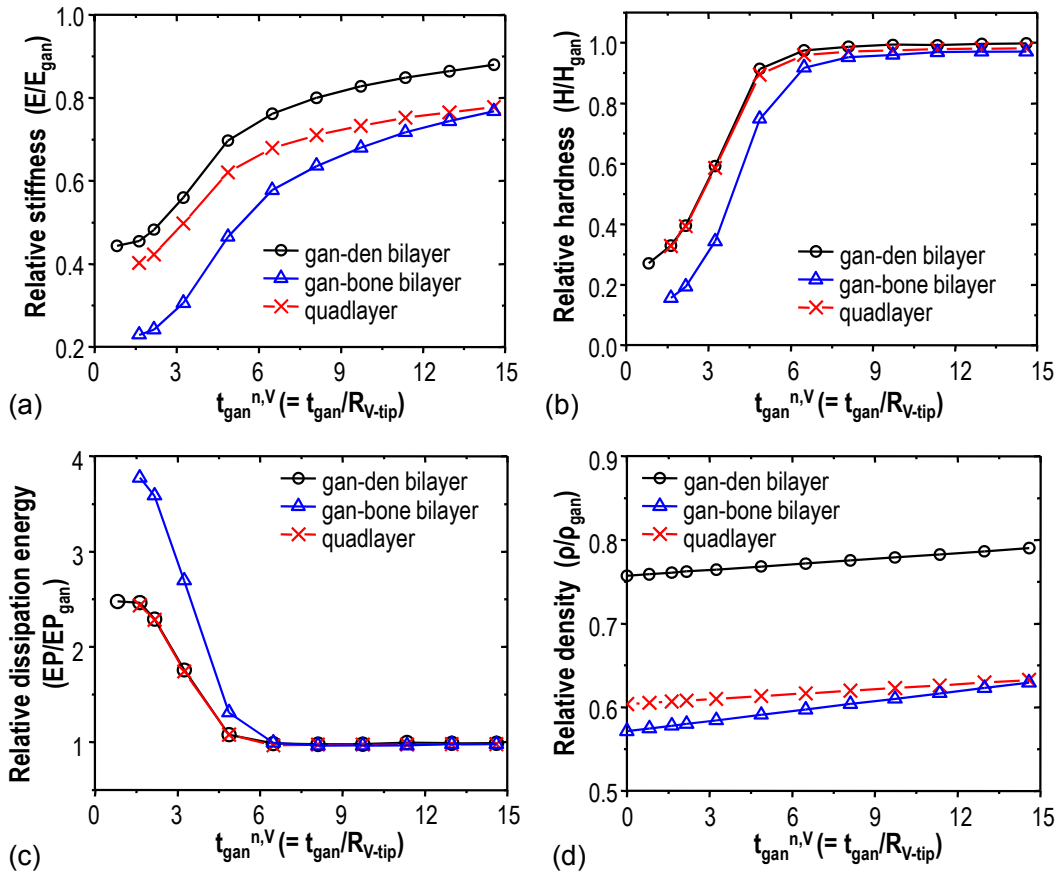
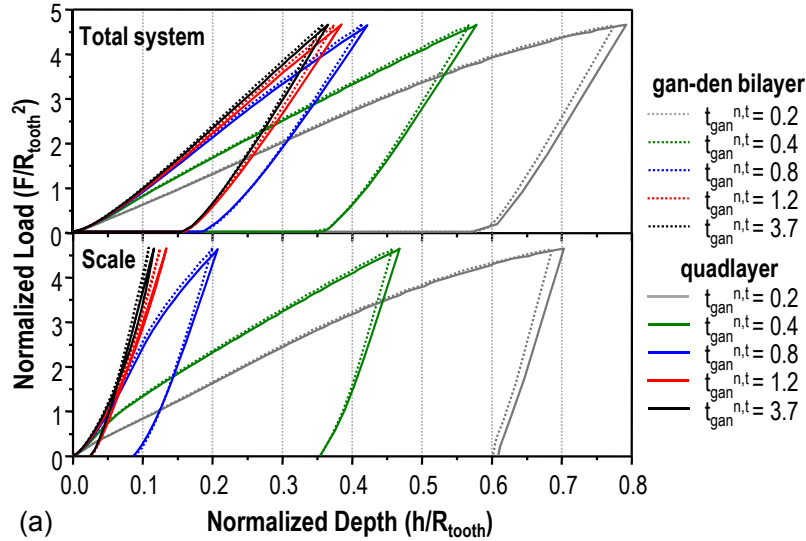
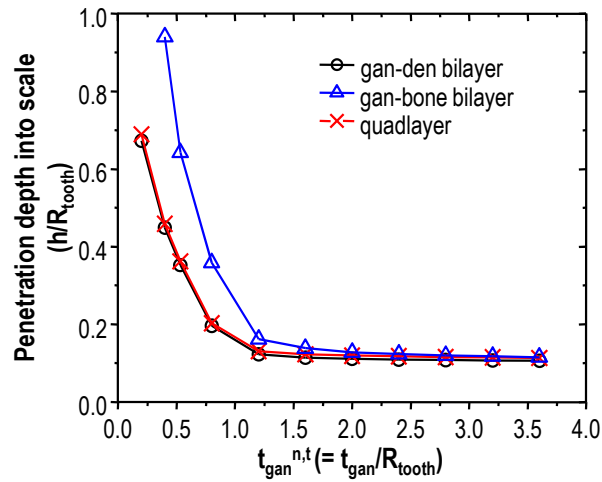


Figure 6-7. The effect of the number of layers (for a perfectly rigid Vickers tip) on the relative mechanical properties, energy dissipation, and density predicted with respect to those of ganoine by finite element simulations during a virtual Vickers microindentation; (a) relative stiffness, (b) relative hardness, (c) relative energy dissipation and (d) relative density as a function of ganoine thickness ($t_{\text{gan}}^{n,V}$) for the gan-den bilayer (black line with open circles), gan-bone bilayer (blue line with open triangles) and quadlayer (red line with cross).



(a)



(b)

Figure 6-8. The effect of the number of layers (for a deformable tooth indenter) on the predicted finite element simulations of the load-depth behavior and normalized penetration depths of the gan-den bilayer FEA models during a virtual microindentation, simulating a hypothetical generic predatory attack of *P. senegalus*; (a) Normalized load-depth curves for different ganoine thicknesses of gan-den bilayer and quadlayer systems, and (b) normalized penetration depths with respect to the total scale thickness (t_{total}^f) as a function of ganoine thickness for the gan-den/gan-bone bilayer and quadlayer models during hypothetical biting events. Penetration depths were normalized the tip end radius of the tooth indenter (R_{tooth}) or total scale thickness (t_{total}^f) and loads were normalized by the square of the tip end radius of the tooth tip (R_{tooth}^2):

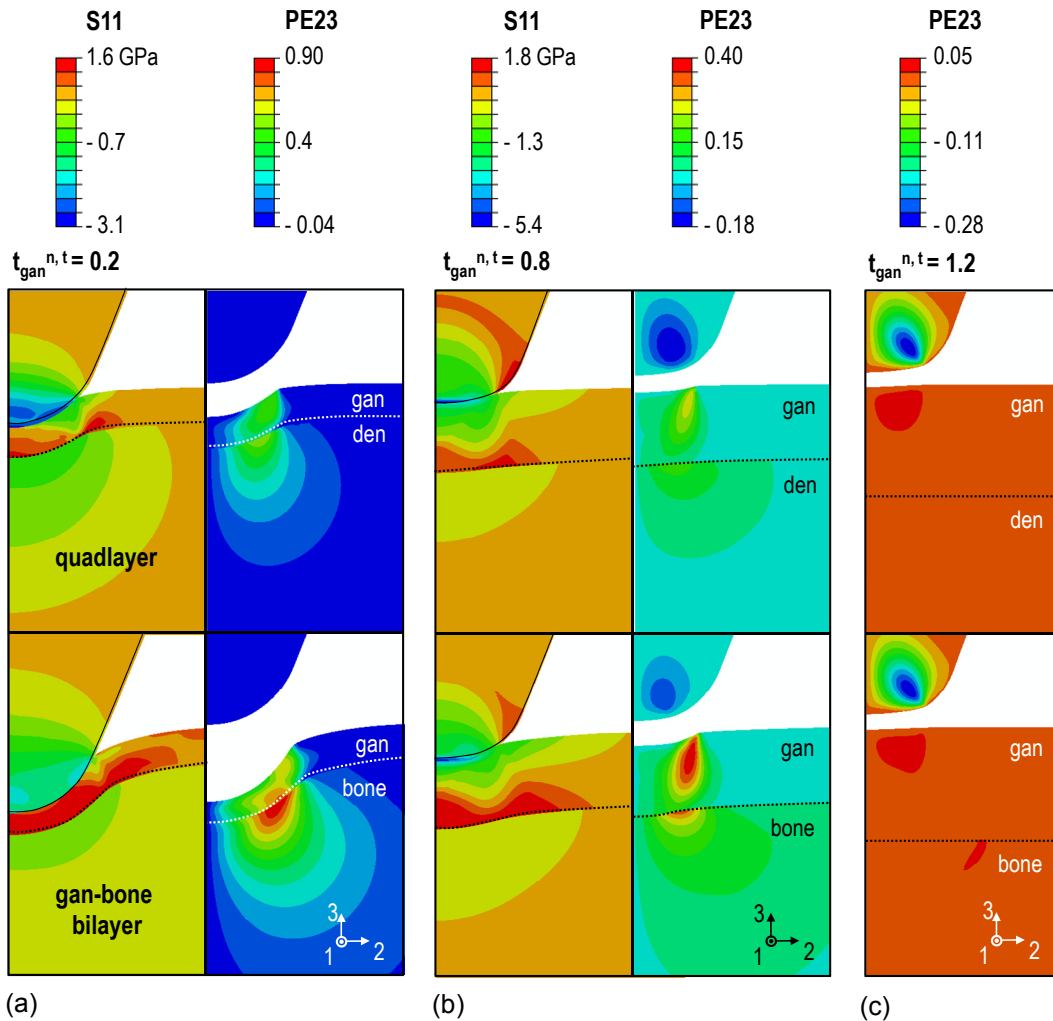


Figure 6-9. The effect of the number of layers on the simulations of contours of stress and plastic equivalent strain, predicted by finite element analysis of a virtual microindentation on the gan-bone bilayer and quadlayer models using a deformable tooth that simulates a hypothetical generic predatory attack of *P. senegalus*. FEA predictions of S11 at a maximum depth when fully loaded, and shear strain (PE23) when fully unloaded for three ganoine thicknesses, (a) $t_g^{n,t} = 0.2$, (b) $t_g^{n,t} = 0.8$ and (c) $t_g^{n,t} = 1.2$.

6.3.3. The Sequence of Layers in the Layered Structure

The outmost layer of natural exoskeletons is often found to be the hardest and stiffest among the constitutive layers in various multilayered systems that also exhibit mechanical gradation through thickness. Virtual Vickers microindentation was carried out using two quadlayered model systems, ‘ganoine-dentin-isopedine-bone (GDIB)’ and ‘dentin-ganoine-isopedine-bone (DGIB)’ at various indentation loads. The predicted load-depth curves of those two multilayered models were shown as compared to two monolithic ganoine and dentin models (‘All Gan’ and ‘All Den’) in Fig. 6-10a. The load-depth curves from two multilayered systems are located in between the load-depth curves of two monolithic systems while the ‘DGIB’ quadlayered model is skewed to dentin, displaying more compliant and softer load-depth behavior than the ‘GDIB’ quadlayered model.

The multilayered systems have load-dependent mechanical behavior against penetration events (Fig. 6-10b and c). The ‘DGIB’ quadlayered model behaves like dentin at the maximum loads of ~ 0.1 N, and becomes stiffer and harder than dentin as the applied maximum loads increase. In the ‘DGIB’ quadlayered model, hardness is less sensitive to the maximum load than stiffness, remaining similar to that of dentin. On the other hand, the ‘GDIB’ model with negative gradient of mechanical properties from ganoine to bone exhibits gradual decreases of effective stiffness and harness. Thus, the ‘GDIB’ model has the high initial effective stiffness that is close to ganoine. Moreover, the outmost dentin layer of the ‘DGIB’ quadlayered model dissipates more energy than the outmost ganoine layer of the ‘GDIB’ quadlayered model up to the maximum load of 0.8 N because of softer and more compliant dentin. However, under higher load conditions (> 1 N), the ‘GDIB’ model begins to dissipate more energy than the ‘DGIB’ model, evident of increased contribution of its underlying dentin layer to energy dissipation.

The calculated contours for stress and plastic equivalent strain are shown in Fig. 6-11 when fully loaded to 0.5 N (S, S11, S22, S33, S23) and after fully unloaded from 0.5 N (PEEQ). The real multilayered design, the ‘GDIB’ model, of *P. senegalus* scales exhibits the tensile radial stress field on the surface (Fig. 6-11a) that leads to highly advantageous circumferential cracking (observed experimentally in Chapter 3), confining crack evolution within the small local region. Simultaneously, the underlying dentin deforms plastically, dissipating energy into a larger area of the entire structure. The stress contours of the ‘DGIB’ model (Fig. 6-11b) elucidate some extremely interesting results; the interfacial tensile normal and shear stress (e.g. S33, S23) are magnified thereby producing susceptibility to interfacial failure through delamination, which is highly undesirable during a penetrating attack. Moreover, an elevated tensile circumferential field (S11) is generated on the surface which also provides susceptibility to radial cracking, and again is undesirable as this can lead to catastrophic failure. All plastic

deformation takes place in the localized dentin layer with pile-up around the imprinted region while the second ganoine layer remains almost intact, deforming elastically.

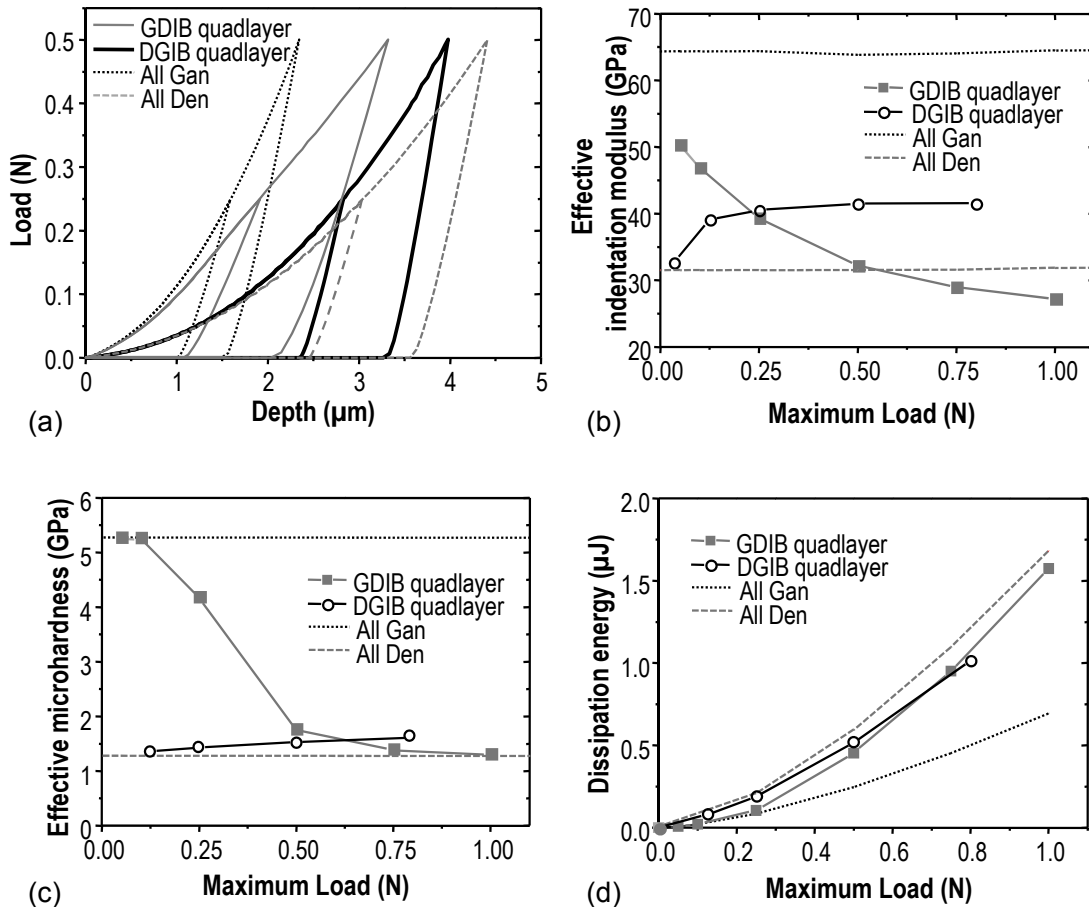
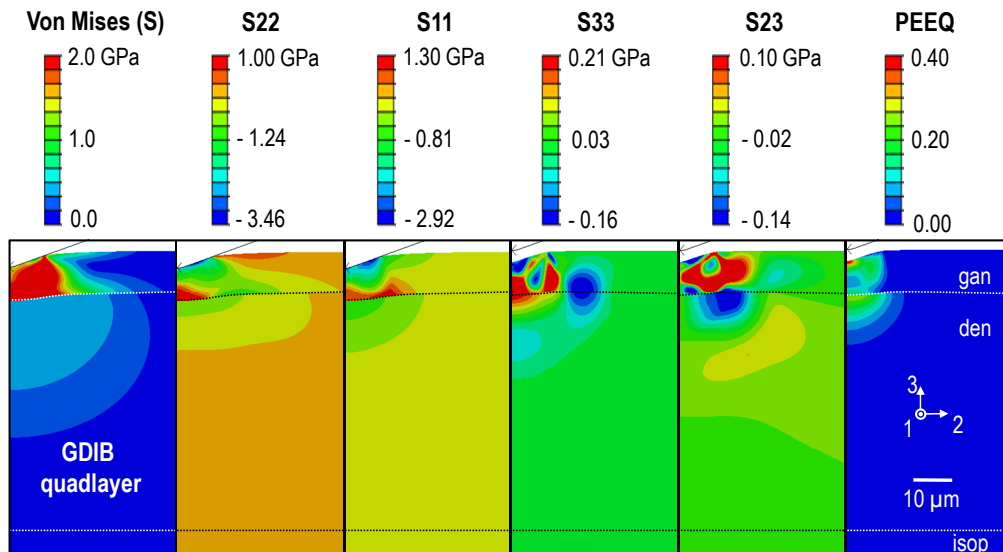
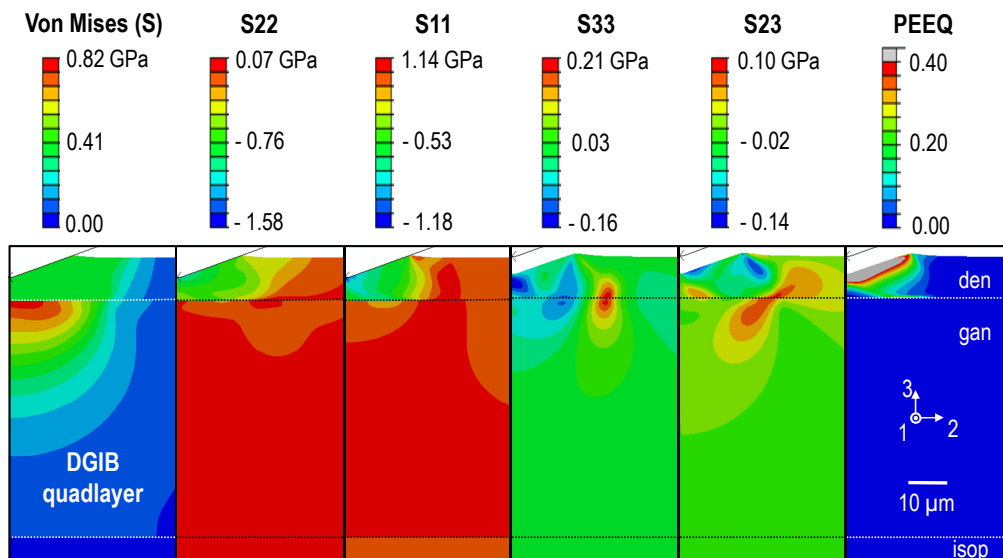


Figure 6-10. The effect of layer sequence (for a perfectly rigid Vickers tip) on the predicted finite element simulations of the load-bearing capability and energy dissipation of the ‘GDIB’ (ganoine-dentin-isopedine-bone) and ‘DGIB’ (dentin-ganoine-isopedine-bone) quadlayer models during a virtual microindentation, simulating a Vickers indentation; (a) Load-depth curves for two different quadlayer systems, (b) effective indentation modulus, (c) effective microhardness, and (d) energy dissipation as a function of maximum indentation load.



(a)



(b)

Figure 6-11. The effect of sequence (for a perfectly rigid Vickers tip) on the simulations of contours of stress and plastic equivalent strain, predicted by finite element analysis of a virtual Vickers microindentation on the ‘GDIB’ and ‘DGIB’ quadlayer models. FEA predictions of Von Mises stress (S), S22, and S11 at a maximum depth when fully loaded, and S33, S23 and equivalent plastic strain (PEEQ) when fully unloaded at the maximum load of 0.5 N for (a) ‘GDIB’ quadlayer model and (b) ‘DGIB’ quadlayer model.

6.4. Discussion

In this Chapter, the various multilayered structures were explored in terms of their mechanical performance as well as relative density by varying the multilayer designs (layer thickness, number, sequence of layers). One of main purposes of multilayer designs in natural exoskeleton systems is to achieve effective penetration/load resistance of armor against potential environmental threats (Spearman, 1973; Wainwright et al., 1976; Uozumi and Suzuki, 1981; Parsons, 1982; Spears et al., 1993; Tirrel, 1994; Wang et al., 1997; Weiner and Addadi, 1997; Currey, 1999; Chateigner et al., 2000; Yannas, 2001; Willmer, 2002; Li et al., 2004; Vincent and Wegst, 2004; Raabe et al., 2005; Rodriguez-Navarro et al., 2006; Fritsch and Hellmich, 2007; Al-Sawalmih et al., 2008; Cheng et al., 2008; Ortiz and Boyce, 2008; Cheng et al., 2009; Sire et al., 2009; Yao et al., 2010). In particular, dermal fish armor accommodates mobility/flexibility in addition to protection by reducing the weight of armor units or articulating segmented armor units. The stiffest and hardest constitutive material layer of multilayered fish scales is frequently observed to be the outmost layer while the number of underlying layers are more compliant and softer, exhibiting the negative mechanical gradient through thickness from surface to the internal body (Fig. 6-12) (Spearman, 1973; Sire et al., 2009). Moreover, the thickness of the outmost layer was found to be influenced by the sharpness of threat system in Chapter 5.

The multilayering behavior of the fish armor system is only observed when the tip end radius of the tooth indenter is comparable to the thickness of the outmost ganoine layer. The underlying dentin layer alters the stress fields of the ganoine surface from tensile circumferential to tensile radial, implying the circumferential cracks are likely to be initiated instead of radial cracks, and dissipates energy into the larger volume, lowering the energy dissipation density effectively. Apparently, the deformable threat system cannot penetrate into the outmost ganoine layer as the thickness of ganoine increases more than the tip end radius of threat. However, the fish armor system also becomes heavier, indicating a trade-off between protection and mobility in terms of the ganoine thickness.

The number of constitutive layers in the fish scale systems facilitates balance between protection and mobility (Gemballa and Bartsch, 2002; Arciszewski and Cornell, 2006). There are three major hydroxyapatite (HAP)-organic nanocomposite systems found in organisms (Moss, 1972; Wainwright et al., 1976; Ruben and Bennett, 1987; Lowenstam and Weiner, 1989; Driessens and Verbeeck, 1990; Wegst and Ashby, 2004; Leventouri, 2006); (i) hypermineralized enamel-like composite (enamel, ganoine, hyaloine etc.); (ii) dentin-like composite (orthodentin, mesodentin, semidentin etc); and (iii) bone-like composite (lamella bone, elasmordine etc.). The mineral content of those

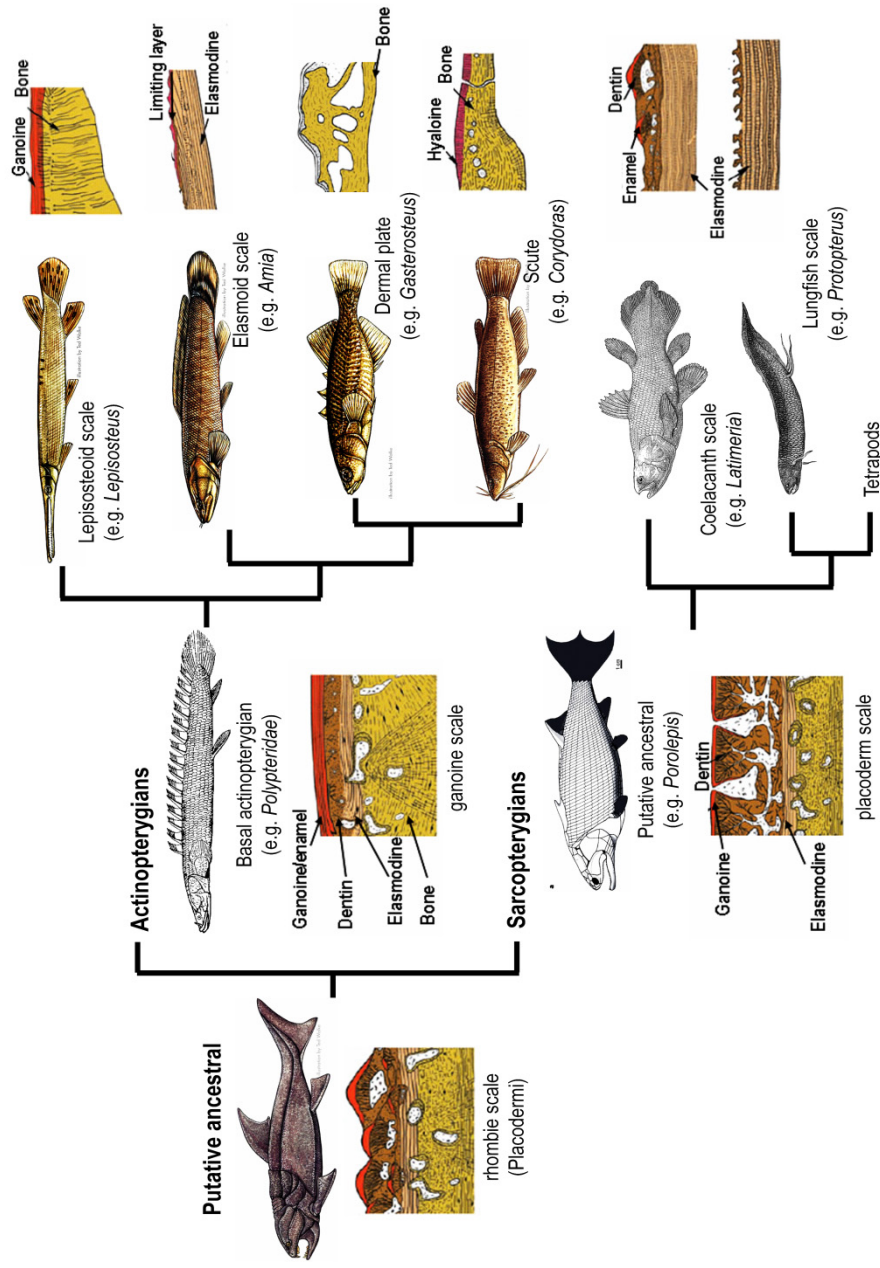


Figure 6-12. Proposed evolution process of the integumentary skeleton in non-tetrapods where two main streams of evolution from ancient fish appear depending on the way to reduce the weight of armor scales: (i) reduction of odontogenic component among actinopterygians, and (ii) incorporated pore canal system among sarcopterygians (Sire et al., 2009). Images were mainly from Sire's 2009 paper (Sire et al., 2009).

†Images of Placodermi (<http://lexikon.freenet.de/Placodermi>, last access on May 16, 2011), Porolepis (Zhu et al., 2009), Polypterus (<http://en.wikipedia.org/wiki/Bichir>, last access on May 16, 2011), Latimeria (<http://cas.bellarmine.edu/tietjen/images/Coelacanth.jpg>, last access on May 16, 2011), Protopterus (http://users.tamuk.edu/kfjab02/Biology/Vertebrate%20Zoology/b3405_ch08.htm, last access on May 16, 2011), Other fish species (<http://www.fish.state.pa.us/pafish/fishtms/chapindx.htm>, last access on May 16, 2011).

HAP composite systems is directly related to their mechanical properties. As shown in material property charts of Fig. 6-13 (Wegst and Ashby, 2004), HAP composite systems exhibit their own material properties, enabling a wider range of materiality with the limited number of constitutive materials: enamel is the stiffest, heaviest with the lowest fracture toughness while bone is the most compliant, lightest with the highest fracture toughness among three HAP composite systems. The multilayer designs combine these HAP composite systems as a layered structure, taking advantages of each of the composite systems. In Fig. 6-7, the quadlayered system has almost the same mechanical properties as the bilayered system with lighter weight at the same thickness of ganoine. Moreover, the additional two layers (isopedine and bone) of the quadlayered system have unique microstructures with higher fracture toughness as compared with the two outer layers (ganoine, dentine). Even though three multilayered systems (ganoine-dentin, ganoine-bone, and ganoine-dentin-isopedine-bone) were explored in this study, other multilayered systems also exist (e.g. various fish scale systems in Fig. 6-12) (Sire et al., 2009). The bilayered structures that have the outer hypermineralized HAP composite layer with the underlying bony basal layer are common in current living fish species (Moss, 1963; Sire, 1990; Sire et al., 2009), which can be lighter than the ganoine-dentin bilayered structures, yet showing the similar mechanical performance. However, as compared to the interface between ganoine and dentin of quadlayered systems, the interface between ganoine and bone layers in ganoine-bone bilayered systems is more vulnerable to delamination because of larger mechanical mismatch (Jayachandran et al., 1995). Therefore, the thickness of the outer hypermineralized layer becomes more crucial in the bilayered system than the quadlayered system. At the same areal density of structures, load-depth behavior, effective material properties and stress/strain distribution of ganoine-bone and ganoine-dentin-isopedine-bone systems are comparable where the ganoine layer of the bilayered structure is thicker than that of quadlayered structure (Figs. 6-7 and 6-9). In terms of mineralization, the quadlayered systems of primitive Polypteridae scales need both odontogenic and osteogenic processes for synthesis of four different layers while the bilayered systems of most teleost fish show reduction or loss of either process, implying that evolution has simplified processing/fabrication of fish armor units (Lowenstam and Weiner, 1989; Driessens and Verbeeck, 1990; Sire et al., 2009).

The sequence of layers in the multilayered systems is also one of important structural parameters (Jayachandran et al., 1995; Suresh, 2001). The sequence of layers is correlated with spatial distribution of mechanical properties through thickness. The *P. senegalus* scales were found to have negative mechanical gradient from ganoine to bone, which is a key factor for multilayering effects as discussed in previous Chapters 3 to 5. The modified multilayered system by means of the reversed of ganoine and dentin layers displays the local positive mechanical gradient from outmost dentin to the underlying

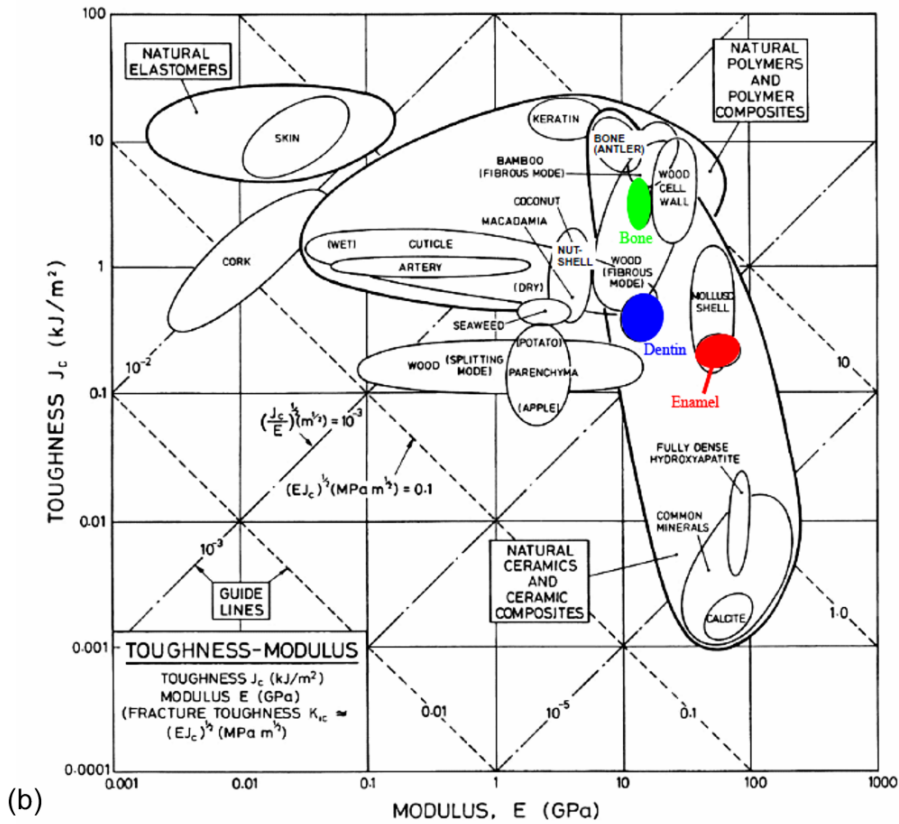
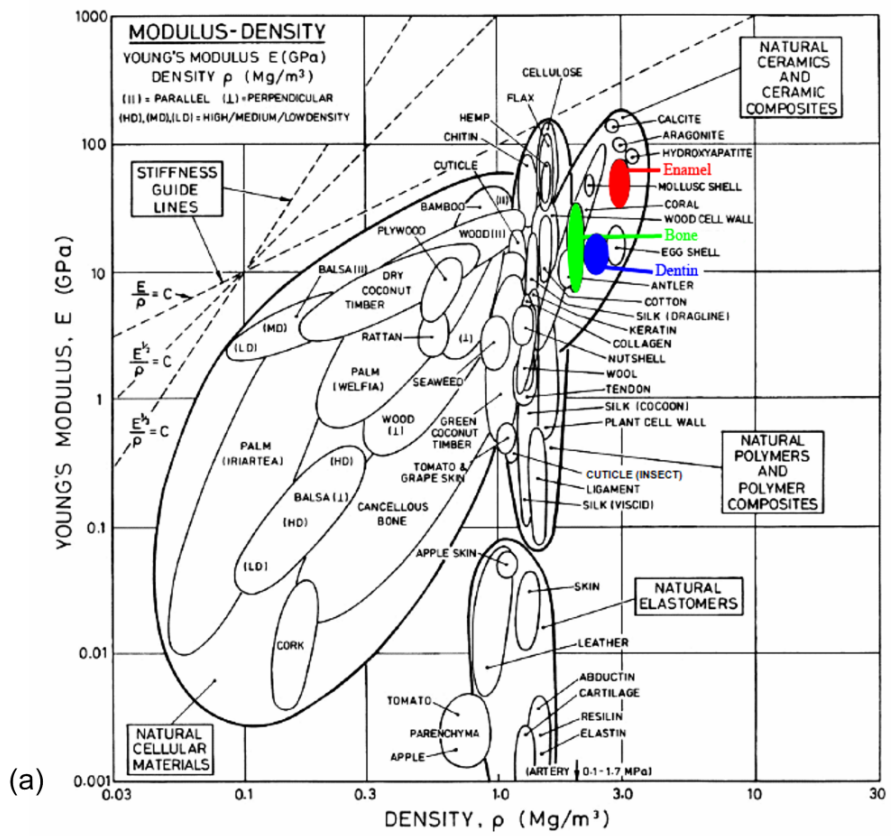


Figure 6-13. Material property charts (Wegst and Ashby, 2004) for natural materials, plotting (a) Young's modulus against density and (b) toughness against Young's modulus. Guidelines identify either structurally efficient materials which are light and stiff (a) or materials best able to resist fracture under various loading conditions (b).

ganoine. The interfacial failure between the dentin and ganoine layers is highly probable because of the concentrated tensile and shear stress fields around the interface. The multilayered systems of some species have a relatively thin organic layer, covering the hard mineralized layers (e.g. dermal fish armor (Ørvig, 1968), endoskeleton of echinoderm (Willmer, 2002)) or densely packed chitin-protein layers (e.g. insects (Wainwright et al., 1976; Cheng et al., 2009), crustacean (Al-Sawalmih et al., 2008; Cheng et al., 2008)) while some mollusk species (e.g. *Crysmallon squamiferum* (Yao et al., 2010)) have an intermediate polymer layer between mineralized layers. The organic layers in the multilayered natural exoskeleton systems can dissipate energy, but often exist for the purpose of other functionality (e.g. optical reflection (Parker et al., 1998), sensing (Montgomery et al., 1995), drag reduction (Bushnell and Moore, 1991), barrier of mineral dissolution (Spearman, 1973), etc.) rather than load-bearing and penetration resistance.

Other structural parameters also diversify multilayered structures. For instance, porosity was one of the evolutionary processes in fish scales (Sire et al., 2009). Sarcopterygians incorporated pore canals in their armor units in order to reduce the armor weight at the effective volume. A porosity gradient observed in sea urchin spines and fish scales or plant cells provides effective mechanical functionality at minimal weight. On the other hand, some organisms have evolved their natural armor systems by means of utilizing a different range of material spectrums and have developed on-demand functionality in response to their environmental constraints in order to maximize their survivability. In this chapter, the HAP-organic composite systems mainly found in the dermal fish armor systems were explored. Calcium carbonate-organic composite systems in invertebrates (Chateigner et al., 2000; Willmer, 2002), silica-organic systems in a few invertebrate species (Woesz et al., 2006), chitin-protein systems in crustaceans and insects (Al-Sawalmih et al., 2008; Cheng et al., 2008; Hild et al., 2008; Cheng et al., 2009; Hild et al., 2009) or cellulose systems in plants (Wainwright et al., 1976; Lucas et al., 2000; Bucur and Declercq, 2006) also appear as multilayered structures with unique functionality.

Multilayer designs of various natural exoskeleton systems enable multifunctionality (e.g. protection and mobility/flexibility of fish armor) by varying the structural parameters and the materiality of individual constitutive material layers. Mechanical properties of individual natural materials in Fig. 6-13 can give an idea about individual constitutive material layer, whereas multilayered systems with the number of those individual material layers enable material properties to be tuned and

multifunctionality to be imposed. For example, biomimetic laminated metallic composite systems inspired by the nacreous layer of mollusk shells have been developed by varying the material of layers and incorporating sensors in the internal layers, exhibiting amplified mechanical performance with sensing capability (Vecchio, 2005; Ortiz and Boyce, 2008). Table 6-3 can provide insights to advantages and disadvantages multilayer designs depending on their structural parameters. A better understanding of multilayer design principles can provide new insights to man-made material systems.

Table 6-3. Tabulated advantages and disadvantages of multilayer designs depending on their structural parameters

Structural parameters of multilayer designs		Advantages	Disadvantages
Thickness of the hardest outmost layer	Too thin	<ul style="list-style-type: none"> • Largest weight reduction 	<ul style="list-style-type: none"> • No mechanical benefit from the outmost layer, exhibiting effective mechanical behavior is closes to one of the second layer • Increased susceptibility to interfacial failure
	Optimal	<ul style="list-style-type: none"> • Multilayering effect • Efficient weight reduction 	<ul style="list-style-type: none"> • Difficulties with determination of a unique optimal solution because it is sensitive to mechanical environments
	Too thick	<ul style="list-style-type: none"> • Increased capability of protection by heavy and hard armor 	<ul style="list-style-type: none"> • Loss of multilayering effect under the loading condition • Increased susceptibility to radial surface crack • Increased weight/increased energetic cost for processing
Layer number	Monolithic hard layer	<ul style="list-style-type: none"> • Relatively simpler processing/fabrication as compared with multilayered systems 	<ul style="list-style-type: none"> • Increased susceptibility to radial surface crack • Required hierarchical and intricate nano-/micro-structures for mechanical amplification (e.g. bone, nacre, etc.) • High energetic cost per volume
	Multilayer	<ul style="list-style-type: none"> • Multilayering effect • Increase potential for multi-functionality with increase of a layer number • Protection mechanisms of each constitutive layer 	<ul style="list-style-type: none"> • Increased interfacial problems • Increased complexity of processing/fabrication
Layer sequence	Hard outer to soft inner	<ul style="list-style-type: none"> • Multilayering effect with penetration resistance 	<ul style="list-style-type: none"> • Reduced mechanical performance (load-bearing capability) with increased load
	Soft outer to hard inner	<ul style="list-style-type: none"> • Non-mechanical functionality of a soft outmost layer, e.g. dissolution barrier, optical reflector, etc. 	<ul style="list-style-type: none"> • Sacrifice of the outer layer during penetration events by threat • Increased susceptibility to interfacial failure between outer soft and underlying hard layers

6.5. Conclusion

Natural exoskeletons are known to exhibit a huge diversity of structure and properties as they have adapted to environmental and predatory threats; typically balancing protection and mobility requirements to maximize survivability. Most exoskeletal materials are composed of different layers of materials where each layer possesses its own unique composite nanostructure, mechanical properties, and deformation mechanisms. The required and desired functionality of a multilayer design can be achieved by varying its structural parameters (e.g. layer thickness, sequence and number). The multilayered structure of *P. senegalus* scale armor facilitates effective penetration resistance to potential threats, achieving a good balance between protection and mobility. The hardest and stiffest ganoine with an optimal thickness (that is often comparable to the sharpness of threat) sustains load, effectively mitigating the penetration of threat, in collaboration with its underlying dentin layer that dissipates energy, transmitted from ganoine. The additional two bottom layers, isopedine and bone, can further reduce weight than the ganoine-dentin layered structure, maintaining the similar level of protection under the same circumstance and also provide their own penetration resistance mechanisms as the third or fourth line of defense to the whole system.

Chapter 7.

Quantitative Microstructural Study of Marine Threespine Stickleback Armor

This chapter was published as a regular article: J.H. Song, S. Reichert, I. Kallai, D. Gazit, M. Wund, M.C. Boyce, and C. Ortiz, Quantitative microstructural studies of the armor of the marine threespine stickleback (*Gasterosteus aculeatus*). *Journal of Structural Biology*, 2010. 171(3): p. 318-331.

7.1. Introduction

The threespine stickleback (*Gasterosteus aculeatus*) has become a promising model system to investigate the genetic and ecological origins of adaptive phenotypic evolution, through the assessment of macroscopic morphology for divergent populations from differing environments (Hagen and Gilbertson, 1973; Bell et al., 1993; Reimchen, 1994; Foster, 1995; Cresko et al., 2007; Kingsley and Peichel, 2007; Östlund-Nilsson et al., 2007; Baker et al., 2008). Morphological assessment of *G. aculeatus* has involved the measurement of body features (e.g. size, shape), as well as the quantification of the dimensions and geometry (e.g. length, shape, position, number) of its distinctive external bony armor components which include: a series of lateral plates, three dorsal spines, a pair of pelvic spines, and a complex pelvic girdle (Nelson, 1971; Reimchen, 1983; Bell, 1987). The dermal plates of the threespine stickleback are anisotropic in shape (oval to rectangular), conformal to the body of the fish, porous, and composed of acellular lamellar bone (Reimchen, 1983; Sire et al., 2009). They additionally interlock with the ascending branch of the pelvic girdle, the basal plate of the dorsal spines, and with each other via an articulation mechanism located along the lateral line, which is shifted towards the dorsal side of the body (Nelson, 1971; Reimchen, 1983; Bell, 1987) (Fig. 7-

1). The pelvic and dorsal spines are attached to the pelvic girdle and basal plate, respectively, with a peg-and-socket interconnection (Nelson, 1971; Reimchen, 1983; Bell, 1987). *G. aculeatus* is known to undergo rapid and dramatic evolutionary adaptations of its armor and associated genetic isolation within as few as eight generations (Bell et al., 2004; Kristjansson, 2005). Marine threespine sticklebacks, which represent the ancestral condition (Bell and Foster, 1994), possess a continuous row of lateral armor plates (~ 30-36, “complete morph,” Fig. 7-1) while evolutionarily derived, freshwater sticklebacks often exhibit a reduction in the number of plates (~ 0-9, “low morph”), or, less commonly, an intermediate number of plates (“partial morph”) (Hagen and Gilbertson, 1973; Bell, 1977; Bell et al., 2004). The loss of armor in freshwater populations has been attributed to a variety of factors: low ion concentrations which increase the mineralization “cost” of armor, a juvenile growth advantage, reduced weight and increased maneuverability affording quicker access to cover from predators, and a decreased range of predators (Giles, 1983; Bell et al., 1993; Reimchen, 1995; Reimchen, 2000; Bergstrom, 2002; Kristjansson, 2005; Marchinko and Schluter, 2007; Östlund-Nilsson et al., 2007). Armor loss in freshwater populations might also be partly due to correlated selection on other traits, since the main genetic locus controlling plate reduction (*Eda*) is linked to loci involved in the regulation of salt secretion and parasite susceptibility (Colosimo et al., 2005; Marchinko and Schluter, 2007).

In this study, we present a quantitative, materials science-based approach to the investigation of the microstructure of field-caught marine *G. aculeatus* armor, which provides useful phylogenetic information and insights into the biomechanical function of the armor of both the evolutionary ancestral state, as well as subsequent morphs. From a comparative morphological perspective, this information is not only relevant to the evolution of armor within the threespine stickleback radiation (e.g. partially armored freshwater, fully armored anadromous), but also could form the basis for comparison with other stickleback species that have lateral plates (e.g. Brook stickleback, *Culaea inconstans*, ninespine stickleback, *Pungitius pungitius*) (Mattern, 2004). Microcomputed tomography (μ CT) was employed to create full three-dimensional images of the dorsal spines and basal plate, lateral plates, pelvic girdle and spines and to assess structural and material properties such as the spatial distribution of thickness, the cross-sectional geometry, plate-to-plate interconnections and overlap, bone mineral density, and bone volume. Three-dimensional printing was employed to create scaled-up macroscopic prototypes from the μ CT data to more clearly visualize the detailed morphometry, as well as to better understand degrees of freedom and ranges of motion of the armor joints. Mercury porosimetry was used to determine the pore size distribution and volume percent porosity of the lateral plates. Back-scattered electron microscopy (BSEM) and energy dispersive X-ray analysis (EDX) were utilized to quantify the weight percent mineral content within individual lateral plates (Lloyd, 1987; Skedros et al., 1993; Bloebaum et

al., 1997; Roschger et al., 1998). Scanning electron microscopy (SEM) and surface profilometry were used to characterize the interior and exterior surface topography of the lateral plates and pelvic spines. Aside from evolutionary relevance, detailed studies of the structure and properties of biological armor hold broad applicability to the development of synthetic engineered, protective penetration-resistant materials (e.g., human body, vehicle, and building structure), protective coatings (e.g., exterior paint of automobiles, motorcycles, etc.), construction applications (e.g., pipelines that need resistance to rock penetration/abrasion), and sporting equipment (e.g., helmets, chest protection, etc.) (Arciszewski and Cornell, 2006; Ortiz and Boyce, 2008; Yao et al., 2010). Particularly relevant are interlocking mechanisms, plate geometry, porosity, compositional gradients, surface topology, and their relation to penetration resistance and biomechanical mobility (mechanical mechanisms of movement in living organisms, e.g. joint degrees of freedom, ranges of motion, etc.). Hence, the results obtained in this study are discussed in the context of mechanical function, performance, fitness, and survival advantage. These data are currently being used to create finite element based-computational models for virtual biomechanical simulations, as well as for the fabrication of biomimetic armor prototypes using three-dimensional printing methods.

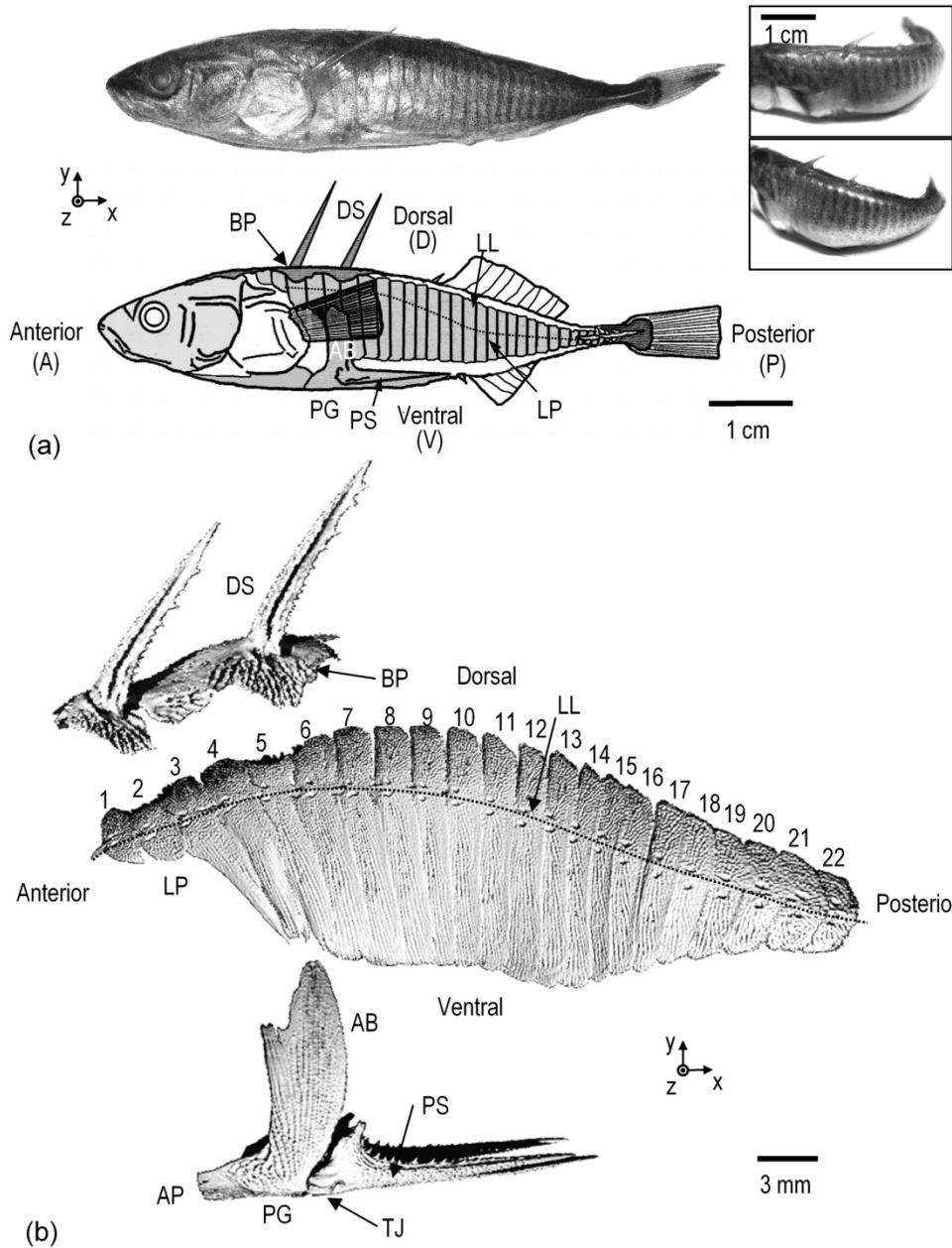


Figure 7-1. Three-dimensional structure of armor plate assembly of marine *Gasterosteus aculeatus* (threespine stickleback); (a) photographs and schematic illustration and (b) μ CT images of disassembled armor components with dorsal spines (top), lateral plates (center), and pelvic girdle/spines (bottom) in rest position. “AB”= ascending branch of the pelvic girdle, “AP”= anterior process, “BP” = basal plate, “DS” = dorsal spines, “LL” = lateral line, “LP” = lateral plates, “PG” = pelvic girdle, “PS”= pelvic spines, and “TJ”= trochlear joint.

7.2. Methods

Samples Field caught marine *G. aculeatus* (threespine stickleback) were collected in South-Central Alaska (“Rabbit Slough,” 61°32'9.87"N, 149°15'14.03"W) in June, 2009. The marine sticklebacks spent approximately two years in the ocean (~ 32 ppt salinity) and were caught on their breeding grounds in freshwater. The fish were euthanized with an overdose of MS-222, a fish anesthetic (Clark University IACUC approval #010R). They were stored frozen until the experiments were carried out. The lateral plates and pelvic spines were removed from the fish body using forceps and dissecting scissors. A few of the lateral plates near the posterior caudal fin were too small to be extracted. Hence, 22 of the ~ 35 lateral plates were removed.

Microcomputed Tomography The lateral plates and pelvic spines were scanned with a micro-CT (μ CT) system (Viva CT40, Scanco Medical AG, Switzerland) operated at 45 kV and 177 μ A. Microtomographic slices were recorded every 10 μ m or 20 μ m and were reconstructed with $10 \times 10 \mu\text{m}$ or $20 \times 20 \mu\text{m}$ voxels (volume elements) in plane. A constrained three-dimensional (3D) Gaussian filter ($\sigma = 0.8$ and support = 1) was used to partially suppress noise in the volumes. In addition to a visual assessment of structural images, the spatial distribution of cross-sectional thickness (z -direction) for an individual plate and the entire lateral plate assembly were determined (Hildebrand et al., 1999). Moreover, the three-dimensional geometric information of the scanned samples was converted into three-dimensional polygonal meshes (stereo-lithography - STL, bilinear and interplane interpolation algorithm) using an interactive medical image control system (MIMICS 9.0, Materialise, Belgium). The converted STL file was imported into a CAD (Computer-aided design) software (RHINOCEROS[®], Robert McNeel and Associates, USA). The mean cross-sectional thickness (z -direction) for: individual lateral plates, the non-overlapping regions of individual lateral plates, and the overlapping region between two lateral plates was calculated as a function of lateral plate number (Appendix D). In order to understand how lateral plates articulate together in the assembly, two interlocking lateral plates (LP9 and 10) on a series of two dimensional μ CT images were contoured and recalculated in three dimensions using MIMICS, and then converted into STL files separately. Surface smoothing and remeshing were subsequently performed to optimize the three-dimensional structure of each lateral plate using RHINOCEROS[®]. In particular, the region near the interlocking joint between two lateral plates was carefully observed in three dimensions. The average bone mineral density (BMD) of each sample was also calculated, related to pure hydroxyapatite as a reference material (Kimelman-Bleich et al., 2009).

3D printing. Macroscopic scaled-up prototypes (approximately $\times 10$) were fabricated via three-dimensional printing (3DP, ZPrinter[®] 310 Plus, ZCorporation, USA) using the Stereolithography (STL) files that were created from micro-computed

tomography data of stickleback armor. It was ensured that the wall thicknesses of the prototype were greater than 2 mm to avoid risk of fracture. The material used was a plaster powder (ZP[®]131 powder, Zcorporation, USA). 89 μm thick layers were laid down using a commercially available binder (Zcorporation, USA) at a vertical build speed of 25 mm/hr. The printed object was rested within the powder bed for more than one hour and subsequently was immersed in a wax bath, which resulted in a smooth and consolidated surface of the final prototype.

Optical / Scanning Electron Microscopy. Lateral plates and pelvic spines were fixed on a steel support using a conductive tape and then sputter-coated with ~ 5 nm of gold-palladium in a Denton Vacuum Desk II (Moorestown, NJ). SEM samples were imaged in a JEOL JSM 6060 (Peabody, MA) scanning electron microscope at the 10 kV acceleration voltage. For cross-sectional imaging, samples were embedded in a low viscosity Spurr resin (Ted Pella Inc., USA) and then sectioned using a diamond impregnated annular wafering saw (Buehler, Isomet 5000 Lake Bluff, IL) at 800–900 rpm. Embedded samples then were polished stepwise with 6 μm and 1 μm silica nanoparticles on a soft pad (Buehler, IL) and with 500 nm silica nanoparticles on microcloth (Buehler, IL). Cross-sectional images of the samples were taken using an optical microscope (Eclipse L150, Nikon, Japan). Backscattered electron microscope (BSEM) images were taken with the JEOL JSM-6700F after all samples were fixed on a steel support. The weight percent mineral contents were estimated based on the image analysis using the BSEM images after calibration with 99.8% pure alumina, 99.9% pure magnesium oxide and 99.9% carbon (Sigma-Aldrich, USA), and 99.9% dense, phase-pure hydroxyapatite (Akao et al., 1981) The mean gray level for BSE images were computed directly from the histogram plot and used to extrapolate the average atomic number based on the calibration of the four known substances and the mean gray level (Lloyd, 1987; Skedros et al., 1993; Bloebaum et al., 1997; Roschger et al., 1998).

Energy Dispersive X-ray Analysis (EDX). The weight percent mineral contents through the cross-section of the scales was quantified by Energy Dispersive X-ray (EDX) spectroscopy analysis using a scanning electron microscope (JEOL JSM-6700F, Japan) equipped with a Noran System Six EDX (Thermo Scientific Co., USA) (Skedros et al., 1993). The data were collected at a 15 kV accelerating voltage with a 10 μA operating current and a 15 cm working distance. For the comparison with results obtained from the BSEM image analysis, the same samples were used for the EDX analysis.

Surface Profilometry. Profilometry (P-16+TM, KLA-Tencor, USA) was used to image the topography of the exterior surface of the lateral plates, e.g. size, density, and inter-spacing distance of tubercles. A 2 μm radius diamond-tipped stylus was scanned (x -direction) at a speed of 50 $\mu\text{m/s}$, an applied force of 2 mg, a sampling rate of 100 Hz, and a spacing of 2 μm in the perpendicular y -direction.

Mercury Porosimetry. The pore size distribution and volume percent porosity of four lateral plates (LP9-12) was measured by a mercury porosimeter (Autopore IV 9500, Micromeritics, USA), which operated at pressures between 3.7 kPa and 14 MPa, corresponding to pore diameters of 404 and 0.107 μm , respectively, at an equilibration rate of 0.03 $\mu\text{l/g}\cdot\text{s}$. A contact angle of 140° was assumed in the pore size calculations.

X-ray Diffraction. The mineral phases of the samples were verified using X-ray diffraction (Philips PANalytical X'Pert PRO diffractometer with $\text{CuK}\alpha$ radiation, Netherlands), operating at 45 kV and 40 mA between 10 and 70° (2θ).

Fourier-Transform Infrared (FTIR) Spectroscopy. The chemical analysis of samples was carried out using a Fourier-Transform Infrared (FTIR) spectroscopy (Nicolet Magma-IR 550 series II, USA) using the KBr method over the wavelength range of $4000 \sim 400 \text{ cm}^{-1}$ at a resolution of 4 cm^{-1} with an average of 128 scans.

Statistical analysis. Statistical analysis was performed using a single factor ANOVA test (Statistics toolbox, MATLAB, MathWorks, USA). P values <0.05 were considered to be significant.

7.3. Results

7.3.1. Three-Dimensional Structure, Dimensions, and Geometry

The marine threespine sticklebacks employed in this study were heavily armored (~30-35 lateral plates), 8 - 9 cm in total length and yet still exhibited significant body flexibility (Fig. 7-1a). The structure and geometry of the armor of a representative fish was derived from three-dimensional renderings of μ CT data, as shown in Fig. 7-1b, which includes the front two of the three dorsal spines (DS) and basal plate (BP) (*top*), the lateral plates (LP, *center*, 1-22 of 35 starting from the anterior), and the pelvic girdle (PG) and spines (PS) (*bottom*), maintaining correct alignment of the components. The pelvic spines are shown in the “rest” position where the spines are parallel to and interlocking with the ventral plates of the pelvic girdle (Fig. 7-1b, *bottom*). These data are consistent with the morphological drawings of refs. (Reimchen, 1983; Bell, 1987) which describe the interconnections between these different armor components. The pelvic ascending branch extended vertically ~ 40% of the body height and overlaid lateral plates 3-6. The lateral plates cover ~ 75 % of the vertical height of the fish body. The pelvic and dorsal spines were ~ 1 cm in length. An interesting exterior surface topography was observed for the lateral plates, pelvic girdle, and pelvic spines (Fig. 7-1b) and will be described in more detail later on.

μ CT was used to quantify the spatial distribution of cross-sectional thickness (z -direction) for a single lateral plate and the lateral plate assembly (Fig. 7-2a). The single lateral plate (LP 10) was found to be centrally thickened (up to ~ 200 μ m) relative to the dorsal and ventral sides (~ 100 μ m) (Fig. 7-2a, *left*). In the lateral plate assembly (Fig. 7-2a, *right*), the region along and below the lateral line was found to exhibit a greater thickness ~ 200-300 μ m compared to the dorsal and ventral sides and this thickness was also greater than that of the single plate (Fig. 7-2a, *left*), presumably due to plate overlap. Figure 7-2b and c show the cross-section of the entire lateral plate assembly, corresponding to the slices indicated in Fig. 7-2a (S1, S2). The first cross-sectional image, S1 (Fig. 7-2b), shows how the lateral plates overlap each other from the anterior to posterior region. Consistent with Fig. 7-2a, the individual lateral plates are centrally thickened relative to its anterior and posterior edges and additionally, each plate overlaps with two neighboring plates on the anterior and posterior sides. Therefore, this heterogeneous cross-sectional geometry combined with dual plate-to-plate overlap results in a relatively constant overall thickness of the armor assembly in the x -direction. The S2 cross-sectional images (Fig. 7-2c) show the dorsal to ventral spatial distribution of thickness for each lateral plate. The dorsal region of LP 1 to 5 is slightly thickened while the other lateral plates show a statistically insignificant variation in thickness vertically (y -direction). Fig. 7-2c also shows the curvature of the lateral plates from the dorsal to ventral sides which allows the armor to remain conformal to the fish body. LPs 1-14

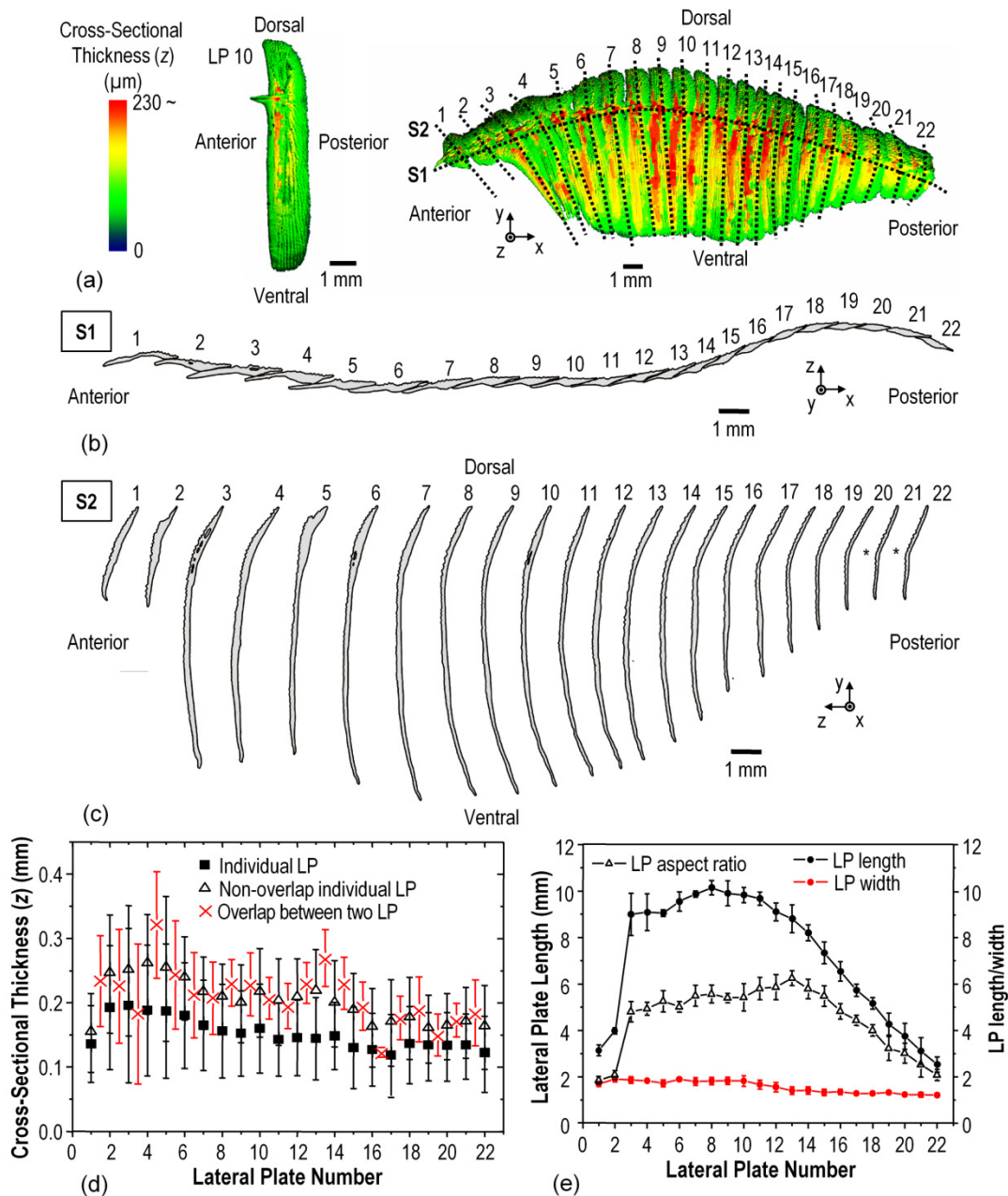


Figure 7-2. Quantitative measurement of the dimensions of a marine *Gasterosteus aculeatus* (threespine stickleback); (a) spatial distribution of thickness for an individual lateral plate (LP 10), *left*, and for the entire lateral plate assembly, *right*. (b) and (c) The schematic cross-section illustrations of entire plate assembly, as indicated in (a); (b) horizontal cross-section image of the assembly (S1) in the x - z plane and (c) vertical cross-section image of the assembly (S2) in the y - z plane), (d) The mean cross-sectional thickness (z -direction) as a function of lateral plate number, calculated from individual lateral plates (filled black square symbols), the non-overlapping regions of individual lateral plates (black triangle symbols), and the overlapping region between two lateral plates (red 'x' symbols) and (e) maximum lateral plate length (filled black circles), width (filled red circle symbols), and aspect ratio (black triangle symbols) as a function of their position in the armor assembly.

maintain an approximately smooth curvature while LPs 15-22 exhibit a increasingly sharper central kink or distinct change in curvature (e.g. see (*) in Fig. 7-2c **LP22**).

In Fig. 7-2d (filled black squares) the mean cross-sectional thickness (z -direction) of the individual lateral plates are plotted as a function of plate number and show a relatively constant value with plate number. The cross-sectional thickness (z -direction) of the non-overlapping regions of the individual LPs (Fig. 7-2d, triangles) and the overlapping regions between two LPs (Fig. 7-2d, crosses) are statistically similar and greater than the mean cross-sectional thickness of the individual lateral plates (Fig. 7-2d, filled black squares) ($p < 0.05$). This result again shows how the heterogeneous cross-sectional geometry combined with dual plate-to-plate overlap results in a relatively constant overall thickness of the armor assembly in the x -direction. The mean thickness of individual plates was found to be $151 \pm 71 \mu\text{m}$, while the plate assembly exhibited a mean thickness of $196 \pm 77 \mu\text{m}$. The lateral plate length (3-10 mm) and aspect ratio (2-6) varied with plate position (Fig. 7-2e) and showed a maximum length of 10 mm (LP10) and aspect ratio of 6 (LP14). The lateral plate width exhibited much less variation, decreasing from 2 to 1.2 mm with plate position from the anterior to the posterior regions (Fig. 7-2e), with a mean value of $1.6 \pm 0.3 \text{ mm}$.

Detailed two-dimensional cross-sectional μCT images of interconnected lateral plates 9, 10, and 11 at four different positions from the dorsal to ventral sides, showed many interesting features (Fig. 7-3a). The non-uniform cross-sectional geometry (x - z) with centrally thickened region that was observed earlier in Fig. 7-2b is shown here in greater detail (Fig. 7-3a). The centrally thickened regions are observed to contain large heterogeneous pores sandwiched between an exterior denser, textured surface region and an interior denser, relatively smooth region (Fig. 7-3a (*right*), note: in some locations it is difficult to see the textured outer layer because of the scan size and contrast, however, it was verified that this layer is in fact continuous). Such a sandwich-like structure is expected to be beneficial for bending stiffness and strength at minimum weight (note: the lateral plate pores are filled with body fluid which is expected to be similar in density to seawater (Moss, 1972)). Features of the interlocking joint are seen in the S2 cross-section of Fig. 7-3a; further details of this joint are shown later. The plate-to-plate overlap (ranging from 0.2 to 0.5 μm , 10 - 25 % of lateral plate cross-sectional width, x -direction) is also apparent in Fig. 7-3a (*right*) and enables the armor assembly to maintain a relatively constant thickness in the x -direction (Fig. 7-3b). Gaps are observed between the overlapping surfaces of lateral plates, presumably where organic material exists (Fig. 7-3a (*right*) and 7-3b). The exterior surface topography observed in Figs. 7-1b, 7-2a and 7-3a (*left*) is seen here to be quite significant relative to the thickness of the plate (Fig. 7-3a (*right*) and b). The cross-sectional areas for lateral plate 10 ranged from 0.16-0.25 mm^2 depending on position in the y -direction (Fig. 7-3a, *right*).

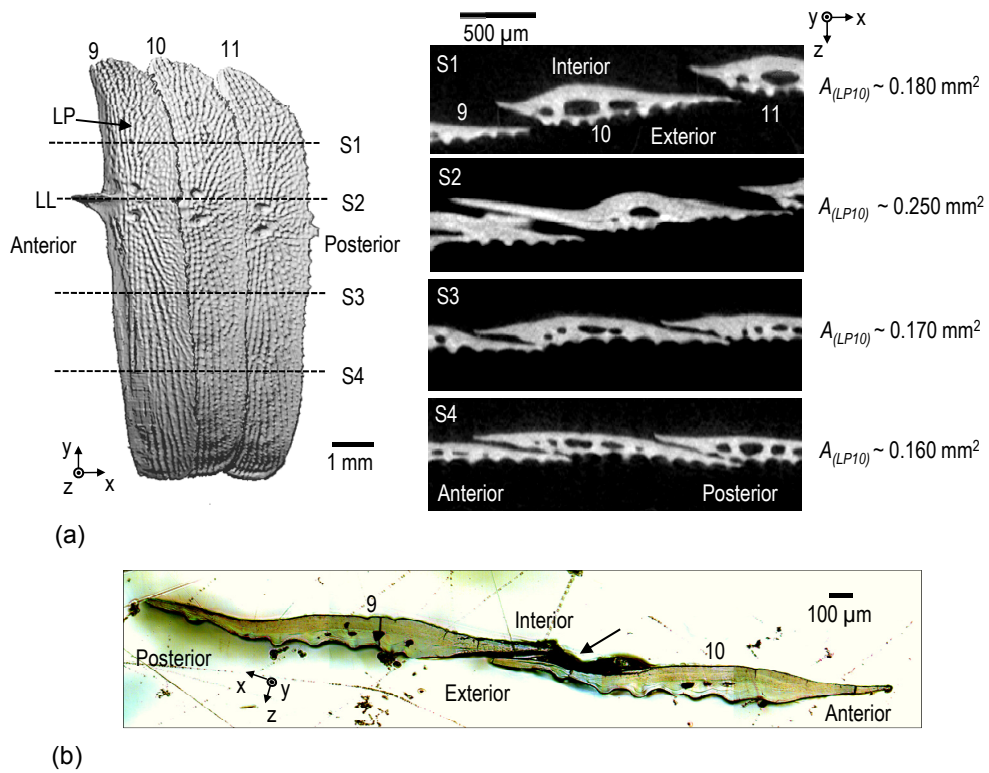


Figure 7-3. Lateral plate cross-section of a marine *Gasterosteus aculeatus* (threespine stickleback); (a) two-dimensional μ CT slices (*right*) corresponding to each section indicated in the three-dimensional structure (*left*) and (b) optical micrograph image of two interconnected lateral plates embedded in epoxy. The black arrow of (b) indicates the connective tissue between two lateral plates.

The three-dimensional structure of the fully formed pelvic girdle viewed from a variety of orientations in the rest state is shown in Figs. 7-4 and 7-5 and is consistent with previously reported morphological drawings (Nelson, 1971; Bell, 1987). Here, many fine details of the structure are revealed. The frequency and amplitude of the zig-zag median suture connecting the two bilateral ventral plates is observed to vary spatially from the anterior process to the posterior (Figs. 7-4a, 7-4b and 7-5a). While the amplitude decreases approximately linearly from the anterior to the posterior, the frequency is observed to be a maximum near the trochlear joint. The exterior surface of the pelvic girdle-spine assembly has a distinct topography (Fig. 7-4a and c), whereas the interior surface is relatively smooth (Fig. 7-4b), similar to the lateral plates. The two interlocking ventral pelvic plates are thickest at the trochlear joint and show a porous internal structure (Figs. 7-4d and 7-5b-d). Fig. 7-4e shows the cross-section of the pelvic girdle and spines, corresponding to the two slices indicated in Fig. 7-4d (S1, S2). The first cross-sectional image, S1 (Fig. 7-4e, *left*), shows the structure of the trochlear joints where the trochlear processes connect the ascending branch to the ventral plates of the pelvic girdle and spines. The highlighted cross-section of the pelvic girdle at this position has a relatively uniform thickness and is porous (S1, Fig. 7-4e, *left*). The cross-sectional images of S2 (Fig. 7-4e, *right*) shows a fascinating interdigitation of the porous structures inside the bilateral ventral plates of the pelvic girdle. One of pelvic spines in Fig. 7-4f was sectioned, polished and imaged optically corresponding to the slice of a pelvic spine (S3) as indicated in Fig. 7-4d and shows that the pelvic spine also is porous with an undulating external surface topography.

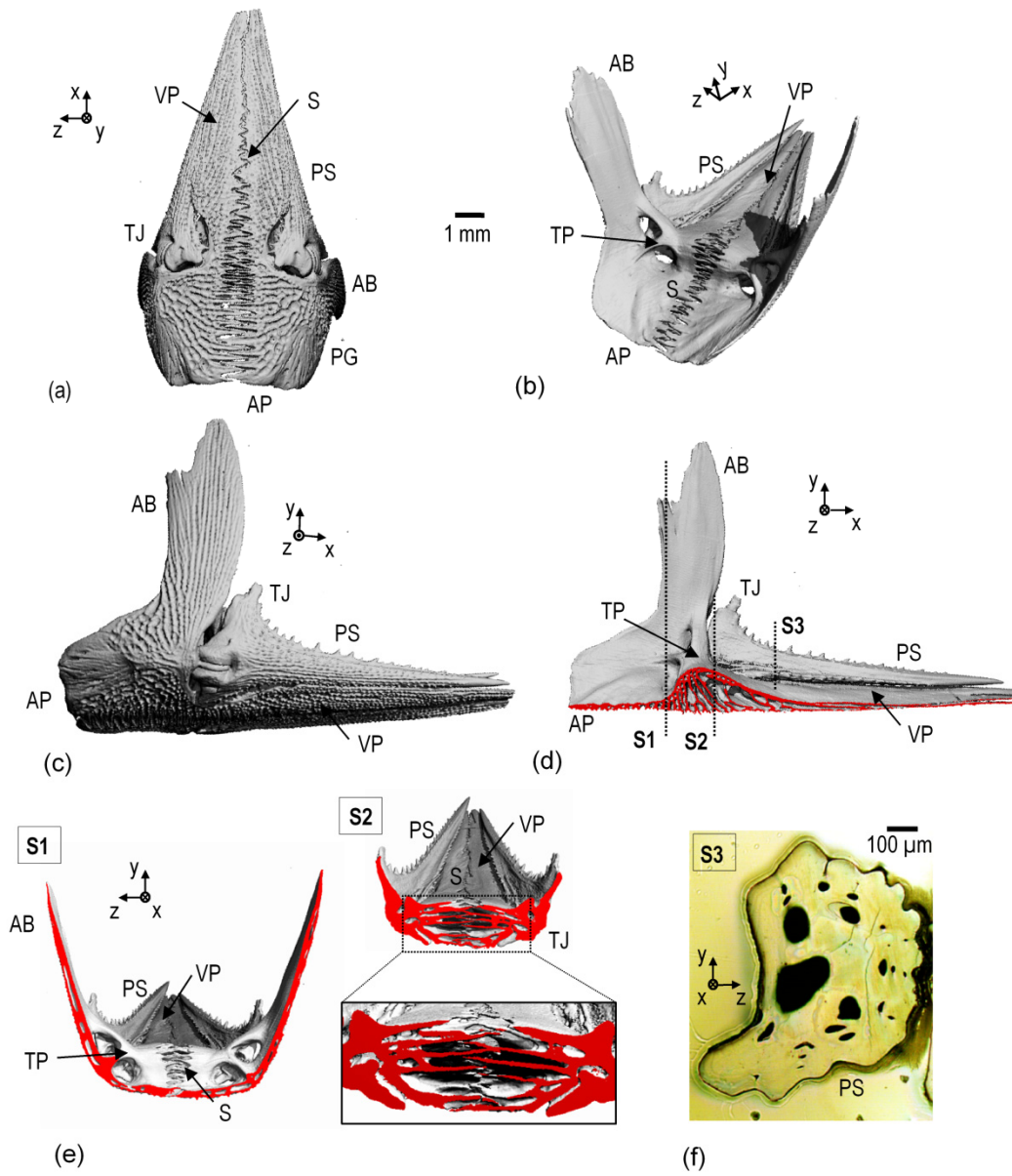


Figure 7-4. Microstructure of the pelvic girdle and spines of a marine *Gasterosteus aculeatus* (threespine stickleback); (a) to (d) three-dimensional μCT images of pelvic spines with the pelvis and ventral plates when the spines are unlocked. (e) μCT image of sectioned three-dimensional images of pelvic girdle and spines corresponding to each section indicated in (d). Highlighted faces in red denote the cross-sectional surfaces. (f) An optical microscope image of a cross-section of a pelvic spine. The scale bar is represented for (a) to (e). “AB” = ascending branch, “AP” = anterior process, “PG” = pelvic girdle, “PP” = pelvic plate and “PS” = pelvic spines, “S” = median suture of pelvic girdle, “TJ” = trochlear joint, and “TP” = trochlear process.

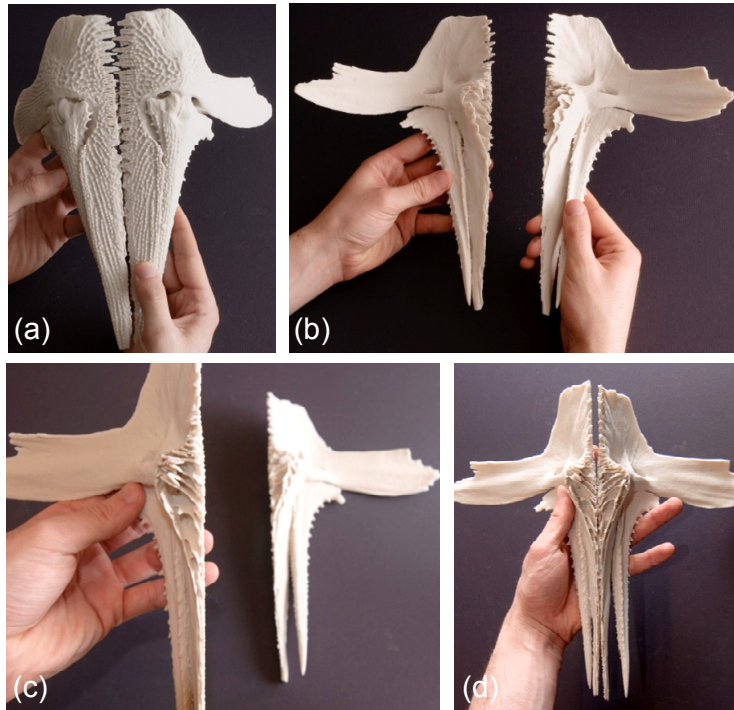


Figure 7-5. Prototypes of 3D printing: (a) and (b) A pelvic girdle-spine assembly when the spines are unlocked; and (c) and (d) a porous internal structure of bilateral pelvic girdles.

7.3.2. Three-Dimensional Structure, Dimensions, and Geometry

The topography of the interior and exterior lateral plate surfaces was further investigated at higher resolutions using SEM and surface profilometry (Figs. 7-6 and 7-7). On the external surface (Fig. 7-6a to d), approximately periodic arrays of hemispherical tubercles (topographical features) were observed corresponding to the roughness and surface undulations shown in the μ CT and optical microscope images of Figs. 7-1b and 7-3. The internal surface of lateral plates exhibited a smoother surface topography with no apparent tubercles (Figs. 7-6e to h) and possessed adhered organic material, presumably for the attachment to underlying soft tissues. The pelvic girdle and spines are seen to have surface undulations on the external surface, as shown in Figs. 7-4a, 7-4b, 7-4f, 7-5 and 7-6i to 7-6k. The trochlear joint is covered with an organic layer, displaying a relatively smooth surface (Fig. 7-6j). The tubercles of the pelvic assembly appear as cones with a tip end radius of $\sim 15 \mu\text{m}$, and a height of $\sim 100 \mu\text{m}$. Approximately 9 rows of tubercles are separated by a distance of $\sim 150 \mu\text{m}$, having a density of ~ 6 tubercles / mm. The bilateral pelvic spines have a tip with an end radius of $30 \mu\text{m}$ (Fig. 7-6l).

The external surface topography of an individual lateral plate above and below the lateral line was quantified by surface profilometry (Fig. 7-7). The tubercles above the lateral line exhibited a hexagonal array, having a mean maximum height of $\sim 50 \mu\text{m}$, and a mean maximum width of $\sim 100 \mu\text{m}$ (Fig. 7-7a and 7-7c). On the other hand, the tubercles below the lateral line radiate out in grooved lines from the lateral pores (Fig. 7-6b). The tubercles on the grooves show a height of $\sim 15 \mu\text{m}$, and are separated by a spacing distance of $\sim 150 \mu\text{m}$ in x and y directions (Figs. 7-6e and 7-7f). In Fig. 7-7a and 7-7b, the packing density of tubercles above the lateral line is found to be greater than that below the lateral line, showing ~ 70 tubercles/ mm^2 and ~ 40 tubercles/ mm^2 , respectively. An increase in surface area due to the presence of the tubercles was estimated to be a factor of ~ 5 relative to a flat surface.

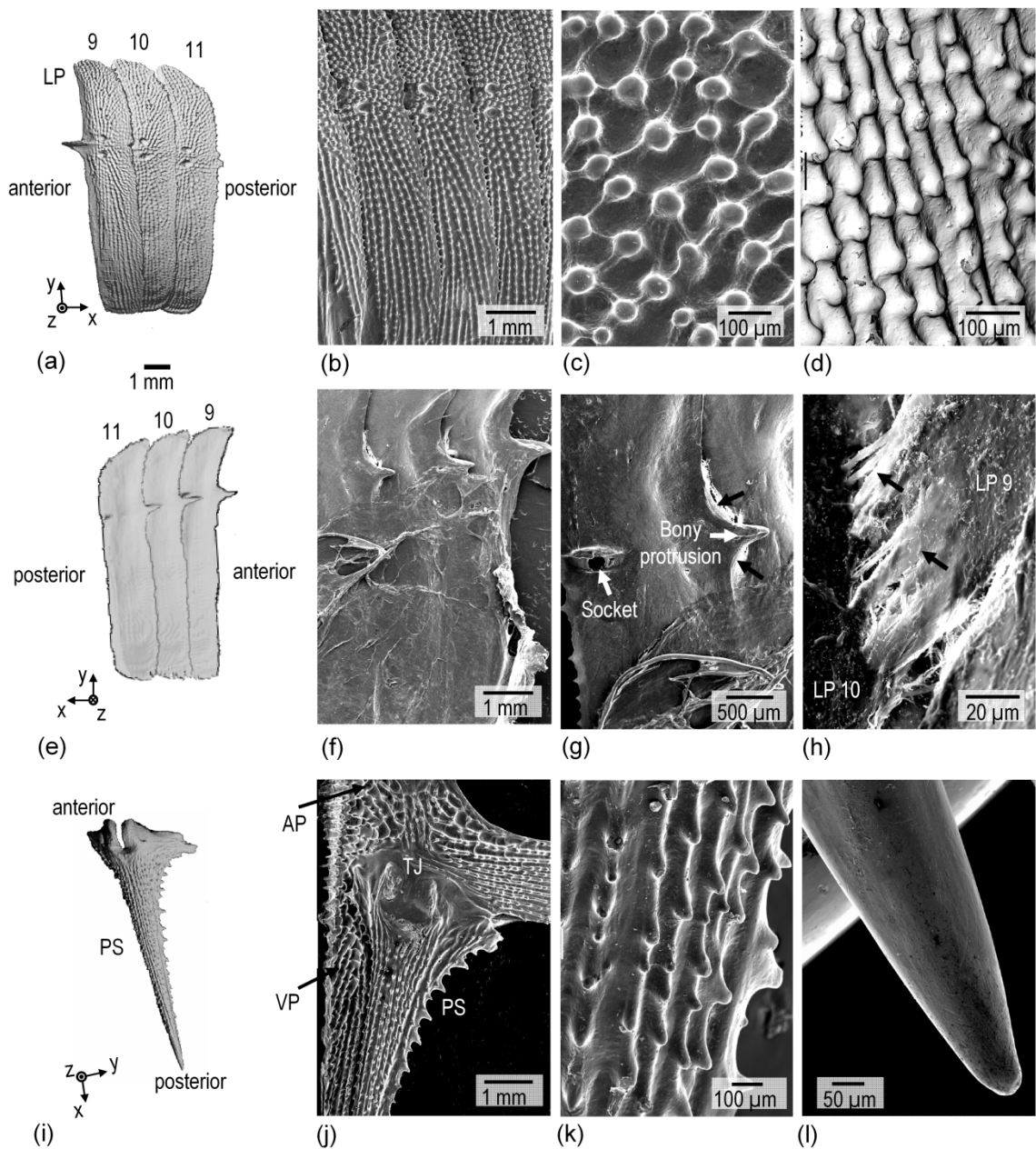


Figure 7-6. Surface morphology of lateral plate and pelvic spines of a marine *Gasterosteus aculeatus* (threespine stickleback); (a) μ CT image of lateral plate, exterior view (b-d) SEM images of lateral plate, exterior view, (e) μ CT image of lateral plate, interior view, (f-h) SEM images of lateral plate, interior view, (i) μ CT image of pelvic spine, exterior view, (j-l) SEM images of pelvic spine, exterior view. The black arrows of (h) indicate the connective tissue between two lateral plates.

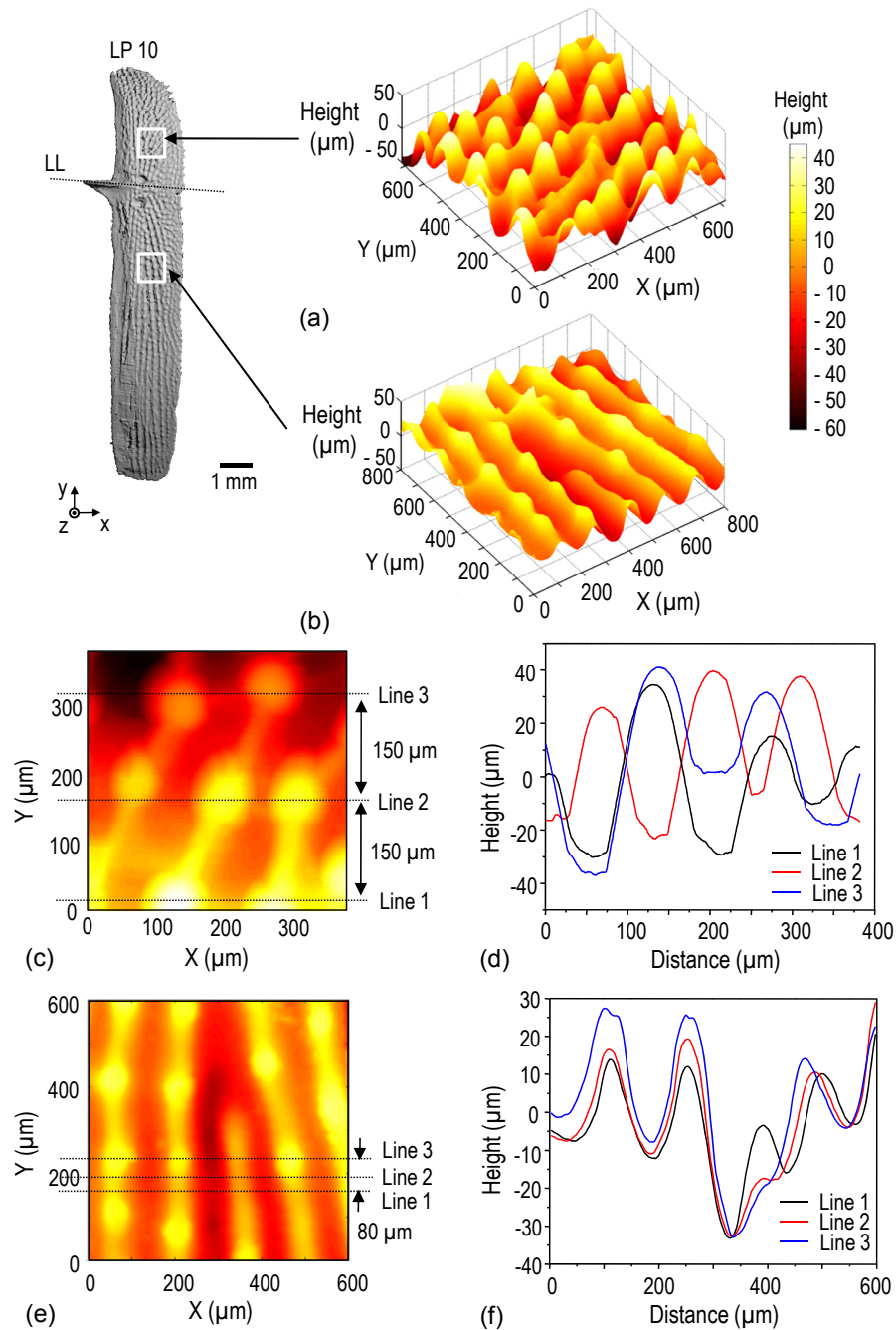


Figure 7-7. Surface topography of a lateral plate measured by surface profilometry; (a) three-dimensional topographical image for tubercles from the upper white square shown in μ CT image to the left, (b) three-dimensional topographical image for tubercles from the lower white square shown in μ CT image to the left. (c) Two-dimensional topographical image of a hexagonal tubercle array corresponding to (a), and (d) the height profile of tubercles as a function of distance across the surface from (c). (e) Two-dimensional topographical image of tubercles on the grooves corresponding to (b), and (f) the height profile of tubercles as a function of distance across the surface from (e).

7.3.3. Lateral Plate Articulation

The lateral plate articulation can be observed in great detail from more detailed analysis of μ CT data of the joint region (Fig. 7-8), as well as from scaled-up macroscopic three-dimensional prototypes prepared by 3D printing (Fig. 7-9a to 7-9h). Each lateral plate possesses a bony protrusion extending out from the anterior region and a socket on the interior surface of the posterior region; the bony protrusion overlaps onto the interior surface socket of the neighboring lateral plate (Figs. 7-6g and 7-8). Connective organic material around the joint was observed (Fig. 7-6h). The interconnecting lateral plate joint serves to register and join neighboring lateral plates while also permitting specific degrees of motion. An elongated ellipsoidal ridge-like feature is observed on surface of the bony protrusion which interfaces with the socket of the neighboring plate (Fig. 7-8a, *right*; Fig. 7-8b, *left*). The socket (Fig. 7-8a, *left*; Fig. 7-8b, *right*) is elongated in shape and is formed by a slight impression into the interior surface combined with two protruding ridges. This socket mates with the ellipsoidal protrusion. Two neighboring lateral plates (LP 9 and 10) are shown separated from each other (*left*) and with the joint interlocking (*right*) in Figs. 7-8c and 7-9a to 7-9d. After interlocking, the socket of LP 9 surrounds the ellipsoidal protrusion of LP 10. A series of two dimensional cross-sectional μ CT images of the interconnecting joint, corresponding to the boxed space from the posterior to anterior sides as indicated in Fig. 7-8c, *right*, display the interlocking configuration in great detail (Fig. 7-8d). This interconnecting joint geometry takes the form of a mixture of a sliding hinge joint and ellipsoidal joint (i.e. an ellipsoidal joint is an anisotropic “ball-and-socket” joint). Thus, the joint not only has the ability to slide along the direction of the long axis of the ellipsoidal protrusion, but also some ability to rotate about that axis (giving a sliding hinge joint, Fig. 7-9e and 7-9f), as well as the ability for a constrained level of rotation about the minor axes of the ellipse (ellipsoidal joint, Fig. 7-9g and 7-9h).

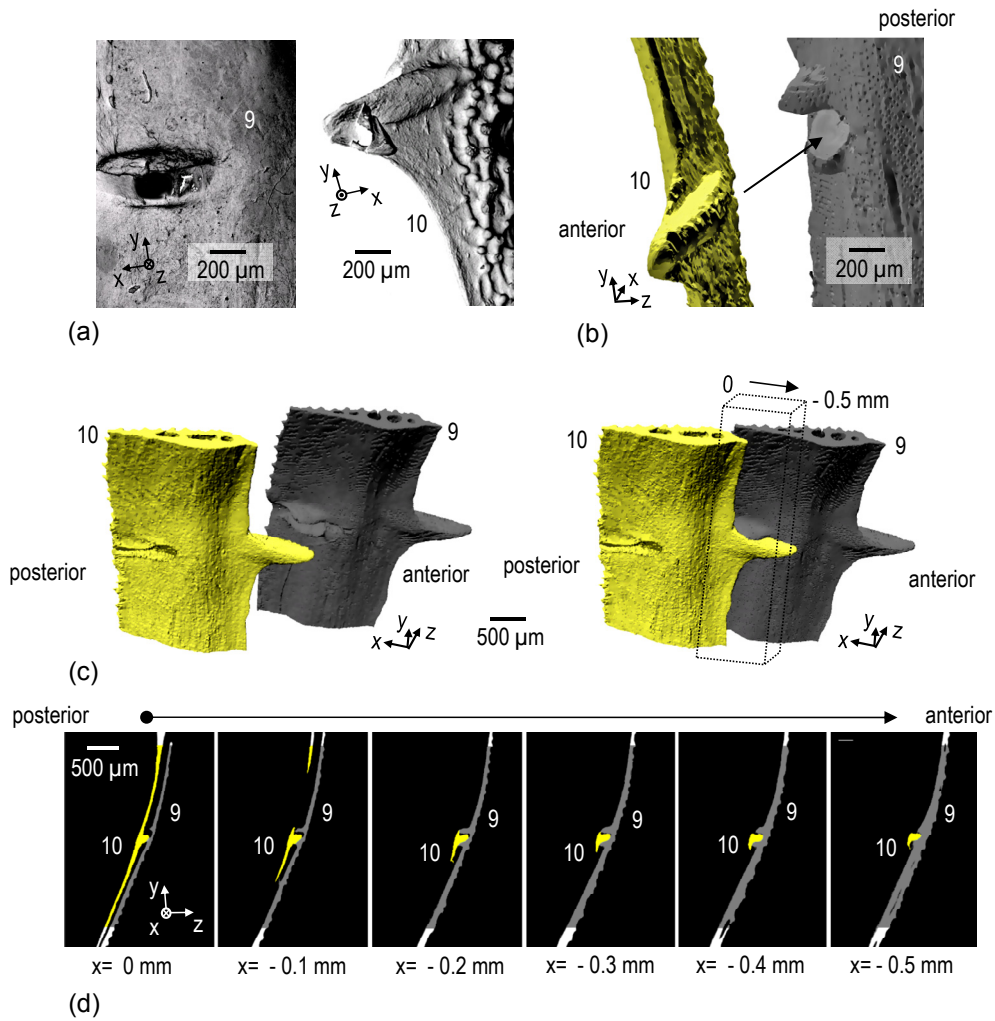


Figure 7-8. Microstructure of the interconnecting joint in neighboring lateral plates; (a) SEM images of a socket (*left*) and a bony protrusion (*right*). (b) Three-dimensional μ CT image of a bony protrusion (LP 10), facing its mating socket of LP 9. (c) Three-dimensional μ CT images of neighboring lateral plates (LP 9 and 10) before and after interlocking. (d) Two-dimensional μ CT images of the interconnecting joint from posterior to ventral sides, as indicated in (c). LP 9 and LP 10 were represented in yellow and dark gray, respectively.

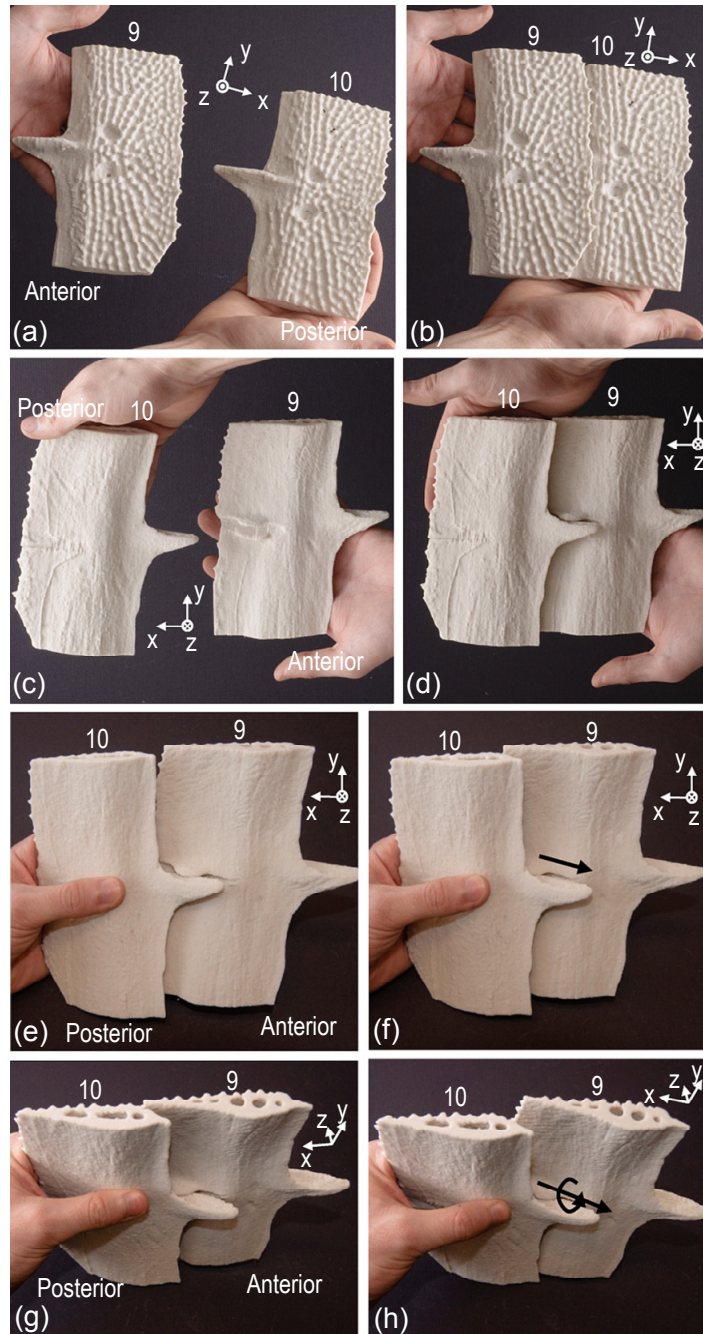


Figure 7-9. Prototypes of 3D printing: (a) and (b) two neighboring lateral plates (LP 9 and 10) before and after interlocking, exterior view; (c) and (d) two neighboring lateral plates (LP 9 and 10) before and after interlocking, interior view; (e) and (f) a sliding motion of the joint along the direction of the long axis of the ellipsoidal protrusion (the hinge sliding motion); and (g) and (h) a rotating motion of the joint about the major axis of the ellipse (the hinge rotation motion). A more limited rotation about the minor axis of the ellipse is also allowed by this joint (not shown).

7.3.4. Porosity, Crystallography, and Composition

The armor assembly of *G. aculeatus* possesses a significant amount of porosity, as shown in Figs. 7-3 and 7-4. For the lateral plates, the measured pore size by mercury porosimetry shows a broad distribution (Fig. 7-10) which was better fit to a bimodal distribution (a continuous probability distribution with two different modes, distinct peaks, or local maxima in the probability density function, $R^2 = 0.85$) rather than a normal Gaussian distribution ($R^2 = 0.70$). In the bimodal fits, two modes (240 and 15 μm) with two corresponding standard deviations (112 and 6 μm) that correspond to two peaks of the distribution were calculated. The larger pores occupy the centrally thickened region of the lateral plates (Fig. 7-3a), while the smaller pores are located throughout the plate. Estimation of the volume percent porosity of LP9-12 from mercury porosimetry yielded a value of $\sim 35\%$. Estimation of the areal percent porosity from two-dimensional images (i.e. four μCT images of LP10 and optical cross-section images of five lateral plates) yielded a value of $25 \pm 5\%$. In addition, the optical microscope cross-sectional images of pelvic spines were analyzed, which resulted in areal porosity of $\sim 15\%$. The lateral plate density was also predicted to be $\sim 1.2\text{ g/cm}^3$ from mercury porosimetry, assuming the density of dense solid was 1.9 g/cm^3 .

XRD patterns showed broad reflections, with characteristic *d*-spacings (e.g. 0.343, 0.280, and 0.225 nm), corresponding to the apatite structure (Fig. 7-11a). All peaks matched with characteristic hydroxyapatite peaks, and no other calcium phosphates or calcium carbonates (e.g. calcite and aragonite) were observed. Fig. 7-11b shows the FTIR spectra of a pelvic spine. Typical IR bands for collagen were observed; N-H stretching at $\sim 3310\text{ cm}^{-1}$ for the amide A, C-H stretching at ~ 3063 and $\sim 2900\text{ cm}^{-1}$, C=O stretching at $1600\text{-}1700\text{ cm}^{-1}$ for the amide I, N-H deformation at $1500\text{-}1550\text{ cm}^{-1}$ for amide II, and N-H deformation at $1200\text{-}1300\text{ cm}^{-1}$ for the amide III bands (Doyle et al., 1975). Moreover, typical phosphate bands (PO_4^{3-}) associated with the apatite structure appeared at $1097\text{-}1110\text{ cm}^{-1}$ and $1030\text{-}1033\text{ cm}^{-1}$ (for ν_3 mode) and $601\text{-}607\text{ cm}^{-1}$ and $563\text{-}569\text{ cm}^{-1}$ (for ν_4 mode) (Chang and Tanaka, 2002). Carbonate bands (CO_3^{2-}) at 1454 cm^{-1} (for ν_3 mode) and 872 cm^{-1} (for ν_2 mode) were slightly observed, implying a portion of apatite is carbonated (Rehman and Bonfield, 1997). The same bands were observed in the FTIR spectra of a lateral plate (*data not shown*).

Quantitative analysis of the weight percent mineral content was assessed via BSEM and EDX of a representative lateral plate at three different positions from the anterior to posterior regions (Fig. 7-12). For the BSEM data, the mineral content of a lateral plate ranged between 55 and 65 wt%, with the mean value of $58 \pm 3\%$, overall (Fig. 7-12a). Unpaired t-tests confirmed that the mineral contents for the three different locations studied were not statistically different ($p=0.069$, $F=4.31$). The mineral content values calculated by EDX correlated well with the results obtained by BSEM (Fig. 7-12b). The mineral content of the pelvic spines were found to be $68 \pm 10\%$ ($N = 2$, *data*

not shown, not statistically different from lateral plates). Bone mineral density (BMD) of lateral plates and pelvic spines, measured by μ CT, are 633.9 ± 98.1 mg HA/ cm^3 , and 748.4 ± 167.7 mg HA/ cm^3 .

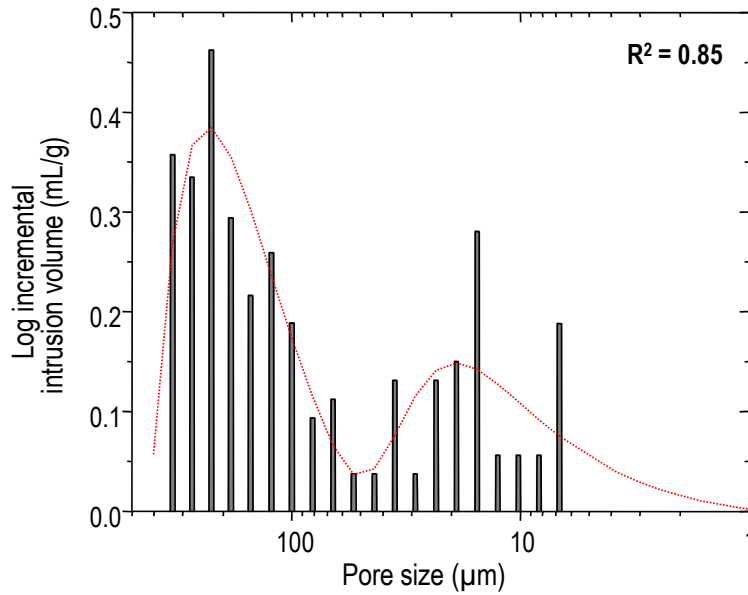


Figure 7-10. Pore size distribution of lateral plates (LP 9-12, N = 4) measured by a mercury porosimeter showing a bimodal distribution with two average pore sizes ($\mu_1 = 15$ μm , $\sigma_1 = 6$ μm , and $\mu_2 = 234$ μm , $\sigma_2 = 112$ μm).

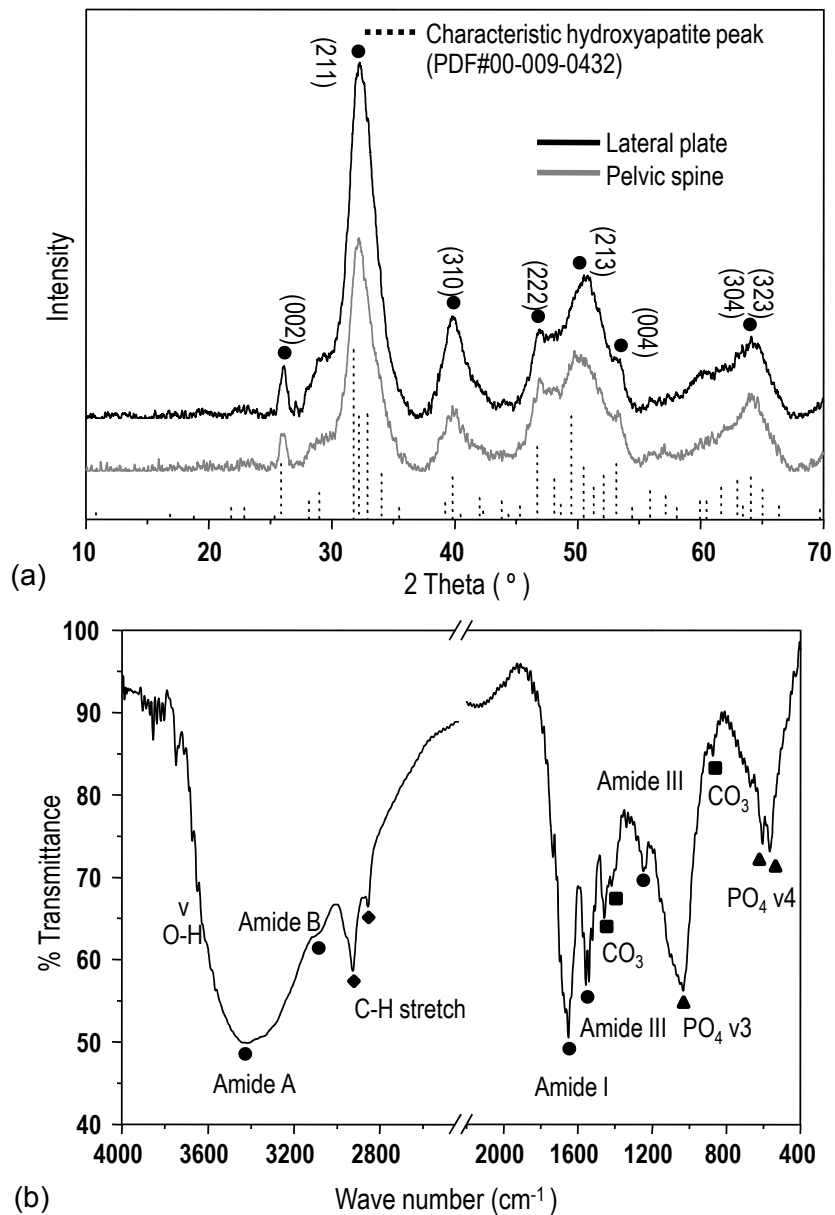


Figure 7-11. Chemical composition of the armor of the marine *Gasterosteus aculeatus* (threespine stickleback); (a) X-ray diffraction pattern of lateral plates and pelvic spines. Broad reflections corresponding to the characteristic peaks (●) of hydroxyapatite are compared. (b) Infrared spectrum of pelvic spine showing amide bands (●) and C-H bands (◆) from collagen fibers and absorbances for phosphate (▲) and carbonate ions (■) in the apatite phase (Doyle et al., 1975; Rehman and Bonfield, 1997; Chang and Tanaka, 2002).

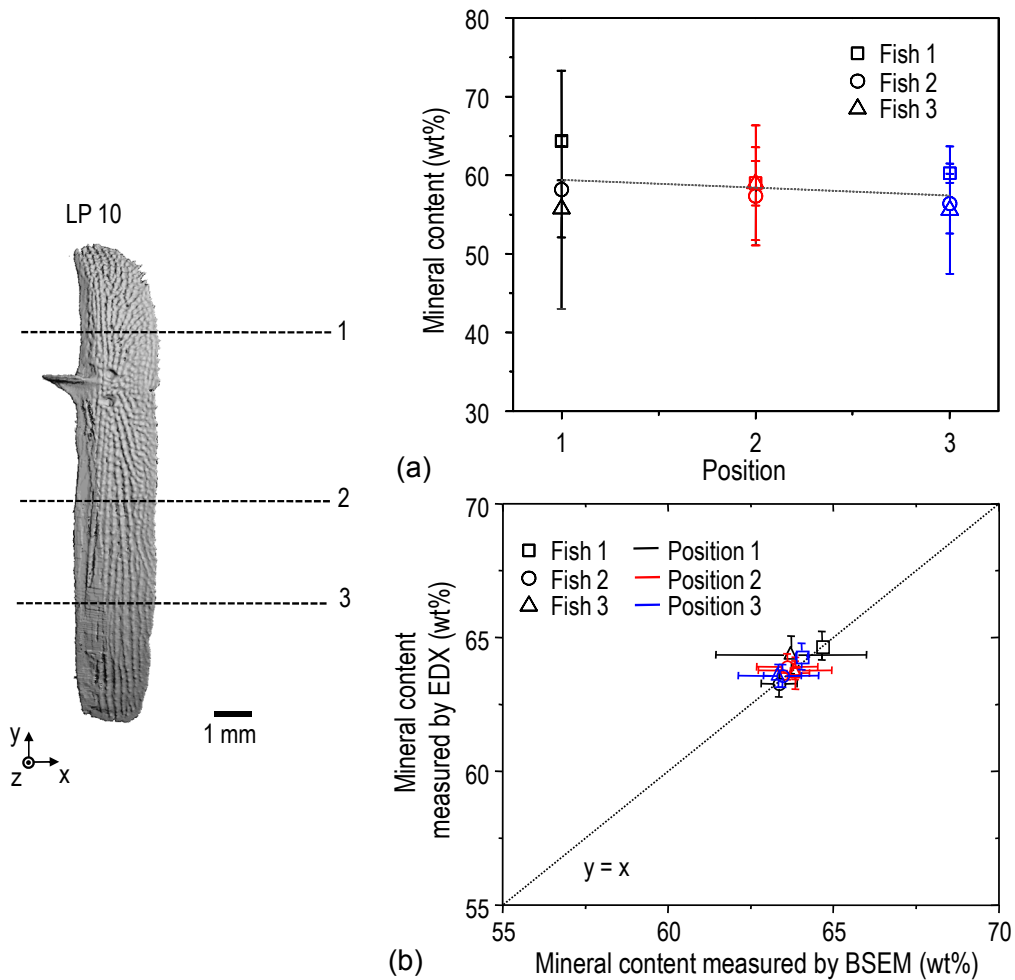


Figure 7-12. Quantitative analysis of mineral contents of the marine *Gasterosteus aculeatus* (threespine stickleback); (a) Mineral contents of three different cross-sections in a lateral plate (LP10), extracted from three fish samples measured by back-scattered electron microscopy (BSEM). (b) Mineral contents measured by energy dispersive X-ray (EDX) analysis combined with BE gray-level measurements of identical bone areas of (a).

7.4. Discussion

The overall objective of this study was to interrogate and quantify morphometric (shape-based) armor design principles which promote protection while simultaneously maintaining mobility and biomechanical function. Quantitative data on the microstructure and composition of the armor assembly of the marine *Gasterosteus aculeatus* (threespine stickleback) is presented including: lateral plate thickness, lateral plate overlap, plate-to-plate junctions, surface topography, internal porosity, and mineral content (Table 7-1), as well as the internal and external structure and junctions of the pelvic girdle and spines. Studies of the armor of marine stickleback, which represents the ancestral condition for the divergent freshwater populations, are significant from an evolutionary perspective. These data provide insights into overarching armor design principles which enable protection while also maintaining mobility and biomechanical function. While numerous factors may affect the morphological diversity of the armor among *G. aculeatus* populations (Giles, 1983; Bell et al., 1993; Kristjansson, 2005; Marchinko and Schluter, 2007; Östlund-Nilsson et al., 2007), it simultaneously is linked to mobility and protection from predators (Reimchen, 1994; Reimchen, 1995; Reimchen, 2000). *G. aculeatus* is known to possess a broad array of predators of at least 68 species due to its small body size, slow swimming speed, and abundance in a large range of habitats and geographical locations (Reimchen, 1994). In one study, predatory punctures were rarely observed on the armor, whereas they were often found on unarmored integument regions (Reimchen, 1992). The dermal armor of *G. aculeatus* serves to protect the fish in different ways, including: 1) resistance to penetrating attacks (e.g. bites from toothed predators), 2) increasing swallowing difficulty and damage to soft mouthparts of predators, and 3) increasing body size when spines are erect, which is an effective deterrent to gape-limited piscivores (Hoogland et al., 1956; Reimchen, 2000). Both the local structure of the individual armor units, as well as the microscopic geometry and articulating mechanisms contribute to the effectiveness of protection.

There are many salient features of *G. aculeatus* armor relative to other armored fish (Sire et al., 2009). In general, the armor is a heterogeneous assembly of geometrically distinct structures conformal to the fish body that includes an active (responsive) offensive component (the spines). First, the internal porosity pore size and distribution provide a sandwich-like structure to the *G. aculeatus* plates which implies a microstructural design that provides stiffness and strength in bending at minimum weight. This internal microstructure also has implications with regards to penetration resistance: a penetrating tooth will first indent and bend the textured outer surface layer of the plate which would provide a greater resilience to penetration events compared to a fully dense internal structure; this structure would also provide greatly different dissipative deformation mechanisms during more aggressive penetration loading where indentation

Table 7-1. The structural and material properties of the armor plate assembly of marine *Gasterosteus aculeatus* (threespine stickleback). Average thickness, bone volume and bone mineral density were determined by morphometric analysis of μ CT images. Mineral contents were measured by BSEM/EDX analysis. Volume porosity and density were obtained by mercury porosimetry. Areal porosity was measured using optical microscopy images. Tubercle dimensions, groove spacing and density of tubercles were calculated by using surface topography images taken by surface profilometry and SEM.

	Average thickness (μm)	Bone volume (mm^3)	Bone mineral density ($\text{mg HA}/\text{cm}^3$)	Mineral content ($\text{wt}\%$)	Porosity (%)	Density (g/cm^3)	Tubercle dimensions (μm)	Groove spacing (μm)	Tubercle density ($\#/\text{mm}^2$)
Lateral plates	Thin plate					1.2			
	151 ± 71 (single)	< 1.8 (one lateral plate)	633.9 ± 98.1	58 ± 3	$20 \sim 25$ (areal) ~ 35 (volume)	(porous lateral plates)	hemispherical ~ 100 (width), ~ 50 (height)	~ 150	50 ± 23
Pelvic spines	196 ± 77 (assembly)					1.9 (bone)			
	Cone-shaped 125.0 ± 74.3 (radius)	~ 27 (the whole pelvic assembly)	748.4 ± 167.7	68 ± 10	$10 \sim 15$ (areal)	NA	Cone-shaped ~ 15 (tip end radius) ~ 100 (height)	~ 150	35 ± 10

will be accommodated by more distributed deformation events compared to a dense structure. This structure suggests a design which provides an interesting combination and tradeoff amongst different effective mechanical properties and weight to produce a lightweight effective armor system. This tradeoff is further enabled by the advantageous presence of the dorsal and pelvic spines which provide an additional defense mechanism. In contrast, our recent work on the ganoid armor scales of *Polypterus senegalus* have elucidated the biomechanical advantages of multilayers (ganoine-dentin-isopedine-bone) in penetration resistance, but at the energetic “cost” of additional biomineralization (Vermeij, 2006) and added weight of the higher density external layers. Next, the convolution of plate geometry in conjunction with plate-to-plate overlap allows a relatively constant armor thickness to be maintained throughout the assembly (Fig. 7-3). This is a significant design principle that is utilized in other segmented natural armor systems (*unpublished data*) which promotes spatially homogeneous penetration resistance, thereby mitigating weakness at the armor unit interconnections.

The structure of the plate-to-plate interconnecting joint has features intermediate between an ellipsoidal joint and a sliding hinge joint which is expected to allow for limited compliance in very specific degrees of freedom: plate rotation in two orthogonal directions (about the lateral line and normal to this line – i.e., following the figure nomenclatures, rotations about the x and y axes) as well as permitting a small level of sliding between plates (i.e., displacement in the x direction). Furthermore, the asymmetric position of the joint in the lateral plate assembly is expected to allow for increased inter-plate displacement of the ventral side of the fish body, possibly owing to holding eggs and eating food (Bell and Foster, 1994; Östlund-Nilsson et al., 2007). It is noted that lateral line is aligned with the armor joint connections; this coincidence may be important to maintaining positioning of the sensing neuromasts which occur in pairs with a neuromast located on either side of the joint. Unlike many other fish species, sticklebacks rely heavily on their pectoral fins, rather than their caudal fin, during swimming (Bergstrom, 2002). The location of a lateral line can be constrained by the need to reduce noise induced by self-generated stimulation, e.g. giving the dorsal displacement of the lateral line above the pectoral fin (Webb, 1989; Montgomery et al., 1995; Wark and Peichel, 2010). Even though the relationship between the lateral line and the interlocking armor joints is not clear, hydrodynamic activity, feeding habits, body mobility, and swimming maneuverability may all play a role. In addition to the protection provided by the lateral plates, the pelvic girdle provides protection by stiffening the ventral underside of the fish body, preventing bending that may occur during predatory interaction with the cantilevered pelvic spines which in turn make the spines a more effective defensive feature. The fascinating interdigitating internal porous structure of the ventral plates of the pelvic girdle suggests a dynamic reconfigurable system for attack and rest positions. The increased amplitude, frequency, and amount of interdigitation of the pelvic suture

near the trochlear joint will enable increased stiffness and load-bearing support and more rapid “locking” at this critical location of the fish, at the base of the pelvic spines and the connection to the lateral plates during spine conformational change and predatory attacks, which will be discussed in detail in Chapter 8. This behavior is similar to sutures in turtle shells which have been measured experimentally (Krauss et al., 2009). Finally, the exterior surface topography of the lateral plates may serve a hydrodynamic role during swimming, e.g. viscous drag reduction of turbulent boundary layers and/or reduction of surface shear stress and skin friction (Walsh, 1983, 1990; Fish and Hui, 1991; Choi et al., 1993; Sudo et al., 2002; Fish and Lauder, 2006) and may also prove important against penetration attacks. The serrated morphology of the cone-shaped tubercles of the spines may simultaneously play a defensive role.

7.5. Conclusions

In summary, the following structural design principles are present in the armor assembly of the marine *Gasterosteus aculeatus* (threespine stickleback): (1) the armor is a hybrid system consisting of dynamically active (spines) and passive (lateral plates) components; (2) the morphometry of the lateral plates and lateral plate interconnections (cross-sectional geometry and plate overlap) allow for a constant armor thickness, promoting spatially homogeneous protection; (3) a unique lateral plate articulation mechanism exists which appears to be a cross between a sliding hinge joint and ellipsoidal joint and allows for limited rotational and translational compliance in specific directions; (4) the interdigitating internal porous structure of the ventral plates of the pelvic girdle suggests a dynamically reconfigurable structure; (5) the sandwich-like porous structure of the lateral plates is advantageous for providing stiffness and strength in bending at minimum weight; and (6) the external surface topography of the armor components will have implications for both penetration resistance and hydrodynamics.

Chapter 8.

Design and Biomechanical Function of the Pelvic Assembly of Threespine Stickleback

8.1. Introduction

Significant advances in the field of molecular biology (i.e. genome-wide linkage mapping) have allowed for the exploration of the molecular mechanisms that underlie phenotypic change, adaptation, divergence, speciation and natural selection (Orr, 2005; Kingsley and Peichel, 2007; Schluter, 2009; Klingenberg, 2010; Wolf et al., 2010). *Gasterosteus aculeatus* (the threespine stickleback) has served as an excellent model system in this regard since this species is known to undergo rapid and dramatic evolutionary adaptations of its external armor and associated genetic isolation within as few as eight generations (Peichel et al., 2001; McKinnon and Rundle, 2002; Barrett et al., 2008). Morphological assessment of divergent populations of *G. aculeatus* has typically involved the measurement of the macroscopic dimensions and overall geometry (e.g., length, shape, position, number) of its armor components, as well as a score method that counts the total number of appearing structural elements in a reduced armor structure, giving the highest score to the fully developed armor structures (Bell and Orti, 1994; Klingenberg, 2010). Also in Chapter 7, a suite of higher resolution materials science-based characterization methods (Constantz et al., 1995; Tai et al., 2005; van Lenthe et al., 2007) has been employed to quantify the material microstructure, surface topography, three-dimensional microscale geometry, porosity and composition of *G. aculeatus* armor, which demonstrated great potential to provide new insights into biomechanical function, performance, fitness, and survivability (Song et al., 2010).

The current study expands on this idea that state-of-the-art experimental and theoretical approaches from the fields of materials science, mechanical engineering and

architecture can contribute significantly to addressing open questions in the field of evolutionary biology, in particular when the phenotype is in essence a “material” (e.g. structural or load-bearing tissue) with a well-defined geometry and the performance (function) is primarily mechanical. For *G. aculeatus* armor the “material” is lamellar bone, the individual armor constituents (e.g. lateral plates, pelvic spring and suture, etc.) have complex geometries and the function is both mobility (e.g. locomotion, body flexibility) and protective (e.g. penetration resistance, load-bearing capability, energy dissipation from predatory attacks). Hence, the classical materials science paradigm can be expanded to *structure-form-property-function-performance relationships* (Smith, 1965; Olson, 1997; Callister, 2003) and mapped to *phenotype-function/performance-fitness/survivability* relationships sought in evolutionary biology. For materials science and engineering new methods include synchrotron x-ray micro and nano-computed tomography for high resolution three-dimensional nondestructive imaging (Ritman, 2004; van Lenthe et al., 2007), high-resolution mechanical testing (Tai et al., 2007; Bruet et al., 2008; Han et al., 2011), nano-/micro-manufacturing for complex material systems (Aizenberg, 2010; Qin et al., 2010). For architecture, variable property design and fabrication (VPD/VPF) for material assemblies with spatially graded properties (Oxman, 2010), form-finding computational tools for structural optimization (Bletzinger and Ramm, 2001; Schumacher, 2009), freeform surfaces of architectural geometry (AG) for highly complex geometries (Pottmann, 2010), 3D morphometrics for three-dimensional quantitative structural analysis. Lastly, all of the detailed structure and geometric information can be incorporated directly in multiscale analytical and computational finite element models through methods of mechanical engineering to predict and assess biomechanical function, efficiency and performance (Wang et al., 2009; Wang and Boyce, 2010). Hence, in this study the question is considered more holistically: why certain divergent phenotypes for populations subjected to different environmental conditions, selective pressures, functional demands and design tradeoffs do translate into superior function and performance, leading to greater survivability and hence, more opportunities to produce offspring.

In this Chapter, I present 1) the mathematically defined criteria that enable both full morph marine and full morph freshwater *G. aculeatus* pelvic complex to be segmented into four distinct regions from the anterior process and capture the salient structural features at each region for the quantitative comparison; 2) identification and quantification of mechanically relevant structure parameters between marine and freshwater *G. aculeatus* pelvic complex, giving insights into their possible mechanical function; and 3) the dynamic defense mechanism associated with the conformational transition of the full-morph pelvic structure from the rest to offensive when attacked. Three Alaskan populations of *G. aculeatus* were investigated and compared; field-caught marine, full-morph pelvis (Rabbit Slough), freshwater full-morph (Beverly Lake) and

freshwater low-morph (Kalmbach Lake). Microcomputed tomography (microCT) was employed to quantify the structural parameters of the pelvic assemblies including the spatial dependence of the suture amplitude and frequency, the suture plate inclination angle and the suture gap. Composite analytical and finite element computational models were developed and used in conjunction with the microCT experimental data to simulate the mechanical behavior of the pelvic assembly, to predict the effective suture stiffness and to understand the conformational change of the pelvic assembly from the “rest” to “offensive” states. This study elucidates the structural and functional differences between different divergent populations of *G. aculeatus* and serves as a model for other systems of interest in evolutionary biology.

8.2. Methods

Samples. Field-caught ancestral marine and freshwater *G. aculeatus* (threespine stickleback) were collected from Rabbit Slough, Beverly Lake, and Kalmbach Lake in South-Central Alaska in June, 2010. The fish were euthanized with an overdose of MS-222, a fish anesthetic (Clark University IACUC approval #010R). They were stored frozen until the experiments were carried out. The pelvic assembly was removed from the fish body using forceps and dissecting scissors.

Microcomputed Tomography. Either extracted pelvic assemblies or the whole body of *G. aculeatus* were scanned with a micro-CT (μ CT) system (Viva CT40, Scanco Medical AG, Switzerland) operated at 45 kV and 177 μ A. Microtomographic slices were recorded every 10 μ m or 20 μ m and were reconstructed with $10 \times 10 \mu\text{m}$ or $20 \times 20 \mu\text{m}$ voxels (volume elements) in plane. A constrained three-dimensional (3D) Gaussian filter ($\sigma = 0.8$ and support = 1) was used to partially suppress noise in the volumes.

Contouring/Segmentation The individual articulating units were contoured / segmented, color coded and reassembled using image control software, MIMICS (MIMICS 14.0, Materialise, Belgium) as follows. The two-dimensional μ CT slices of pelvic assembly that have multiple structural units will be imported into MIMICS, maintaining the same spatial resolutions as the experimental set-up. The individual slices were contoured by MIMICS multiple slice editing functions while structural units appearing in each slide were identified using different colors. Calculations of the whole contoured and color-coded slice set provided the separated three-dimensional structure of each structural unit. Lastly, the whole structure was reassembled by importing all segmented structural elements into one three-dimensional space.

Image Analysis Structural parameters of pelvic assembly were quantified using IMAGEJ software (NIH, <http://rsb.info.nih.gov/ij>) and MATLAB software (The MathWorks Inc., Natick, MA). The exported BMP images of the pelvic assembly were imported in IMAGEJ. The contour of pelvic suture lines was first extracted using the IMAGEJ function, 'Find edges' and then was converted into binary images that can be further modified by the binary process embedded in IMAGEJ. The skeletonized lines with reasonable simplicity, yet without loss of important structural details (e.g. frequency, amplitude of suture lines) were exported as XY coordinates of suture lines (text files). Post-data processing with the text files was carried out using MATLAB. Frequency, amplitude and contour length of suture lines were measured by built-in MATLAB functions (e.g. peakfinder, differentiation/integration).

Animation. To visualize the biomechanical movement and the actuation of the pelvic spines, an animation was created to simulate the conformational change of pelvic spines that takes place in the fish when attacked. The animation was created and rendered in 3D Studio Max software package, using three dimensional mesh reconstructions

obtained from micro CT data of the actual skeleton. To produce the animation of the conformational change in the stickleback pelvic girdle, two stages of the skeleton conformation were taken as extreme conditions and the positional change is interpolated between them. For each stage of the pelvic girdle assembly, the degrees of freedom of each articulation were defined, and the angular position for each range of motion. Each component of the pelvic girdle is assembled in a linked model, where the motion of any member was conditioned by the position of the others. The last part of the animation was set up in order to pull apart the assembly and allow for a better visualization of the bone plates and micro-structures of the pelvic suture (S. Araya).

8.3. Results

8.3.1. Four Distinct Regions of Full-Morph Pelvic Assembly

Bilateral, full-morph pelvic girdles interdigitate via a median suture where the bottom ventral plates and internal structures of the pelvic girdles exhibit pronounced suture morphology from the anterior to the posterior as well as among different *G. aculeatus* populations (e.g. ancestral fully-armored marine vs. partially-armored freshwater), as shown in Figs. 8-1a and 8-2a. Three-dimensionally constructed geometry of pelvic girdle-spine assembly from two-dimensional microCT sectional images shows spatially heterogeneous suture morphology on the bottom ventral plates and the three-dimensional interdigitation of the internal plates of the pelvic girdles though dorsal-to-ventral thickness (following the figure nomenclature, z height), varying from the anterior to the posterior and displaying the largest height around the trochlear joints. These morphological variations in two and three dimensions enable the full-morph pelvic assembly to be classified into four regions, as shown in Fig.1a and 2a. The boundaries of those four regions are quantitatively determined by the first derivative of z height calculated from the z height profile shown in Fig. 8-2b (Appendix E): (i) region I consists of the single-layered ventral plates with approximately constant z-height in the ascending process; (ii) region II exhibits abrupt increase and decrease of z height associated with spatially oriented internal plates located in between the top and bottom ventral plates (up to the negative inflexion point) and contains a pair of ascending branches and trochlear joints articulating with condyles of pelvic spines; (iii) region III is the transition from region II to IV with the gradual decrease of z height up to the nearly constant value ($dz/dx = 0$); and (iv) region IV is the rest of the pelvic girdles, appearing with the constant z height). Those criteria can be applied to the full-morph pelvic assembly of different *G. aculeatus* populations. The primitive and full morph pelvis from the marine *G. aculeatus* exhibits the complete four regions, whereas a full morph pelvis from the

freshwater *G. aculeatus* has complete three regions II, III and IV except for the reduced region I with no suture.

A conventional quantitative assessment of pelvic phenotypes is a four-point score for each side of bilateral pelvic assembly by imposing the number from 4 to 0 depending on the existence of four pelvic elements (pelvis spine, anterior and posterior process, and ascending branch) (Bell and Orti, 1994), resulting in the total score from 8 to 0. According to the scoring method, both full-morph pelvic assemblies were assigned as the full 8 score. However, quantification and mechanical prediction of pelvic structures show that the detail structural differences between two similar pelvis result in the mechanical dissimilarities [will discuss in following sections]. In addition, the relative span of each region in those two *G. aculeatus* pelvis is different; 15% (I), 15% (II), 30% (III), and 40% (IV) for marine *G. aculeatus* pelvis; and 25% (I), 25% (II), 20% (III) and 30% (IV) for freshwater *G. aculeatus* pelvis, indicating the size reduction of each region in pelvic assembly is not proportional to that of the total size reduction and the relative width of each region is also one of reduced elements.

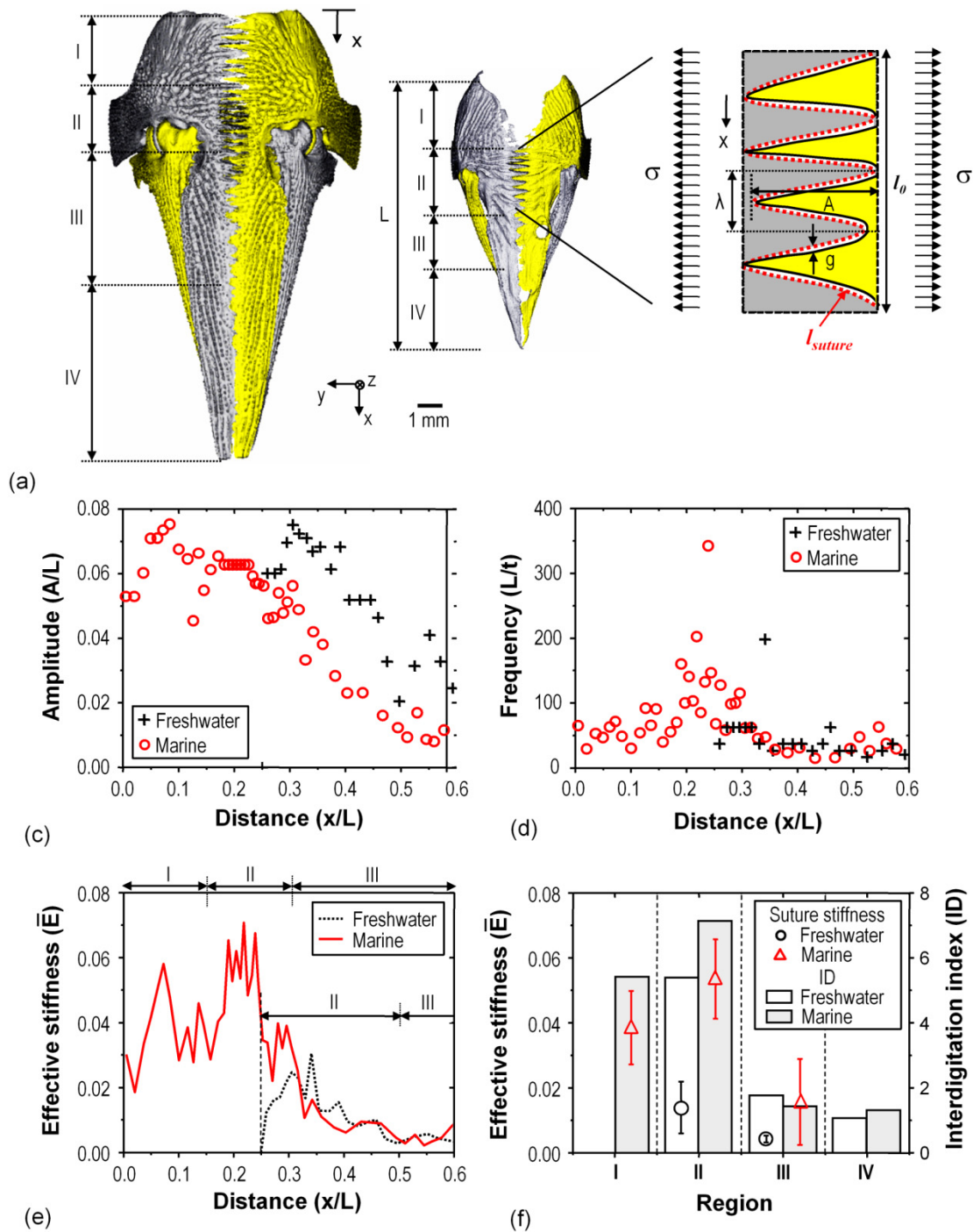


Figure 8-1. Two-dimensional morphology of the median suture of bilateral pelvic girdles from marine and freshwater *G. aculeatus*; (a) Ventral view of three-dimensional μ CT images of the pelvic girdles (rest position) from marine (left) and freshwater (right) *G. aculeatus*, (b) schematic diagram of a two-dimensional suture model, (c) to (e) the dorsal to ventral spatial distribution of: (c) relative amplitude (A/L), (d) spatial frequency (L/λ) and predicted suture stiffness of the median suture in both *G. aculeatus* populations, and (f) average stiffness and ID of four regions in marine and freshwater *G. aculeatus*.

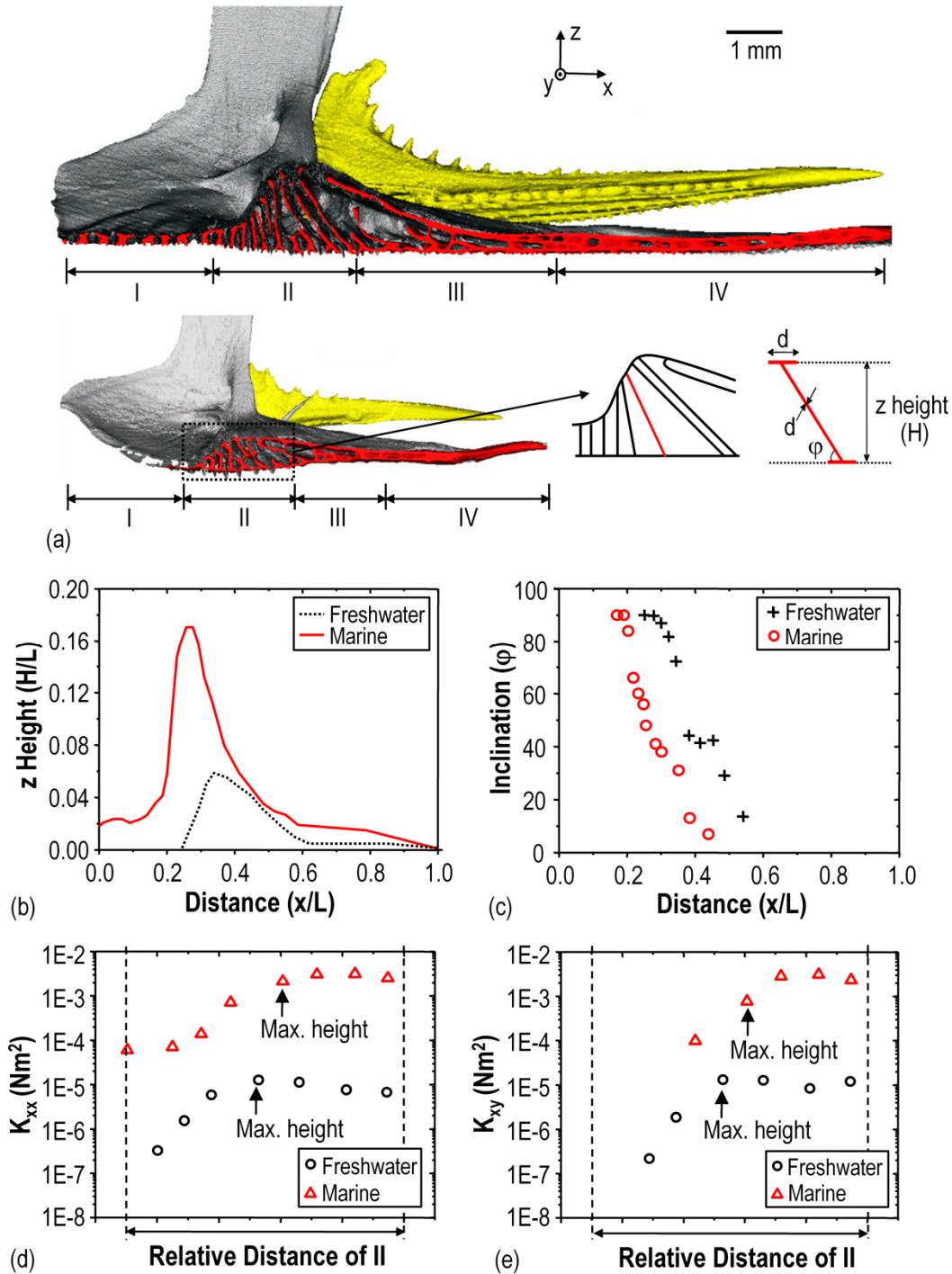


Figure 8-2. Three-dimensional morphology of the median suture of the pelvic girdles from marine and freshwater *G. aculeatus*; (a) lateral view of three-dimensional μ CT images of the pelvic girdles (rest position) from marine (top) and freshwater (bottom) *G. aculeatus* with the schematic diagram of internal plates, (b) and (c) the dorsal to ventral spatial distribution of (b) z Height (H/L) and (c) inclination of the pelvic girdle in marine and freshwater *G. aculeatus*, (d) predicted bending stiffness in region II of the pelvic girdles for both *G. aculeatus* populations and (e) the coupling effect of inclined internal plates in bending stiffness.

8.3.2. Two-dimensional Morphological Features of Suture and their Mechanical Relevance

Two-dimensional suture morphology on the bottom ventral plates is described with three independent structural parameters, amplitude (A), wavelength (λ) and the width of the organic layer between neighboring ventral suture-teeth (g), as indicated in the schematic drawing of the suture in Fig. 8-1a. The amplitude A and the wavelength λ are non-dimensionalized by the total length of the pelvic girdle (L) as the amplitude index (A/L) and spatial frequency of a corrugated suture (L/λ), which display significant spatial variations as shown in Fig. 8-1c and 8-1d. The gap along in x distance is almost constant. For both marine and freshwater *G. aculeatus* pelvic sutures, an approximately negative linear gradation (from the anterior to the posterior) in amplitude was found except that region I of the freshwater one is completely reduced (Fig. 8-1c and 8-1d). The spatial frequency shows a peak in region II and also the mean value is higher in region II than other regions. The amplitude indices of two suture structures appear with the same magnitude, but the spatial frequency of the freshwater pelvic suture in region II is significantly lower than that of the marine one by a factor of ~ 3 (Fig. 8-1c and d). In region IV, amplitude and the spatial frequency of both suture structures diminish. In addition, the interdigitation index (ID), which is defined as the ratio of the contour length of the suture to the straight line between two end points (Rafferty and Herring, 1999), as shown in (Fig. 1b) was calculated for each region of both species and shown in Fig. 8-1f. ID is positively correlated with amplitude and frequency. IDs of region II are highest among all regions for both species and are asymptotic to one (a straight line) from region III to region IV.

An effective stiffness, \bar{E} , of the interdigitating ventral plates was predicted with a two-dimensional analytical model (Li et al., *in review*), the schematic diagram of which is shown in Fig. 8-1b (Appendix E). The geometry of this model is determined by three structural parameters (normalized amplitude (A), spatial frequency ($1/\lambda$) and gap (g)), as also shown in the Fig. 8-1b. The suture structure consists of triangular skeleton teeth (yellow and gray, which are used to identify teeth from two pelvic girdle to highlight the interdigitating pattern between them.) interdigitating via organic tissues (light green). The stiffness ratio of two phases (E_1/E_0) of a suture is taken as a value of 100 (Norman et al., 1995; Jager and Fratzl, 2000), and the suture is subject to local tensile stress, σ , normal to the suture axis, as shown in Fig. 8-1b. The spatial distribution of the effective stiffness, \bar{E}_0 , related to the skeletal bone stiffness, E_1 , is predicted by this analytical model, as shown in Fig. 8-1e. The median suture in Region II is the stiffest and therefore can provide the stiffest mechanical support around the area of trochlear joint and the marine *G. aculeatus* suture is roughly four times stiffer than the freshwater one. Region I is the second stiffest region for the marine *G. aculeatus*, and is completely missing in

freshwater *G. aculeatus* pelvis. IDs of four regions in both samples are positively correlated with the predicted average effective stiffness as shown in Fig. 8-1f.

Region II of the pelvic assembly is clearly associated with the trochlear joints and pelvic spines, providing the highest stiffness for mechanical support of the trochlear joints. The second stiffest region I of the full-morph marine pelvic suture disappear in the full-morph freshwater pelvis and this reduction has been reported among full-morph freshwater pelvis from various freshwater populations (Bell, 1987; Bell and Orti, 1994). In marine *G. aculeatus*, the anterior processes of the pelvic assembly articulate with the pectoral girdles and the median pelvic suture is extended into the end of the anterior process, fully covering the anterior abdomen for protection. The stiff region II also may provide additional rigidity in conjunction with the articulation of the anterior processes with the pectoral girdles to the anterior buttress that consists of the pelvic girdles, lateral plates and the dorsal spines and their basal plates. Among the freshwater *G. aculeatus* populations, the suture of region I is reduced, which may improve the abdomen distention for reproduction or feeding with the minimal coverage in the anterior region (Mori, 1987; Baker et al., 1995). Mechanical reduction in full morph pelvis from marine to freshwater *G. aculeatus* populations is clearly associated with the reduced amplitude and frequency of the median suture, maintaining the stiffest region II as the stiffest region.

8.3.3. Three-Dimensional Morphological Features of Suture and their Mechanical Relevance

Three-dimensional micro-CT images of the two *G. aculeatus* pelvic assembly in Fig. 8-2a show that the single layer ventral plate in region I smoothly transitions into the top and bottom plates in region II and III, where the top ventral plate reach a peak height in region II and then smoothly decreases, and eventually becomes parallel in region IV. In region II and III, the space between those two plates is occupied by multiple internal plates, which are gradually inclined one by one across region II and region III, supporting the top ventral plate through the width. Two important structural parameters, z-height (H) and inclination (φ), are indicated in the schematic drawing of the fully developed three-dimensional suture of the marine *G. aculeatus* in Fig. 8-2a *bottom right*. From anterior to posterior, the internal plates are almost vertical to the bottom ventral plates up to $\sim 1/3$ of region II, and then eight internal plates are inclined from 82° to about 10° in conjunction with the z height profile in both full-morph *G. aculeatus* pelvis (Fig. 8-2b and 8-2c). Around the trochlear joints, the z-height of the internal plates reaches the maximum value with an inclination of $\sim 45^\circ$ and the inclined plates supported by the intersecting short plates on the bottom ventral plate. Another horizontal plate right beneath the top ventral appears and extends from two thirds of region II up to region III, stacking with its

counterpart from the other pelvic girdle in z direction. In region IV, a sandwich-like, porous cross-sectional structure is observed for both pelvic assemblies.

The three-dimensional, full morph *G. aculeatus* pelvic assembly displays the featured y-z cross-sectional structure in region II that can be analogous to a parallel connection of multiple I-beams, which is known to provide an optimal effective bending stiffness per unit weight while resisting the bending moment in x direction (M_{xx}). The analytical models with the inclined I-beam structure subjected to bending moment in x direction were developed to predict bending stiffness for each internal plate located in region II (Fig. 8-2d and 8-2e), and were compared to the numerical finite element analysis (FEA) models for further verification (Appendix E). Analytical and numerical predictions show good agreement. The trend of two bending stiffness elements in region II appears to be almost identical in both full-morph marine and freshwater pelvis except for the magnitude. The inclination (ϕ) of the internal plates enables the corresponding bending stiffness matrix of pelvis to have two important non-zero stiffness elements, K_{xx} and K_{xy} . There are two salient features of inclined plates for effective bending stiffness of full-morph pelvis: (1) bending stiffness, K_{xx} increased by a factor of $1/\sin\phi$ and (2) the coupled bending stiffness, K_{xy} , increased from 0 (a vertical plate to bottom surface, $\phi = 90^\circ$) to $K_{xy} = \tan\phi \cdot K_{xx}$ as a function of ϕ . The inclination (ϕ) of both full-morph pelvis decreases from 90° to 45° in region II (Fig. 8-2b and 8-2c), and the corresponding bending stiffness elements K_{xx} and K_{xy} increase and eventually reach the maximum value around the trochlear joints (Fig. 8-2d and 8-2e). The reduced height of region II in freshwater pelvis results in the decreased bending stiffness by two orders of magnitude as compared to bending stiffness of marine pelvis (K_{xx} is also proportional to the cube root of height). The coupling term indicates that a bending moment M_x leads not only to bending curvature κ_x , but also to bending curvature κ_y which will be shown to lead to enhanced bending stiffness when changing from rest to offensive configuration.

8.3.4. Potential Mechanical Roles of Pelvis in Conformational Transition from Rest to Offensive

The pelvic spines can take on two main configurations; (1) in the absence of a predatory threat, a “rest” position whereby the long axis of the pelvic spines are adjacent and parallel to the long axis of ventral plates and (2) in the presence of a predatory threat, an “offensive” position whereby the spines rotate outward and take a position with their long axis perpendicular to the long axis of the ventral plates, thereby increasing the effective body size of the fish (Hoogland et al., 1956; Reimchen, 1983). During defense, the pelvic girdles have to support the pelvic spines against axial compression and bending and should also minimize the back deflection of the armor into the soft tissues. Structural diversity of the pelvis in sticklebacks often influences the corresponding mechanical

functionality. The conformational transition of pelvis spines in full-morph marine *G. aculeatus* pelvic assembly is shown in Fig. 8-3 (from rest to offensive, Fig. 8-3a; from offensive to rest, Fig. 8-3b).

The three-dimensional μ CT images of the fully developed marine pelvic assembly were obtained in both rest and offensive configurations for comparison (Fig. 8-4a and 8-4b). During the conformational transition from rest to offensive position, the pelvic spines rotate about the trochlear axis and their condyles gradually interlock with a pair of foramina dorsal and ventral of the trochlear joints. The free body diagram (Fig. 8-4c) of the full-morph pelvic assembly during the transition indicates the boundary conditions of *G. aculeatus* armor, especially the anterior region which behaves like a rigid buttress via lateral plates that bridge between the dorsal spine-basal plate assembly and the pelvic assembly. When the condyles of pelvic spines are locked into the foramina of the trochlear joints, the pelvic girdles are pushed inward, inducing internal reaction forces: (1) compression ($F_{AL} = F_{LA}$) of lateral plates via a pair of ascending processes and (2) compression ($F_{RL} = F_{LR}$) and (3) moment ($M_{RL} = M_{LR}$) of the median suture. Due to rotation of the pelvic girdle in y-z plane, the suture on the bottom ventral plates is subjected to compression, especially concentrated around the trochlear joints. The conformational changes of pelvic spines and induced internal reaction forces impose the spatial rearrangement of the microstructure on the pelvic girdles. The y-z cross-sections of each region in two configurations are compared in Fig. 8-5b. In the offensive configuration, the rotation of the bilateral pelvic girdles in y-z plane is clearly observed while the top ventral and internal plates are in contact with their counterparts. Moreover, the four x-y slices from the dorsal to ventral (H1 to H4 of Fig. 8-5a) in Fig. 8-5c also display rotation in x-y plane with significantly increased overlapping and contact area in the offensive configuration as compared to the rest one.

Based on the suture morphology in Fig. 8-1a and 8-2a and its predicted mechanical properties in two and three dimensions, the numerical model containing all important structural features (e.g. internal plates of region II and suture on the bottom ventral plates) were constructed in order to understand their mechanical roles in the conformational transition (Fig. 8-6a). From the simulation, we found two important stiffening mechanisms in region II that was subjected to bending moment in x direction while mimicking the boundary conditions associated with the conformational change of pelvic spines (Fig. 8-4c): first, increased overlapping and contact area among top ventral and internal plates increases bending resistance in x direction significantly (Figs. 8-5b and 8-6d); second, the coupled component of the bending stiffness, K_{xy} , induced by the inclination of internal plates, additionally generates a rotation of the two pelvic girdles in x-z plane, which helps increase the contact area between inner layers remarkably as opposed to a pair of vertical internal plates that only allow overlapping without direct contact with each other during bending (Figs. 8-5c and 8-6e). The inclined internal plates

are locked by each other via contact, which provides the additional locking mechanism for enhanced bending resistance in region II of full-morph pelvic assembly. Moreover, at the maximum rotation, the top surfaces are closed and the whole pelvic girdle structure is fully locked, reaching the highest stiffness (Fig. 8-6b and 8-6c). In the meantime, the median suture of the bottom ventral plates is applied to compression (Figs. 8-4c, 8-6b) and the suture with effective stiffness holds the pelvic girdles against the rotation in x direction, in particular, around the trochlear joint of region II. Therefore, all these two- and three-dimensional structural features of pelvic girdles are mechanically conjugated, providing the effective stiffening mechanism to the whole system in the conformational transition from rest to offensive in order to support the extended pelvic spines with the maximized bending stiffness by means of defense against a threat in the environments.

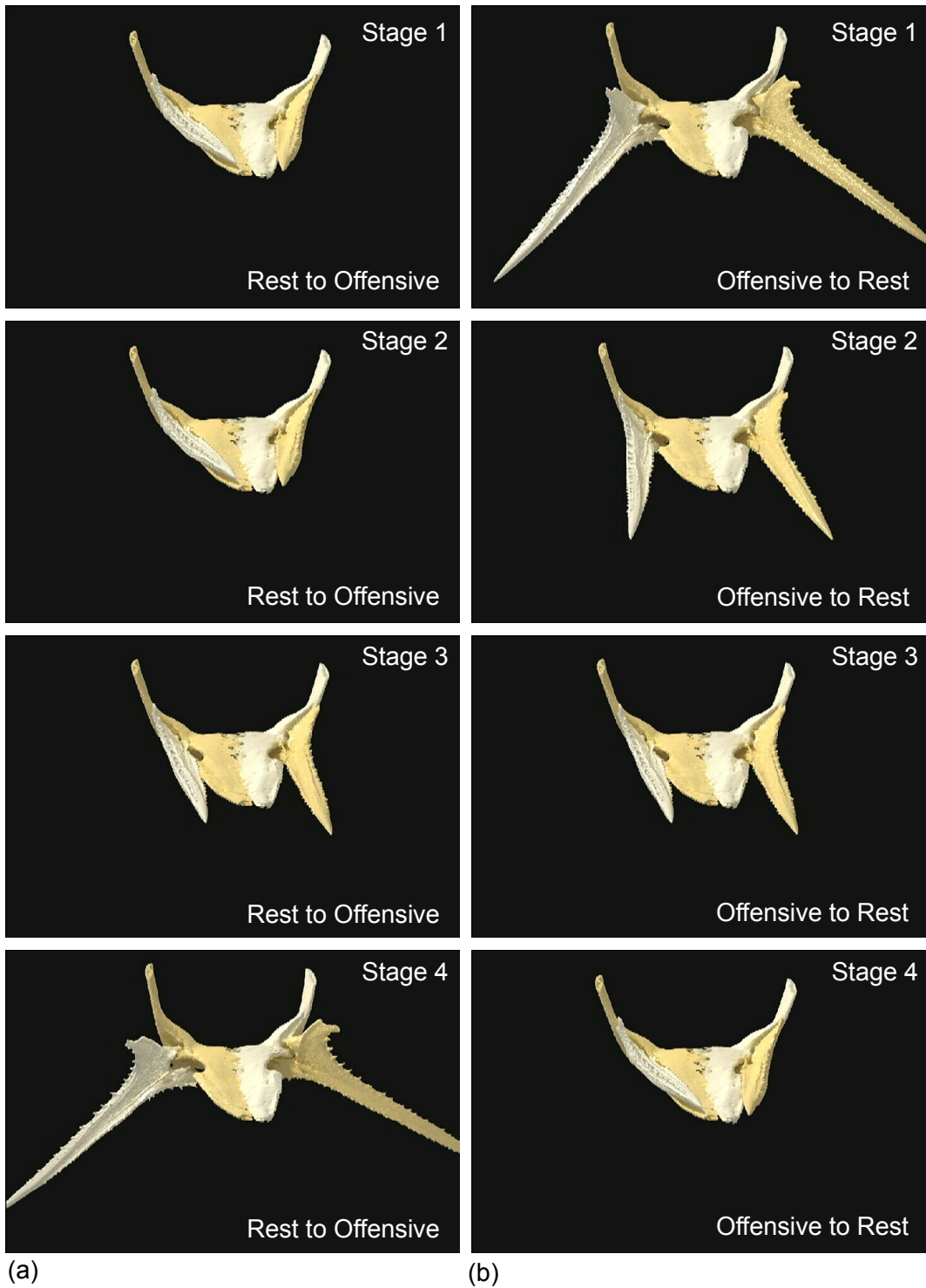


Figure 8-3. Conformational transition of pelvic spines (a) from rest to offensive and (b) offensive to rest. The images were taken from the animation movie created by S. Araya.

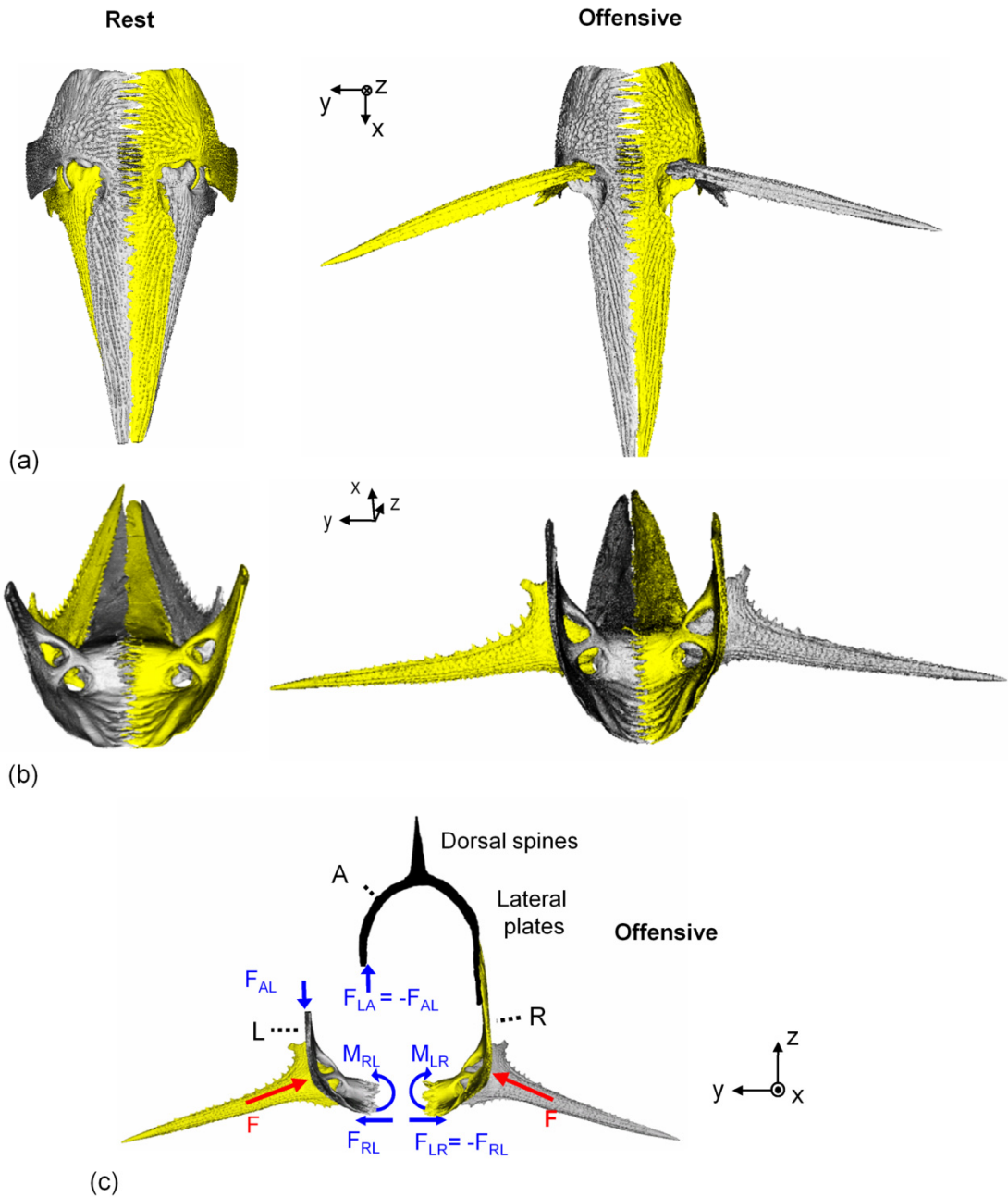


Figure 8-4. Three-dimensional structures of pelvic assembly of a marine *G. aculeatus* in rest and offensive configurations; (a) Pelvic assembly, bottom view, (b) pelvic assembly, top view and (c) free body diagram of fully armored marine *G. aculeatus* armor when the two pelvic spines are fully extended during conformational transition from rest to offensive and three-dimensional structural comparison of pelvic girdle-spine assembly in two states (*rest vs. offensive*).

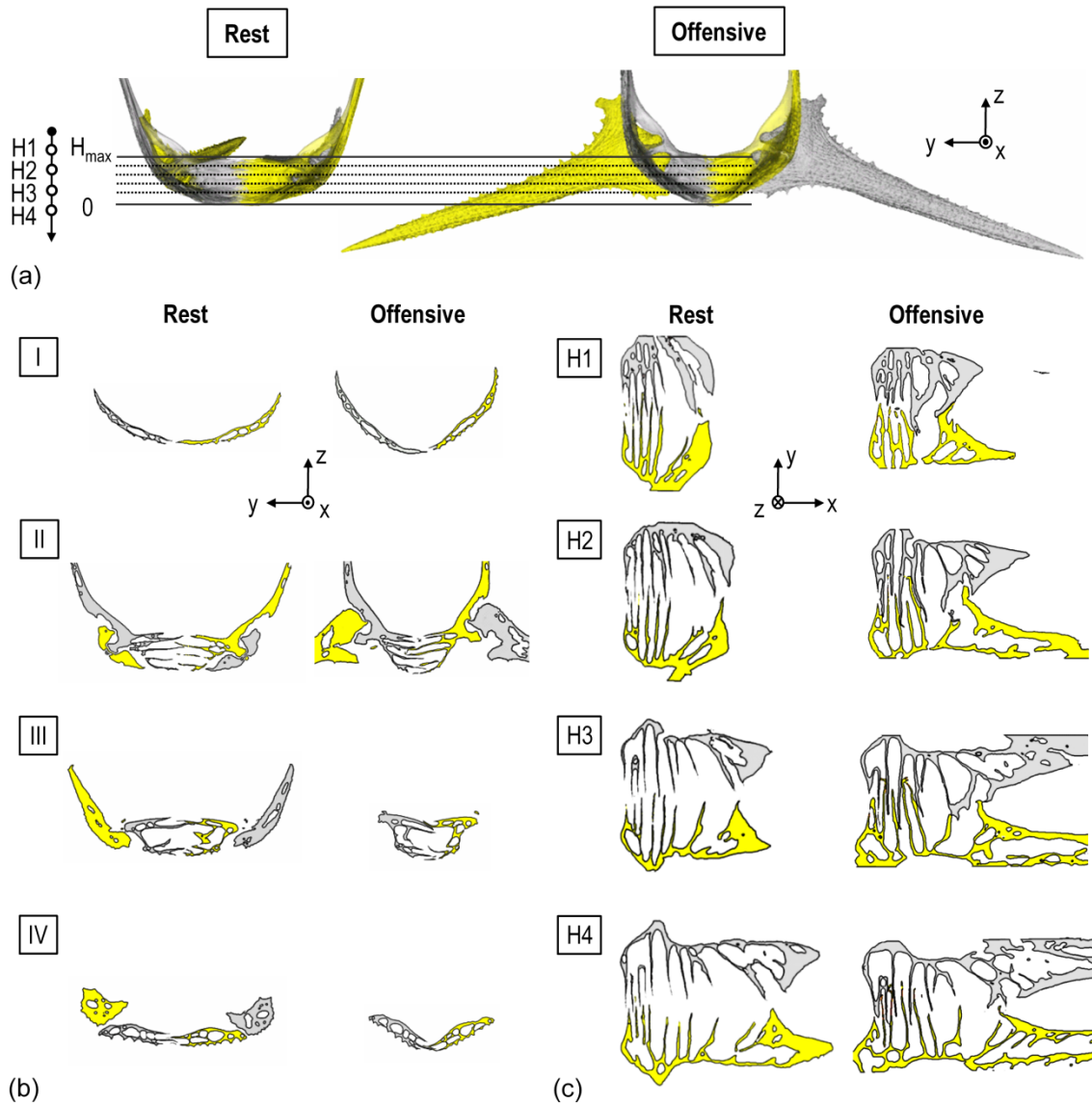


Figure 8-5. Structural comparison of a full-morph pelvic assembly in conformational transition from rest to offensive; (a) three-dimensional structures of pelvic assembly in rest and offensive configurations, indicating the sectioned planes from the top to bottom ventral plates, (b) two dimensional y-z slices of four regions and (c) two dimensional x-y slices corresponding to each section (H1 to H4) indicated in the three-dimensional structure of (a).

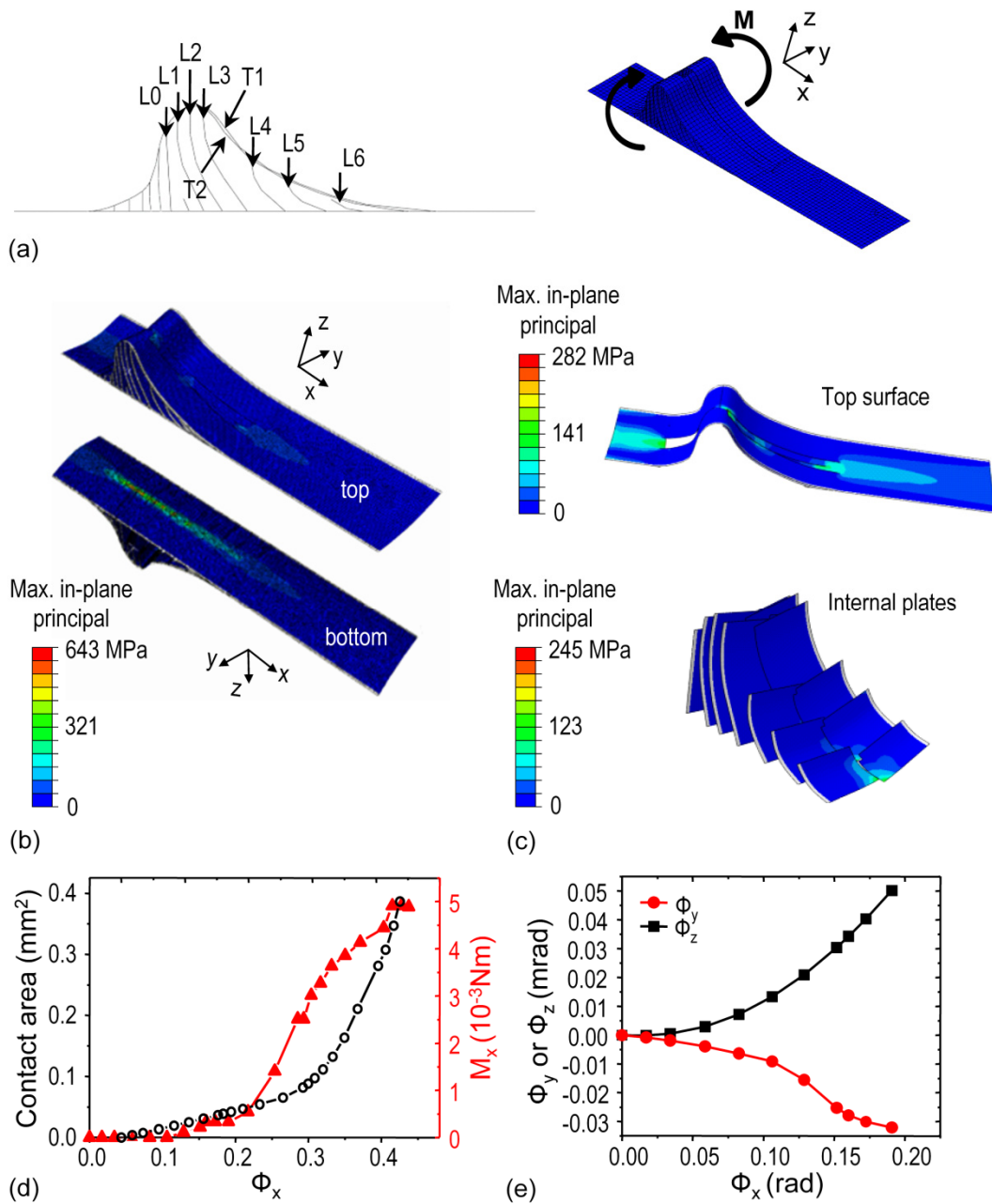


Figure 8-6. Stiffening mechanism of conformational transition of *G. aculeatus* pelvic assembly from the ‘rest’ to ‘offensive’ positions: (a) sketch of the top surfaces and internal layers and the whole structure with the applied moment (M), (b) and (c) max. in-plane principal stress distribution of (b) the whole pelvic girdle (top view, *top*; bottom view, *bottom*) and (c) the top surface (*top*) and internal plates (*bottom*) in the offensive position, (c) deformation of the outer top surface and the internal layers in two positions, (d) total contact area and moment of the whole structure as a function of the degree of rotation, and (e) the coupling effects of the rotation. Figure by Y.N. Li.

8.4. Discussion

In this Chapter, material and mechanical approaches were made to explore how structural variation of a natural exoskeleton plays a role in its mechanical functionality. Mechanical properties of the pelvis using composite analytical and finite element computational models in conjunction with the microCT experimental data indicate the functional variation even within the close full-morph pelvic assemblies. A better understanding of the locking mechanism of pelvic spines that originates from their conformational transition from rest to offensive imposes that the structural elements of pelvic assembly are mechanically conjugated; (1) the internal structure of the trochlear joints, filled with the number of thin, discrete and inclined plates, provides the effective bending stiffness in response to the induced bending moment by means of the increased z-height, coupled bending stiffness and increased overlapping/contact of the internal plates; (2) the median suture on the ventral plates holds the pelvic girdles against the separation caused by induced compression; and (3) ascending branches transmit the force into lateral plates, increasing the force distribution and avoiding the localized pressure (anterior processes are also in contact with the skull, contributing to the additional force transmission). Reduced dimensions and geometric complexity of these structural components result in decreased biomechanical performance of the corresponding pelvic structure. Therefore, the full-morph freshwater *G. aculeatus* pelvis supports the extended pelvic spines in the same way as the marine one, whereas the magnitude of its effective bending stiffness is significantly reduced by the lowered suture interdigitation and decreased z-height.

The evolution of pelvic reduction has been observed in two modes, paedomorphosis and gradual truncation of distal elements (Bell, 1987). In the less popular paedomorphic mode observed among the *G. aculeatus* fossils or the small number of California populations, the developmental sequence of individual structural elements is likely to influence the progress of pelvic reduction. In this case, the immaturity of the pelvic structure deteriorates mechanical functionality during the conformational change of pelvic spines for the purpose of offensive defense. Most *G. aculeatus* populations exhibit gradual truncation of distal elements with the similar pattern of the pelvic reduction: the loss of pelvic spine and additional following abbreviation of the other elements (Bell, 1987). This evolutionary process can be called the ‘transition of pelvis from offensive to passive defense.’ The fully developed pelvic assembly of marine *G. aculeatus* supports the extended pelvic spines by mechanically conjugated structural elements, whereas the reduced pelvic assembly protects the body against the penetration by means of the mineralized plates covering the abdomen in the same manner as the lateral plates do at minimal weight (Reimchen, 1983; Reimchen, 1992; Bell and Foster, 1994; Reimchen, 2000; Song et al., 2010). One *G. aculeatus*

population from the Kalmbach Lake, South Alaska exhibits the two-scored pelvis with the complete loss of spine, trochlear joints, internal plates, posterior process and the vestiges of a median suture in addition to the typical notched anterior process (Fig. 8-7). Almost all structural components involved in the offensive defense significantly disappear, implying the role of pelvic armor plates as the protection of the anterior abdomen against the penetration.

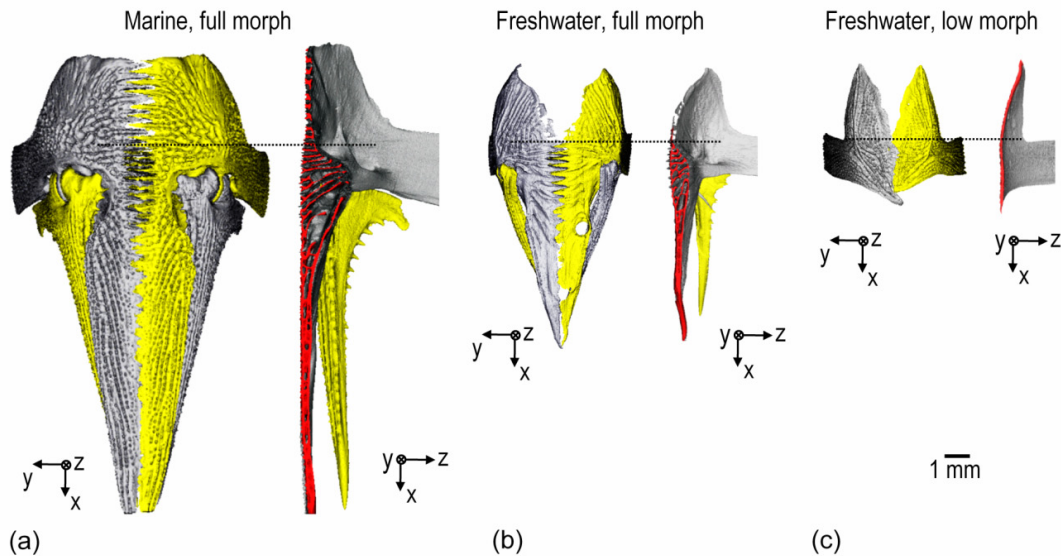


Figure 8-7. Morphological variations of pelvic assembly; (a) full morph marine *G. aculeatus* from Rabbit Slough, (b) full morph freshwater *G. aculeatus* from Beverly Lake and (c) low morph freshwater *G. aculeatus* with loss of pelvic spines from Kalmbach Lake.

Two or three dominant mechanisms of pelvic reduction among freshwater populations have been proposed: antipredation (Reimchen, 1980; Bell et al., 1993; Reimchen, 1994; Reimchen and Nosil, 2002), calcium limitation (Giles, 1983; Bell et al., 1993) and growth rate (Reimchen, 1991; Marchinko and Schluter, 2007; Barrett et al., 2008). In particular, antipredation significantly influences the loss of pelvis spines depending on the type of predators. Pelvic spines are vulnerable to insect predation because they are easily grabbed, which is likely to induce the complete loss in pelvic assembly (Reimchen, 1980; Bell et al., 1993). Calcium limitation and growth rate give the freshwater populations to set the margin between the armor defense and other survival strategies, provoking the sequential reduction of pelvic assembly with the increased independence of the heavy armor. As compensation, increased body size, flexibility and mobility are better achieved (Reimchen, 1991; Bergstrom, 2002; Barrett et al., 2008). Even the increased flexibility of pelvic assembly by reduced suture benefits feeding and reproduction because of the larger abdominal distention that enables the

increased amount of food intake and storage at minimal times, and the enhanced fertility with the larger number of eggs (Mori, 1987; Baker et al., 1995). This observation is also found during the evolution of other natural exoskeleton systems or human body armor (Arciszewski and Cornell, 2006; Sire et al., 2009). The armor design is concerned about a trade-off between protection and mobility/flexibility and in particular fish armor usually achieves a good balance between those two conflicting functionalities (Bruet et al., 2008). The phenotypic variations of the pelvis are governed by a small number of regulatory genes in Pix 1, 2 at single mutation leaps, which help the freshwater *G. aculeatus* populations interact with various environment constraints within the relatively shorter evolutionary time as compared to other species (Shapiro et al., 2004; Chan et al., 2010). On-demand functionalities of *G. aculeatus* armor in response to the various environmental threats can be achieved by the proper armor structures that are designed and processed by the customized gene expression in accordance with the small number of regulatory mutations.

Making a blue print of the evolutionary processes encompassing all of the related factors at the different levels from molecules to macroscopic structures and their corresponding functionalities in order to optimize fitness and survivability to the environment provides a better understanding in the field of evolutionary biology. Especially the definitive functional variation of the structures can give a better insight to natural selection, answering the question about what factors are more dominant and how they influence the system in various aspects. Furthermore, the whole process on imposed functionality by a designed structure from genetic processing at molecular levels can give a better idea about the design principles and processing for bioinspired material systems.

8.5. Conclusion

Phenotypic variation of threespine stickleback pelvis originating from gene regulation has been treated as a good evolutionary evidence for natural selection, whereas the corresponding functional variation that is directly related to fitness/survivability to the environments is still less investigated. Quantification and mechanical assessments of complex *G. aculeatus* pelvis were performed by material and mechanical approaches in terms of a structure-property-function relationship using up-to-date experimental and mathematical/computational tools. The structural components of pelvic assembly are mechanically conjugated, increasing bending stiffness and structural rigidity in order to support the locked pelvic spines in the offensive position. Reduced dimensions or structural abbreviation of freshwater *G. aculeatus* pelvis decreases mechanical functionality, ultimately altering the defense mechanism from offensive to passive in compensation of flexibility/mobility, growth rate, and calcium consumption.

Understanding functionality of *G. aculeatus* armor structures can provide more direct evidence of natural selection in the corresponding environments.

Chapter 9.

Conclusion & Future Work

9.1. Conclusion

Structural biological materials hold great potential for engineering designs that aim for multifunctional and energetically efficient performance, and mechanical amplification, based on lessons from biological organisms that have evolved a veritable encyclopedia of environmentally-friendly engineering designs for protection against specific predatory and environmental threats. Novel and efficient threat-protection design concepts have emerged through the lengthy evolutionary processes which satisfy the requirements and constraints of the given engineering problem. Hence, significant information can also be gained about the optimization of hierarchical structural design for differing threats and loading conditions. Abstracting design principles of complex natural exoskeleton systems is another challenge. A structure-property-function approach can provide a fundamental understanding of hierarchical biological systems at multi-length scales, capturing the interaction among different levels of structure parameters from atomic structure to the whole armor. This thesis has focused on "armored" fish which have highly mineralized articulating scales whereby the nano-/micro-scale materials design of the individual scales works in conjunction with a host of larger length scale geometries and interlocking mechanisms to enable biomechanical flexibility and mobility. The ultimate goal of this thesis was to uncover a set of the material and mechanical design principles of the two fish armor model systems, *Polypterus senegalus* and *Gasterosteus aculeatus*, in terms of their corresponding environments.

Individual *P. senegalus* scales have the ganoine-dentin-isopedine-bone quad-layered structure with the structurally anisotropic ganoine outmost layer and functionally graded interfaces between two different material layers. The structural features of *P. senegalus* scales provide salient penetration resistance mechanisms, which include (i)

load-dependent effective indentation modulus and hardness, (ii) enhanced stress and dissipation transmission to the underlying more compliant and softer dentin layer, (iii) lowered ganoine/dentin interfacial stresses and, hence, reducing any propensity toward delamination, (iv) the suppression of catastrophic radial surface cracking, and promoting localized circumferential cracking, and (v) the crack arrest mechanism by providing discrete structural pathways for circumferential cracks to propagate normal to the surface for easy arrest by means of the underlying dentin layer, thereby minimizing damage. The quad-layered structure of *P. senegalus* scale armor has been evolved and optimized by varying structural parameters such as thickness, number or sequence of the constitutive material layers in response to dynamic stimuli by its interactive threat systems (e.g. teeth of other *P. senegalus* during territorial fights) in the environment. The nano- and micro-level structural optimization of individual *P. senegalus* scales is a key factor to achieve a balance between protection and mobility, in conjunction with their macroscopic geometry (Fig. 9-1).

On the other hand, *G. aculeatus* armor that is composed of two major armor components, lateral plates and pelvic assembly, is made of the single-layered sandwich-like lamellar bone with micro-size pores, exhibiting effective bending stiffness at minimum weight. The overview of *G. aculeatus* armor at multi-length scales is shown in Fig. 9-2. The morphological features of the lateral plates and lateral plate interconnections (cross-sectional geometry and plate overlap) allow for a constant armor thickness, promoting spatially homogeneous protection and modulate mobility/flexibility via a mixture of a sliding hinge joint and an ellipsoidal joint for limited rotational and translational compliance in specific directions. Pelvic assembly of *G. aculeatus* has complex morphology that is closely correlated with its biomechanical functionality. Extended pelvic spines against a toothed predator for offensive defense can be supported by the stiffened pelvic assembly during conformational transition from rest to offensive through the structural locking mechanisms of the two- and three-dimensionally interdigitating median suture that connects the bilateral pelvic girdles. Different levels of armor reduction in *G. aculeatus* were found among freshwater populations in evolution, caused by various environmental factors, which may lead to mechanical and functional reduction of armor in response to environmental changes.

There has been much progress in the design of protective systems over the last decade; but a significant number of challenges remain: weight reduction and increased flexibility/mobility without degradation of protection capabilities, improved multi-hit capability, and multifunctional performance across diverse operational environments. Therefore, detailed studies of the structure and properties of biological armor hold broad applicability to the development of synthetic engineered, protective penetration-resistant materials (e.g., for human body, vehicle and building protection), protective coatings (e.g., exterior paint of automobiles, motorcycles, etc.), construction applications (e.g.,

pipelines that need resistance to rock penetration/abrasion), and sports equipment (e.g., helmets, chest protectors, etc.). Moreover, in conjunction with evolutionary processes of fish armor systems, these studies can provide useful phylogenetic information and insights into the biomechanical function of the armor of both the evolutionary ancestral state, as well as subsequent morphs.

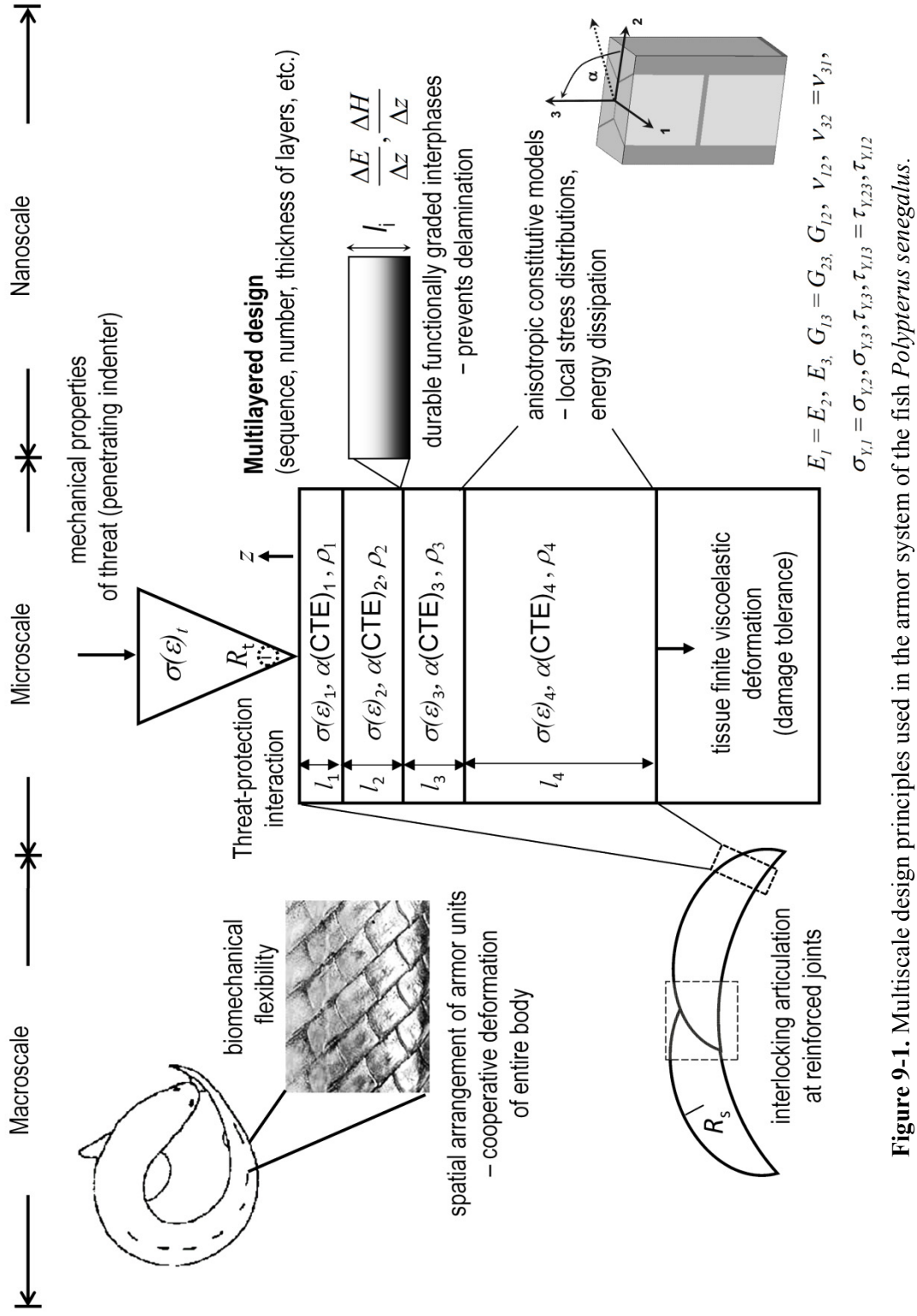


Figure 9-1. Multiscale design principles used in the armor system of the fish *Polypterus senegalus*.

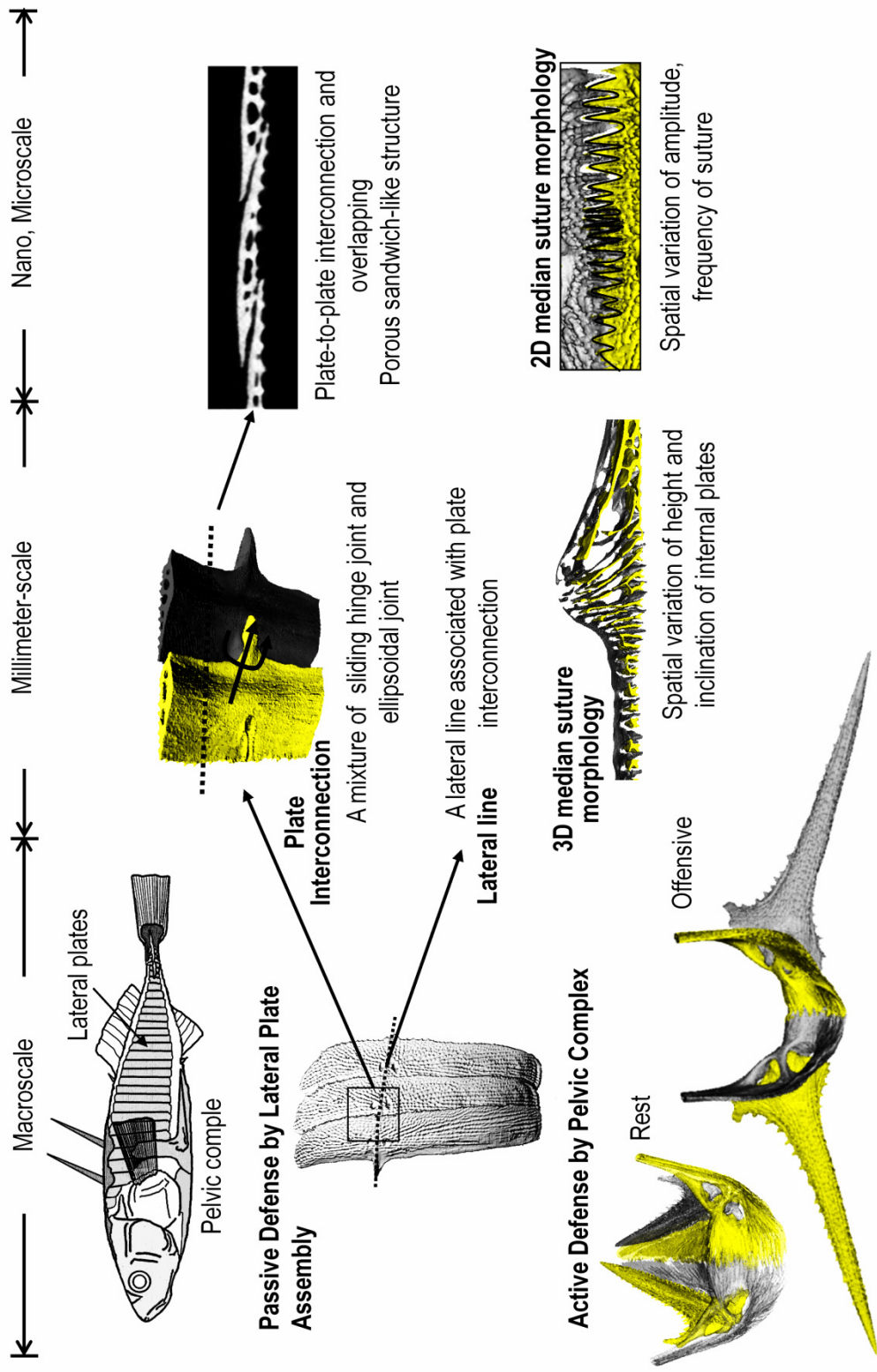


Figure 9-2. Multiscale design principles used in the armor system of the fish *Gasterosteus aculeatus*

9.2. Future Work

9.2.1. Failure Mechanisms of Biological Structural Materials

In this thesis, the mechanical behavior of fish armor systems has been explored in response to Vickers microindentation or hypothetical tooth biting, but there are still many open questions about crack propagation and energy dissipation mechanisms under physiological conditions of fish armor that often include high impact loads in various aquatic environments. The higher load deformation and failure mechanisms of fish armor can be explored using a new instrument prototype, BioDentTM (Active Life Technologies, USA) that has the capability of higher load instrumented indentation measurements (up to ~10 N) in aqueous in vitro environments, and importantly extending the measurements to in vivo measurements of living animals. The BioDentTM is originally designed for the bone diagnostics in vivo without any surgery, thus its unique test probe/reference probe geometry enables direct measurements to be made on bone that is covered with skin and soft tissue (Fig. 9-3a and 9-3b) (Hansma et al., 2009; Randall et al., 2009). During in vivo measurements, the long and slender reference probe/test probe assembly is inserted through the skin until reaching the bone surface. Then, the test probe begins to slide for indentation with respect to the reference probe while the reference probe serves as a reference for the calculation of the indenting distance of the test probe (Hansma et al., 2009). Preliminary instrumented indentation up to a maximum load of ~ 3N was carried out on *P. senegalus* scales in aqueous solution under cyclic loading conditions (loading cycle number = 5), using the BioDentTM. After the experiments, the indented samples were observed by scanning electron microscopy and images show the surface fracture modes of *P. senegalus* scales (Figs. 9-3c). Advantageous circumferential cracking was still observed as the dominant surface fracture mode, even at these higher loads, where the damaged regions were still highly localized, thus avoiding catastrophic failure of the entire armor unit. Damage localization and multi-hit capability of natural exoskeletons will be explored by experimental and computational approach. The spatial-dependence of armor penetration resistance will also be quantified to see if it is maintained throughout or if weaker spots exist. Based on experimental observation and quantitative fracture data, computational fracture models will be developed in order to understand failure mechanisms of *P. senegalus* scales. The developed methodologies will be generally applicable to all biomaterials, and especially powerful for biomineralized hierarchical structural materials.

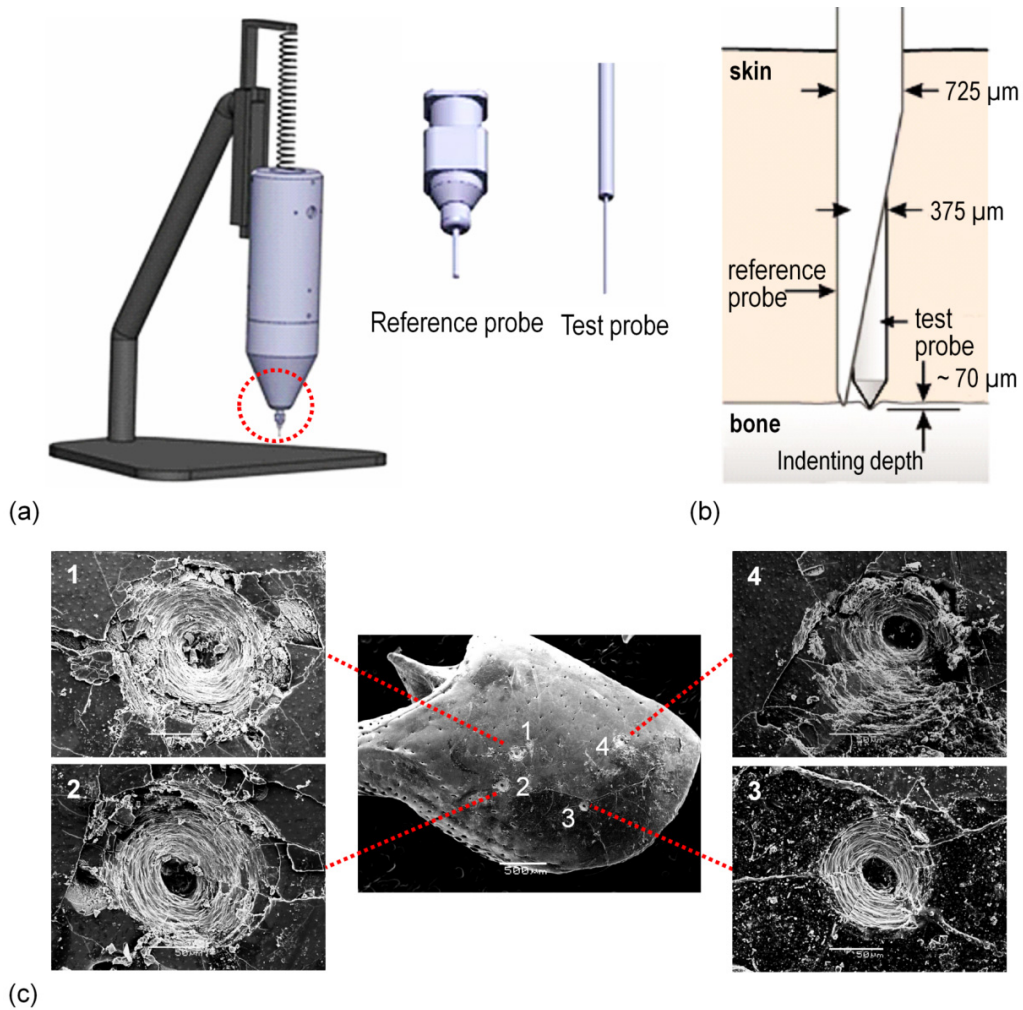
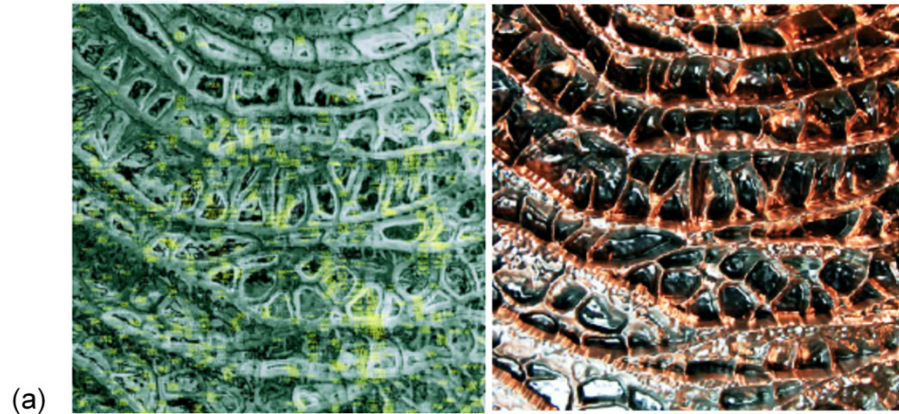


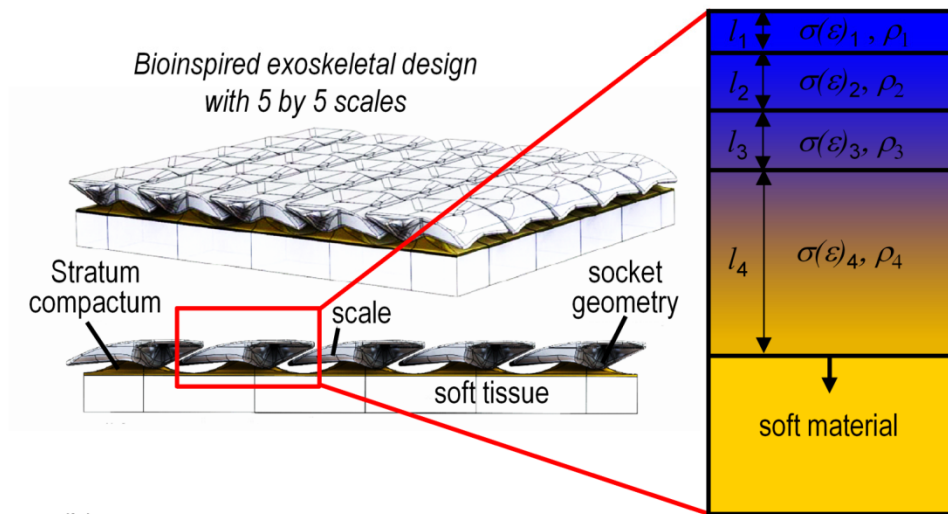
Figure 9-3. *In vitro/in vivo* microindentation by BioDent™; (a) a schematic drawing of the BioDent™ instrument with the reference probe (left) and the test probe (right) (Randall et al., 2009), (b) a schematic drawing that shows how the reference probe/test probe assembly is working during *in vivo* indentation (Hansma et al., 2009) and (c) preliminary *in vitro* microindentation to the maximum load of ~ 3N on a *P. senegalus* scale in water with localized circumferential cracks on the scale surface, demonstrating its multi-hit capability.

9.2.2. Hybrid Material-Morphometric Exoskeletal Design

The current bio-inspired exoskeletal designs have been created in collaboration with the architecture student, S. Reichert, as introduced in Chapter 2 of this thesis. The results obtained from morphometric analysis of *P. senegalus* scales were mainly utilized to create the bio-inspired exoskeletal design using parametric computer-aided-design (CAD) software (Reichert, 2010). The new exoskeletal designs can be interfaced with material-based studies of this thesis to assess how inherent structure and properties work together with form to achieve threat-specific protective function. In this hybrid approach, just as in biology, the spatial distribution of material properties works in conjunction with geometric form to achieve performance. Variable Property Design (VPD) and Variable Property Rapid Prototyping (VPRP), which are the architectural methodological tools, developed by Oxman, will be applied to create new threat-specific hybrid bio-inspired functional flexible protective design (Fig. 9-4a) (Oxman, 2010). VPD will provide a methodological framework by which to model, simulate and fabricate material assemblies with gradient properties designed to correspond with multiple and continuously varied functional constraints. Such capability is characterized by the ability to strategically control the density and directionality of material substance in the generation of form. The VPRP technology combines a novel software environment coined Variable Property Modeling (VPM) with a mechanical output tool designed as a 3-D printer, and will enable the controlled variation of material properties as continuous gradients across the surface and volume area of individual armor units in flexible armor assemblies. Parametric VPM models will be directly utilized to create physical prototypes using the multimaterial 3D printer Objet Connex 500. The materially graded and continuous flexible systems will take full advantage of multimaterial three-dimensional printing manufacturing capabilities by implementing gradient material composites into individual armor units in order to mimic the *P. senegalus* scales that are composed of four constitutive material layers with gradient mechanical properties through thickness (Fig. 9-4b). The 3D prototypes with varying spatial material distribution will be evaluated with lab-based mechanical experiments in various loading conditions in terms of the degree of freedom and anisotropic biomechanical behavior. In addition, optimal processing parameters (e.g. materiality, geometry) of the 3D prototypes will be explored in order to provide the best mechanical performance in response to expected operating conditions including tensile loading, compressive loading, shearing, and bending as well as combined loading conditions. Accordingly, computational mechanical models will be constructed to predict the mechanical behavior of the 3D prototypes based on experimental observation and quantitative data.



(a)



(b)

Figure 9-4. Bioinspired hybrid exoskeletal designs in conjunction with material-based research; (a) variable property analysis (*left*) and fabrication (*right*) of a hybrid design, inspired by biological tissues, which was made of the aluminum and low carbon steel composite (N. Oxman) (Oxman, 2010) and (b) example of hybrid exoskeletal designs mimicking the spatial distribution of *P. senegalus* scales by combining two materials, hard (blue) and soft (yellow) materials through thickness.

9.2.3. Interdisciplinary Approach of *G. aculeatus* Armor

Conventional evolutionary approach tried to explain natural selection using the relationship between the apparent structures and fitness/adaptation of biological systems, considering on the corresponding environmental constraints in evolution, but couldn't explain how the biological systems have interacted with environments explicitly with a lack of direct scientific evidence (Figure 9-5) (Darwin, 1859).

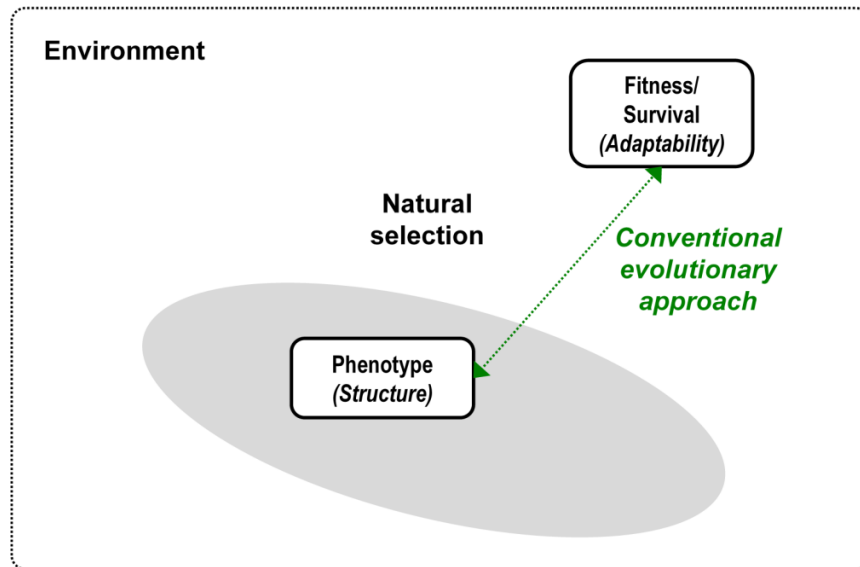


Figure 9-5. Natural selection mechanism by conventional approaches in evolutionary biology.

Recent genetic approach has resolved many unsolved problems in evolutionary biology, providing insight into genetic-based structural variation for natural selection, adaptation and speciation (Figure 9-6; the blue line between genetic alteration and phenotype) (Shapiro et al., 2004; Orr, 2005; Noor and Feder, 2006; Klingenberg, 2010; Wolf et al., 2010). The fields of engineering and architecture hold great potential to contribute to elucidating the mechanisms of evolutionary biology, filling in the gap between phenotypic variation and related functionality by means of a structure-property-function relationship approach (Fig. 9-6) (Elices, 2000; Callister, 2003). Therefore, the proposed interdisciplinary approach in the field of evolutionary biology incorporates genetic and engineering approaches into the conventional evolutionary approach (Fig. 9-6).

The study on *G. aculeatus* in this thesis has elucidated the structural and functional differences among divergent populations of *G. aculeatus*, which were the consequences of adaptation and fitness to their environments. Field-caught *G. aculeatus* samples (from Rabbi Slough and other Alaskan lakes) that were used in this thesis have been extensively investigated by Cresko and his colleagues who have confirmed that

there is a genetic basis to armor variation (both lateral plate and pelvic phenotypes) between Rabbit Slough and Alaskan freshwater populations (Cresko et al., 2004). Also, the lab-reared *G. aculeatus* offspring, bred in the lab, exhibit apparently the same armor phenotypes as their parents do in the wild, Rabbit Slough and Alaskan freshwater lakes and genetically manipulated lab-reared *G. aculeatus* under controlled environment constraints have been used for experimental evidence to support the hypothesis that genetic variation is indeed responsible for a large proportion of phenotypic variation in stickleback armor (Cresko et al., 2004; Shapiro et al., 2004; Kingsley and Peichel, 2007; Baird et al., 2008; Barrett et al., 2008; Chan et al., 2010). Collaboration between genetic/evolutionary biologists and material/mechanical scientists will establish the comprehensive and interdisciplinary approach for evolutionary biology, providing perspective on many unsolved evolutionary problems.

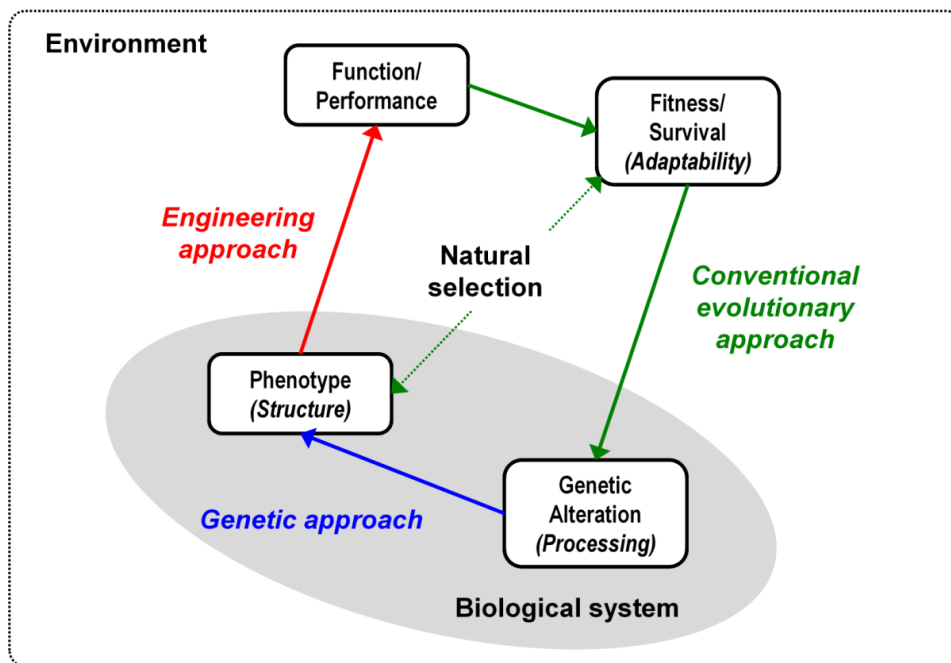


Figure 9-6. Proposed natural selection mechanism in evolutionary biology by interdisciplinary approach (conventional evolutionary, genetic and engineering approaches)

Appendix A.

Determination of Best Fit to Indentation Curves

A.1 Determination of Elastic-Perfectly Plastic Best Fits

In this thesis, elastic-perfectly plastic mechanical properties of the individual constitutive material layers of *P. senegalus* scales were assumed in order to determine material properties from nanoindentation experiments with a Berkovich tip. The O-P method (Oliver and Pharr, 1992) can reduce effective indentation modulus and stiffness directly from a nanoindentation curve, thus the parametric study examines the effect of the precise value of the σ_Y on the prediction of the experimentally measured indentation force-depth data. As in the simulations presented in Chapter 3, a three dimensional FEA model of the indentation was conducted using the tip geometry described in the method session of Chapter 3 and with the dentin discretized with a mesh of tri-linear brick elements; a mesh refinement study was performed to ascertain the necessary mesh density for an accurate solution. Figure A-1 depicts the experimentally measured averaged load-depth data for dentin (averaged over 20 experiments, black solid line, x-range error bars equivalent to one standard deviation) compared to four simulations: perfectly elastic ($E=25$ GPa) and three elastic-perfectly plastic cases with $\sigma_Y = 530$ MPa, 600 MPa, and 700 MPa assuming Poisson's ratio of 0.25. E was set to 25 GPa as determined using the O-P analysis of the unloading curve (Oliver and Pharr, 1992); this value for E also provides an accurate prediction of the loading curve at very small indent levels prior to any yielding of the material at depths less than ≈ 5 nm. Figure A-1 also plots the % error, ξ , per a given load value at 25 μN increments, where $\xi = |F_{FEA} - F_{EXP}|/F_{EXP}$ (where F_{FEA} is the indentation force as predicted from FEA at a particular depth and F_{EXP} is the corresponding experimental force). Hence, the error (abscissa) is a function of the load (ordinate) in this plot (Fig. A-1). For example, the error plots quantitatively show the 700 MPa case to provide the lowest error (best fit) at loads less than 200 μN , but the highest error at the larger loads. The % error was then averaged over the entire curve to give an average error when compared to loading data, unloading data, and over the combined loading-unloading data (Table A-1). For the case of the elastic-perfectly plastic material model, $\sigma_Y = 600$ MPa was found to provide the best fit to the experimental data when considering the entire load and unload history. In Chapter 3, predicted simulation nanoindentation curves were fit to the averaged indentation curves of ganoine, dentin, isopedine and bone and the proper yield stress for each material layer was chosen from the best fit when assuming Poisson's ratio of 0.3; 2 GPa for ganoine, 400 MPa for dentin, 215 MPa for isopedine and 180 MPa for bone.

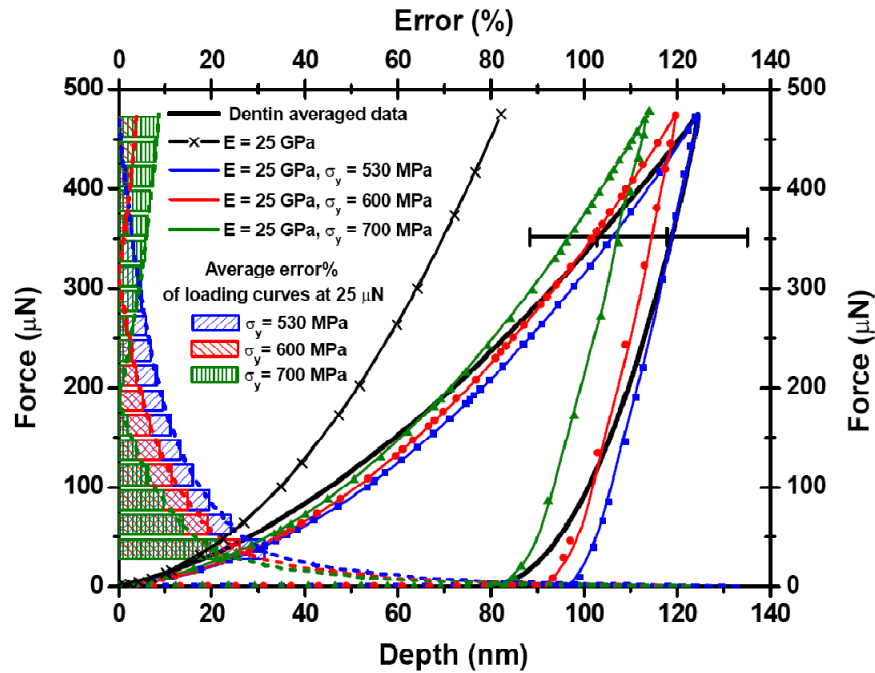


Figure A-1. Nanoindentation data of dentin compared to FEA elastic and elastic-perfectly plastic simulations plotted with error analysis. Averaged experimentally measured load vs. depth data for dentin (averaged over 20 experiments) and the FEA predictions assuming elastic behavior ($E=25$ GPa) and three cases of elastic-perfectly plastic behavior with (E, σ_y) pairs of (25 GPa, 530 MPa), (25 GPa, 600 MPa), and (25 GPa, 700 MPa). Also shown are the absolute value of the % error between each predicted curve and the experimental curve as a function of indentation load.

Table A-1. Assessment of the fit of elastic-perfectly plastic material models to the indentation load-depth data for dentin (where an average error during loading and unloading is obtained after constructing the error analysis curves illustrated in Fig. A-1 for each material)

Model	σ_y (MPa)	Average error (%)		
		Loaded	Unloaded	Overall
Elastic-Perfectly Plastic Model (isotropic)	400	19.99	14.40	17.10
	450	15.31	10.06	12.61
	530	9.16	2.82	5.91
	600	6.39	3.11	4.70
	700	6.33	8.45	7.42
	750	6.77	10.16	8.51
	825	7.76	13.64	10.78

A.2 Effect of Linear and Ramberg-Osgood hardening

In addition to the simplest elastic-perfectly plastic models, the effect of using more sophisticated elastic-plastic models on simulations of the indentation force-depth data for dentin was explored. In particular, the post-yield behavior was taken to exhibit yield followed by linear strain hardening and also yield followed by power-law hardening (using a Ramberg-Osgood relationship (Ramberg and Osgood, 1943)). The representative stress-strain curve for each strain hardening model is shown in Fig. A-2.

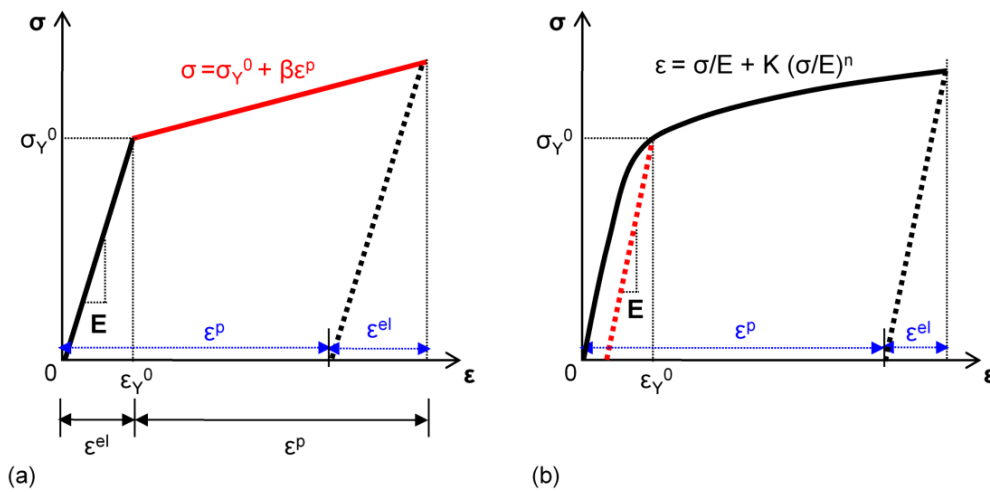


Figure A-2. Generic representation of stress-strain curves including strain hardening behavior after yielding by means of two strain hardening models; (a) linear strain hardening model and (b) the Ramberg–Osgood strain hardening model (Ramberg and Osgood, 1943). In case of the Ramberg–Osgood model, strain corresponding to the yield point is the sum of the elastic and plastic components.

In order to provide a consistency in the curves, noting that the average strain beneath the indenter is approximately 0.142 (Johnson, 1987; Suresh and Giannakopoulos, 1998; Giannakopoulos and Suresh, 1999), the yield and hardening properties were fit such that the same value of σ_Y is predicted at a ϵ of 0.14 for all material models. The uniaxial σ - ϵ curves for the linear and Ramberg-Osgood hardening are shown in Fig. A-3a with corresponding predicted indentation force-depth curves shown in Fig. A-3b compared to the Dentin averaged experimental data; the average % error values are provided in Table A-3. Figure A-3b shows the results of the more sophisticated material models to closely track those of the elastic-perfectly plastic case and do not provide any substantial difference in either the fit to the data or the value of the yield stress.

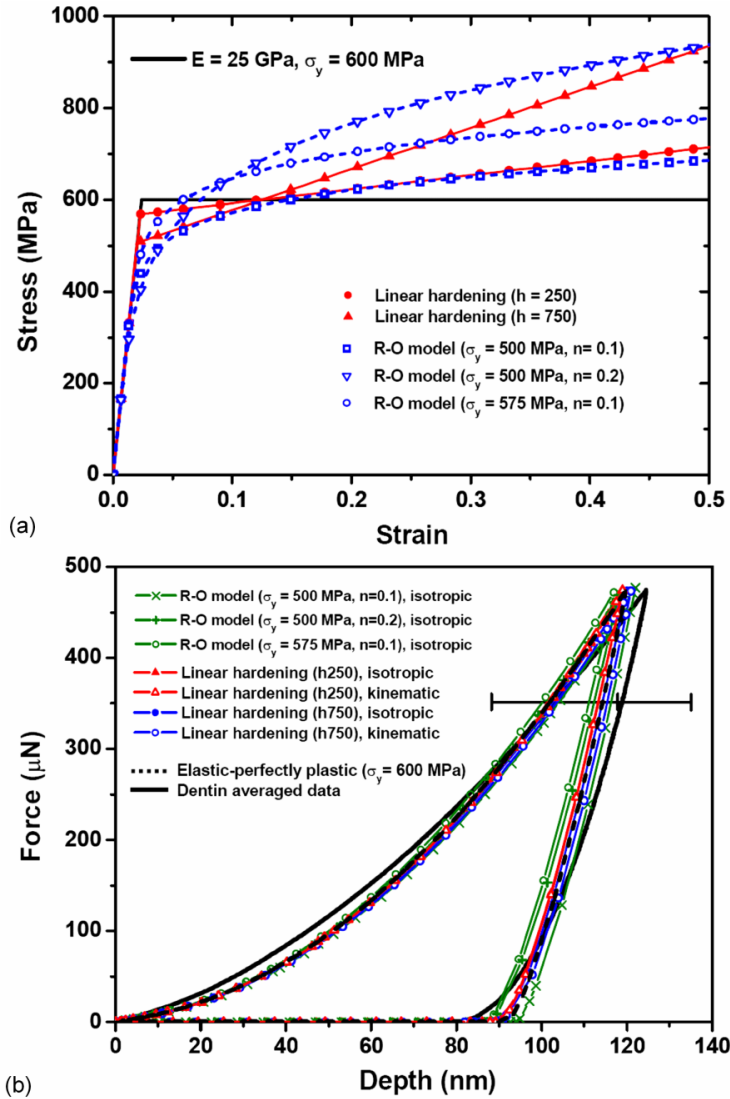


Figure A-3. (a) Uniaxial elastic-plastic behavior of the elastic-plastic material (dentin) including the perfectly plastic case as well as linear hardening and Ramberg-Osgood hardening models and (b) indentation load vs. depth curves for dentin showing the averaged experimental curve (averaged over 20 experiments) and the FEA predictions using the indicated elastic-plastic material models which include post-yield strain hardening. Including strain hardening does not substantially improve the prediction when compared to use of an elastic-perfectly plastic model.

Table A-2. Assessment of the fit of various elastic-plastic material models to the indentation load-depth data for dentin (where an average error during loading and unloading is obtained after constructing the error analysis curves illustrated in Fig. A-3 for each material)

Model	σ_Y (MPa)	Hardening coefficient	Average error (%)		
			Loaded	Unloaded	Overall
Elastic-Perfectly Plastic (isotropic)	600	0	6.39	3.11	4.70
Linear hardening (Isotropic)	569	h250	6.78	3.70	5.20
	506	h750	7.05	2.99	4.97
Linear hardening (Kinematic)	569	h250	6.84	3.64	5.20
	506	h750	7.48	2.44	4.89
Ramberg-Osgood (isotropic)	500	n=0.1	8.11	2.21	5.13
	500	n=0.2	7.77	2.64	5.31
	575	n=0.1	6.06	5.27	5.65

Residual topography predictions for the cases of Fig. A-1 and A-3 are shown in Fig. A-4 together with atomic force microscope (AFM) imaging measurements of the topography of residual indents from five experiments. These results show excellent agreement with the data, capturing the depth as well as the slope and pileup geometry found in the experiments which further supports the E and σ_Y estimated from the load-depth data. While the influence of the hardening on the predicted residual topographies is modest, I do note that strain hardening does provide a slightly better prediction. In summary, the use of the more sophisticated constitutive models has no significant effect on the nature of the predicted load-indentation response or the residual topography. These results indicate that the assumption of an elastic-perfectly plastic material behavior provides a good fit for obtaining a basic value for the magnitude of the σ_Y for these materials.

A.3 Structural and Experimental Relevance for Accurate Prediction

Direct mechanical assessment and multiscale structural observation of a biological material can provide the more accurate constitutive law, capturing detail mechanical behavior of the material under expected loading conditions in its environment. Chapter 4 of this thesis could determine the three-dimensional anisotropic mechanical properties of the outmost ganoine layer of *P. senegalus* scales based on its structural anisotropy associated with aligned mineral prisms normal to the surface. In Chapter 4, the nanoindentation data on ganoine in two different orientations were compared with predicted anisotropic mechanical properties of the layer by

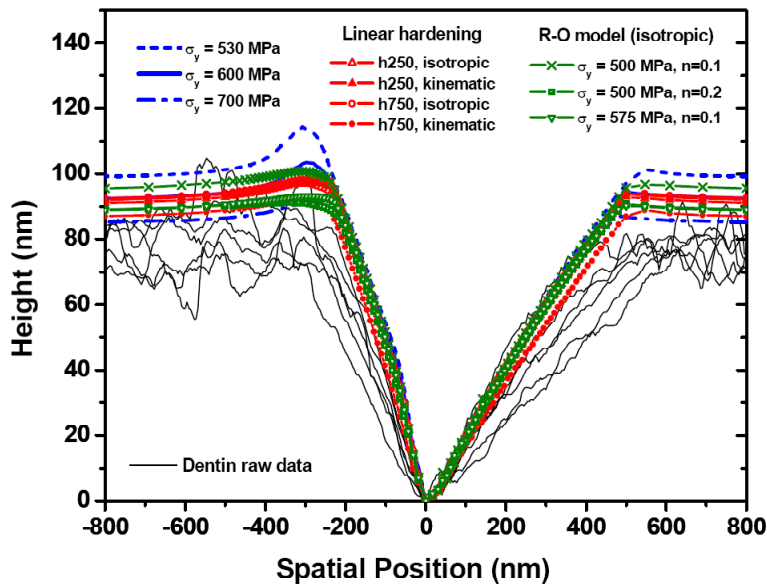


Figure A-4. Residual surface topography as measured by AFM (measurements from five different experiments shown) and as predicted by the FEM simulations with the indicated elastic-plastic material models.

parametric computational approach and the set of anisotropic mechanical properties that gave the best fit was finally determined after iterative fitting processes. However, as discussed above, multiaxial nanoindentation data in conjunction with AFM imaging analysis cannot provide a unique solution of mechanical properties of a material by itself. Recent technical advance in nanomechanics holds great potential for direct mechanical assessment of a biological material at the nano and micro scales: Focused Ion Beam technique is one of examples that can prepare a nano-scale sample for uniaxial tension or compression with properly designed mechanical testers (Greer et al., 2005; Kiener et al., 2008). Han and his colleagues have carried out nanomechanical testing with the FIB technique to directly measure anisotropic mechanical properties of goaite in conjunction with computational approach (Han et al., in press). The nanocompression data of goaite in different orientations revealed strain hardening behavior because of structural irregularity of individual mineral prisms in goaite, which increases shear resistance between geometrically interlocking prismatic crystallites during the evolution of plastic deformation. Therefore, the work done by Han et al (Han et al., in press) successfully demonstrates strain hardening behavior of the goaite layer, which couldn't be observed by means of nanoindentation experiments that led to overestimated yield stresses with elastic-perfectly plastic material models. Also, the origin of strain hardening in goaite is analogous to that found in nacre of mollusk shells where a waviness of individual nacre tablets plays a key role in strain hardening (Barthelat and Espinosa, 2007).

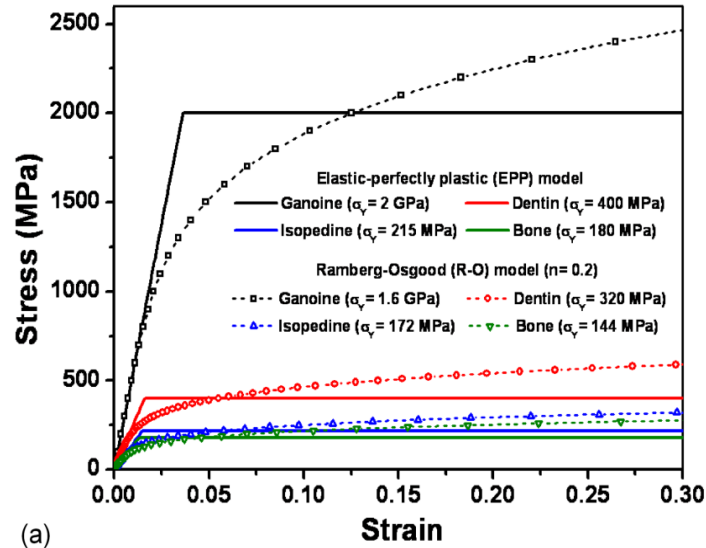
Appendix B.

Prediction of Multilayered Structure Behavior during Microindentation

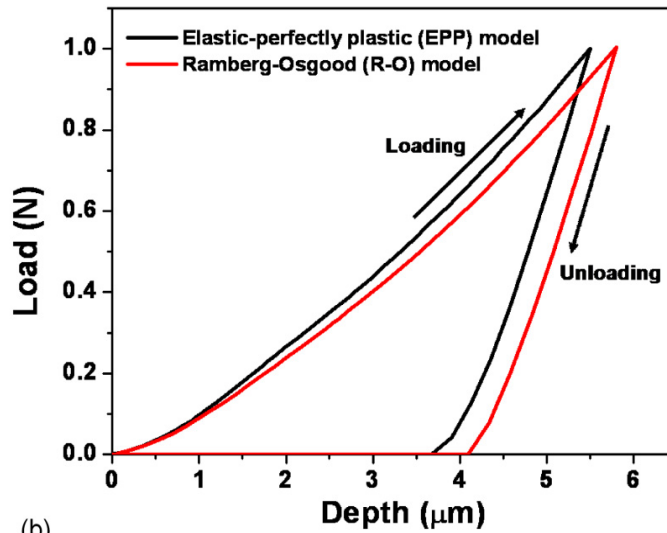
In the multilayer simulations of the main thesis chapters, the stress-strain behavior of the constituent materials was idealized as elastic-perfectly plastic. Here I examine the effect of more sophisticated elastic-plastic material models for the constituent layers on the resulting prediction of the multilayer behavior during indentation; two specific models are studied: (i) an elastic-plastic model with a Ramberg-Osgood power-law hardening; (ii) an elastic-perfectly plastic model where the yield stress, although independent of strain magnitude, is taken to depend on the magnitude of the strain rate. Results from simulation of the microindentation of the multilayered structure using each of these more sophisticated material models are compared to those obtained using the elastic-perfectly plastic model.

B.1 Ramberg-Osgood Hardening Model

The uniaxial σ - ϵ curves of the four materials assuming elastic-plastic with Ramberg-Osgood (R-O) strain hardening and assuming elastic-perfectly plastic (EPP) are shown in Fig. B-1a. The R-O model was taken to have a hardening exponent of 0.20 which provides a modestly large amount of hardening for comparison purposes; the parameters were then chosen such that the R-O material hardens to the yield stress of the EPP material after 0.05 ~ 0.10 plastic strain. The corresponding predictions of the load-depth curves from microindentation into the multilayered scale were shown in Fig. B-1b and reveal the model results using the R-O material behavior to closely track those using the EPP material behavior. The R-O model prediction is slightly more compliant than the EPP model due to the earlier yielding of the R-O materials (refer to Fig. B-1a). Figure B-2 compares the stress contours (Von Mises, S22, S11) after loading to a maximum load of 1 N and the stress contours (S33, S23) and equivalent plastic strain contour after unloading for the R-O and the EPP models. The contours are all found to follow the same basic trends independent of the constitutive model used for the layers. These results indicate that the assumption of an elastic-perfectly plastic material behavior provides a good prediction to understand the load-resistance mechanism of the multilayered material system.



(a)



(b)

Figure B-1. (a) Uniaxial elastic-plastic behavior of the four materials showing the elastic-perfectly plastic (EPP) case as well as Ramberg-Osgood (R-O) hardening model, and (b) simulated load versus depth curves for the microindentation of the multilayered finite element analysis (FEA) simulations showing loading and unloading to a maximum load of 1 N comparing the R-O strain hardening model to the EPP model.

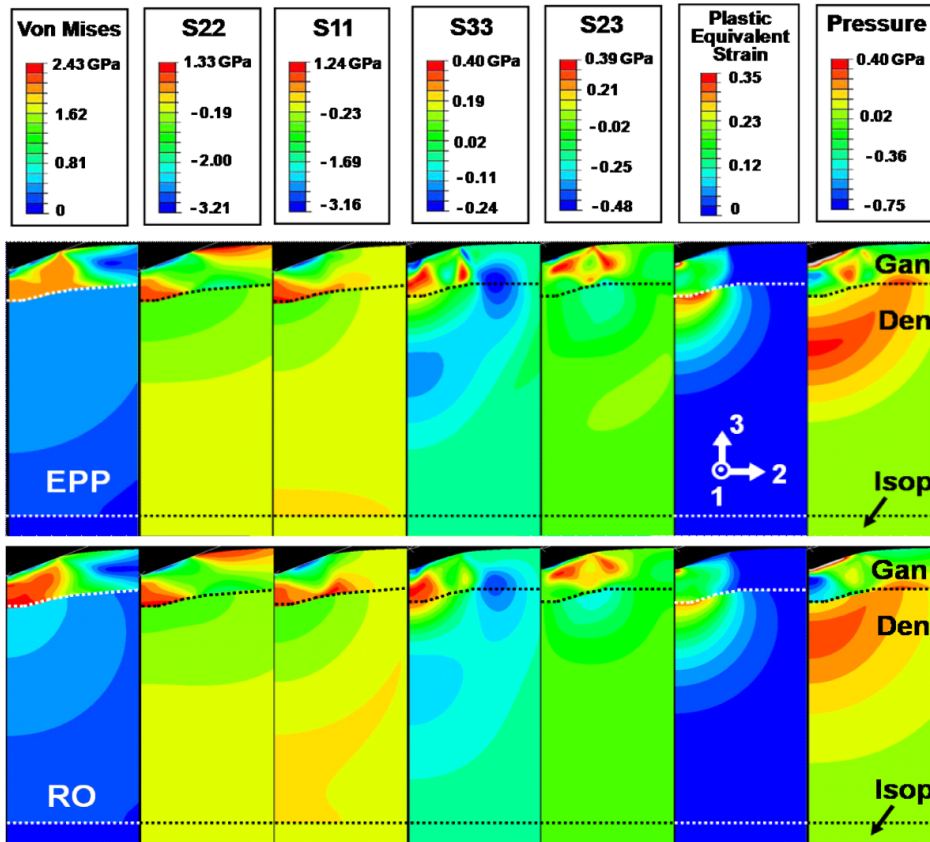


Figure B-2. Simulation contours of stress components and plastic strain for the EPP case (top) and the R-O case (bottom). FEA prediction of von Mises field, S22, and S11 when fully loaded and S33, S23, plastic equivalent strain and pressure after fully unloaded for the two models for 1N maximum load indentation. The inclusion of strain hardening in the material behavior does not substantially change the overall stress fields or the local stress fields on the surface or at the junction, indicating both models provide the same conclusions regarding the load-resistance mechanisms of the multilayered scale.

B. 2. Rate Dependence Models

The indentation rates employed in this thesis were $\sim 0.02 \mu\text{m/s}$ (nanoindentation experiments) and $\sim 5 \mu\text{m/s}$ (microindentation simulations). Given the magnitude of strain experienced in the material during indentation, these two penetration rates correspond to $\sim 0.01\text{s}^{-1}$ (nanoindentation) and $\sim 0.3\text{s}^{-1}$ (microindentation). The primary penetration event that a fish scale guards against is a fish bite during an attack from its own species. The average strain rate for a typical *P. senegalus* bite (Lauder, 1980) is $\dot{\epsilon} \approx 5 \text{s}^{-1}$, which constitutes a rate of loading higher than that tested in our experiments. In order to examine any influence of rate dependent material behavior on conclusions of this thesis regarding the penetration resistance mechanisms of the multilayered scale design, rate dependent plasticity of the material behavior was incorporated into the outer ganoine and

dentin layers as shown in Fig. B-3. Rate dependent plasticity was incorporated into the material models by taking the yield stress to depend on the strain rate (an option available model in the Abaqus code). Since the rate dependent plasticity of the ganoine and dentin layers of *P. senegalus* scales is currently unknown, the rate dependence of bone was employed as a "worst case" approximation (Gupta et al., 2007). Given that bone has the greatest organic content among the four layers in the scale, it will have the highest rate dependence; hence, using the rate dependence of bone overestimates the rate dependence of ganoine and dentin. Figure B-3 shows the rate dependent behavior assigned to the materials by following the rate dependence of bone as scaled by the yield behavior of either ganoine or dentin.

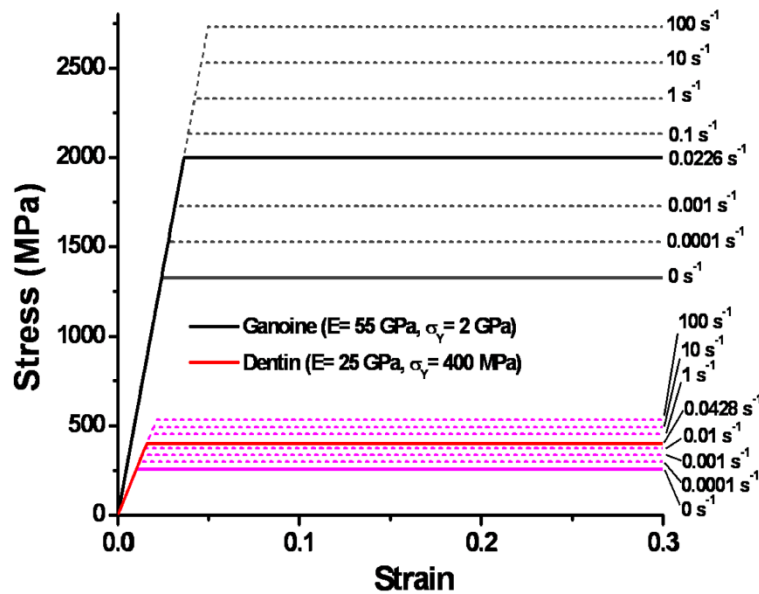


Figure B-3. Uniaxial elastic-perfectly plastic behavior of the two outer layer materials (ganoine, dentin) in the multilayered models including those with rate dependent yield (σ_Y scaled according to $\dot{\epsilon}$, values provided to the right of each stress-strain curve)

Table B-1. Four types of rate-dependent FEA multilayered models.

Multilayered model	Description
Model 1	Only ganoine is rate-dependent and exhibits a rate dependence similar to bone but with base yield stress equal to that of ganoine
Model 2	Only dentin is rate-dependent and exhibits a rate dependence similar to bone but with base yield stress equal to that of ganoine
Model 3	Ganoine and dentin are both rate-dependent
Model 4	Ganoine and dentin are not rate-dependent (original care used in this thesis)

To examine the possible influence of rate, microindentation simulations were carried out, taking rate dependent yield behavior into account, as shown in Table B-1. Figure B-4 shows the simulated penetration load versus depth behavior for the four models listed in the Table B-1. The results for all models including rate dependent material behavior were found to be very similar to that of the original rate-independent case and hence were found to provide the same conclusions regarding the underlying mechanisms of the multilayered structure design.

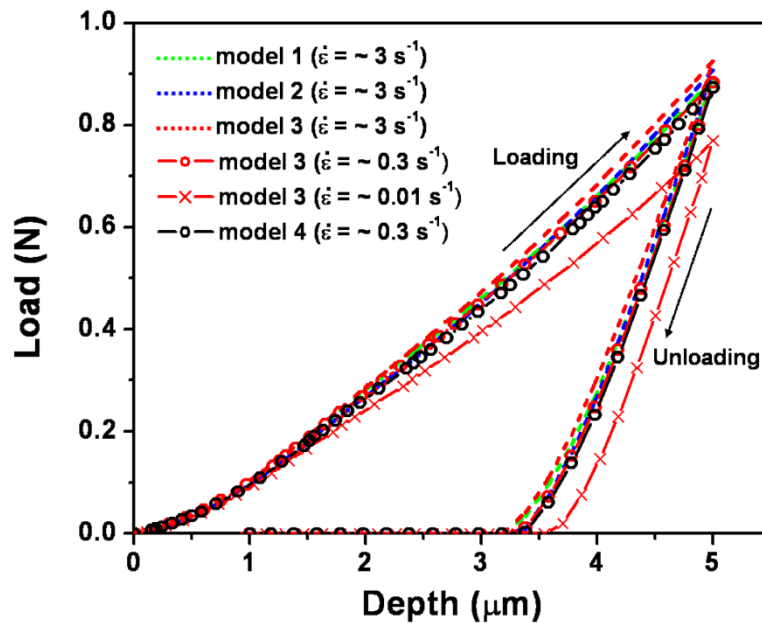


Figure B-4. Simulated microindentation load vs. depth curves comparing rate dependent models to rate independent models, Model 1: only ganoine is rate-dependent, Model 2: only dentin is rate-dependent, Model 3: ganoine and dentin are both rate-dependent, Model 4: ganoine and dentin are rate independent (i.e. the case reported in the manuscript). The effect of $\dot{\epsilon}$ was also investigated for Model 3.

Appendix C.

Validation of Boundary Conditions for Multilayer Simulations

C.1 Biting Force of *Polypterus senegalus*

All multilayer simulations of this thesis presumed that the critical load of individual *P. senegalus* scales is approximately 1 N based on the Vicker's microindentation tests where circumferential cracks began to be observed. However, there is no current report on the physiological biting force of *P. senegalus* in literatures, taking territorial fighting between *P. senegalus* into account. The feeding mechanisms have been investigated using the elasmobranchs (including sharks, skates and rays) as model systems, focusing on the relationship between cranial morphology, biting force and feeding ecology in fishes because the jaw system of these fish is generally found to have few movable parts with a high degree of functional diversity (Huber et al., 2006). In particular, cranial morphology of fish is closely related to its feeding mechanism. Therefore, in order to predict the range of *P. senegalus* biting force, the biting force of fish with the similar body size and jaw structure as compared to *P. senegalus* was explored in literature. Theoretical biting force was positively allometric with respect to total body length (TL) in the same species of fish (Huber et al., 2006). Reported biting forces of different fish species are shown in Table C-1. Moreover, force transmission from muscles (force generator by deformation) to the tips of jaw is not 100% efficient: mechanical advantage (MA) can be associate with this efficiency, implying low MA jaws emphasize velocity of jaw opening or closing and high MA jaws transmit relatively more force in order to maximize biting force by sacrificing speed (Westneat, 2004).

Matured *P. senegalus* has the typical body length of ~ 20 cm (the largest may be around 30 cm), and *P. senegalus* used in this thesis was 21 cm long (Kodera, 1994). The fish species in Table C-1 with the body length of ~ 20 cm are likely to produce the maximum biting force of 3 ~ 15 N according to linear regression analysis of biting force with respect to the total body length. Interestingly, some fish species (e.g. *Lachnolaimus maximus*) in the family Labridae have the remarkably large maximum biting force of 250 ~ 500 N with the body length of 18 ~ 30 cm (Clifton and Motta, 1998). The diet of *Lachnolaimus maximus* (200 ~ 500 N for 18 ~ 30 cm fish) mostly consists of hard-shelled preys such as taxa scallops, oysters, and portunid and pagurid crabs while *Halichoeres maculipinna* (2~10 N for 5 ~ 13 cm fish) consumes hard-shelled prey items (55.36% of diet) and softer-bodied items (44.64% of diet) (Clifton and Motta, 1998). This indicates

that diet is closely related to the level of required biting force. The diet of *P. senegalus* is provided in Table C-2, where all prey items are relatively softer than ones of fish species in the family Labridae (Raji et al., 2003). Therefore, the biting force of *P. senegalus* can be estimated as 3~15 N, based on biting force of four fish species (*Aphanopus carbo*, *Trichiurus lepturus*, *Cheilinus trilobatus*, *Squalus acanthias*) in Table C-1 whose diet mostly consists of soft-bodied preys. Besides, *P. senegalus* transmits up to 42% of muscle force to the jaw tips for biting, thus the acting force for the jaw tips may range from 1.2 ~ 6.3 N roughly. As a result, individual *P. senegalus* teeth are likely to produce the maximum force of less than 1 N if the total number of acting teeth during a biting event is ~ 10.

Table C-1. Biting force (from muscles of jaws) of several fish species. This is not the real acting force for the biting event and mechanical advantage needs to be taken into account for the acting biting force at the tip end of teeth.

Species	Scientific Classification	Body size (cm)	Static biting force (N)
<i>Aphanopus carbo</i> (de Schepper et al., 2008)	Actinopterygii > Perciformes	110~125	~60
<i>Trichiurus lepturus</i> (de Schepper et al., 2008)	Actinopterygii > Perciformes	83~100	~15
<i>Carcharhinus limbatus</i> (Huber et al., 2006)	Chondrichthyes>Elasmobranchii > Carcharhiniformes	61 ~ 152	32~1083
<i>Cheilinus trilobatus</i> (Westneat, 2003)	Actinopterygii > Perciformes	14	~3
<i>Heterodontus francisci</i> (Huber, 2005)	Chondrichthyes>Elasmobranchii > Heterodontiformes	63~74	~ 128
<i>Squalus acanthias</i> (Huber and Motta, 2004)	Chondrichthyes>Elasmobranchii > Squaliformes	37 ~ 54	4~20

Table C-2. The type and frequency of the identified food items found in the stomach of *Polypterus senegalus* (n = 80) from Lake Chad in Nigeria (Raji et al., 2003).

Items	Frequency (sample number=80)	Relative Frequency
Fish		
<i>Tilapia</i>	38	47.5
<i>Eulropius niloticus</i>	12	15
Insects		
<i>Dragonfly nymph</i>	15	18.75
<i>Mayfly nymph</i>	10	12.5
Other items	10	12.5

C.2 Fixed Force vs. Fixed Work Conditions

In the main chapters of this thesis, the multilayered structures were subjected to a fixed force of indentation, presuming that *P. senegalus* should confront biting attack by teeth of their own species and relatives during territorial fighting. Under various circumstances, sometimes fixed work of indentation with a series of multiple biting is likely to occur. One case of fixed work of indentation with three types of fish teeth was considered in this context. Five biting cycles were applied to one biting event where the first biting cycle occurred at 0.75 N (75% force transmission efficiency) as compared with the 1N multilayer microindentation simulations of *P. senegalus* scales in this thesis. All model parameters and geometry were described in the method section of Chapter 5 in the thesis, except for a fixed work of indentation.

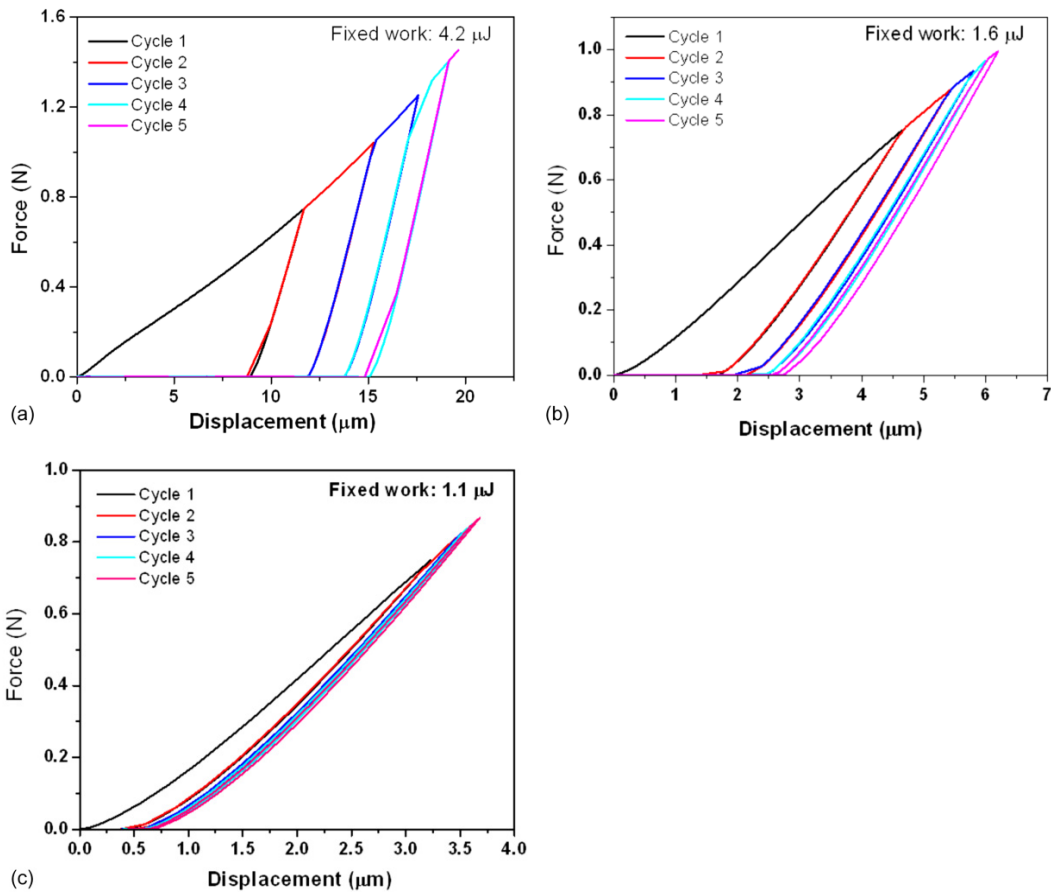


Figure C-1. Load-depth behavior of the ganoine-dentin-isopedine-bone quadlayer models that emulated *P. senegalus* scales subjected to hypothetical tooth biting at 0.75N of the initial load; (a) the case of the tooth biting with a tip end radius of $R_{\text{tip}}^n = 0.42$, (b) the case of the tooth biting with a tip end radius of $R_{\text{tip}}^n = 1.25$ and (c) the case of the tooth biting with a tip end radius of $R_{\text{tip}}^n = 2.5$. After the first biting occurred, four following biting were applied with the same work of indentation, resulting in the total biting cycles of five.

The same work of indentation at each cycle increases the indentation depths and loads accordingly, but the penetration efficiency of threat was found to depend on the geometry of threat (Fig. C-1). The sharper tip requires the larger amount of force increment at each cycle, which induces higher stress concentration fields at the tip end of the threat system. The indentation load and corresponding penetration depth of the threat system into its counterpart are shown in Fig. C-2. When the tip end radius of threat is comparable to the outmost ganoine thickness of armor, the penetration efficiency can be the largest among the three cases, keeping the indentation load less than 1 N (that is the upper limit of biting force for *P. senegalus* as shown in section C.1) during the five-cyclic biting event.

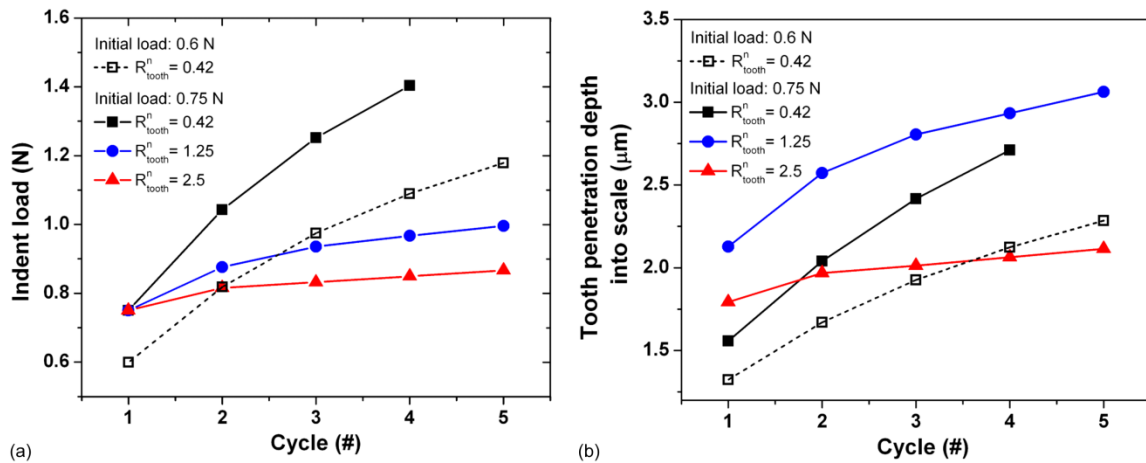


Figure C-2. (a) Indentation loads and (b) tooth penetration depth into scale as a function of the number of cycles at different tip end radii of the threat models

When the fixed work of indentation was subjected to the three cases with the same amount of energy, 1.1 μJ , the threat system with a larger tip end radius seems to have better penetration efficiency, reaching the larger maximum biting force (Fig. C-3). Due to the localized plastic deformation of a sharper tooth system, the most of the applied work is transformed into energy dissipation at a lower indentation load, decreasing the penetration depth into the armor system. Therefore, fixed force or fixed work of indentation derives a different conclusion for the optimization problem of both threat and armor systems. Biting speed associated with kinetic energy during various biting events is one of the important parameters in feeding mechanisms of fish.

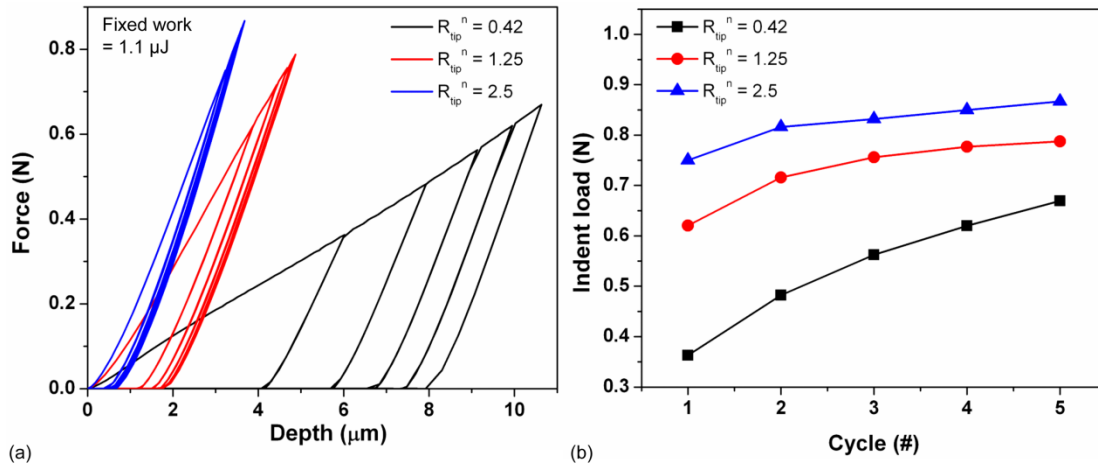


Figure C-3. (a) Indentation loads and (b) tooth penetration depth into scale as a function of the number of cycles at different tip end radii of the threat models

C.3. Effect of Underlying Soft Tissues

The stratified collagenous stratum compactum, consisting of highly aligned collagen fibers like tendon, beneath the mineralized scales in *Polypterus senegalus* has been reported in some papers (Gemballa and Bartsch, 2002; Gemballa and Roder, 2004). According to the high resolution electron microscopic images in their paper, the thickness of the stratum compactum is approximately a few hundred micrometers. Underneath the stratum compactum, soft tissues, organs and skeleton are located. The half of the used *P. senegalus* body in this thesis was about ~ 1 mm thick from the optical image. The mechanical properties of those two organic matrices can be approximated by the other organic tissues with the comparable structures in literature. The stratum compactum is similar to tendon because of its highly oriented fibrous structure, assuming that its mechanical property is hyper-elastic with elastic modulus of $1 \sim 10$ MPa with a Poisson's ratio of 0.5 (Rigby et al., 1959; Reddy et al., 1999). On the other hand, the soft matrix is assumed to be hyper-elastic and visco-elastic like brain tissues that have instantaneous modulus of $C_{100} = 263$ Pa, $C_{200} = 491$ Pa with two characteristic times of $t_1 = 0.5$ s ($g_1 = 0.450$), and $t_2 = 50$ s ($g_2 = 0.365$) (Miller and Chinzei, 1997; Miller, 1999). Prior to the simulations with the layered structure, the microindentation simulations on the soft tissue were carried out in order to check its rate-dependent visco-elastic behavior at three different loading rates as shown in Fig. C-4.

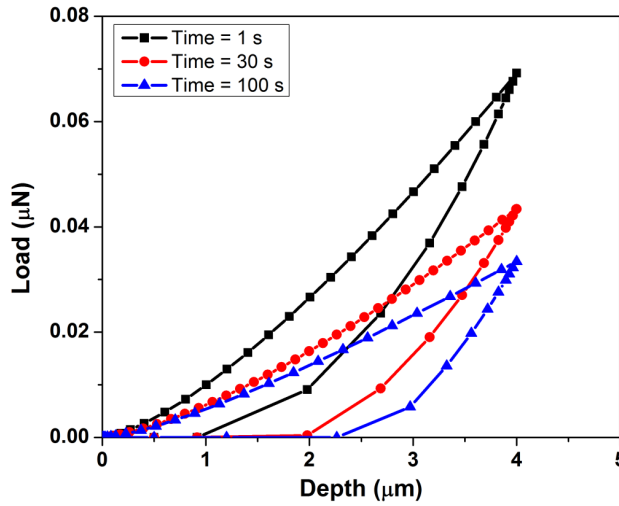


Figure C-4. Rate-dependent mechanical behavior of soft tissue at the maximum indentation depth of 4 μm at three indentation rates of 4 $\mu\text{m/s}$, 0.13 $\mu\text{m/s}$, and 0.04 $\mu\text{m/s}$.

The ‘scale-only’ model was constructed as same as the previous multilayer models used in this thesis, applied by the same boundary conditions. The ‘scale-tissue’ models were composed of a quad-layered scale and underlying two additional organic layers (stratum compactum and soft tissue) as described in Table C-4. The bottom surface of the scale in the ‘scale-tissue’ model was not perfectly fixed as opposed to the ‘scale-only’ model. Instead, the bottom surface of the innermost soft tissue was symmetric in the loading direction because the model captured a half of the fish body from one flank up to the center of the body. The hypothetical biting events were carried out using the emulating tooth indenter that is made up with enamel only ($E = 55 \text{ GPa}$, $\sigma_Y = 2 \text{ GPa}$), with a tip end radius of 15 μm at the maximum load of 1 N.

Table C-3. Material properties of individual scales and underlying organic tissues

Layer	Thickness	Constitutive law	Properties
Mineralized Scale	Ganoine	Elastic-perfectly plastic	$E = 55 \text{ GPa}$, $\sigma_Y = 2 \text{ GPa}$
	Dentin		$E = 25 \text{ GPa}$, $\sigma_Y = 0.4 \text{ GPa}$
	Isopedine		$E = 14.5 \text{ GPa}$, $\sigma_Y = 0.21 \text{ GPa}$
	bone		$E = 13.5 \text{ GPa}$, $\sigma_Y = 0.18 \text{ GPa}$
Stratum compactum (Rigby et al., 1959; Reddy et al., 1999)	$\sim 200 \mu\text{m}$	Hyperelastic (Neo-Hookean)	$C10 = 1 \text{ MPa}$, $\nu = 0.5$
Soft tissue (Miller and Chinzei, 1997; Miller, 1999)	$\sim 90000 \mu\text{m}$	Hyperelastic & Viscoelastic (Reduced polynomial)	$C10 = 263 \text{ Pa}$, $C20 = 491 \text{ Pa}$ $t_1 = 0.5 \text{ s}$, $g_1 = 0.45$ $t_1 = 50 \text{ s}$, $g_2 = 0.365$

The load-depth behavior of the ‘scale-only’ model is stiffer than that of the ‘scale-tissue’ models because the compliant organic tissues beneath the scale contribute to the deformation, which makes the mechanical response more compliant (Fig. C-5). Interestingly, three indentation times ($t = 1, 30, 100$ s) applied to the ‘scale-tissue’ model didn’t result in different mechanical behavior at this length scale, implying that time-dependency of the whole system is almost negligible providing the minimal difference.

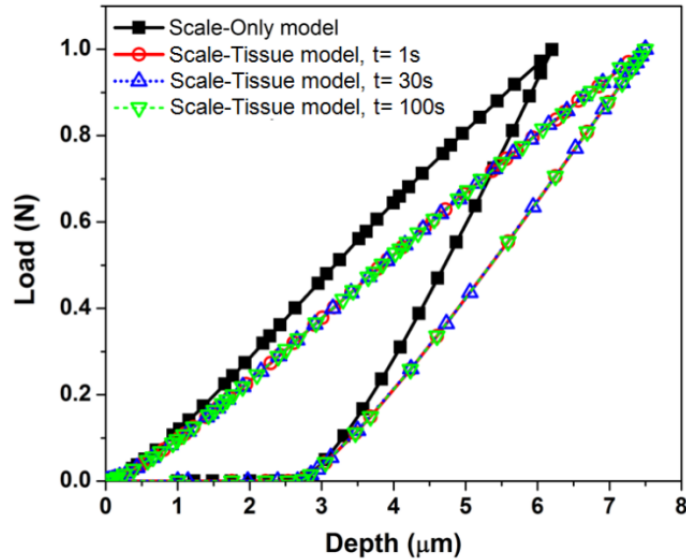


Figure C-5. Load-depth curves of two ‘scale-only’ and ‘scale-tissue’ models at three indentation times of 1, 30 and 100s at the maximum load of 1 N.

Stress and strain distributions of scale and tooth systems are important evidence of mechanical interaction between the two systems during loading and unloading. The stress and plastic strain contours in the ‘scale-only’ and ‘scale-tissue’ models were compared. The magnitudes and distribution of stresses and plastic strain are almost identical in both model cases as shown in Fig. C-6. The visco-elastic soft tissue also dissipates energy during a penetration event, whereas the amount of energy dissipation in two organic layers is almost negligible as compared that of ganoine, dentin, isopedine, bone layers of the mineralized scale (Fig. C-7). Almost all energy dissipation is found to occur in ganoine and dentin layers of the scale system and enamel of the tooth system. The energy distribution and magnitude of the ‘scale-only’ and ‘scale-tissue’ models show less than 1 % difference, indicating the minimal difference between two model cases.

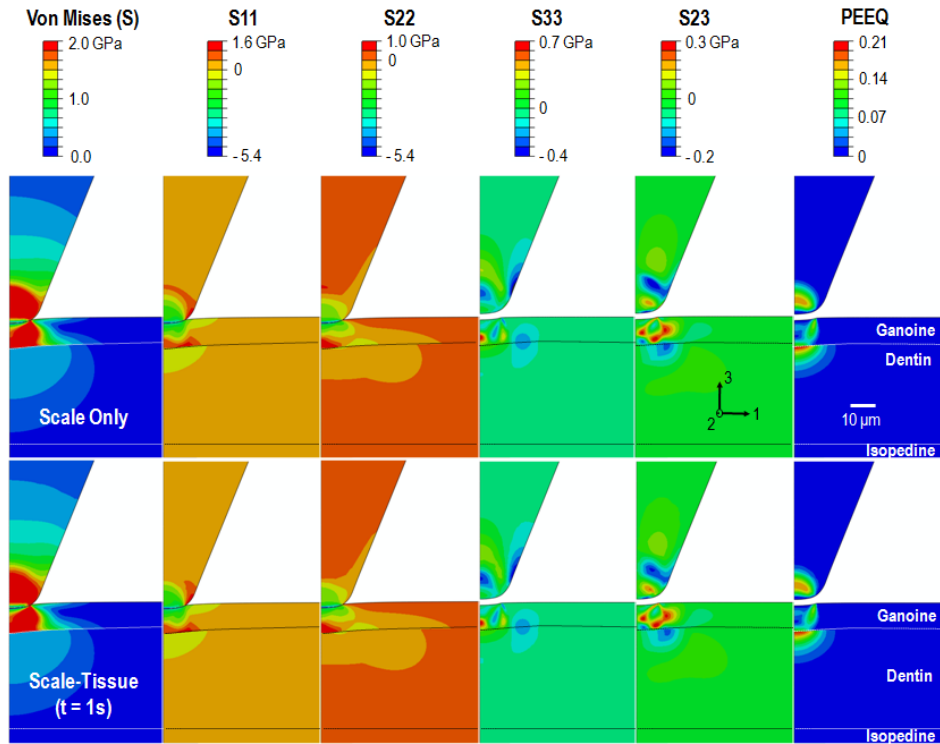


Figure C-6. Stress and strain contours of the ‘scale-only’ and ‘scale-tissue’ models when loading at the maximum load of 1 N and fully unloading

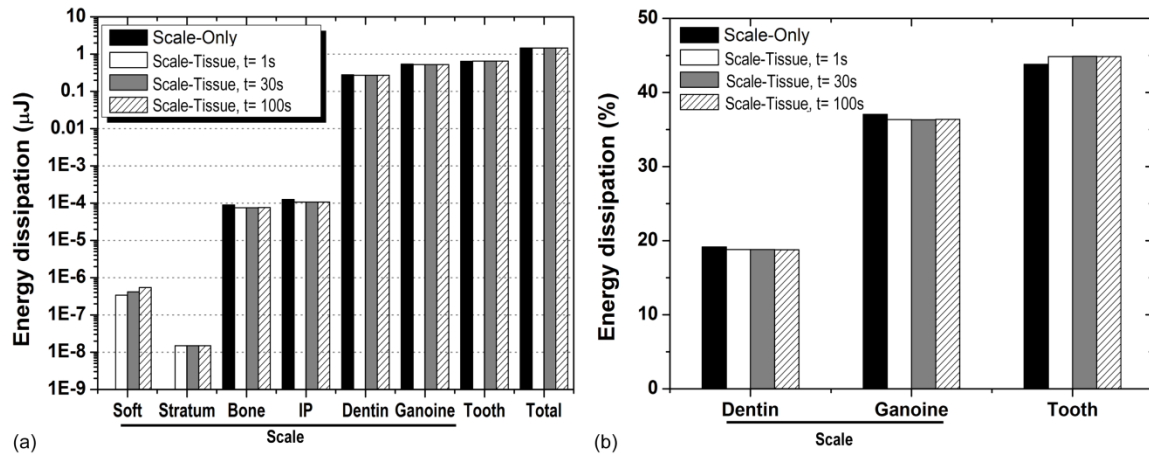


Figure C-7. (a) Energy dissipation of each material layers in the scale and tooth systems for the ‘scale-only’ and ‘scale-tissue’ model cases at three indentation times and (b) relative energy dissipation of dentin and ganoine of the scale system and enamel of the tooth system, indicating 99.9% of energy dissipation occurs in those three material layers.

The macroscopic structure (i.e. scale size, shape, interconnections) and properties of *P. senegalus* armor has been studied in detail in a paper (Gemballa and Bartsch, 2002) who determined that its primary function is to control the biomechanical motion of the

entire fish body. To summarize briefly, changes in scale overlap between rows, fibers of collagen layers of the stratum compactum, and the lateral myoseptal structures which follow the same oblique orientation of the scale rows all work together to allow for extreme bending curvatures, while simultaneously damping torsion, of the entire fish body. Our own manipulations of an anesthetized *P. senegalus* confirm these large global bending curvatures and interestingly, also show that simultaneously the fish body can achieve high compressive rigidity locally at the level of a few scales which likely is due to ossified endoskeletal structures (e.g. vertebrae, rib bones which articulate with the scales, etc.) and internal body pressure (e.g. due in part to the air-filled swim bladder) and reduces joint deflections normal to the fish body. During a biting attack, this local rigidity mitigates large compressive strains of the fish body and damage to internal tissues and organs and allows the outstanding quad-layered material properties of the scale to mediate the resistance to penetration and serve its primary function as a protective armor.

Appendix D.

Morphometric Parameters from MicroCT Data

Analysis

A microCT system used in this thesis was a Viva CT40 scanner (e.g. a Viva CT40, Scanco Medical AG, Bassersdorf, Switzerland). The following information on morphometric analysis and corresponding morphometric parameters of microCT data was extracted from the Scanco User's manual (Scanco Medical AG, Bassersdorf, Switzerland) and the established protocol of Prof. Gazit's lab of Hebrew University in Israel (authors: Ilan Kallad and Olga Mizrahi). The micro-focus x-ray source of a Viva CT40 scanner illuminates the object while a planar detector collects projection images at the proper resolution and simultaneously the equipped computer synthesizes a stack of virtual cross sections with acquired angular views from rotating the sample object. The cross-sections are interpolating sections along different projection planes, for the purpose of inspection of the internal structure. Based on this data, the computer can reconstruct the whole 3D structural image of the sample and slice the 3D image along with z-axis of the global coordinate system (default; you can rotate the slicing axis if necessary), which can provide two-dimensional sectional images of the sample for image analysis. 2D- and 3D-histomorphometric evaluation can be performed on either a rectangular/cubic volume or any irregular shaped ROI/VOI (Region/Volume Of Interest). The ROI/VOI is defined by a set of Graphical Objects (GOBJs), which has to be drawn on a slice-based method (so-called 'segmentation' or 'contouring'). The Scanco software can perform 3D evaluation analysis using the segmented ROI/VOI of microCT data, providing quantified bone structural parameters as listed in Table D-1 (Gundersen et al., 1978; Odgaard and Gundersen, 1993; Hildebrand and Rüeggsegger, 1997; Hildebrand et al., 1999).

Table D-1. Morphometric material parameters obtained from MicroCT data analysis by Scanco software (User's guide for microCT 40; Scanco Medical AG, Bassersdorf, Switzerland). Ratios (BV/TV, BS/TV, BS/BV) are the normalized indices. The model-independent indices are marked with an asterisk (*).

Parameter		Unit	Definition
<i>Primary indices</i>			
BS	Bone surface area	mm ²	The triangulated surface of the mineralized bone
BV	Bone volume	mm ³	The enclosed volume of the triangulated surface
TV	Total volume	mm ³	The volume of the whole sample
<i>Traditionally derived indices</i>			<i>Derived from the primary indices assuming a constant structure model (plate model)</i>
Tb.Th	Trabecular thickness	mm	derived from the bone surface-to-volume ratio
Tb.Sp	Trabecular separation	mm	derived from the marrow surface-to-volume ratio
Tb.N	Trabecular number	1/mm	the number of plates per unit length
<i>Directly assessed indices</i>			<i>Do not rely on an assumed model type.</i>
Tb.Th*			the average thickness of all bone voxels
Tb.Sp*			the thickness of the marrow cavities
Tb.N*			the inverse of the mean distance between the midaxes of the observed structure.
CONN. D.	Connectivity density	1/mm ³	The connectivity (C) of a two-component system, i.e., bone and marrow, is derived directly from the Euler number, by $C = 1 - E$, if all the trabecular and bone marrow cavities are connected without isolated marrow cavities inside the bone (Odgaard and Gundersen, 1993). It is normalized by examined tissue volume and reported as connectivity density
SMI	Structure model index		an estimation of the plate-rod characteristic of the structure. For an ideal plate structure the SMI value is 0 and for ideal rod the value is 3 (Hildebrand and Rüeggsegger, 1997)
DA	Degree of anisotropy		the ratio between the maximal and the minimal radius of the MIL ellipsoid (MIL=mean intercept length) (Gundersen et al., 1978)
Bone Molecular Density		mgHA/ccm	how many grams of calcium and other bone minerals are packed into a segment of bone

Appendix E.

Mechanical Modeling of the Pelvic Assembly of Threespine Stickleback

E.1. Four Regions of a *G. aculeatus* Pelvic Assembly

Four distinct suture regions can be defined, based on the 1st derivative of a suture height profile (Fig. 8-2(a) of Chapter 8 in this thesis) as shown in Fig. E-1.

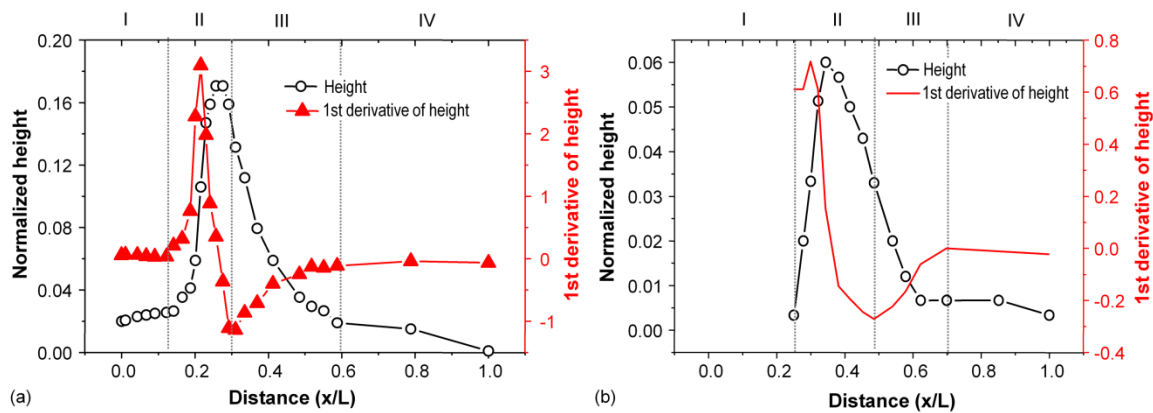


Figure E-1. The z-height profile and 1st derivative of z-height of (a) marine *G. aculeatus* full-morph pelvic assembly and (b) freshwater *G. aculeatus* full morph pelvic assembly. Four regions are indicated based on the 1st derivative of height.

The features of each region as indicated in Fig. E-1a and E-1b can be described as follows:

- Region I: relatively small 1st derivative of z-height in the anterior region of the pelvic girdles
- Region II: abrupt increase and decrease of the 1st derivatives of z-heights
- Region III: from the minimum value of 1st derivative of z-height until the value becomes zero
- Region IV: the relatively constant values (nearly zero) of the 1st derivative of z-heights

E.2. Two-dimensional Suture Model

In Chapter 8 of this thesis, an analytical two-dimensional suture model was developed by Li, Y.N. (Li et al., *in review*) in order to predict the effective stiffness of the median suture in *P. senegalus* pelvic assembly. The preferential loading of the pelvic median suture is along the longitudinal direction of the teeth as shown in Fig. E-2, where important structural parameters including amplitude (A), the width of a suture teeth (t), and the width of the organic layer between neighboring ventral suture-teeth (g), are indicated, having the relationship of $\tan\theta = \frac{t}{2A}$.

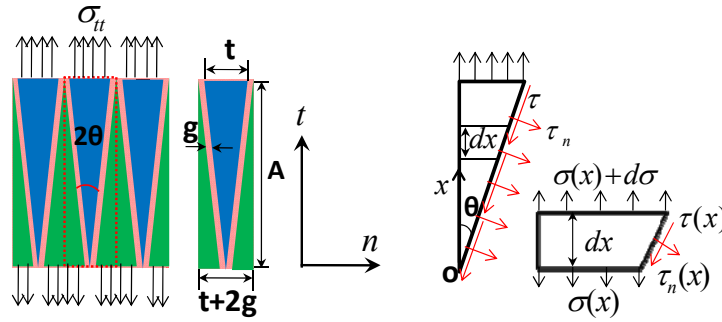


Figure E-2. Sketch of the Representative Volume Elements (RVEs) of a pelvic median suture (left), and the free body diagram of a triangular tooth (right) under longitudinal loading (Li et al., *in review*).

From the free body diagram of a suture tooth, the equations of an equilibrium triangular tooth were obtained (Fig. E-2). The relationship between the longitudinal normal stress along the teeth, σ , and the shear stress along the interface, τ , can be expressed as follows:

$$\tau(x)dx = \sin\theta \cos\theta [\sigma(x)dx + x d\sigma] \cdots (1)$$

where, x is the coordinate along a tooth originating from the tooth tip.

The longitudinal normal tensile stress, σ , must be a constant and satisfy, assuming the shear stress along the interface, τ , is a constant along x , from Eq. (1),

$$\tau = \sin\theta \cos\theta \sigma \cdots (2)$$

The uniform stress distributions in the triangular teeth and organic layer of the median suture is one of the most remarkable features as opposed to the inhomogeneous stress distribution of a rectangular-shaped suture.

From Eq. (2) and the geometric analysis of the small deformation of both the teeth and the organic layers, the effective stiffness, \bar{E} , of the triangular suture joint is derived as a function of the geometric and material parameters:

$$\bar{E} = \frac{E_t}{E_1} \left(\alpha, \quad \theta, \quad \frac{E_1}{G_0}, \quad \frac{E_1}{E_0} \right) = \left\{ \left(\alpha \frac{E_1}{G_0} \sin^2 \theta \cos^2 \theta \right) (1 + \alpha) \right\}^{-1} \dots (3)$$

where, G_0 is the shear modulus of the interphase, $\alpha = \frac{2g}{t}$ and $\theta = tg^{-1} \left(\frac{t}{2A} \right)$. Actually, the volume fraction of the skeleton teeth, f_v , is closely related to α , thus exhibiting the relationship of $f_v = (1 + \alpha)^{-1}$. In addition, the interdigitation index (ID), which is defined as the ratio of the contour length of the suture to the straight line between two end points (Rafferty and Herring, 1999), can be expressed by the following equation:

$$ID = \frac{f_v}{\sin \theta} \dots (4)$$

E.3. Three-dimensional Suture Model

Resistance to bending is closely related to the geometry of a pelvic median suture in three dimensions. The following figure E-3 shows how to define the effective moment of inertia for each inclined plates between top and bottom ventral plates (see Fig. 8-2a of Chapter 8).

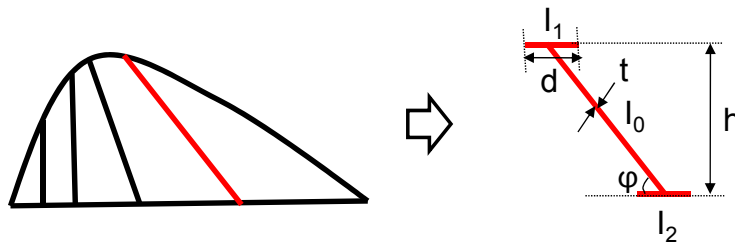


Figure E-3. Schematic diagram of inclined plates between two ventral plates of a pelvic girdle; each cross-section of the plates has the inclination angle of ϕ , which is connected with top and bottom plates with the width of d . The skeleton of the structure has the thickness of t . The effective moment of inertia for the cross-section of each internal inclined plate is composed of three moments of inertia (I_0 , I_1 and I_2).

Based on the geometry of an internal inclined plate (assumed as an ‘I-beam’) with $\varphi=90^\circ$, its effective moment of inertia can be expressed as follows:

$$EI_{90^\circ} = E_1I_1 + E_2I_2 + E_0I_0 \cdots (5)$$

The structure is made of the same material, thus $E_0 = E_1 = E_2$. Also, to simplify the equation (5), I_1 is equivalent to I_2 because of the same width. Therefore, the effective moment of inertia can be rewritten as the following equation (6):

$$I_{90^\circ} = I_0 + 2I_1 = \frac{th^3}{12} + \frac{dth^2}{2} \cdots (6)$$

When an internal inclined plate has an inclination angle of φ , its effective moment of inertia has the relationship of $I_\varphi = I_{90^\circ} / \sin \varphi$. Using the derived effective moment of inertia, the corresponding effective bending stiffness can be written as follows:

$$K_{xx} = EI_{\varphi,xx} = EI_{90^\circ} \cdot \sin \varphi \cdots (7)$$

$$K_{xy} = EI_{\varphi,xy} = EI_{90^\circ} \cdot \cot \varphi \cdots (8)$$

The predicted bending stiffness of an inclined plate with an inclination angle of φ was confirmed by the numerical simulations that showed a good agreement with the analytical results obtained from equations (7) and (8). The analytical and numerical modeling described in this section was developed and carried out by my collaborator, Dr. Y.N. Li.

Bibliography

Agrawal, A.A., 2001. Phenotypic plasticity in the interactions and evolution of species. *Science* 294, 321-326.

Aizenberg, J., 2010. New Nanofabrication Strategies: Inspired by Biomineralization. *Mrs Bulletin* 35, 323-330.

Aizenberg, J., Weaver, J.C., Thanawala, M.S., Sundar, V.C., Morse, D.E., Fratzl, P., 2005. Skeleton of *Euplectella* sp.: Structural hierarchy from the nanoscale to the macroscale. *Science* 309, 275-278.

Akao, M., Aoki, H., Kato, K., 1981. Mechanical-Properties of Sintered Hydroxyapatite for Prosthetic Applications. *Journal of Materials Science* 16, 809-812.

Al-Sawalmih, A., Li, C.H., Siegel, S., Fabritius, H., Yi, S.B., Raabe, D., Fratzl, P., Paris, O., 2008. Microtexture and Chitin/Calcite Orientation Relationship in the Mineralized Exoskeleton of the American Lobster. *Advanced Functional Materials* 18, 3307-3314.

Anderson, P.S.L., Westneat, M.W., 2007. Feeding mechanics and bite force modelling of the skull of *Dunkleosteus terrelli*, an ancient apex predator. *Biology Letters* 3, 76-79.

Arciszewski, T., Cornell, J., 2006. *Bio-inspiration: Learning creative design principia*. ed. Smith, I.F.C., Springer, Berlin, 32-53.

Azizi, E., Gillis, G.B., Brainerd, E.L., 2002. Morphology and mechanics of myosepta in a swimming salamander (*Siren lacertina*). *Comparative Biochemistry and Physiology a-Molecular and Integrative Physiology* 133, 967-978.

Baird, N.A., Etter, P.D., Atwood, T.S., Currey, M.C., Shiver, A.L., Lewis, Z.A., Selker, E.U., Cresko, W.A., Johnson, E.A., 2008. Rapid SNP Discovery and Genetic Mapping Using Sequenced RAD Markers. *Plos One* 3.

Baker, J.A., Foster, S.A., Bell, M.A., 1995. Armor Morphology and Reproductive Output in Threespine Stickleback, *Gasterosteus-Aculeatus*. *Environmental Biology of Fishes* 44, 225-233.

Baker, J.A., Heins, D.C., Foster, S.A., King, R.W., 2008. An overview of life-history variation in female threespine stickleback. *Behaviour* 145, 579-602.

Balooch, G., Marshall, G.W., Marshall, S.J., Warren, O.L., Asif, S.A.S., Balooch, M., 2004. Evaluation of a new modulus mapping technique to investigate microstructural features of human teeth. *Journal of Biomechanics* 37, 1223-1232.

Bar-Cohen, Y., 2006. Biomimetics-using nature to inspire human innovation. *Bioinsp. Biomim.* 1, P1-P12.

Barbakadze, N., Enders, S., Gorb, S., Arzt, E., 2006. Local mechanical properties of the head articulation cuticle in the beetle *Pachnoda marginata* (Coleoptera, Scarabaeidae). *Journal of Experimental Biology* 209, 722-730.

Barrett, R.D.H., Rogers, S.M., Schluter, D., 2008. Natural selection on a major armor gene in threespine stickleback. *Science* 322, 255-257.

Barthelat, F., 2010. Nacre from mollusk shells: a model for high-performance structural materials. *Bioinspiration & Biomimetics* 5.

Barthelat, F., Espinosa, H.D., 2007. An experimental investigation of deformation and fracture of nacre-mother of pearl. *Experimental Mechanics* 47, 311-324.

Barthelat, F., Li, C.M., Comi, C., Espinosa, H.D., 2006. Mechanical properties of nacre constituents and their impact on mechanical performance. *Journal Of Materials Research* 21, 1977-1986.

Bell, M.A., 1977. A Late Miocene marine threespine stickleback, *Gasterosteus aculeatus aculeatus*, and its zoogeographic and evolutionary significance. *Copeia* 1977, 277-282.

Bell, M.A., 1987. Interacting Evolutionary Constraints in Pelvic Reduction of Threespine Sticklebacks, *Gasterosteus-Aculeatus* (Pisces, Gasterosteidae). *Biological Journal of the Linnean Society* 31, 347-382.

Bell, M.A., 1987. Interacting evolutionary constraints in pelvic reduction of threespine sticklebacks, *Gasterosteus Aculeatus* (Pisces, Gasterosteidae). *Biol. J. Linn. Soc.* 31, 347-382.

Bell, M.A., Aguirre, W.E., Buck, N.J., 2004. Twelve years of contemporary armor evolution in a threespine stickleback population. *Evolution* 58, 814-824.

Bell, M.A., Foster, S.A., 1994. *The evolutionary biology of the threespine stickleback.* Oxford, Oxford University Press.

Bell, M.A., Francis, R.C., Havens, A.C., 1985. Pelvic Reduction and Its Directional Asymmetry in Threespine Sticklebacks from the Cook Inlet Region, Alaska. *Copeia*, 437-444.

Bell, M.A., Orti, G., 1994. Pelvic Reduction in Threespine Stickleback from Cook Inlet Lakes - G Geographical-Distribution and Intrapopulation Variation. *Copeia*, 314-325.

- Bell, M.A., Orti, G., Walker, J.A., Koenings, J.P., 1993. Evolution of Pelvic Reduction in Threespine Stickleback Fish - a Test of Competing Hypotheses. *Evolution* 47, 906-914.
- Bell, M.A., Stewart, J.D., Park, P.J., 2009. The world's oldest fossil threespine stickleback fish. *Copeia* 2, 256-265.
- Bergstrom, C.A., 2002. Fast-start swimming performance and reduction in lateral plate number in threespine stickleback. *Can. J. Zool.* 80, 207-213.
- Bletzinger, K.U., Ramm, E., 2001. Structural optimization and form finding of light weight structures. *Computers & Structures* 79, 2053-2062.
- Bloebaum, R.D., Skedros, J.G., Vajda, E.G., Bachus, K.N., Constantz, B.R., 1997. Determining mineral content variations in bone using backscattered electron imaging. *Bone* 20, 485-490.
- Bonderer, L.J., Studart, A.R., Gauckler, L.J., 2008. Bioinspired design and assembly of platelet reinforced polymer films. *Science* 319, 1069-1073.
- Bozec, L., van der Heijden, G., Horton, M., 2007. Collagen fibrils: Nanoscale ropes. *Biophysical Journal* 92, 70-75.
- Brainerd, E.L., Liem, K.F., Samper, C.T., 1989. Air Ventilation by Recoil Aspiration in Polypterid Fishes. *Science* 246, 1593-1595.
- Brett, C.E., Walker, S.E., 2002. The fossil record of predator-prey arms races: coevolution and escalation hypothesis, p. 93-118. In Kowalewski, M., and Kelley, P.H., eds., *The Fossil Record of Predation: The Paleontological Society Papers* v.8.
- Bruet, B.J.F. (2008). *Multiscale Structural and Mechanical Design of Mineralized Biocomposites*, unpublished thesis (Ph.D.) in Dept. of Materials Science and Engineering, Massachusetts Institute of Technology.
- Bruet, B.J.F., Qi, H.J., Boyce, M.C., Panas, R., Tai, K., Frick, L., Ortiz, C., 2005. Nanoscale morphology and indentation of individual nacre tablets from the gastropod mollusc *Trochus niloticus*. *Journal of Materials Research* 20, 2400-2419.
- Bruet, B.J.F., Song, J.H., Boyce, M.C., Ortiz, C., 2008. Materials design principles of ancient fish armour. *Nature Materials* 7, 748-756.
- Bucur, V., Declercq, N.F., 2006. The anisotropy of biological composites studied with ultrasonic technique. *Ultrasonics* 44, E829-E831.
- Buehler, M.J., 2007. Molecular nanomechanics of nascent bone: fibrillar toughening by mineralization. *Nanotechnology* 18.

- Bushnell, D.M., Moore, K.J., 1991. Drag Reduction in Nature. *Annual Review of Fluid Mechanics* 23, 65-79.
- Caldwell, R.L., Dingle, H., 1975. Stomatopods. *Sci. Am.* 234, 81-89.
- Callister, W.D., 2003. *Materials science and engineering: an introduction*. Wiley, New York.
- Carroll, R.L., 1988. *Vertebrate Paleontology and Evolution*. W.H. Freeman and Company, New York.
- Chan, Y.F., Marks, M.E., Jones, F.C., Villarreal, G., Shapiro, M.D., Brady, S.D., Southwick, A.M., Absher, D.M., Grimwood, J., Schmutz, J., Myers, R.M., Petrov, D., Jonsson, B., Schluter, D., Bell, M.A., Kingsley, D.M., 2010. Adaptive Evolution of Pelvic Reduction in Sticklebacks by Recurrent Deletion of a Pitx1 Enhancer. *Science* 327, 302-305.
- Chang, M.C., Tanaka, J., 2002. FT-IR study for hydroxyapatite/collagen nanocomposite cross-linked by glutaraldehyde. *Biomaterials* 23, 4811-4818.
- Chateigner, D., Hedegaard, C., Wenk, H.R., 2000. Mollusc shell microstructures and crystallographic textures. *Journal of Structural Geology* 22, 1723-1735.
- Chen, T.T. (2011). *Microstructure and Micromechanics of the Sea Urchin, Colobocentrotus atratus*, unpublished thesis (MS.) in Department of Mechanical Engineering, Massachusetts Institute of Technology.
- Cheng, L., Wang, L.Y., Karlsson, A.M., 2008. Image analyses of two crustacean exoskeletons and implications of the exoskeletal microstructure on the mechanical behavior. *Journal of Materials Research* 23, 2854-2872.
- Cheng, L., Wang, L.Y., Karlsson, A.M., 2009. Mechanics-based analysis of selected features of the exoskeletal microstructure of *Popillia japonica*. *Journal of Materials Research* 24, 3253-3267.
- Choi, H., Moin, P., Kim, J., 1993. Direct Numerical-Simulation of Turbulent-Flow over Riblets. *Journal of Fluid Mechanics* 255, 503-539.
- Clemen, G., Bartsch, P., Wacker, K., 1998. Dentition and dentigerous bones in juveniles and adults of *Polypterus senegalus* (Cladistia, Actinopterygii). *Ann. Anat.* 180, 211-221.
- Clifton, K.B., Motta, P.J., 1998. Feeding morphology, diet, and ecomorphological relationships among five Caribbean labrids (Teleostei, Labridae). *Copeia*, 953-966.
- Coburn, M.M., Gaglione, J.I., 1992. A comparative study of Percid scales (Teleostei: Perciformes). *Copeia* 4, 986-1001.

- Colbert, E.H., 1955. Evolution of the vertebrates. John Wiley and Sons, Inc, New York.
- Colosimo, P.F., Hosemann, K.E., Balabhadra, S., Villarreal, G., Dickson, M., Grimwood, J., Schmutz, J., Myers, R.M., Schluter, D., Kingsley, D.M., 2005. Widespread parallel evolution in sticklebacks by repeated fixation of ectodysplasin alleles. *Science* 307, 1928-1933.
- Constantz, B.R., Ison, I.C., Fulmer, M.T., Poser, R.D., Smith, S.T., Vanwagoner, M., Ross, J., Goldstein, S.A., Jupiter, J.B., Rosenthal, D.I., 1995. Skeletal Repair by in-Situ Formation of the Mineral Phase of Bone. *Science* 267, 1796-1799.
- Cresko, W.A., 2008. Armor development and fitness. *Science* 322, 204-206.
- Cresko, W.A., Amores, A., Wilson, C., Murphy, J., Currey, M., Phillips, P., Bell, M.A., Kimmel, C.B., Postlethwait, J.H., 2004. Parallel genetic basis for repeated evolution of armor loss in Alaskan threespine stickleback populations. *Proceedings of the National Academy of Sciences of the United States of America* 101, 6050-6055.
- Cresko, W.A., McGuigan, K.L., Phillips, P.C., Postlethwait, J.H., 2007. Studies of threespine stickleback developmental evolution: progress and promise. *Genetica* 129, 105-126.
- Currey, J.D., 1999. The design of mineralised hard tissues for their mechanical functions. *Journal of Experimental Biology* 202, 3285-3294.
- Currey, J.D., Taylor, J.D., 1974. Mechanical-Behavior of Some Molluscan Hard Tissues. *Journal of Zoology* 173, 395-406.
- Daget, J., Gayet, M., Meunier, F.J., Sire, J.-Y., 2001. Major discoveries on the dermal skeleton of fossil and Recent polypteriforms: a review. *Fish and Fisheries* 2, 113-124.
- Daget, J., Gayet, M., Meunier, F.J., Sire, J.Y., 2001. Major discoveries on the dermal skeleton of fossil and Recent polypteriforms: a review. *Fish and Fisheries* 2, 113-124.
- Danielsson, M., Parks, D.M., Boyce, M.C., 2002. Three-dimensional micromechanical modeling of voided polymeric materials. *Journal of the Mechanics and Physics of Solids* 50, 351-379.
- Danielsson, M., Parks, D.M., Boyce, M.C., 2007. Micromechanics, macromechanics and constitutive modeling of the elasto-viscoplastic deformation of rubber-toughened glassy polymers. *Journal of the Mechanics and Physics of Solids* 55, 533-561.
- Darwin, C., 1859. *The Origin of Species by Means of Natural Selection*, London: John Murray.

- de Schepper, N., Van Wassenbergh, S., Adriaens, D., 2008. Morphology of the jaw system in trichiurids: trade-offs between mouth closing and biting performance. *Zoological Journal of the Linnean Society* 152, 717-736.
- Dietl, G.P., Kelley, P.H., 2002. The fossil record of predator-prey arms races: coevolution and escalation hypothesis, p. 353-374. In Kowalewski, M., and Kelley, P.H., eds., *The Fossil Record of Predation: The Paleontological Society Papers* v.8.
- Dill, K.A., 1990. Dominant Forces in Protein Folding. *Biochemistry* 29, 7133-7155.
- Doyle, B.B., Bendit, E.G., Blout, E.R., 1975. Infrared Spectroscopy of Collagen and Collagen-Like Polypeptides. *Biopolymers* 14, 937-957.
- Driessens, F.C.M., Verbeeck, R.M.H., 1990. *Biomaterials*, CRC Press, Boca Raton, FL.
- Dunlop, J.W.C., Fratzl, P., 2010. Biological Composites. *Annual Review of Materials Research* 40, 1-24.
- Dunlop, J.W.C., Weinkamer, R., Fratzl, P., 2011. Artful interfaces within biological materials. *Materials Today* 14, 70-78.
- Easterling, K.E., Harrysson, R., Gibson, L.J., Ashby, M.F., 1982. On the Mechanics of Balsa and Other Woods. *Proceedings of the Royal Society of London Series a-Mathematical Physical and Engineering Sciences* 383, 31-41.
- Egginton, S., Taylor, E.W., Raven, J.A., 1999. *Regulation of acid-base status in animals and plants*, Cambridge University Press.
- Eldredge, N., Stanley, S.M., 1984. *Living Fossil*, Springer Verlag, New York, Berlin.
- Elices, M., 2000. *Structural Biological Materials: Design and Structure-Property Relationships*, Elsevier Science Ltd., UK.
- Elnor, R.W., 1978. Mechanics of predation by shore crab, *Carcinus Maenas* (L.), on edible mussel, *Mytilus edulis* L. *Oecologia* 36, 333-344.
- Espinosa, H.D., Rim, J.E., Barthelat, F., Buehler, M.J., 2009. Merger of structure and material in nacre and bone - Perspectives on de novo biomimetic materials. *Progress in Materials Science* 54, 1059-1100.
- Fantner, G.E., Hassenkam, T., Kindt, J.H., Weaver, J.C., Birkedal, H., Pechenik, L., Cutroni, J.A., Cidade, G.A.G., Stucky, G.D., Morse, D.E., Hansma, P.K., 2005. Sacrificial bonds and hidden length dissipate energy as mineralized fibrils separate during bone fracture. *Nature Materials* 4, 612-616.
- Fish, F.E., Hui, C.A., 1991. Dolphin swimming-a review. *Mammal Review* 21, 181-195.

Fish, F.E., Lauder, G.V., 2006. Passive and active flow control by swimming fishes and mammals. *Annual Review of Fluid Mechanics* 38, 193-224.

Foster, S.A., 1995. Understanding the evolution of behavior in threespine stickleback: The value of geographic variation. *Behaviour* 132, 1107-1129.

Foster, S.A., Garcia, V.B., Town, M.Y., 1988. Cannibalism as the Cause of an Ontogenetic Shift in Habitat Use by Fry of the Threespine Stickleback. *Oecologia* 74, 577-585.

Fritsch, A., Hellmich, C., 2007. "Universal" microstructural patterns in cortical and trabecular, extracellular and extravascular bone materials: Micromechanics-based prediction of anisotropic elasticity. *J. Theor. Biol* 244, 597-620.

Gao, H.J., Ji, B.H., Jager, I.L., Arzt, E., Fratzl, P., 2003. Materials become insensitive to flaws at nanoscale: Lessons from nature. *Proceedings of the National Academy of Sciences of the United States of America* 100, 5597-5600.

Geller, J.B., 1990. Reproductive Responses to Shell Damage by the Gastropod *Nucella-Emarginata* (Deshayes). *Journal of Experimental Marine Biology and Ecology* 136, 77-87.

Gemballa, S., Bartsch, P., 2002. Architecture of the integument in lower Teleostomes: Functional morphology and evolutionary implications. *Journal of Morphology* 253, 290-309.

Gemballa, S., Roder, K., 2004. From head to tail: The myoseptal system in basal actinopterygians. *Journal of Morphology* 259, 155-171.

Giannakopoulos, A.E., Suresh, S., 1999. Determination of elastoplastic properties by instrumented sharp indentation. *Scripta Materialia* 40, 1191-1198.

Giles, N., 1983. The Possible Role of Environmental Calcium Levels during the Evolution of Phenotypic Diversity in Outer-Hebridean Populations of the 3-Spined Stickleback, *Gasterosteus-Aculeatus*. *Journal of Zoology* 199, 535-544.

Giles, N., 1983. The possible role of environmental calcium levels during the evolution of phenotypic diversity in outer-Hebridean populations of the 3-spined stickleback, *Gasterosteus aculeatus*. *Journal of Zoology* 199, 535-544.

Greer, J.R., Oliver, W.C., Nix, W.D., 2005. Size dependence of mechanical properties of gold at the micron scale in the absence of strain gradients. *Acta Materialia* 53, 1821-1830.

Gundersen, H.J.G., Jensen, T.B., Osterby, R., 1978. Distribution of Membrane Thickness Determined by Lineal Analysis. *Journal of Microscopy-Oxford* 113, 27-43.

Gupta, H.S., Fratzl, P., Kerschnitzki, M., Benecke, G., Wagermaier, W., Kirchner, H.O.K., 2007. Evidence for an elementary process in bone plasticity with an activation enthalpy of 1 eV. *Journal of the Royal Society Interface* 4, 277-282.

Gupta, H.S., Wagermaier, W., Zickler, G.A., Aroush, D.R.B., Funari, S.S., Roschger, P., Wagner, H.D., Fratzl, P., 2005. Nanoscale deformation mechanisms in bone. *Nano Letters* 5, 2108-2111.

Habelitz, S., Marshall, S.J., Marshall, G.W., Balooch, M., 2001. Mechanical properties of human dental enamel on the nanometre scale. *Archives of Oral Biology* 46, 173-183.

Hagen, D.W., Gilbertson, L.G., 1973. Selective predation and the intensity of selection acting upon the lateral plates of threespine sticklebacks. *Heredity* 30, 272-287.

Halstead, L., Shieber, W., Canterbu, J., Reiss, E., Avioli, L., 1974. Role of Kidney in Maintaining Ionized Calcium Levels in Acute Uremic State. *Journal of Clinical Investigation* 53, A31-a31.

Hamm, C.E., Merkel, R., Springer, O., Jurkojc, P., Maier, C., Prectel, K., Smetacek, V., 2003. Architecture and material properties of diatom shells provide effective mechanical protection. *Nature* 421, 841-843.

Han, L., Frank, E.H., Greene, J.J., Lee, H.Y., Hung, H.H.K., Grodzinsky, A.J., Ortiz, C., 2011. Time-Dependent Nanomechanics of Cartilage. *Biophysical Journal* 100, 1846-1854.

Han, L., Wang, L., Song, J., Boyce, M.C., Ortiz, C., in press. Direct quantification of the mechanical anisotropy and fracture of an individual exoskeleton layer via uniaxial compression of micropillars. *Nano Letters*.

Hansma, P., Turner, P., Drake, B., Yurtsev, E., Proctor, A., Mathews, P., Lulejian, J., Randall, C., Adams, J., Jungmann, R., Garza-de-Leon, F., Fantner, G., Mkrтчyan, H., Pontin, M., Weaver, A., Brown, M.B., Sahar, N., Rossello, R., Kohn, D., 2009. The bone diagnostic instrument II: Indentation distance increase. *Rev Sci Instrum* 80, 064303.

Hassan, R., Caputo, A.A., Bunshah, R.F., 1981. Fracture-Toughness of Human-Enamel. *Journal of Dental Research* 60, 820-827.

Hatfield, T., 1997. Fluctuating asymmetry and reproductive isolation between two sticklebacks. *Environmental Biology Of Fishes* 49, 63-69.

Herre, E.A., 1999. Laws governing species interactions? Encouragement and caution from figs and their associates, p. 209-237, In L. Keller (ed.), *Levels of Selection in Evolution*. Princeton University Press, Princeton.

Hild, S., Marti, O., Ziegler, A., 2008. Spatial distribution of calcite and amorphous calcium carbonate in the cuticle of the terrestrial crustaceans *Porcellio scaber* and *Armadillidium vulgare*. *Journal of Structural Biology* 163, 100-108.

Hild, S., Neues, F., Znidarsic, N., Strus, J., Epple, M., Marti, O., Ziegler, A., 2009. Ultrastructure and mineral distribution in the tergal cuticle of the terrestrial isopod *Titanethes albus*. Adaptations to a karst cave biotope. *Journal of Structural Biology* 168, 426-436.

Hildebrand, T., Laib, A., Muller, R., Dequeker, J., Ruegsegger, P., 1999. Direct three-dimensional morphometric analysis of human cancellous bone: Microstructural data from spine, femur, iliac crest, and calcaneus. *Journal of Bone and Mineral Research* 14, 1167-1174.

Hildebrand, T., Ruegsegger, P., 1997. Quantification of bone microarchitecture with the structure model index. *Comp Meth Biomech Biomed Eng* 1, 15-23.

Hoedeman, J.J., 1975. *Naturalists Guide to Fresh Water Aquarium Fish*, Sterling Publishing Co., Oak Tree press Co. Ltd, New York, London, and Sydney.

Hoogland, R., Morris, D., Tinbergen, N., 1956. The spines of sticklebacks (*Gasterosteus* and *Pygosteus*) as means of defence against predators (*Perca* and *Esox*). *Behaviour* 10, 205-236.

Huber, D.R., 2005. Analysis of the bite force and mechanical design of the feeding mechanism of the durophagous horn shark *Heterodontus francisci*. *Journal of Experimental Biology* 208, 3553-3571.

Huber, D.R., Motta, P.J., 2004. Comparative analysis of methods for determining bite force in the spiny dogfish *Squalus acanthias*. *Journal of Experimental Zoology Part a-Comparative Experimental Biology* 301A, 26-37.

Huber, D.R., Weggelaar, C.L., Motta, P.J., 2006. Scaling of bite force in the blacktip shark *Carcharhinus limbatus*. *Zoology* 109, 109-119.

Hughes, R.N., 1989. Foraging behavior of a tropical crab, *Ozius verreauxii*. *Proceedings of the Royal Society of London Series B-Biological Sciences* 237, 201-212.

Huntingford, F., Coyle, S., 2007. Antipredator defenses in stickleback: trade-offs, risk-sensitivity, and behavioral syndromes, In: Ostlund-Nilsson, S, Mayer, I., Huntingford, F.A. (Eds.), *Biology of the Three-spined Stickleback*. CRC Press, Boca Raton, Florida, pp. 127-156.

Ikoma, T., Kobayashi, H., Tanaka, J., Walsh, D., Mann, S., 2003. Microstructure, mechanical, and biomimetic properties of fish scales from *Pagrus major*. *Journal of Structural Biology* 142, 327-333.

- Imbeni, V., Kruzic, J.J., Marshall, G.W., Marshall, S.J., Ritchie, R.O., 2005. The dentin-enamel junction and the fracture of human teeth. *Nature Materials* 4, 229-232.
- Jager, I., Fratzl, P., 2000. Mineralized collagen fibrils: a mechanical model with a staggered arrangement of mineral particles. *Biophys. J.* 79, 1737-1746.
- Jayachandran, R., Boyce, M.C., Argon, A.S., 1995. Design of multilayer polymeric coatings for indentation resistance. *Journal of Computer-Aided Materials Design* 2, 151.
- Johnson, K.L., 1987. *Contact Mechanics*, Cambridge University Press, UK.
- Katti, D.R., Katti, K.S., Sopp, J.M., Sarikaya, M., 2001. 3D finite element modeling of mechanical response in nacre-based hybrid nanocomposites. *Computational and Theoretical Polymer Science* 11, 397-404.
- Katz, J.L., Ukrainci, K., 1971. Anisotropic Elastic Properties of Hydroxyapatite. *Journal of Biomechanics* 4, 221-227.
- Kent, B.W., 1983. Patterns of coexistence in Busyconine whelks. *J. Exp. Mar. Biol. Ecol.* 66, 257-283.
- Kiener, D., Grosinger, W., Dehm, G., Pippan, R., 2008. A further step towards an understanding of size-dependent crystal plasticity: In situ tension experiments of miniaturized single-crystal copper samples. *Acta Materialia* 56, 580-592.
- Kimelman-Bleich, N., Pelled, G., Sheyn, D., Kallai, I., Zilberman, Y., Mizrahi, O., Tal, Y., Tawackoli, W., Gazit, Z., Gazit, D., 2009. The use of a synthetic oxygen carrier-enriched hydrogel to enhance mesenchymal stem cell-based bone formation in vivo. *Biomaterials* 30, 4639-4648.
- Kingsley, D.M., Peichel, C.L., 2007. The molecular genetics of evolutionary change in sticklebacks, In: Ostlund-Nilsson, S, Mayer, I., Huntingford, F.A. (Eds.), *Biology of the Three-spined Stickleback*. CRC Press, Boca Raton, Florida, pp. 41-81.
- Klingenberg, C.P., 2010. Evolution and development of shape: integrating quantitative approaches. *Nature Reviews Genetics* 11, 623-635.
- Kodera, H., 1994. *Jurassic fishes: selection, care, behavior*, T.H.F. Publications, New Jersey.
- Krauss, S., Monsonego-Ornan, E., Zelzer, E., Fratzl, P., Shahar, R., 2009. Mechanical Function of a Complex Three-Dimensional Suture Joining the Bony Elements in the Shell of the Red-Eared Slider Turtle. *Advanced Materials* 21, 407-412.
- Kristjansson, B.K., 2005. Rapid morphological changes in threespine stickleback, *Gasterosteus aculeatus*, in freshwater. *Environmental Biology Of Fishes* 74, 357-363.

- Lauder, G.V., 1980. Evolution of the Feeding Mechanism in Primitive Actinopterygian Fishes - a Functional Anatomical Analysis of Polypterus, Lepisosteus, and Amia. *Journal of Morphology* 163, 283-317.
- Launey, M.E., Buehler, M.J., Ritchie, R.O., 2010. On the Mechanistic Origins of Toughness in Bone. *Annual Review of Materials Research* 40, 25-53.
- Lawn, B.R., Lee, J.J.W., Chai, H., 2010. Teeth: Among Nature's Most Durable Biocomposites. *Annual Review of Materials Research* 40, 55-75.
- Lee, W.T., Dove, M.T., Salje, E.K.H., 2000. Surface relaxations in hydroxyapatite. *Journal of Physics: Condensed Matter* 12, 9829-9841.
- Leventouri, T., 2006. Synthetic and biological hydroxyapatites: Crystal structure questions. *Biomaterials* 27, 3339-3342.
- Li, X.D., Chang, W.C., Chao, Y.J., Wang, R.Z., Chang, M., 2004. Nanoscale structural and mechanical characterization of a natural nanocomposite material: The shell of red abalone. *Nano Letters* 4, 613-617.
- Li, Y.N., Ortiz, C., Boyce, M.C., *in review*. Stiffness and strength of a suture joint model.
- Lin, A.Y.M., Meyers, M.A., Vecchio, K.S., 2006. Mechanical properties and structure of *Strombus gigas*, *Tridacna gigas*, and *Haliotis rufescens* sea shells: A comparative study. *Materials Science & Engineering C-Biomimetic and Supramolecular Systems* 26, 1380-1389.
- Lippert, F., Parker, D.M., Jandt, K.D., 2004. In vitro demineralization/remineralization cycles at human tooth enamel surfaces investigated by AFM and nanoindentation. *J Colloid Interface Sci* 280, 442-448.
- Lloyd, G.E., 1987. Atomic-Number and Crystallographic Contrast Images with the Sem - a Review of Backscattered Electron Techniques. *Mineralogical Magazine* 51, 3-19.
- Long, J.H., Nipper, K.S., 1996. The importance of body stiffness in undulatory propulsion. *Amer. Zool.* 36, 678-694.
- Lowenstam, H.A., Weiner, S., 1989. *On biomineralization*, Oxford University Press, New York.
- Lucas, P.W., Turner, I.M., Dominy, N.J., Yamashita, N., 2000. Mechanical defences to herbivory. *Annals of Botany* 86, 913-920.
- Magalhaes, H., 1948. An ecological study of snails of the Genus *Busycon* at Beaufort, North Carolina. *Ecological Monographs* 18, 377-409.

- Mahoney, E., Ismail, F.S.M., Kilpatrick, N., Swain, M., 2004. Mechanical properties across hypomineralized/hypoplastic enamel of first permanent molar teeth. *European Journal Of Oral Sciences* 112, 497-502.
- Mapes, R.H., Fahrner, T.R., Babcock, L.E., 1989. Sublethal and Lethal Injuries of Pennsylvanian Conulariids from Oklahoma. *Journal of Paleontology* 63, 34-37.
- Marchinko, K.B., 2009. Predation's Role in Repeated Phenotypic and Genetic Divergence of Armor in Threespine Stickleback. *Evolution* 63, 127-138.
- Marchinko, K.B., Schluter, D., 2007. Parallel evolution by correlated response: Lateral plate reduction in threespine stickleback. *Evolution* 61, 1084-1090.
- Markey, M.J., Main, R.P., Marshall, C.R., 2006. In vivo cranial suture function and suture morphology in the extant fish *Polypterus*: implications for inferring skull function in living and fossil fish. *Journal of Experimental Biology* 209, 2085-2102.
- Marshall, G.W., Balooch, M., Gallagher, R.R., Gansky, S.A., Marshall, S.J., 2001. Mechanical properties of the dentinoenamel junction: AFM studies of nanohardness, elastic modulus, and fracture. *Journal of Biomedical Materials Research* 54, 87-95.
- Mattern, M.Y., 2004. Molecular phylogeny of the Gasterosteidae: the importance of using multiple genes. *Molecular Phylogenetics and Evolution* 30, 366-377.
- Mcclanahan, T.R., Muthiga, N.A., 1989. Patterns of Predation on a Sea-Urchin, *Echinometra-Mathaei* (Deblainville), on Kenyan Coral Reefs. *Journal of Experimental Marine Biology and Ecology* 126, 77-94.
- McKinnon, J.S., Rundle, H.D., 2002. Speciation in nature: the threespine stickleback model systems. *Trends in Ecology & Evolution* 17, 480-488.
- Meinke, D.K., Skinner, H.C.W., Thomson, K.S., 1979. X-ray diffraction of the calcified tissues in *Polypterus*. *Calcif. Tissue Int.* 28, 37-42.
- Meunier, F.J., 1980. Recherches histologiques sur le squelette dermique des Polypteridae. *Archives de Zoologie Expérimentale et Générale* 121, 279-295.
- Meunier, F.J., 1987. Os cellulaire, os acellulaire et tissus derives chez les Osteichthyens: Les phonomenes de l'acellularisation et de la perte de mineralisation. *Ann. Biol* 4, 201-225.
- Meyers, M.A., Chen, P.Y., Lin, A.Y.M., Seki, Y., 2008. Biological materials: Structure and mechanical properties. *Progress in Materials Science* 53, 1-206.
- Miller, K., 1999. Constitutive model of brain tissue suitable for finite element analysis of surgical procedures. *Journal of Biomechanics* 32, 531-537.

- Miller, K., Chinzei, K., 1997. Constitutive modelling of brain tissue: Experiment and theory. *Journal of Biomechanics* 30, 1115-1121.
- Montgomery, J., Coombs, S., Halstead, M., 1995. Biology of the Mechanosensory Lateral-Line in Fishes. *Reviews in Fish Biology and Fisheries* 5, 399-416.
- Mori, S., 1987. Divergence in Reproductive Ecology of the 3-Spined Stickleback, *Gasterosteus-Aculeatus*. *Japanese Journal of Ichthyology* 34, 165-175.
- Moss, M.L., 1963. Biology of Acellular Teleost Bone. *Annals of the New York Academy of Sciences* 109, 337-350.
- Moss, M.L., 1972. Vertebrate Dermis and Integumental Skeleton. *American Zoologist* 12, 27-34.
- Nalla, R.K., Kinney, J.H., Ritchie, R.O., 2003. Mechanistic fracture criteria for the failure of human cortical bone. *Nature Materials* 2, 164-168.
- Nelson, J.S., 1971. Comparison of Pectoral and Pelvic Skeletons and of Some Other Bones and Their Phylogenetic Implications in Aulorhynchidae and Gasterosteidae (Pices). *Journal of the Fisheries Research Board of Canada* 28, 427-442.
- Ng, L., Grodzinsky, A.J., Patwari, P., Sandy, J., Plaas, A., Ortiz, C., 2003. Individual cartilage aggrecan macromolecules and their constituent glycosaminoglycans visualized via atomic force microscopy. *Journal of Structural Biology* 143, 242-257.
- Nicholls, S.P., Gathercole, L.J., Keller, A., Shah, J.S., 1983. Crimping in Rat Tail Tendon Collagen - Morphology and Transverse Mechanical Anisotropy. *International Journal of Biological Macromolecules* 5, 283-288.
- Noor, M.A.F., Feder, J.L., 2006. Speciation genetics: evolving approaches. *Nature Reviews Genetics* 7, 851-861.
- Norman, T.L., Vashishth, D., Burr, D.B., 1995. Fracture toughness of human bone under tension. *Journal of Biomechanics* 28, 309-320.
- Odgaard, A., Gundersen, H.J.G., 1993. Quantification of Connectivity in Cancellous Bone, with Special Emphasis on 3-D Reconstructions. *Bone* 14, 173-182.
- Oliver, W.C., Pharr, G.M., 1992. An Improved Technique for Determining Hardness and Elastic-Modulus Using Load and Displacement Sensing Indentation Experiments. *Journal of Materials Research* 7, 1564-1583.
- Olson, G.B., 1997. Computational design of hierarchically structured materials. *Science* 277, 1237-1242.

- Orr, H.A., 2005. The genetic theory of adaptation: A brief history. *Nature Reviews Genetics* 6, 119-127.
- Ortiz, C., Boyce, M.C., 2008. Bioinspired structural materials. *Science* 319, 1053-1054.
- Ortiz, C., Boyce, M.C., Song, J., Reichert, S., 2010. Articulating Protective System for Resisting Mechanical Loads. Provisional Patent App. M0925.70294US00.
- Ørvig, T., 1967. Phylogeny of tooth tissues: evolution of some calcified tissues in early vertebrates. *Structural and Chemical Organization of Teeth* 1, 45–110.
- Ørvig, T., 1968. The dermal skeleton: general considerations. *Current Problems of Lower Vertebrate Phylogeny. Proc. of the 4th Nobel Symposium*. T. Ørvig, ed. Almquist and Wiskell, Stockholm, 373–397.
- Östlund-Nilsson, S., Mayer, I., Huntingford, F.A., 2007. *Biology of the Three-Spined Stickleback*.
- Oxman, N., 2010. Structuring Materiality Design Fabrication of Heterogeneous Materials. *Architectural Design*, 78-85.
- Parker, A.R., McKenzie, D.R., Large, M.C.J., 1998. Multilayer reflectors in animals using green and gold beetles as contrasting examples. *Journal of Experimental Biology* 201, 1307-1313.
- Parsons, A.H., 1982. Structure of the eggshell. *Poultry science* 61, 2013-2021.
- Patek, S.N., Caldwell, R.L., 2005. Extreme impact and cavitation forces of a biological hammer: strike forces of the peacock mantis shrimp *Odontodactylus scyllarus*. *Journal of Experimental Biology* 208, 3655-3664.
- Pautard, F.G.E., 1970. Mineral Phase of Calcified Cartilage, Bone and Baleen. *Calcified Tissue Research* 4, 34-&.
- Peichel, C.L., Nereng, K.S., Ohgi, K.A., Cole, B.L.E., Colosimo, P.F., Buerkle, C.A., Schluter, D., Kingsley, D.M., 2001. The genetic architecture of divergence between threespine stickleback species. *Nature* 414, 901-905.
- Pharr, G.M., Oliver, W.C., Brotzen, F.R., 1992. On the Generality of the Relationship among Contact Stiffness, Contact Area, and Elastic-Modulus during Indentation. *Journal of Materials Research* 7, 613-617.
- Podsiadlo, P., Kaushik, A.K., Arruda, E.M., Waas, A.M., Shim, B.S., Xu, J.D., Nandivada, H., Pumphlin, B.G., Lahann, J., Ramamoorthy, A., Kotov, N.A., 2007. Ultrastrong and stiff layered polymer nanocomposites. *Science* 318, 80-83.

Posner, A.S., Betts, F., 1981. Molecular control of tissue mineralization, in *Chemistry and Biology of Mineralized Connective Tissues*, edited by A. Veis, Elsevier, Amsterdam.

Pottmann, H., 2010. Architectural Geometry as Design Knowledge. *Architectural Design*, 72-77.

Qin, Y., Brockett, A., Ma, Y., Razali, A., Zhao, J., Harrison, C., Pan, W., Dai, X., Loziak, D., 2010. Micro-manufacturing: research, technology outcomes and development issues. *International Journal of Advanced Manufacturing Technology* 47, 821-837.

Raabe, D., Sachs, C., Romano, P., 2005. The crustacean exoskeleton as an example of a structurally and mechanically graded biological nanocomposite material. *Acta Materialia* 53, 4281-4292.

Rafferty, K.L., Herring, S.W., 1999. Craniofacial sutures: Morphology, growth, and in vivo masticatory strains. *Journal of Morphology* 242, 167-179.

Raji, A., Saidu, A.K., Maryam, A.T., 2003. Preliminary studies on food and feeding habits of *Polypterus endlicheri* and *Polypterus senegalus* in Lake Chad. 18th Annual Conference of the Fisheries Society of Nigeria (FISON).

Ramberg, W., Osgood, W.R., 1943. Description of stress-strain curves by three parameters. Technical Note No. 902, National Advisory Committee For Aeronautics, Washington DC.

Randall, C., Mathews, P., Yurtsev, E., Sahar, N., Kohn, D., Hansma, P., 2009. The bone diagnostic instrument III: Testing mouse femora. *Rev Sci Instrum* 80, 065108.

Raschi, W., Tabit, C., 1992. Functional-Aspects of Placoid Scales - a Review and Update. *Australian Journal of Marine and Freshwater Research* 43, 123-147.

Reddy, G.K., Stehno-Bittel, L., Enwemeka, C.S., 1999. Matrix remodeling in healing rabbit Achilles tendon. *Wound Repair and Regeneration* 7, 518-527.

Rehman, I., Bonfield, W., 1997. Characterization of hydroxyapatite and carbonated apatite by photo acoustic FTIR spectroscopy. *Journal of Materials Science-Materials in Medicine* 8, 1-4.

Reichert, S. (2010). *Reverse Engineering Nature: Design Principles for Flexible Protection Inspired by Ancient Fish Armor of Polypteridae*, unpublished thesis (MS.) in Department of Architecture, Massachusetts Institute of Technology.

Reimchen, T.E., 1980. Spine Deficiency and Polymorphism in a Population of *Gasterosteus-Aculeatus* - an Adaptation to Predators. *Canadian Journal of Zoology- Revue Canadienne De Zoologie* 58, 1232-1244.

- Reimchen, T.E., 1983. Structural relationships between spines and lateral plates in threespine stickleback (*Gasterosteus Aculeatus*). *Evolution* 37, 931-946.
- Reimchen, T.E., 1988. Inefficient predators and prey injuries in a population of giant stickleback. *Can J. Zool.* 66, 2036-2044.
- Reimchen, T.E., 1991. Trout Foraging Failures and the Evolution of Body Size in Stickleback. *Copeia*, 1098-1104.
- Reimchen, T.E., 1992. Injuries on stickleback from attacks by a toothed predator (*Oncorhynchus*) and implications for the evolution of lateral plates. *Evolution* 46, 1224-1230.
- Reimchen, T.E., 1994. Predators and evolution in threespine stickleback., In: Bell, M.A., Foster, S.A. (Eds.), *The Evolution of the Threespine Stickleback*. Oxford University Press, Oxford, NY, USA. pp. 240-276.
- Reimchen, T.E., 1995. Predator-induced cyclical changes in lateral plate frequencies of *Gasterosteus*. *Behaviour* 132, 1079 -1094
- Reimchen, T.E., 2000. Predator handling failures of lateral plate morphs in *Gasterosteus aculeatus*: Functional implications for the ancestral plate condition. *Behaviour* 137, 1081-1096.
- Reimchen, T.E., Nosil, P., 2002. Temporal variation in divergent selection on spine number in threespine stickleback. *Evolution* 56, 2472-2483.
- Reimchen, T.E., Nosil, P., 2004. Variable predation regimes predict the evolution of sexual dimorphism in a population of threespine stickleback. *Evolution* 58, 1274-1281.
- Rey, C., Combes, C., Drouet, C., Sfihi, H., Barroug, A., 2007. Physico-chemical properties of nanocrystalline apatites: Implications for biominerals and biomaterials. *Materials Science & Engineering C-Biomimetic and Supramolecular Systems* 27, 198-205.
- Rho, J.Y., Kuhn-Spearing, L., Zioupos, P., 1998. Mechanical properties and the hierarchical structure of bone. *Medical Engineering & Physics* 20, 92-102.
- Rigby, B.J., Hirai, N., Spikes, J.D., Eyring, H., 1959. The Mechanical Properties of Rat Tail Tendon. *Journal of General Physiology* 43, 265-283.
- Ritman, E.L., 2004. Micro-computed tomography-current status and developments. *Annual Review of Biomedical Engineering* 6, 185-208.
- Rodriguez-Navarro, A.B., CabraldeMelo, C., Batista, N., Morimoto, N., Alvarez-Lloret, P., Ortega-Huertas, M., Fuenzalida, V.M., Arias, J.I., Wiff, J.P., Arias, J.L., 2006.

Microstructure and crystallographic-texture of giant barnacle (*Austromegabalanus psittacus*) shell. *Journal of Structural Biology* 156, 355-362.

Romer, A.S., 1933. Eurypterid influence on vertebrate history. *Science* 78, 114-117.

Roschger, P., Fratzl, P., Eschberger, J., Klaushofer, K., 1998. Validation of quantitative backscattered electron imaging for the measurement of mineral density distribution in human bone biopsies. *Bone* 23, 319-326.

Ruben, J.A., Bennett, A.A., 1987. The Evolution of Bone. *Evolution* 41, 1187-1197.

Sanchez, C., Arribart, H., Guille, M.M.G., 2005. Biomimetism and bioinspiration as tools for the design of innovative materials and systems. *Nature Materials* 4, 277-288.

Sasagawa, I., Ishiyama, M., Yokosuka, H., Mikami, M., Uchida, T., 2009. Tooth enamel and enameloid in actinopterygian fish. *Frontiers of Materials Science in China* 3, 174-182.

Schluter, D., 2009. Evidence for Ecological Speciation and Its Alternative. *Science* 323, 737-741.

Schmahl, W.W., Griesshaber, E., Merkel, C., Kelm, K., Deuschle, J., Neuser, R.D., Göetz, A.J., Sehrbrock, A., Mader, W., 2008. Hierarchical fibre composite structure and micromechanical properties of phosphatic and calcitic brachiopod shell biomaterials - Overview. *Mineralogical Magazine* 72, 541-562.

Schumacher, P., 2009. Parametricism: A New Global Style for Architecture and Urban Design. *Architectural Design* 79, 14-23.

Seed, R., Hughes, R.N., 1995. Criteria for prey size-selection in molluscivorous crabs with contrasting claw morphologies. *Journal of Experimental Marine Biology and Ecology* 193, 177-195.

Shapiro, M.D., Marks, M.E., Peichel, C.L., Blackman, B.K., Nereng, K.S., Jonsson, B., Schluter, D., Kingsley, D.M., 2004. Genetic and developmental basis of evolutionary pelvic reduction in threespine sticklebacks. *Nature* 428, 717-723.

Shimizu, D., Macho, G.A., 2007. Functional significance of the microstructural detail of the primate dentino-enamel junction: A possible example of exaptation. *Journal of Human Evolution* 52, 103-111.

Sire, J.-Y., 1989. Scales in young *Polypterus senegalus* are elasmoid: New phylogenetic implications. *Am. J. Anat.* 186, 315-323.

Sire, J.-Y., 1990. From ganoine to elasmoid scales in the Actinopterygian fishes. *Neth. J. Zool.* 40, 75-92.

Sire, J.-Y., 1994. Light and TEM study of nongenerated and experimentally regenerated scales of *Lepisoteus oculatus* (Holostei) with particular attention to ganoine formation. *Anat. Rec.* 240, 189-207.

Sire, J.Y., Donoghue, P.C.J., Vickaryous, M.K., 2009. Origin and evolution of the integumentary skeleton in non-tetrapod vertebrates. *Journal of Anatomy* 214, 409-440.

Skedros, J.G., Bloebaum, R.D., Bachus, K.N., Boyce, T.M., 1993. The Meaning of Graylevels in Backscattered Electron Images of Bone. *Journal of Biomedical Materials Research* 27, 47-56.

Smith, C.S., 1965. Materials and Development of Civilization and Science - Empiricism and Esthetic Selection Led to Discovery of Many Properties on Which Material Science Is Based. *Science* 148, 908-&.

Song, J.H., Reichert, S., Kallai, I., Gazit, D., Wund, M., Boyce, M.C., Ortiz, C., 2010. Quantitative microstructural studies of the armor of the marine threespine stickleback (*Gasterosteus aculeatus*). *Journal of Structural Biology* 171, 318-331.

Spearman, R.I.C., 1973. *The integument: A textbook of skin biology*, Cambridge University Press.

Spears, I.R., 1997. A three-dimensional finite element model of prismatic enamel: a re-appraisal of the data on the Young's modulus of enamel. *Journal of Dental Research* 76, 1690-1697.

Spears, I.R., van Noort, R., Crompton, R.H., Cardew, G.E., Howard, I.C., 1993. The Effects Of Enamel Anisotropy On The Distribution Of Stress In A Tooth. *Journal Of Dental Research* 72, 1526-1531.

Sudo, S., Tsuyuki, K., Ito, Y., Ikohaji, T., 2002. A study on the surface shape of fish scales. *JSME International Journal, Series C* 45, 1100-1105.

Suresh, S., 2001. Graded materials for resistance to contact deformation and damage. *Science* 292, 2447-2451.

Suresh, S., Giannakopoulos, A.E., 1998. A new method for estimating residual stresses by instrumented sharp indentation. *Acta Materialia* 46, 5755-5767.

Tai, K., Dao, M., Suresh, S., Palazoglu, A., Ortiz, C., 2007. Nanoscale heterogeneity promotes energy dissipation in bone. *Nature Materials* 6, 454-462.

Tai, K., Ulm, F.J., Ortiz, C., 2006. Nanogranular origins of the strength of bone. *Nano Letters* 6, 2520-2525.

Tai, K.S., Qi, H.J., Ortiz, C., 2005. Effect of mineral content on the nanoindentation properties and nanoscale deformation mechanisms of bovine tibial cortical bone. *Journal of Materials Science-Materials in Medicine* 16, 947-959.

Taylor, G.M., 2000. Maximum force production: why are crabs so strong? *Proceedings of the Royal Society of London Series B-Biological Sciences* 267, 1475-1480.

Tirrel, D.A., 1994. Hierarchical structural in biology as a guide for new materials technology, Natl. Acad. Press, Washington, DC.

Tytell, E.D., Lauder, G.V., 2002. The C-start escape response of *Polypterus senegalus*: bilateral muscle activity and variation during stage 1 and 2. *The Journal of Experimental Biology* 205, 2591-2603.

Uozumi, S., Suzuki, S., 1981. The evolution of shell structures in the bivalvia. Study of Molluscan paleobiology Prof M. Omori Memorial Volume, 63-77.

Vamosi, S.M., 2002. Predation sharpens the adaptive peaks: survival trade-offs in sympatric sticklebacks. *Annales Zoologici Fennici* 39, 237-248.

Vamosi, S.M., 2003. The presence of other fish species affects speciation in threespine sticklebacks. *Evolutionary Ecology Research* 5, 717-730.

van der Wal, P., Giesen, H.J., Videler, J.J., 2000. Radular teeth as models for the improvement of industrial cutting devices. *Materials Science & Engineering C-Biomimetic and Supramolecular Systems* 7, 129-142.

van Lenthe, G.H., Hagenmuller, H., Bohner, M., Hollister, S.J., Meinel, L., Muller, R., 2007. Nondestructive micro-computed tomography for biological imaging and quantification of scaffold-bone interaction in vivo. *Biomaterials* 28, 2479-2490.

Vecchio, K.S., 2005. Synthetic multifunctional metallic-intermetallic laminate composites. *Jom* 57, 25-31.

Vermeij, G.J., 1982. Unsuccessful Predation and Evolution. *American Naturalist* 120, 701-720.

Vermeij, G.J., 1987. *Evolution & Escalation: An Ecological History of Life*, Princeton University Press, Princeton, NJ.

Vermeij, G.J., 2006. *Nature: An Economic History*, Princeton University Press, Princeton, NJ.

Vincent, J.F.V., 1990. *Structural biomaterials*, Princeton, NJ: Princeton University Press.

Vincent, J.F.V., Wegst, U.G.K., 2004. Design and mechanical properties of insect cuticle. *Arthropod Structure & Development* 33, 187-199.

- Viswanath, B., Raghavan, R., Ramamurty, U., Ravishankar, N., 2007. Mechanical properties and anisotropy in hydroxyapatite single crystals. *Scripta Materialia* 57, 361-364.
- Vogel, S., 2003. *Comparative Biomechanics*, Princeton Univ. Press, Princeton, NJ.
- Wacker, K., Bartsch, P., Clemen, G., 2001. The development of the tooth pattern and dentigerous bones in *Polypterus senegalus* (Cladistia, Actinopterygii). *Ann. Anat.* 183, 37-52.
- Wainwright, S.A., 1969. Stress and design in bivalved mollusc shell. *Nature* 224, 777.
- Wainwright, S.A., Biggs, W.D., Currey, J.D., Gosline, J.M., 1976. *Mechanical Design in Organisms*. New York, John Wiley & Sons.
- Walsh, M.J., 1983. Riblets as a Viscous Drag Reduction Technique. *Aiaa Journal* 21, 485-486.
- Walsh, M.J., 1990. Riblets. *Prog. Astro. Aero* 123, 203-261.
- Wang, L.F., Boyce, M.C., 2010. Bioinspired Structural Material Exhibiting Post-Yield Lateral Expansion and Volumetric Energy Dissipation During Tension. *Advanced Functional Materials* 20, 3025-3030.
- Wang, L.F., Song, J.H., Ortiz, C., Boyce, M.C., 2009. Anisotropic design of a multilayered biological exoskeleton. *Journal of Materials Research* 24, 3477-3494.
- Wang, R.Z., Addadi, L., Weiner, S., 1997. Design strategies of sea urchin teeth: Structure, composition and micromechanical relations to function. *Philosophical Transactions of the Royal Society of London Series B-Biological Sciences* 352, 469-480.
- Wang, R.Z., Gupta, H.S., *In press*. Deformation and Fracture Mechanisms of Bone and Nacre. *Annual Review of Materials Research*, Vol 40 10.1146/annurev-matsci-062910-095806.
- Wang, R.Z., Suo, Z., Evans, A.G., Yao, N., Aksay, I.A., 2001. Deformation mechanisms in nacre. *Journal of Materials Research* 16, 2485-2493.
- Wark, A.R., Peichel, C.L., 2010. Lateral line diversity among ecologically divergent threespine stickleback populations. *Journal of Experimental Biology* 213, 108-117.
- Webb, J.F., 1989. Gross Morphology and Evolution of the Mechanoreceptive Lateral-Line System in Teleost Fishes. *Brain Behavior and Evolution* 33, 34-53.
- Wegst, U.G.K., Ashby, M.F., 2004. The mechanical efficiency of natural materials. *Philosophical Magazine* 84, 2167-2181.

- Weiner, S., 2006. Transient precursor strategy in mineral formation of bone. *Bone* 39, 431-433.
- Weiner, S., Addadi, L., 1997. Design strategies in mineralized biological materials. *Journal of Materials Chemistry* 7, 689-702.
- Weiner, S., Addadi, L., Wagner, H.D., 2000. Materials design in biology. *Materials Science & Engineering C-Biomimetic and Supramolecular Systems* 11, 1-8.
- Westneat, M.W., 2003. Biomechanical models of feeding in fishes: New applications of lever and linkage theory. *Integrative and Comparative Biology* 43, 825-825.
- Westneat, M.W., 2004. Evolution of levers and linkages in the feeding mechanisms of fishes. *Integrative and Comparative Biology* 44, 378-389.
- White, S.N., Luo, W., Paine, M.L., Fong, H., Sarikaya, M., Snead, M.L., 2001. Biological organization of hydroxyapatite crystallites into a fibrous continuum toughens and controls anisotropy in human enamel. *Journal of Dental Research* 80, 321-326.
- Williams, M.J., 1978. Opening of bivalve shells by mud crab *scylla serrata* forskal. *Australian Journal of Marine and Freshwater Research* 29, 699-702.
- Willmer, P., 2002. Invertebrate Skeletons. *ENCYCLOPEDIA OF LIFE SCIENCES*, 1-6.
- Woesz, A., Weaver, J.C., Kazanci, M., Dauphin, Y., Aizenberg, J., Morse, D.E., Fratzl, P., 2006. Micromechanical properties of biological silica in skeletons of deep-sea sponges. *Journal of Materials Research* 21, 2068-2078.
- Wolf, J.B.W., Lindell, J., Backstrom, N., 2010. Speciation genetics: current status and evolving approaches. *Philosophical Transactions of the Royal Society B-Biological Sciences* 365, 1717-1733.
- Woo, S.L.Y., Akeson, W.H., Jemott, G.F., 1976. Measurements of nonhomogeneous, directional mechanical properties of articular cartilage in tension. *Journal of Biomechanics* 9, 785-791.
- Wootton, R.J., 1994. Energy allocation in the threespine stickleback, In: Bell, M.A., Foster, S.A. (Eds.), *The Evolution of the Threespine Stickleback*. Oxford University Press, Oxford, NY, USA. pp. 240-276.
- Wyneken, J., Godfrey, M.H., Bels, V., 2008. *Biology of turtles*, CRC Press.
- Yannas, I.V., 2001. *Tissue and Organ Regeneration in Adults*, Springer-Verlag New York, Inc.

Yao, H., Dao, M., Imholt, T., Huang, J., Wheeler, K., Bonilla, A., Suresh, S., Ortiz, C., 2010. Protection mechanisms of the iron-plated armor of a deep-sea hydrothermal vent gastropod. *Proc. Nat. Acad. Sci. USA* 107, 987-992.

Zhu, M., Zhao, W.J., Jia, L.T., Lu, J., Qiao, T., Qu, Q.M., 2009. The oldest articulated osteichthyan reveals mosaic gnathostome characters. *Nature* 458, 469-474.

Zuschin, M., Stachowitsch, M., Stanton, R.J., 2003. Patterns and processes of shell fragmentation in modern and ancient marine environments. *Earth-Science Reviews* 63, 33-82.